Deformation, Strains and Velocities for the Alpine Himalayan Belt from trans-continental Sentinel-1 InSAR & GNSS

J. R. Elliott[a], J. Fang[a], M. Lazeck´y[a], Y. Maghsoudi[b], Q. Ou[c], J. A. Payne[a], C. Rollins[d], D. Wang[a], A. Hooper[a], T, J. Wright[a]

[a]COMET, School of Earth & Environment, University of Leeds, Woodhouse Lane, Leeds, LS2 9JT, West Yorkshire, UK

[b]Centre for Environmental Mathematics, University of Exeter, Penryn Campus, Nr Falmouth, TR10 9FE, Cornwall, UK

[c]School of GeoSciences, University of Edinburgh, Drummond Street, Edinburgh, EH8 9XP, West Lothian, UK

[d]Earthquake Physics and Statistics, GNS Science, 1 Fairway Drive, Avalon, 5011, Lower Hutt, New Zealand

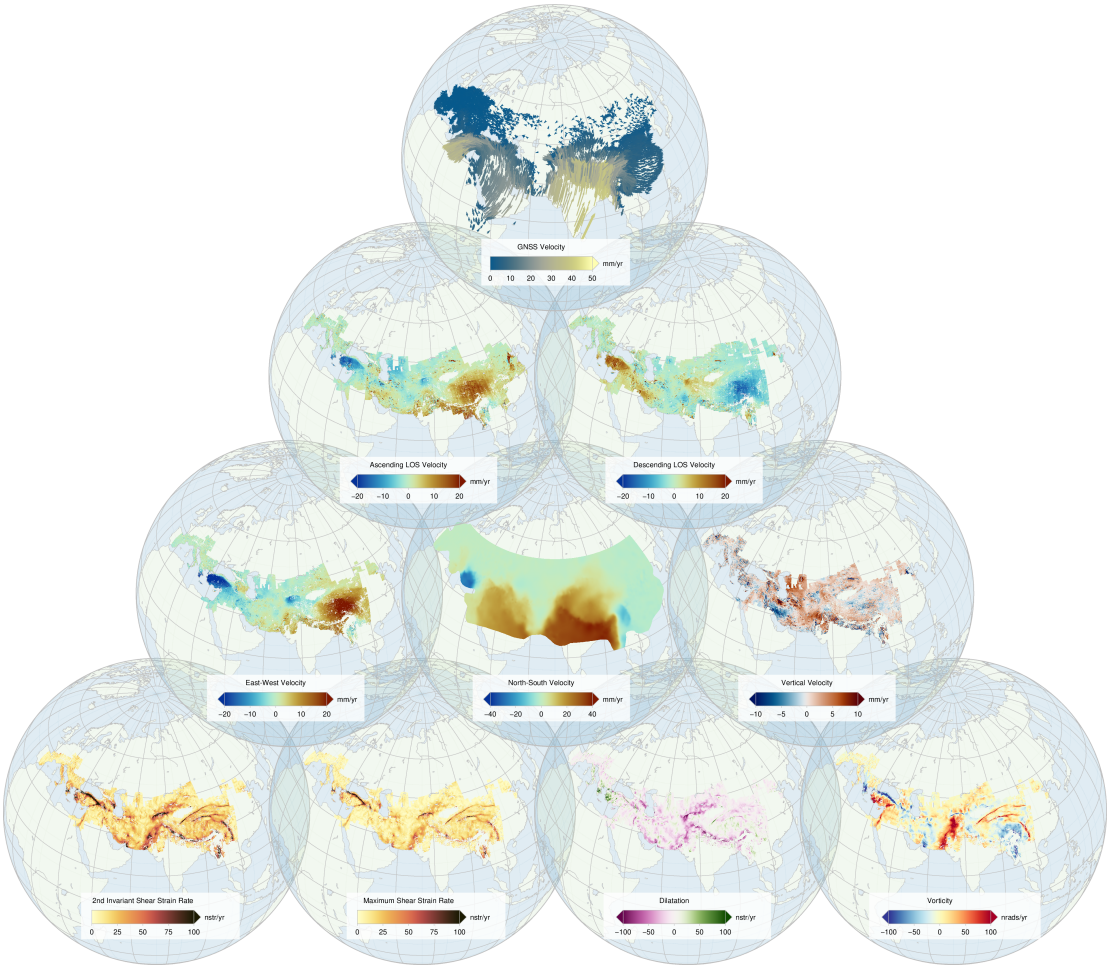
j.elliott@leeds.ac.uk, j.fang@leeds.ac.uk, m.lazecky@leeds.ac.uk, y.maghsoudi-mehrani@exeter.ac.uk, Qi.Ou@ed.ac.uk, eejap@leeds.ac.uk, c.rollins@gns.cri.nz, eedwa@leeds.ac.uk, a.hooper@leeds.ac.uk, t.j.wright@leeds.ac.uk

This paper is a non-peer reviewed preprint submitted to EarthArXiv. The preprint was submitted to a journal for peer review and is currently in review with Remote Sensing of the Environment.

Graphical Abstract

Deformation, Strains and Velocities for the Alpine Himalayan Belt from trans-continental Sentinel-1 InSAR & GNSS

J. R. Elliott, J. Fang, M. Lazecký, Y. Maghsoudi, Q. Ou, J. A. Payne, C. Rollins, D. Wang, A. Hooper, T, J. Wright



Highlights

Deformation, Strains and Velocities for the Alpine Himalayan Belt from trans-continental Sentinel-1 InSAR & GNSS

J. R. Elliott, J. Fang, M. Lazecký, Y. Maghsoudi, Q. Ou, J. A. Payne, C. Rollins, D. Wang, A. Hooper, T, J. Wright

- First 3D velocity field of Alpine-Himalayan Belt derived from Sentinel-1 InSAR & GNSS
- Strain localised on major faults with diffuse deformation extensive across continents
- Horizontal motion is dominated by tectonics; vertical from aquifer-driven subsidence

Deformation, Strains and Velocities for the Alpine Himalayan Belt from trans-continental Sentinel-1 InSAR & GNSS

J. R. Elliott[a], J. Fang[a], M. Lazecký[a], Y. Maghsoudi[b], Q. Ou[c], J. A. Payne[a], C. Rollins[d], D. Wang[a], A. Hooper[a], T, J. Wright[a]

[a] *COMET, School of Earth & Environment, University of Leeds, Woodhouse Lane, Leeds, LS2 9JT, West Yorkshire, UK*
[b] *Centre for Environmental Mathematics, University of Exeter, Penryn Campus, Nr Falmouth, TR10 9FE, Cornwall, UK*
[c] *School of GeoSciences, University of Edinburgh, Drummond Street, Edinburgh, EH8 9XP, West Lothian, UK*
[d] *Earthquake Physics and Statistics, GNS Science, 1 Fairway Drive, Avalon, 5011, Lower Hutt, New Zealand*

Abstract

Surface velocities and strain rates from satellite geodesy have become essential tools for understanding the distribution of tectonic deformation, faulting and seismic hazard. However, across large regions of distributed continental deformation, such as the Alpine-Himalayan Belt, data are only sparsely available. While previous studies have mainly used spatially sparse GNSS to measure deformation at such large scales, these approaches cannot characterize shorter wavelength features of deformation in many places. We use Sentinel-1 radar images acquired during 2016-2024 to provide trans-national average surface velocities and time series at 1 km spatial resolution stretching a distance of over 11,000 km from south-western Europe to eastern China, covering an area more than 20 million square kilometres. We produce the velocity field by combining data from over 222,000 Sentinel-1 SAR images with a new belt-wide compilation of GNSS velocities, all combined in a consistent Eurasian reference frame. Horizontal strain rates are derived from gradients of the velocity field, yielding near-continuous spatial deformation information over the entirety of the largest deforming region on the planet. The horizontal velocities and strains are dominated by tectonic deformation, which has a bimodal behaviour – focused on major faults but distributed elsewhere. Shorter-wavelength vertical velocities are dominated by non-tectonic processes, in particular the widespread

over-exploitation of groundwater. Our new velocity and strain rates are foundational data sets that reveal the details of how the continents deform for the first time at trans-continental scale.

Keywords: Radar remote sensing, GNSS, Sentinel-1, InSAR, Active Tectonics, Continental Deformation, Faulting, Strain, Seismic Hazard, Earthquakes

1. Introduction

The collision of the African, Arabian, and Indian plates with Eurasia has created the Alpine Himalayan Belt (AHB), a vast region of thickened crust and mountain ranges spanning the southern margin of the Eurasian continent (Figure 1) and reaching ~2,000 km into its interior in places. This major orogeny creates, supports and shapes the highest mountains in the world and has been a long-standing focus of research on the deformation of the continents (Molnar and Tapponnier, 1978; England and Jackson, 1989). The region is marred by numerous active seismogenic faults (Styron and Pagani, 2020), generating some of the largest, and often most fatal, earthquakes (Bilham, 2019) – 75% of earthquakes that have killed more than 10,000 people since 1900 have occurred here (England and Jackson, 2011). Understanding the kinematics of this range is important for constraining the style of tectonics of the continents (Jackson and McKenzie, 1984; Yin, 2010), which in turn act as first-order constraints on dynamical models of deformation (England and Molnar, 1997; Vergnolle et al., 2007) and how the continents and margins might evolve through time (McKenzie, 2025). Increasingly, deformation data are important inputs for seismic hazard assessments, providing independent constraints on slip rates of major faults and spatial maps of moment accumulation rates (Bird et al., 2015; Field et al., 2015; Stevens and Avouac, 2021).

The recent explosion in the availability of remotely-sensed data from satellite platforms, particularly this past decade by the European Space Agency's Sentinel-1 radar mission (Salvi et al., 2012; Potin et al., 2016), has enabled a step change in the scale of Interferometric Synthetic Aperture Radar (InSAR) measurements of surface deformation (Gabriel et al., 1989). The open Sentinel-1 archive and advances in big data processing

(e.g., Lazecký et al., 2020) have enabled us to produce the first transcontinental, decadal time series of surface velocities at a resolution of 1 km. This allows us to resolve details of tectonic processes at scale. From the Sentinel-1 data, and our new compilation of Global Navigation Satellite System (GNSS) data, we derive three-component average surface velocities in a consistent Eurasian reference frame, and estimates of horizontal surface strain rates. The results show the contrast in tectonic deformation between regions of high strain localisation and those with more distributed deformation, as well as highlighting non-tectonic processes, particularly those associated with exploitation of groundwater. We make these new time series, velocities and strain rates freely available for further analysis and modelling by the wider community.

1.1. Motivation: Understanding the deformation of the continents

Understanding present-day deformation of the continents is important for assessing the distribution of seismic hazard through the calculation of strain rates (Ward, 1998; Bird et al., 2010), and for constraining crustal tectonic kinematics to allow testing and assessment of continental deformation dynamics (e.g., Flesch et al., 2001; Wang and Barbot, 2023; Fang et al., 2024a).

It has long been recognized that plate tectonics operates differently in the continents than oceans (McKenzie, 1972; Molnar and Tapponnier, 1975; McKenzie, 2025), but understanding how continents deform has been hampered by the lack of observations with the spatial resolution required to resolve tectonic processes. Understanding where and why contrasting styles of deformation are observed remain key questions in active tectonics (Thatcher, 2007). For example, why does seismicity and strain in some regions appear largely focused on large block-bounding faults such as the North Anatolian Fault (Weiss et al., 2020), similar to the behaviour seen in oceanic lithosphere, whereas other regions appear more diffuse (Watson et al., 2024)? Establishing this is useful for calculating the distribution of hazard (Liu and Stein, 2016), and determining the degree to which continents experience on-fault versus off-fault deformation (Zeng and Shen, 2016). We want to be able to determine the seismic moment accumulation rate as this sets the budget for future earthquakes; geodetic strain-rate observations al-

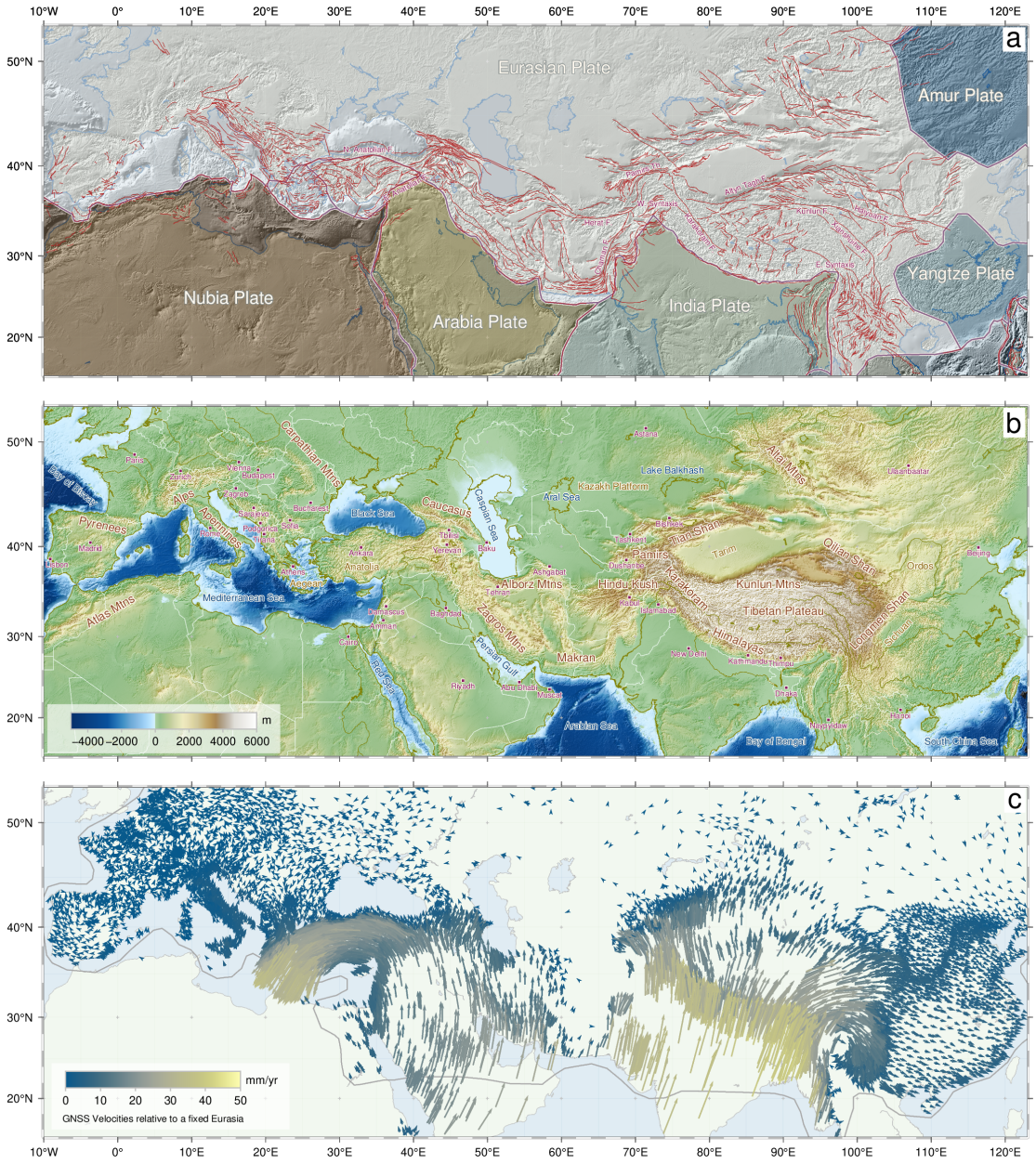


Figure 1: (a) Major active faults of the Alpine Himalayan orogeny (Styron and Pagani, 2020) with the tectonic plates of the region outlined from Bird (2003) and the major faults (F.) named in the text marked. (b) Topographic map of the belt with major mountain zones marked in brown and capital cities denoted by squares. (c) Compiled and aligned GNSS locations used in this study (Tables SA1–SA2) with velocities shown with respect to a fixed Eurasia reference frame (velocities with respect to the ITRF14 are shown in Figure SB1). The combined InSAR-GNSS velocity field coverage is denoted by the dark grey polygon.

low us to estimate this (Guns et al., 2024). At a crustal scale, a long-standing argument has been determining the most parsimonious way of describing the kinematic behaviour of the continental crust in terms of block-like behaviour (Thatcher, 2007), continuum behaviour (Houseman and England, 1986), or a mixture of both (Wang and Barbot, 2023; Fang et al., 2024a,b).

To address these questions, we require the current rates of surface deformation and the degree of localisation of strain, as these provide key inputs for constraining future models and act as secular rates to compare against when exploring time-varying behaviour of crustal deformation. Previous studies made significant progress using sparser GNSS data (Reilinger et al., 2006; Thatcher, 2009; Stamps and Kreemer, 2024), or local and regional InSAR based studies (Elliott et al., 2016). The widespread availability of Sentinel-1 data (Torres et al., 2012) is a timely opportunity to produce an internally referenced and consistent continent-wide InSAR-derived velocity field. This is particularly important for areas that, unlike Europe (Piña-Valdés et al., 2022) and the Western U.S. (Herring et al., 2016), lack (and are unlikely to readily achieve) dense GNSS coverage.

Here we introduce previous regional scale deformation studies, before presenting the two principal datasets of GNSS and InSAR. We describe our compilation of previously-published GNSS velocities and how we align them to create a consistently referenced set of data. We then provide our methodological and systematic approach to generating and correcting the InSAR time series before illustrating how we integrate this with the GNSS constraints to generate velocity and strain rate fields at a trans-continental scale. We show the resulting components of velocity and measures of strain across the Alpine Himalayan Belt as a whole, before focusing on a few key deforming tectonic areas. We discuss the sources of these signals and the limitations of measuring strain in the presence of the remaining noise in our time series. We finish by discussing the potential implications for our broader understanding of continental deformation and the outlook for improvements expected with data from future satellite missions.

2. Background

The AHB has long been recognised as a wide collisional zone (Argand, 1922) and exhibits a range of deformation styles running from west-to-east (Jackson and McKenzie, 1984). There are three major sections of the collisional zone that predominantly align with the three converging plates to the south of Eurasia (Figure 1) the tectonics of which are discussed further in the Supplementary Information (Section 2).

2.1. Remotely Sensed Data and Technological Advances

Our ability to determine the deformation of the continents has been greatly advanced in the past two decades by space-based technologies and data sets (Elliott et al., 2016; Stamps and Kreemer, 2024). Initial progress was made through regional GNSS studies (Feigl et al., 1993; Abdrakhmatov et al., 1996; Reilinger et al., 1997; Wang et al., 2001; Calais et al., 2003; Nocquet and Calais, 2003), before the global strain rate model (GSRM-1) provided horizontal velocities and low-resolution strain rates for most of the deforming plate boundary zones from over 3,000 GNSS sites globally (Kreemer et al., 2003). This was advanced in version 2.1 of GSRM (Kreemer et al., 2014) by incorporating over 22,000 velocities in the model. The most recent Europe Velocity model for 2022 (EuVeM2022) is constrained by data from 2,549 GNSS sites with an output resolution of 0.1° (Steffen et al., 2025) and covers Europe and Anatolia.

Distributed measurements of surface velocities from InSAR over deforming regions, when suitably referenced with GNSS data, can advance our understanding of continental deformation by increasing the resolution of velocity fields (and the strain rates calculated from them) where GNSS coverage is sparse. There has been a transition from the earliest studies with InSAR on deforming regions which solely focused on single tracks of data less than 100 km in extent (Peltzer et al., 2001; Wright et al., 2001), largely with ERS-1/2 data (Bürgmann et al., 2000), to entire fault systems (Tong et al., 2013; Hussain et al., 2018) predominately with ENVISAT data, and more recently using Sentinel-1 SAR to capture deformation over large tectonically deforming regions (Xu et al., 2021; Lemrabet et al., 2023; Fang et al., 2024a) and whole country scales (Dehls et al., 2019;

Drouin and Sigmundsson, 2019; Weiss et al., 2020; Festa et al., 2022; Zhang et al., 2024), and now large fractions of continents (Costantini et al., 2021).

In addition to technical advancements in SAR instrumentation, typified by the changes from ERS-1/2 (Attema et al., 1998) through ENVISAT-ASAR (Desnos et al., 2000) to Sentinel-1A/B (Torres et al., 2017) enabling more systematic acquisitions and observations suitable for interferometry, there have been improvements in processing SAR (Goldstein and Werner, 1998; Rosen et al., 2012; Sandwell et al., 2011), mitigating atmospheric noise (Lohman and Simons, 2005; Li et al., 2005; Jolivet et al., 2014; Bekaert et al., 2015) and enhancing time series analysis (Hooper et al., 2004; Hetland et al., 2012). This has enabled imaging of ever smaller displacement rate signals (mm/yr) over larger spatial scales of many hundreds of kilometres. Improvements accounting for tropospheric variability in delay using weather models (Jolivet et al., 2011; Murray et al., 2019) and the ionosphere (Liang et al., 2019) using global ionospheric maps, enables smaller signals over longer wavelengths to be increasingly discernable.

Large data volumes have necessitated changes in approach (input data alone is PetaByte scale), with automation of processing of Big Data needed in pipelines on High Performance Computing (HPC), as used here (Lazecký et al., 2020). Various groups have initiatives for covering areas or providing on-demand processing to derive analysis-ready data, enabling wider adoption by the broader community without need for large computing power. ForM@Ter LArge-scale multi-Temporal Sentinel-1 InterferoMetry (FLATSIM, Doin et al., 2011) is an initiative providing processed products over broad regions for research. The Alaska SAR Facility (ASF) archives the SLC data from ESA and provides processing capability (Meyer et al., 2025). They also host the Jet Propulsion Laboratory (JPL) geocoded and unwrapped interferograms (Bekaert et al., 2023) and velocities for North America. The European Ground Motion Service is available for (most of) Europe (Costantini et al., 2021) with high-resolution velocities available. The German Aerospace Center (DLR) has a pipeline for processing all major deforming regions (Gomba et al., 2024). Efforts to make InSAR data easier to use are progressing in the form of Analysis Ready Data (Wang et al., 2022b).

2.2. Challenges and Approach Taken Here

A number of challenges exist in generating continental-scale velocity and strain rate fields given the large spatial scale (tens of millions of square kilometres) and fine sensitivity sought (mm/yr velocities and strain rates of tens of nanostrain per year). The data volumes and their ongoing acquisition, whilst very welcome for science, present constant data handling and processing challenges. Whilst Sentinel-1 SLC (Single Look Complex) data has pixel spacings of ∼4 m in ground range and 14 m in azimuth, it has been necessary to multilook the interferometric images to 50 m and downsample further to 110 m as a compromise to facilitate processing and storage. With the time series analysis and velocity field generation, further downsampling to 1 km has been necessary to make processing tractable.

Stratified layered noise introduced from water vapour and pressure path delay differences in the troposphere between acquisitions can be significantly reduced by applying weather model corrections (Bekaert et al., 2015; Murray et al., 2019). However, this correction is less accurate in regions of steep topography with large gradients in water vapour or in regions with complex and highly convective weather patterns and fronts, as weather reanalysis models do not well capture short-wavelength turbulent weather conditions. The assessment of long-wavelength ionospheric corrections is still developing, as the total electron content variability, which advances the phase of the signal, depends on latitude and time of acquisition (Liang et al., 2019). Being C-band, Sentinel-1 is less susceptible to ionospheric phase variability than L-band satellites, but the signal is still significant. The 11-year solar cycle (Hathaway, 2015) has a large impact on the ionosphere (Roma-Dollase et al., 2018); the solar cycle 24 high occurred around the launch of Sentinel-1A in early 2014, and solar activity was therefore decreasing for the early part of our time series (starting early 2016), but it has been increasing and was more elevated than expected by our end date in early 2024.

Whilst shorter wavelength C-band is better in terms of ionospheric noise, it is less good in terms of phase coherence than L-band, leading to a loss of data coverage in some areas, in particular those that are more vegetated and cultivated, where surface

properties change rapidly (Kellndorfer et al., 2022). This affects the AHB most markedly in the west (Europe to Anatolia) and in the south-east (around the Himalayas and Eastern Tibet). This is in part mitigated by the short revisit time of Sentinel-1, which was particularly good when S1A and S1B were both in operation, until the loss of the SAR antenna power supply unit on S1B on 23rd December 2021. Issues of coherence were further compounded when there were large acquisition gaps (sometimes year-long gaps) over certain regions due to limitations of the duty cycle. Additionally, data was not acquired in Eastern China (Figure SB2). High mountain areas with steep relief such as the Caucasus and Himalayas (Grandin et al., 2012) lead to further gaps in data coverage and large phase unwrapping errors due to the loss of connected coherence across our scenes.

Interferometric coherence with Sentinel-1 has been better maintained, when compared to ENVISAT and ERS-1/2, by improved orbital control. The orbital tube target originally targeted ~ 100 m (Prats-Iraola et al., 2015), keeping it well within the critical baseline for interferometry. However, recent reduced orbital inclination control on S1A, from partial failure of the thruster for out-of-plane manoeuvres in February 2024, has led to increasingly large perpendicular baselines (Pinjeiro, 2024) that are likely to have a detrimental impact on interferometric performance and capabilities.

InSAR data, when used alone, is severely hampered by providing a single line-of-sight and only relative deformation (Hu et al., 2014). Even when two look directions are combined, polar-orbiting satellites that look to one side only, are largely insensitive to north-south motion (Wright et al., 2004b). North-south information can be extracted from burst overlap areas Sentinel-1 (Li et al., 2021a), but the coverage is poor. Due to this lack of 3-component information and the need to reference the InSAR data, we also use GNSS data. There are significant numbers of GNSS sites in Europe and Eastern China, but there is a low density of sites in the centre of the AHB around Afghanistan and Pakistan (Figure SB1). This presents challenges when trying to reference the InSAR data and interpret long-wavelength deformation patterns.

Our aim is to measure surface displacements and calculate velocities that are repre-

sentative of tectonic processes due to deep-seated deformation sources of stress causing strain over long wavelengths. However, near-surface processes such as land subsidence (Haghshenas Haghighi and Motagh, 2024; Wu et al., 2022) and permafrost (Chen et al., 2022; Fan et al., 2025) mask deeper-seated tectonic strains, in particular in regions where we would want to measure uplift rates reliably, and therefore these areas must be interpreted carefully.

We derive decadal surface velocity fields from which we calculate crustal horizontal strain rates. Our aim is to capture the long-term, interseismic part of the earthquake cycle (Wright, 2002) in these measurements. However, the velocity field is calculated over a finite duration and incorporates the coseismic offsets of recent earthquakes, which we need to remove from our time series as they otherwise manifest as large strains due to the elastic release of strain accumulation. Furthermore, the stress from the earthquakes themselves results in postseismic deformation that can be attributed to a number of causes (Hearn, 2003; Feigl and Thatcher, 2006; Wright et al., 2013) and lasts for many years and potentially decades. Given that the earth behaves viscoelastically, and faults can slip aseismically, it is not straightforward to attribute interseismic strain accumulation to fault slip potential (Hussain et al., 2018), depending on the rheology of the fault zone and crust (Hilley et al., 2009) and when within the earthquake cycle the deformation is measured (Savage and Prescott, 1978; Wang et al., 2021). A knowledge of historical earthquake locations enables us to test to what degree the elevated strains we are measuring today result from the postseismic deformation of past seismicity.

Sentinel-1 presents relatively moderate resolution SAR data at the 5–20 m scale. However, it is necessary to work with multi-looked data for increased spatial correlation, producing pixels of equal dimensions and reducing data volumes in the Small Baseline Subset (SBAS) process. However, the process of multi-looking of interferograms results in mis-closure of the phase loops because the filtering effect is non-conservative for some land cover types (De Zan et al., 2015). This is attributed to the vegetation and soil water content (De Zan et al., 2014; De Zan and Gomba, 2018). In regions of agriculture, careful interpretation of the apparent ground deformation is required (Jiang and Lohman, 2021)

as these regions result in large signals varying in space and time if cultivated. Soil moisture effects phase closure in arid regions (Lohman and Bürgi, 2023). This issue is exacerbated for short-period, multi-looked interferograms such as used here that result in a fading bias (Ansari et al., 2021), a situation now prevalent with the shorter revisit time of 1–2 weeks offered by Sentinel-1 when compared to ENVISAT and ERS-1/2 acquisitions (typically spanning more than a month). There are empirical mitigation approaches that may be possible to apply at scale in future (Maghsoudi et al., 2022).

Some of these challenges have been addressed here with our processing strategies and this study provides an important historical record of recent deformation and a baseline for change detection in upcoming decades. However, future upcoming missions should also provide improvements in these areas. The recently launched Sentinel-1C/D satellites, NISAR (Kellogg et al., 2020) and planned missions such as Harmony (Kääb et al., 2024), ROSE-L (Davidson and Furnell, 2021), and Sentinel NG (Torres et al., 2024) will be discussed later in this context.

2.2.1. Aims and Objectives

We aim to produce a dataset useful for informing ideas of continental deformation and improving seismic hazard assessment. Our objectives are to produce a compilation of GNSS velocities for the AHB and use these with InSAR data to create a geodetically constrained displacement time series and average velocity fields of use to the wider community. Our approach builds on areas in the Belt we previously produced velocity fields using Sentinel-1 from Türkiye (Weiss et al., 2020) through Iran (Watson et al., 2024), the Tian Shan and onto the Tibetan Plateau (Ou et al., 2022; Wright et al., 2026; Shen et al., 2024a; Wang et al., 2024; Fang et al., 2024a). We have updated these, and greatly expanded the spatial coverage to unify them into a single velocity field, by performing near-uniform interferometric processing with common time spans where possible. This is then tied to the new compilation of GNSS velocities we generate here for the Eurasian plate to provide a fully referenced dataset.

3. Data

Our velocity field is derived by compiling and combining two key geodetic data types that image the present-day motion of the Earth's surface: 1) GNSS and other point velocities, which provide a comparatively sparse but accurate picture of surface motion in an internally consistent reference system; and 2) InSAR time series of distributed surface displacements, which provide dense estimates of relative velocity across broad areas, but which need to be suitably referenced to reliably be interpreted over longer wavelengths.

3.1. GNSS and other point velocities

To align and reference the InSAR velocities, we compile 73,335 point velocities of surface motion across the Alpine-Himalayan Belt (Figure SB3) from 171 studies and datasets (Tables SA1–SA3). These include 63,120 GNSS velocities (of which 27,401 are 3D, 31,576 are horizontal-only and 4,143 are vertical-only), 10,074 levelling rates, and 24 DORIS, 83 SLR and 34 VLBI velocities. Some of the 171 sources themselves include velocities from preceding publications; for example, the Global Strain Rate Model 2.1 (GSRM) dataset (Kreemer et al., 2014) includes velocities from 109 older studies in our study area. We do aim to prioritise velocities that are at least partially based on measurements from the Sentinel-1 era, for consistency with the InSAR data; so most of the 171 main sources are from 2014 or later (Tables SA1–SA3). Section 4.1 describes the eight-step procedure we use to combine these velocities into an underpinning 3D point-velocity field (including removing many superseded older velocities in favor of newer high-quality velocities).

3.2. SAR

We use Single Look Complex (SLC) data from the Sentinel-1 C-band SAR instrument (centre frequency 5.405 GHz) with Vertical Transmit–Vertical Receive (VV) polarisation acquired by the European Space Agency (ESA). We use these data to derive surface displacement measurements across the Alpine Himalayan Belt using differential interferometry (Section 4.2). The Sentinel-1 mission provides systematic near-global radar

imaging (Torres et al., 2012; Potin et al., 2016), enabling precise monitoring of long-term ground deformation at a continental scale. Most of the tectonic belts are imaged with both ascending and descending orbits (Figure SB2), providing two independent viewing geometries that enable us to separate east-west and vertical deformation.

We source the data from both the Alaska SAR Facility (Meyer et al., 2025) and also through the Near Line Archive at UK's data analysis facility for environmental science (JASMIN). The data we select typically span from early 2016 (beginning of March) to early 2024 (end of February, see Supplementary Material Appendix C for exact dates) except when we choose to initiate the time series late or finish it early to mitigate the effects of earthquakes (Section 4.4). The satellite constellation comprises both Sentinel-1A and its near identical pair Sentinel-1B (Miranda et al., 2017) during much of this time. The AHB from southern Europe to eastern China is captured by 62 partially-overlapping, 250-km-wide orbital tracks in each of the ascending and descending directions (Figure SB2). At lower latitudinal areas in our study (25°N), the tracks overlap by about two-thirds of a subswath (∼50 km), and at the highest latitude (50°N) by over one subswath (∼100 km). This yields complete spatial coverage and some redundancy in each direction, except at the edges of the polygon shown on Figure 1c, and which we use for velocity uncertainty analysis (Section 4.7). Data are typically available in both look directions, enabling us to resolve east-west and vertical components of motion with the use of GNSS to constrain north-south motions (e.g., Wright et al., 2004b; Weiss et al., 2020). An exception is the easternmost part where there is a gap in descending data between the Eastern Tibetan Plateau and Beijing around the Ordos Plateau (Figures 1 & SB2).

We divide the entire AHB into 928 LiCSAR (Looking inside the Continents from Space) frames (Lazecký et al., 2020), consisting of 469 ascending and 459 descending frames (Figure SB2). Each frame comprises multiple bursts (typically 13 in each of the 3 subswaths) acquired in Interferometric Wide Swath (IW) mode (Geudtner et al., 2014) using Terrain Observation by Progressive Scans (TOPS) (Yagüe-Martínez et al., 2016). The total dataset includes 221,319 Sentinel-1 epochs, providing a dense spatio-temporal

sampling of surface displacement across the region. From 2016 to 2021, the region from southern Europe to eastern Türkiye was covered by 6-day repeat-pass acquisitions, benefiting from the combined operation of Sentinel-1A and Sentinel-1B. However, following the failure of Sentinel-1B in December 2021, the acquisition frequency for this region was reduced to 12 days. For the rest of the study area, including the central and eastern portions of the AHB, the 12-day repeat cycle was used throughout the observation period where possible, although some tracks experience longer revisit times and temporal data gaps.

3.3. Ancillary data

In addition to the SAR datasets themselves, a number of ancillary datasets are needed in the processing chain (Figure 2), in particular to apply corrections to the interferograms for phase changes resulting from the changing atmosphere (Section 4.3), including phase delays through the troposphere (Yu et al., 2018b), and phase advances through the ionosphere (Yunjun et al., 2022).

We also require precise orbital ephemerides (POE) data for satellite positions to facilitate the coregistration steps between SLCs, provided by ESA (Fernández et al., 2024). In the InSAR processing, it is also necessary to account for topography in the simulated phase. Additionally, a geographic dataset is required to reference the interferograms from radar to the geographic coordinate system. To address these two requirements, we use either the SRTM (Farr et al., 2007) or Copernicus GLO-30 (Rizzoli et al., 2017) Digital Elevation Models (DEMs) (as recorded in the metadata for each frame).

4. Methodology

Our approach starts with combining published GNSS and point velocities into an underpinning (lower-resolution) 3D velocity field across the Alpine-Himalayan Belt (Figure 1). We then create line-of-sight velocities and time series from ESA Sentinel-1 satellite radar data through interferometric processing. The InSAR velocities are combined with the aligned GNSS velocities to create surface velocities in a Eurasia-fixed reference frame and strain rates as output datasets for further interpretation (Figure 2).

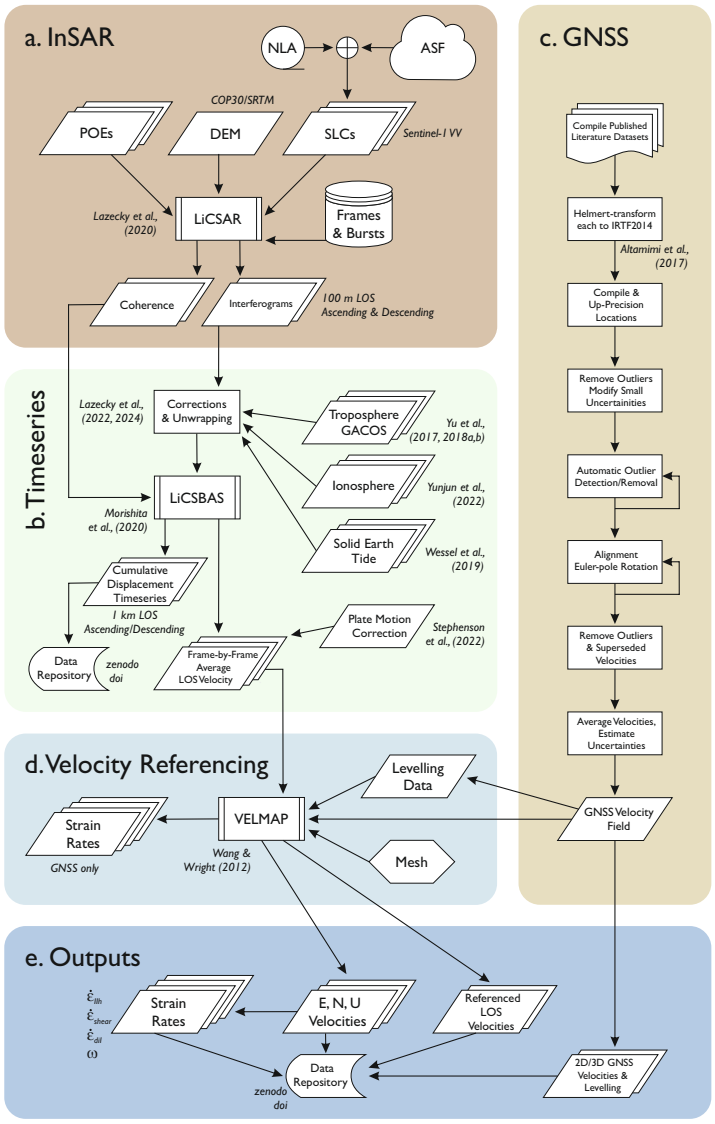


Figure 2: Workflow for (a) InSAR processing chain and (b) correction and time series calculation, (c) GNSS compilation, quality control and alignment, (d) unified velocity generation and (e) final strain rate field calculations and outputs. InSAR - Interferometric Synthetic Aperture Radar, NLA - Near-Line Archive, ASF - Alaska SAR Facility, POE - Precise Orbital Ephemerides, DEM - Digital Elevation Model, COP30 - Copernicus 30 m, SRTM - Shuttle Radar Topography Mission, SLC - Single Look Complex, VV - Vertical Transmit–Vertical Receive Single Polarisation, LiCSAR - Looking inside the Continents from Space SAR, LOS - Line-of-Sight, LiCSBAS - Looking inside the Continents from Space Small Baseline Subset, GACOS - Generic Atmospheric Correction Online Service, GNSS - Global Navigation Satellite System, ITRF2014 - International Terrestrial Reference Frame, E, N, U - East North, Up. $\dot{\varepsilon}_{II_h}$ = second invariant of strain rate, $\dot{\varepsilon}_{shear}$ = maximum shear strain rate, $\dot{\varepsilon}_{dil}$ = horizontal dilatation rate, ω = vorticity, (Savage et al., 2001).

4.1. GNSS: generating a reference frame

We use an eight-step procedure to combine the GNSS and point-velocity datasets into a unified velocity field (Figure 2c). In step 1, we transform each individual dataset's velocity field into the ITRF2014 no-net-rotation (NNR) reference frame (Altamimi et al., 2017) using *itrstrafo* (Wasmeier, 2025). Because different studies used different reference velocities and methods to get into their original reference frames, some systematic differences will remain between these rotated velocity fields; we handle these in step 5.

In step 2, we "up-precision" the GNSS station locations by grouping collocated velocities and using the most precise available location for each station as the single location for all velocities at that station. Because the original compiled station locations are not identical (usually due to studies' varying rounding practices), we define that two velocities are collocated if (1) they have the same station code and their locations are no more than 1.6 km from each other (equivalent to a 0.01° difference in both longitude and latitude, to allow for the case of one study truncating 0.005°E, 0.005°N as 0.00°E, 0.00°N while another study rounds it to 0.01°E, 0.01°N), or (2) their locations (regardless of station codes) are within 0.16 km of each other (a 0.001° difference in longitude and latitude). We use a larger threshold distance in case (1) for a few studies that round locations to the nearest 0.1° or contain numerous location errors. We then rotate all of the velocities into the ITRF2014 Eurasia-fixed reference frame (Altamimi et al., 2017) for easier visual inspection (Figure SB3).

In step 3, we begin filtering the velocity field. We first remove 1,469 velocities that (1) have implausibly large horizontal components ($>$ 100 mm/yr) in either the ITRF2014 NNR or ITRF2014 Eurasia-fixed frame, (2) have uplift or subsidence rates of $>$ 40 mm/yr (indicating likely contamination by nontectonic processes such as subsidence from water extraction), (3) are based on $<$ 1.5 years of data, (4) have relatively large uncertainties of $>$ 5 mm/yr in the east or north component or $>$ 8 mm/yr in the vertical component, (5) have uncertainties that are unspecified or are given as zero and cannot be re-estimated from station metadata, (6) are indicated to be problematic by their contributing studies or subsequent studies, or (7) are otherwise clearly problem-

atic but are not flagged by the automatic outlier-removal algorithm we use subsequently (usually due to having too few velocities nearby). These threshold values were all set based on testing and/or external considerations: for example, we use a duration cutoff of 1.5 yr rather than the commonly used 2.5 yr (Blewitt and Lavallée, 2002) in order to retain some of the only available velocities in Afghanistan.

There are 102 other velocities for which the uncertainties are unspecified or given as zero but can be re-estimated using the indicated data timespans and numbers of occupations at each station. We use these metadata to re-estimate these 102 uncertainties using a model of combined random-walk, white and flicker noise, with noise coefficients taken from Castro-Perdomo et al. (2022), Williams et al. (2004) and Wang et al. (2012) and equations from Beavan et al. (2016), Williams (2003) and Bos et al. (2008). We also change very small nonzero GNSS velocity uncertainties to "minimum reasonable" values, which we estimate from the lower ends of the distributions of velocity uncertainties in Steffen et al. (2025), Piña-Valdés et al. (2022), Socquet and Janex (2019) and Serpelloni et al. (2022). We take the 0.135th-percentile uncertainty value from each of these studies (which would be the -3σ value in a normal distribution) and compute the geometric mean of these values (separately for horizontal and vertical components), yielding "minimum reasonable" uncertainties of 0.042 mm/yr for horizontal components and 0.15 mm/yr for verticals. Nonzero uncertainties smaller than these values are changed to them.

In step 4, we filter the velocity field further by using an iterative procedure to automatically identify and remove anomalous velocities. For each velocity V_A, we compare each component V_{Ai} of that velocity to the distribution of that component of velocity at nearby stations, $[V_{Bi}, ..., V_{Ni}]$. "Nearby" is formally within a maximum distance from V_A. Through trial and error, we set this maximum distance to 175 km, just less than the widths of most of the Red Sea and Persian Gulf and of the central parts of the Black and Caspian Seas (in order to avoid mixing velocities across them). As implemented, if V_{Ai} differs from both the median and mean of $[V_{Bi}, ..., V_{Ni}]$ by more than ∼3–4 times the mean absolute deviations (MADs) of $[V_{Bi}, ..., V_{Ni}]$ about those central values, then V_A

is flagged as an outlier. In order to flag the largest outliers first and remove them from subsequent evaluations of other velocities, we implement that "∼3–4" above is formally a gradually decreasing scalar multiple C of the MADs, with more and more outliers progressively flagged and removed over many iterations as C is decreased towards a minimum value. Through trial and error, we choose a minimum value of 3.25 for C. For robustness, we require that a V_{Ai} cannot be evaluated as a possible outlier unless there are at least 5 uniquely located velocities within 175 km of it (with component i); and to increase spatial adaptiveness, if there are more than 25 uniquely located velocities with component i within 175 km of V_A (the case for most sites in Europe), we only use velocities from the nearest 25 locations. These parameter values were set through extensive testing, and versions of the algorithm without one or more of these constraints yielded less satisfactory results. As implemented, this algorithm flags and removes 6,799 outliers, leaving 65,066 velocities (Figure SB4).

In step 5, we align the velocity datasets (minimise the remaining systematic differences between them) using an iterative approach. For each study S_A, we tabulate the differences in horizontal velocities between it and all other studies $[S_B, ..., S_Z]$ at sites $i, j...$ that S_A shares with each. This velocity differences vector is here called $[D_{AiBi}, D_{AjBj}, ..., D_{AgZg}, D_{AhZh}]$, and we also compute the formal uncertainty on each velocity difference. The idea is to fit $[D_{AiBi}, D_{AjBj}, ..., D_{AgZg}, D_{AhZh}]$ to a rotation about an Euler pole, R_A, using least squares (Ader et al., 2012); R_A would then be subtracted from S_A to reduce its systematic velocity differences from other studies. If S_A is systematically misaligned with other overlapping datasets, R_A should be a coherent rotational adjustment, while if S_A is well aligned with others, the velocity differences should be incoherent and R_A should have effectively zero magnitude. In estimating R_A, we implement several measures to guard against model overfitting. First, we do not include velocity differences between S_A and S_B if they share < 3 sites (Rui and Stamps, 2019) or only share sites over a very small total area. Second, rather than fitting $[D_{AiBi}, D_{AjBj}, ..., D_{AgZg}, D_{AhZh}]$ to a single Euler-pole model, we take 1,000 random-length subsamples of that difference vector and add random noise to each subsample

(normally distributed random noise scaled by the formal uncertainties on the velocity differences included). We then fit each "noised" subsample to an Euler-pole rotation model and compute the model-predicted velocity adjustments at all sites in S_A. If these predicted adjustments vary in azimuth by $\geq$90° across S_A, we infer that the model is overfit and discard the solution. If more than 900 solutions out of 1,000 are discarded, we replace the Euler-pole rotation with a model of a uniform shift in eastward and northward motion and recompute all 1,000 models. In either case, we take the median of the non-discarded model predictions as the adjustment to be applied to S_A.

The iterative approach we use is to estimate these adjustments for each of the 171 datasets simultaneously, apply 5% of each adjustment to its study, recompute all the adjustments, apply 5% of each new adjustment, and so on for N iterations. (Applying 5% at a time yielded better convergence than any larger fraction.) To choose the number of iterations N, we note that progressively subtracting 5% of a number (e.g., a velocity difference) N times leaves 0.95^N of the original number, and 135 is the lowest N for which $0.95^N < 0.001$, so we use $N = 135$ iterations. The final issue is how to treat studies that include previous studies' velocities and have already aligned these within their own combinations (e.g., Kreemer et al. (2014), Khorrami et al. (2019), Wang and Shen (2020)). Here we refer to these as compilations for brevity (although they are not purely compilations as they usually include their own processed velocities as well). In principle these compilations could be treated as single unified datasets, although on inspection we do observe some systematic (generally small) differences between how different compilations align and handle older velocities. Therefore, we first run 135 alignment iterations in which we treat compilations as single datasets, then run a second 135 iterations in which we split compilations out into their constituent parts and treat those as independent datasets (approximately 315 in total). (The one exception is that we split out (Kreemer et al., 2014) into its constituent parts from the beginning.) The aligned velocity field after these 270 total iterations is shown in Figure SB5.

In step 6, we rerun the automatic outlier detector on the aligned velocities and remove 62 additional velocities that now qualify as outliers. In step 7, we filter out duplicate

and superseded velocities in favour of velocities from studies with relatively few outliers. First, we separate the 171 studies into those that provide 3D velocities, horizontal-only velocities (2D), a mix of 3D and horizontal-only ("2.5D"), and vertical-only. We define a threshold fraction, T that is incrementally decreased from 1.0 to a minimum of 0.1. For each value of T, we find any study, S_A, that has had a fraction larger than T of its original velocities flagged as outliers and removed. If there is an overlapping study S_B that (1) has an outlier fraction less than T and (2) has a dimensionality at least as large as S_A (e.g., S_A provides horizontal velocities and S_B provides 3D, 2.5D or 2D velocities), then all of S_A's velocities at sites also covered by S_B are removed. (The one exception to the dimensionality rule is that studies with vertical-only velocities cannot be superseded by studies that are horizontal-only or 2.5D.) This procedure removes 21,436 velocities, leaving 43,568 remaining (Figure SB6). Most of the velocities based wholly on pre-2014 (pre-Sentinel) data are removed in this step: many of those were contributed by the compilations of Kreemer et al. (2014) as well as by Palano et al. (2018) and Serpelloni et al. (2013), and those studies have relatively low outlier fractions of 0.12, 0.14 and 0.17, but nevertheless retain only 18%, 9% and 7% of their velocities after this step (respectively) due to mostly overlapping with studies with even lower outlier fractions such as Wang and Shen (2020) (outlier fraction 0.015), Khorrami et al. (2019) (0.018), Pintori et al. (2022) (0.018), Piña-Valdés et al. (2022) (0.042), Steffen et al. (2025) (0.049) and others. A few studies completely overlap with another study with a lower outlier fraction (and at least the same dimensionality) and so have no velocities retained (Tables SA1–SA3).

Finally, in step 8, we combine velocities that are collocated (here defined as within 1.6 km of each other). At locations with multiple velocities, we take the combined velocity in each component (east, north and up) to be halfway between the mean and the median of the available velocities in that component. To estimate the uncertainty on this combination, we represent each of the available velocities by a Gaussian PDF (with sigma equal to its velocity uncertainty) and combine these into a single PDF. We compute two uncertainty metrics for the mean - the standard deviation of the combined

PDF, and the MAD of the combined PDF about the mean multiplied by 1.2533 (Geary, 1935) - and likewise for the median, yielding four possible pairings with which to formally represent the uncertainty on the average of the mean and median. We compute the sum of squares of each pair (halving the individual uncertainties, as we are estimating the overall uncertainty on half the mean plus half the median) and average these as the preferred uncertainty estimate for each component of velocity. At locations with only one velocity, we simply use it and its uncertainty as the final values.

At the end of this combination of steps (Figure 2c), there are 21,476 point velocities spanning the Alpine-Himalayan Belt, including 6,668 3D velocities, 5,384 horizontal velocities and 9,424 vertical rates (Figure 3). In total, 12,052 velocities provide constraints on horizontal surface motion (i.e., are 2D or 3D) and 16,092 constrain vertical motion (are 3D or pure vertical).

4.2. LiCSAR: from SAR to InSAR

We adapt the methodology outlined in Lazecký et al. (2020), starting from Level-1 Single Look Complex data from Sentinel-1A/B (Figure 2) to generate a redundant network of over 1,200,000 interferograms over the Alpine-Himalayan Belt. The interferograms are multilooked and geocoded to grids of 0.001 degrees (approx. 110 m) resolution in the WGS-84 reference system. The good orbital control of the Sentinel-1 constellation results in a relatively tight orbital tube with perpendicular baselines typically within ±200 m that enables us to more easily generate coherent interferograms without applying baseline thresholds. As well as the standard four consecutive interferometric connections (forwards and backwards) per temporal epoch (same for both 6 or 12 days revisit time), we densify the network forming additional combinations that cover longer time periods of up to 12 months for some regions such as the Tian Shan. Including long-span interferograms in such networks helps overcome limitations such as data gaps due to decorrelation resulting from the presence of seasonal snow and a fading phase bias that can affect short-span interferograms (Maghsoudi et al., 2022).

To ensure data consistency and avoid errors from the early time-series, we select the time period from March 2016 up to March 2024, and perform an updated phase

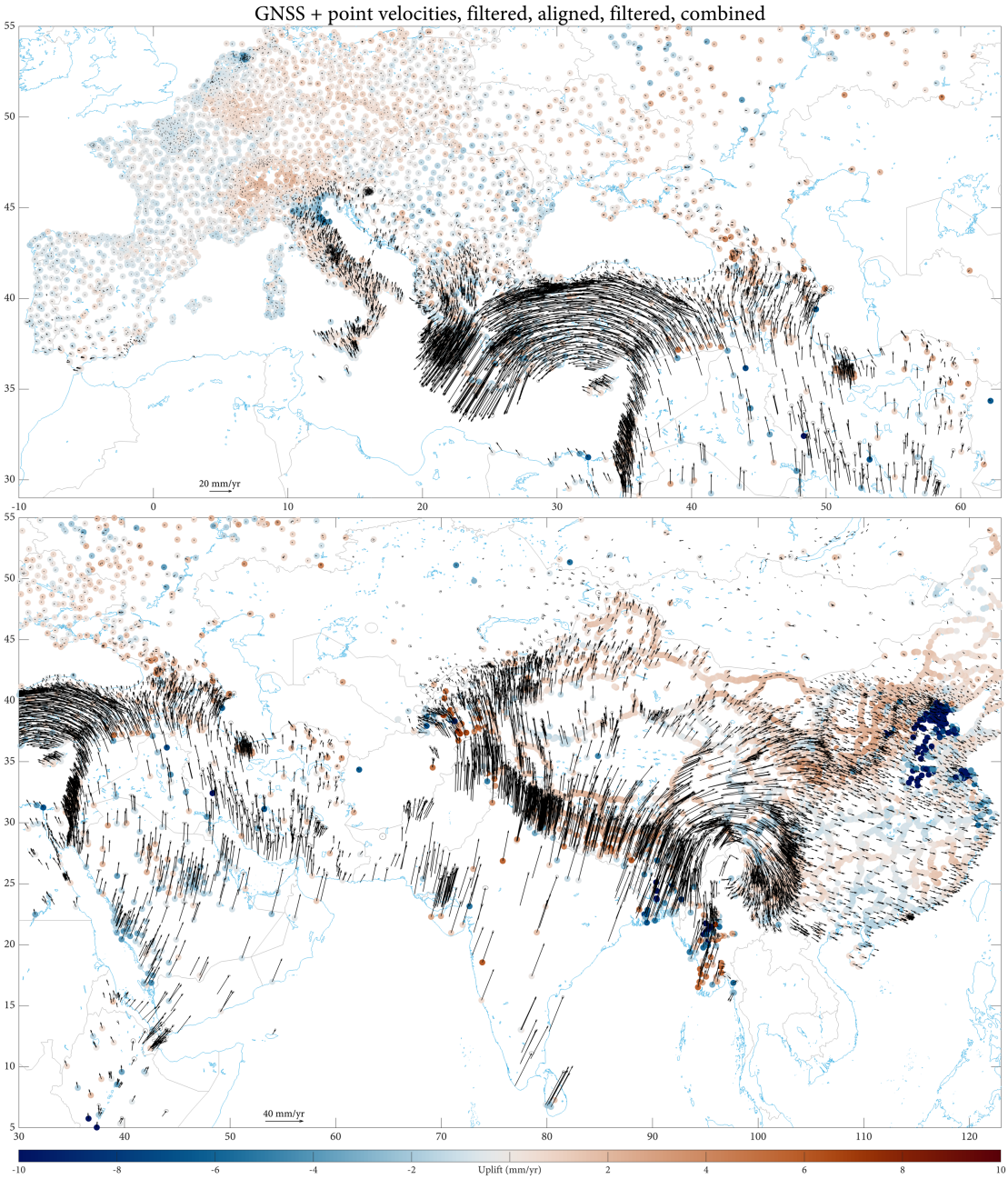


Figure 3: The prepared 3D combination of GNSS and point velocities used to reference and align the InSAR data, in the western AHB (top) and central/eastern AHB (bottom). Arrows show horizontal motions with respect to the ITRF2014 Eurasia-fixed reference frame (Altamimi et al., 2017); coloured circles show vertical motion rates.

unwrapping routine (Lazecky et al., 2022). The phase unwrapping utilizes an up-to-date version of SNAPHU at its core (Chen and Zebker, 2002) and is performed on the original LiCSAR geocoded unfiltered interferograms that are further multilooked by a factor of 10 in both latitude and longitude, yielding the final resolution of 0.01 × 0.01 degree (approximately 1×1 km), and corrected for some of the non-tectonic signals (Section 4.3), where line-of-sight correction maps were generated per epoch and combined to form simulated correction interferograms. Removal of these terms improves the quality of the unwrapping procedure as observed in LiCSBAS (Looking Inside the Continents from Space Small Baseline Subset) quality metrics (Morishita et al., 2020) described later. For a portion of frames, the unwrapped data with coherence (Figure SB9) estimated below 0.15 were masked prior to the time series inversion, effectively avoiding the propagation of errors due to noise into the inversion. The processing parameters were optimised for each individual frame, with parameters listed in Supplementary Materials Appendix C.

4.3. Corrections of atmospheric and tidal signals in interferograms

A number of corrections are made on an epoch-by-epoch basis to reduce the noise (Figure 2). This includes phase delays/advances from both the troposphere and ionosphere and non-tectonic surface deformation from solid earth tides, which we can model and remove. An analysis of average correction gradients shows that the effect of the troposphere is an order of magnitude higher than the other terms (Figures SB7 and SB8). The velocities inverted from ionosphere corrections also display significant quasi-planar ramps (Figure 4) for ascending frames (acquired at ∼6 p.m. local time).

4.3.1. Troposphere

We use the tropospheric corrections derived by the Generic Atmospheric Correction Online Service for InSAR (GACOS, Yu et al. (2018b,a)), which generates zenith total delay maps (combined wet and hydrostatic delays) from the High Resolution ECMWF weather model at 0.1-degree spatial and 6-hour temporal resolutions. We convert them to slant range delays using the incidence angle for each pixel based on our East, North, Up unit vector files for each frame for the line-of-sight pointing vector from the satellite

to the ground (Figure SB10).

4.3.2. Ionosphere

We follow the method of Yunjun et al. (2022) and extract total electron content (TEC) values from GNSS-based global ionospheric maps (GIMs) produced by the Center for Orbit Determination in Europe (CODE) to infer the ionospheric phase advance. We interpolate TEC values with rotation and extract them at the ionospheric piercing points, assumed to be at an altitude of 450 km, with 20 km sampling. We assume that 85% of the GIM TEC is below the satellite (Sentinel-1 orbits at $\sim$ 700 km), as suggested by an analysis using the IRI2016 model (Bilitza et al., 2017), although this ratio will vary by time of day, season and latitude. We then calculate the slant range ionospheric phase advance modified by refraction (Lazecký et al., 2023) and upsample it using bilinear interpolation to provide the correction (Figure SB11).

4.3.3. Solid Earth Tides

The long-wave signal from the tides due to lunisolar gravitational forces on the solid Earth has a regular periodicity and can be modelled with high accuracy, allowing correction of InSAR results to prevent temporal aliasing (Xu and Sandwell, 2020). We use the standard model, as implemented in the *earthtide* tool of Generic Mapping Tools (GMT) (Wessel et al., 2019), to calculate vectors of tidal displacements, which we transform to slant range direction and use for correction (Figure SB12).

Corrections for ocean tide loading (periodic water mass redistribution from Earth-Moon interaction, DiCaprio and Simons (2008)) can also be made. However, this is more important for regions with large tidal ranges, such as NW Europe. However, the impact on mean velocities for long time series averaged over many years, as in this study, is below 1 mm/year (Wu et al., 2024) and we do not apply the correction here.

4.4. LiCSBAS: time series inversion and corrections

We perform time series inversion of the input networks of unwrapped corrected interferograms with $0.01° \times 0.01°$ resolution using a Small Baselines Subset (SBAS) method

that allows for high spatial coverage in regions with reasonable interferometric coherence (Li et al., 2022). Specifically, we use an updated version of the LiCSBAS algorithm (Morishita et al., 2020; Morishita, 2021) that implements a method that retains some data points that were previously masked due to transient noise or incoherence, on the assumption of a constant velocity. We initially use the full network of interferograms generated with temporal and perpendicular baselines as described in Section 4.2.

Prior to the time series inversion, we identify and exclude coseismic interferograms over significant earthquakes (Section 4.4.1), introducing data gaps in the input network. Those gaps are spanned during the later inversion on the assumption of a constant velocity. We identify relatively stable reference areas based on spatio-temporal statistics of the interferometric network and generate interferometric phase loop closure triplets $I_{ABC} = I_{AB}+I_{BC}-I_{AC}$ for all possible combinations of interferograms I from acquisition dates A, B, C. We assume that residuals in triplets formed from correctly unwrapped interferograms should be smaller than π radians. As our interferometric network is highly redundant, we use the phase loop closure information to identify and drop pixels with unwrapping errors (Shen et al., 2024b; Lazecký et al., 2024). We also allow for possible overall shifts of up to ± 2 phase cycles due to an inconsistent reference area. Additionally, we calculate the mean of the absolute wrapped phase loop error per pixel, as an indicator of potential phase bias (Figure SB13). This is later used as one of the quality measures for the masking of noisy pixels.

Using weights derived from individual coherence maps (Morishita et al., 2020), we perform weighted least squares inversion of the interferometric network into temporal increments that, after cumulating in time, form displacement time series. We store the root mean square error (RMSE) of residuals from this inversion and use its average value per interferogram to identify and drop noisy input interferograms from the network for some frames, then repeat the inversion. This is done exceptionally for whole interferograms where the average loop closure phase is extremely high (over 10 radians). Typically, though, we apply a pixelwise nullification approach (Shen et al., 2024b) that reduces the inversion RMSE by removing only noisy pixels within individual interfero-

grams rather than whole interferogram (with a default value of 12 mm for most frames). The pixel-wise residual RMSE is also used as one of the quality measures for masking of noisy pixels (Supplementary Information Appendix C).

After masking noisy pixels using the phase bias indicator, RMSE, and several other quality measures (Morishita et al., 2020), we perform spatio-temporal filtering of the cumulative time series to estimate residual atmosphere that is correlated spatially but not temporally on short time scales (Hooper et al., 2007). This is achieved by high-pass filtering in time (using a Gaussian window of width of usually 36 or 72 days, which is three times the average interval between epochs) and low-pass spatial filtering (using a Gaussian window of 2 km width at 1σ truncated at 8σ to yield a 17×17 pixel kernel, given the 1 km pixel spacing). After subtracting the estimated atmosphere, we estimate the mean velocity using unweighted least squares. We use the original unfiltered time series to estimate the velocity standard deviation using bootstrapping (Efron and Tibshirani, 1986), which we further flatten based on a semivariogram analysis to remove the influence of distance from the reference area (Ou et al., 2022) and give a measure of the velocity uncertainty (Figure SB15). Finally, we estimate and subtract Eurasian plate motion for all frames (Figure SB14), including those outside Eurasia, by calculating velocities of rotation around the Eurasian plate Euler pole (Stephenson et al., 2022). Some of the key processing parameters are listed in Supplementary Information Appendix C per frame, as they vary by frame, particularly in individual masking thresholds.

4.4.1. Earthquakes

InSAR is good at capturing the deformation associated with shallow crustal earthquakes of moderate to large magnitude (Funning and Garcia, 2019). However, the presence of coseismic displacements results in errors when estimating the long-term velocities associated with interseismic strain accumulation from the time series of interferogram displacements. Therefore, a mitigation strategy is employed to remove the primary effect of the earthquake coseismic deformation field itself. In order to solve for coseismic offsets or truncate the time series to mitigate against such effects, we extract a list of significant earthquakes with locations and depths from the USGS catalogue. We limit

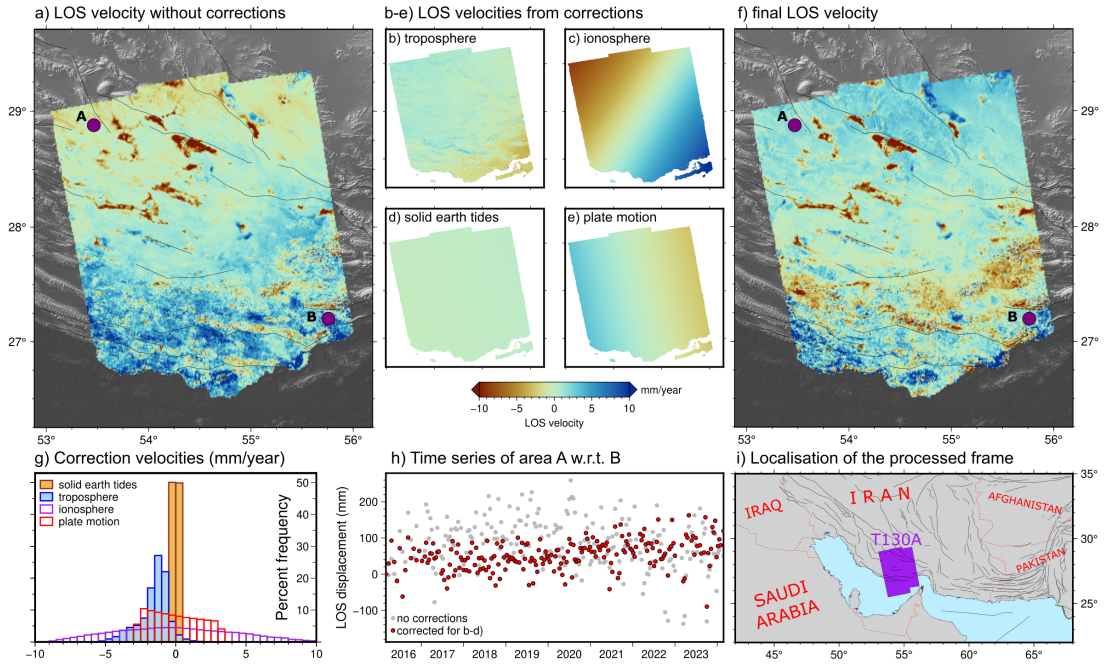


Figure 4: Application of corrections on example frame 130A_06248_212118 over the Zagros mountains of southern Iran: a) LOS average velocity from original time series of uncorrected interferograms; b-d) velocity inverted from time series corrections on troposphere, ionosphere and solid earth tides, respectively; e) plate motion velocity correction (Figure SB14); f) normalized frequency histogram of the b–e correction velocities; g) final LOS velocity with all corrections applied; h) relative LOS displacement time series between locations A and B (reference), locations shown in subpanels a,f, from both datasets before and after b–d corrections. i) Inset map of Iran with location of frame coverage extents denoted in purple.

ourselves to moderately sized earthquakes with magnitudes $M_w > 6.0$ which are also sufficiently shallow (< 35 km) to potentially produce a displacement signal at the surface (29 events, excluding aftershocks, Table SA4 and Figure SB16). We then manually review each event to ascertain the number of frames affected and decide whether to truncate the time series by starting it after the earthquake (if near the beginning of our time series in 2016) or stopping it before the event (if it occurs towards 2024), or, as in most cases, allowing for an offset in the time series to be solved for across the earthquake date (Table SA4). This greatly reduces the impact of the earthquake on the velocity estimation, although the impacts of any long-term postseismic signals associated with

these events will still be present.

4.5. VELMAP

Following the completion of LiCSAR/LiCSBAS processing (Figure 2), each frame is independently referenced for line-of-sight (LOS) velocity estimation (Figure SB17). To construct a unified velocity field in a Eurasia-fixed reference frame, we integrate these LOS velocities with compiled GNSS data (Figure 3) using the approach coded from Wang and Wright (2012) called VELMAP (Wang and Wright, 2025).

We first define the outline of the triangular mesh by applying a 75 km buffer along the outermost frame boundaries, ensuring adequate GNSS and levelling coverage near the mesh edges (Figure SB18). To enhance computational efficiency and memory management, we generate the mesh with vertices spaced at approximately 40 km.

The inversion simultaneously estimates velocities at each triangular mesh node, reference frame adjustment parameters, a linear atmospheric correction term based on elevation, and a long-wavelength quadratic ramp for each frame (Wang and Wright, 2012). Three-dimensional (3D) velocities at InSAR and GNSS observation points are interpolated from the triangular mesh nodes. Before the VELMAP inversion, InSAR LOS rates are downsampled to a resolution of ∼10 km. As part of the regularisation, we apply Laplacian smoothing in the inversion, adjusting the relative strength of the smoothing term to achieve a balance between solution roughness and misfit. The combined geodetic solution is then used to generate mosaics of ascending and descending LOS velocities in a Eurasia-fixed reference frame (Figure 6) at the original resolution of 0.01° (∼1 km).

Uncertainties in the line-of-sight velocities are propagated to uncertainties in 3D velocity model using the standard equations (Wright et al., 2004b). We construct an initial covariance matrix for the GNSS data using their formal uncertainties (Figure 3), and for the InSAR data using the rescaled line-of-sight uncertainties estimated by LiCSBAS (Figure SB15). We then iteratively update the GNSS and InSAR covariance matrices using a variance component estimation method until their relative ratio approaches unity (Grafarend, 1984). We extract variances and covariances from the variance-covariance

matrix of the estimated model parameters (3D velocity at each vertex of the triangular mesh).

4.6. 3D Velocity and Strain Rate generation

With ascending and descending referenced line-of-sight (LOS) velocities (Figure SB17), we only have two independent components of the 3D velocity field (Wright et al., 2004b). To decompose these into the more readily interpretable eastward and vertical velocities, we follow the approach of Hussain et al. (2018) and Weiss et al. (2020) — we apply a pixel-by-pixel inversion at ∼1 km resolution, with the northward velocity constrained to be equal to the coarse resolution velocity field obtained from the VELMAP inversion (Figure 7a).

We then compute the strain rate fields by taking the gradients of the median-filtered InSAR eastward velocities (Figure SB19) and the smoothed GNSS northward velocities (Figure 7). The horizontal strain-rate tensor, $\dot{\varepsilon}_h$, represents the symmetric component of the velocity gradient tensor. We derive the second invariant ($\dot{\varepsilon}_{II_h}$), maximum shear ($\dot{\varepsilon}_{shear}$), and dilatation ($\dot{\varepsilon}_{dil}$) of the horizontal strain-rate tensor. The second invariant of the strain rate tensor represents the overall magnitude of strain and provides a scalar measure of strain rate that is independent of coordinate orientation. The maximum shear component characterises the peak shearing deformation. Horizontal dilatation corresponds to the trace of the strain rate tensor and indicates areal extension or contraction. These are defined, including the spherical correction terms, where θ is the colatitude of each pixel and r is the Earth's radius (r=6,378 km), as follows (Savage et al., 2001; Kreemer et al., 2014; Sandwell and Wessel, 2016; Wang and Shen, 2020):

$$\dot{\varepsilon}_h = \begin{bmatrix} \dot{\varepsilon}_{xx} & \dot{\varepsilon}_{xy} \\ \dot{\varepsilon}_{yx} & \dot{\varepsilon}_{yy} \end{bmatrix} = \begin{bmatrix} \dfrac{\partial V_E}{\partial x} - \dfrac{V_N \cos\theta}{r \sin\theta} & -\dfrac{1}{2}\left(\dfrac{\partial V_E}{\partial y} + \dfrac{\partial V_N}{\partial x} + \dfrac{V_E \cos\theta}{r \sin\theta}\right) \\ -\dfrac{1}{2}\left(\dfrac{\partial V_N}{\partial x} + \dfrac{\partial V_E}{\partial y} + \dfrac{V_E \cos\theta}{r \sin\theta}\right) & \dfrac{\partial V_N}{\partial y} \end{bmatrix} \tag{1}$$

$$\dot{\varepsilon}_{II_h} = \sqrt{\dot{\varepsilon}_{xx}^2 + 2\dot{\varepsilon}_{xy}^2 + \dot{\varepsilon}_{yy}^2} \tag{2}$$

$$\dot{\varepsilon}_{shear} = \sqrt{\dot{\varepsilon}_{xy}^2 + \frac{(\dot{\varepsilon}_{xx} - \dot{\varepsilon}_{yy})^2}{4}} \tag{3}$$

$$\dot{\varepsilon}_{dil} = \dot{\varepsilon}_{xx} + \dot{\varepsilon}_{yy} \tag{4}$$

The rotation rate tensor is the antisymmetric part of the velocity gradient tensor. The vorticity vector, ω, is twice the rotation rate tensor (Liu et al., 2018).

$$\omega = \frac{\partial V_N}{\partial x} - \frac{\partial V_E}{\partial y} \tag{5}$$

We have masked out regions where the absolute magnitude of the vertical velocities exceeds 20 mm/yr (Figure 7c), as these values are unlikely to represent tectonic signals. These regions are prevalent across Iran, and there are also large areas in China (east of the Tian Shan and south of Beijing). We have applied the same mask to the eastward velocities to ensure that these anomalous regions do not influence the overall strain analysis. To mitigate short-wavelength noise in the InSAR eastward velocities, a median filter is applied to non-NaN pixels to derive the preferred strain rate fields using a window size of ~150 km. Although this filtering approach reduces noise, it also damps down any real short-wavelength strain signals visible in the data, for example, due to fault creep (Section 5.3.1).

4.7. LOS Uncertainty Analysis

The mosaics of the two InSAR line-of-sight (LOS) velocities in a common reference frame, as well as the VELMAP north velocities from GNSS, allow us to evaluate the uncertainties of our LOS velocities at track overlaps, where we have a redundancy of one LOS velocity measurement in ascending or descending (Figure 5). Following Wright et al. (2026), we first divided the LOS velocity tracks into four groups, A1, A2, D1, and D2, each containing alternate tracks in the ascending (A) or descending (D) geometry. Instead of using all four groups of LOS velocities and the VELMAP north velocities to derive east and vertical velocities for the entire coverage, we can perform the same operation using a subset three of the groups (e.g., A2, D1 and D2) to produce a version

of the east and vertical velocities that partially overlaps with the group left out (e.g., A1). Using east and vertical velocities derived without group A1, we can independently reconstruct the estimated LOS velocities at pixels overlapping with group A1 using the observation geometries of group A1. The root-mean-square (RMS) differences between the actual observed and independently reconstructed LOS velocities are 2.7 mm/yr and 2.6 mm/yr for the ascending and descending geometries, respectively (Figure 5c-f). The largest differences we observe typically occur in areas with snow or vegetation cover, such as the Himalayan front and northern India, central Europe, and the Caucasus (Figure 5a,b).

The above-reported values are RMS of LOS differences between 1 and 99 percentiles, corresponding to ∼-12 mm/yr and ∼12 mm/yr, respectively. With all pixels included, the RMS differences would have been 4.0 mm/yr and 4.4 mm/yr for ascending and descending geometries, respectively, which are inconsistent with the narrower histogram peaks observed in Figure 5d,f than in Figure 5c,e. To avoid bias from extreme values in the lowest and highest percentiles, we therefore evaluate uncertainties based on differences between 1 and 99 percentiles for subsequent analysis.

The differences between the observed and reconstructed LOS velocities do not result from equal contributions of errors within the two datasets, as the reconstructed LOS is itself estimated from east and vertical velocities derived from three other LOS velocities, as well as the north velocities constrained by GNSS and the mesh. We first estimate the uncertainties of east and vertical velocities by calculating the differences between two independent estimates of east and vertical velocities in the diamond-shaped areas ($\sim 70 \times 300$ km,varying by latitude) that result when the land surface is overlapped by observations in all four geometries (A1+D1 versus A2+D2 and A1+D2 versus A2+D1). The RMS of 1–99% of the differences in these independently decomposed east and vertical velocities are 2.9–3.1 mm/yr and 2.4–2.5 mm/yr, respectively (Figure SB20). Split equally between the two independent estimates, the uncertainties of east and vertical velocities derived from one ascending geometry and one descending geometry are 2.1 mm/yr and 1.7 mm/yr, respectively.

The uncertainty of the reconstructed LOS velocities can then be estimated by projecting these uncertainties of east (2.1 mm/yr) and vertical (1.7 mm/yr) velocities, and a conservative estimate of 3 mm/yr for the north velocity uncertainty (Figure SB21a) into the satellite's LOS (Wright et al., 2026). Taking the resulting 1.9 mm/yr uncertainty of the reconstructed LOS (which is typically dominated most by the vertical and least by the northern uncertainty due to the viewing geometry), out of the 2.7 mm/yr and 2.6 mm/yr differences between observed and reconstructed ascending and descending LOS velocities yields an estimated 1.9 mm/yr and 1.8 mm/yr uncertainties of the observed ascending and descending LOS velocities respectively.

The slightly lower uncertainty of the descending LOS velocities compared to that of the ascending LOS velocities is expected as the interferograms created from data acquired along descending tracks contain lower levels of tropospheric and ionospheric noise, being acquired at dawn rather than dusk (Figures SB7, SB8, SB10 and SB11). This is a time when the troposphere experiences less convective turbulence than at the end of the day and also, a period when the ionosphere is only beginning to increase in ionisation and generate its extra sublayers in the daytime.

We then propagate the LOS uncertainties through the decomposition equation to derive pixel-wise uncertainties of east and vertical velocities (Figure SB22). The RMS of the pixel-wise uncertainties are 1.9 mm/yr for east velocities and 1.5 mm/yr for vertical velocities, lower than before because of constraints from all geometries.

These uncertainties compare well with the 2.4 mm/yr differences between InSAR and GNSS east velocities, 3.1 mm/yr differences between InSAR and GNSS vertical velocities, and 1.8 mm/yr differences between InSAR and levelling vertical velocities (Figure SB23). These results are consistent with our expectations of InSAR east velocities being less accurate than GNSS east velocities, and InSAR vertical velocities being more accurate than GNSS vertical velocities (due to InSAR's incidence angles between 30–45°), but less accurate than levelling-derived vertical velocities.

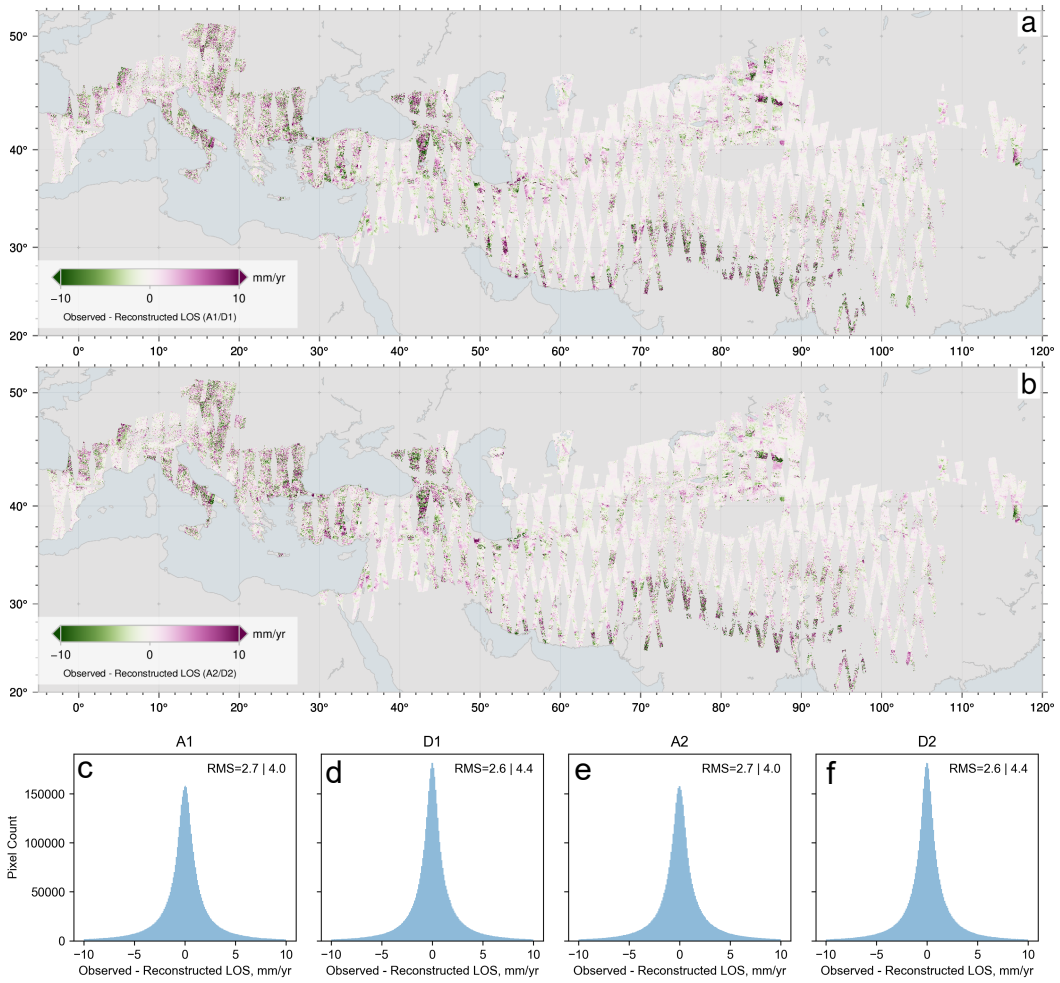


Figure 5: LOS uncertainty analysis through the differences between observed and reconstructed LOS velocities at track overlaps. The observed LOS velocities in Figure 6 are split into four non-overlapping groups of ascending and descending tracks, A1, A2, D1, and D2. (a-b) A1 represents the differences between the observed LOS velocities in A1 and the reconstructed LOS velocities at A1's pixel locations using LOS velocities in A2, D1, and D2. The same applies to D1, A2, and D2, respectively. (c-f) Residual and Root-mean-square (RMS) differences between the corresponding observed and reconstructed LOS velocities. The differences are reported first as RMS of 1-99 percentiles, and then of all pixels.

5. Results

We first describe the line of sight velocity fields that result from combining all the individual frames, before moving on to the 3 components of velocity from the combined decomposition of InSAR and GNSS data. We then show our results for the strain rate calculations for the whole AHB. A zoomed in discussion of the details of the velocity and strain rates for each of the major tectonic region is given in the Supplementary Information (Section 3), where we focused in on the regions deforming as a response of the Arabia collision zone of Turkey (Figure S1), Iran and Makran (Figures S2 & S3) before moving onto those responding to the India collision in the Pamirs (Figure S4), Tian Shan (Figure S5) and across the Tibetan Plateau (Figures S6 & S7). We finish here by showing signals across the AHB associated with creeping faults, postseismic deformation following major earthquakes, and land subsidence due to water extraction.

5.1. Surface Velocities

The Eurasia-fixed ascending and descending LOS velocities (Figure 6) offer a comprehensive view of surface motions across the entire AHB. The most notable feature is the pronounced gradient in velocity across the major fault systems, such as the North and East Anatolian Faults (Figure S1), Main Pamir (Figure S4), Altyn Tagh (Figure S6), Haiyuan, Kunlun, and Xianshuihe Faults (Figure S7). Additional features include localized regions where there is apparent motion away from the satellite in both ascending and descending geometries. This consistent motion in both directions suggests subsidence in these areas, likely due to human activities such as water extraction, as observed in regions such as Türkiye, Iran, and the North China Plain (Section 5.3.3).

The northward velocity field (Figure 7a), largely controlled by the GNSS (Figure 3), reveals the well-recognised north-south shortening as a result of the ongoing plate collisions. The overall gradient in the N-S velocity field at the India collision point is approximately 40 mm/yr over a distance of ∼3000 km, with around 20 mm/yr of shortening observed across the Himalayas (Figure 8a), except where it is much sharper gradient across the Chaman Fault. These gradients reflect the intense compressional forces re-

sulting from the ongoing collision between the Indian and Eurasian plates, driving the tectonic deformation in the region. The decomposed E-W velocity field (Figure 7b) reveals large-scale motion across the region, with Anatolia experiencing westward motion at a rate of 20–25 mm/yr relative to Eurasia, and Tibet moving at a similar rate eastwards, with rapid rotations around the eastern Himalayan syntaxis. A localized eastward velocity gradient is observed across the major faults, as shown by a ∼8000 km profile crossing the North Anatolian, Main Pamir Thrust, Altyn Tagh, and Xiaojiang Fault systems (Figure 8c). The vertical velocity field (Figure 7c) is likely dominated by non-tectonic processes such as groundwater depletion and permafrost and is also noisier and harder to interpret. Values larger than +/-10 mm/yr are unlikely to be tectonically related. The ∼4500 km profile (Figure 8e) reveals vertical deformation across the region, with uplift north of the Makran, subsidence around the western syntaxis, Karakoram-Altyn Tagh uplift, subsidence in Qilian Shan due to permafrost, and uplift associated with plateau growth in the north-east.

The comparison between InSAR-derived velocities and GNSS data (Figure 3) for the entire AHB shows an RMS of 2.4 mm/yr for eastward velocity (Ve) and 2.4 mm/yr for vertical velocity (Vu), with RMS values of 3.1 mm/yr for GNSS Vu and 1.8 mm/yr for levelling (Figure SB23). For individual regions, the RMS values are 2.5 mm/yr for Ve and 3.3 mm/yr for Vu in Europe (Figure SB24), 2.9 mm/yr for Ve and 3.5 mm/yr for Vu in Anatolia (Figure SB25), 1.5 mm/yr for Ve and 1.7 mm/yr for Vu in the Pamir and Tian Shan (Figure SB26), and 2.3 mm/yr for Ve and 1.8 mm/yr for Vu in Tibet (Figure SB27). These values suggest that, while InSAR captures surface motion with reasonable accuracy, there are still noticeable discrepancies, particularly in the vertical velocity component. The higher RMS value for vertical velocity may be attributed to factors such as atmospheric noise, vegetation, phase bias, or other non-tectonic influences that affect InSAR data. The formal uncertainties from the velocity decomposition of < 1 mm/yr for many areas (Figure SB15), which are propagated from the line-of-sight uncertainties of similar magnitude, do not fully capture the level of noise. The uncertainty estimates from the overlapping frame analysis (Figure 5) of ∼2.5–3.0 mm/yr and

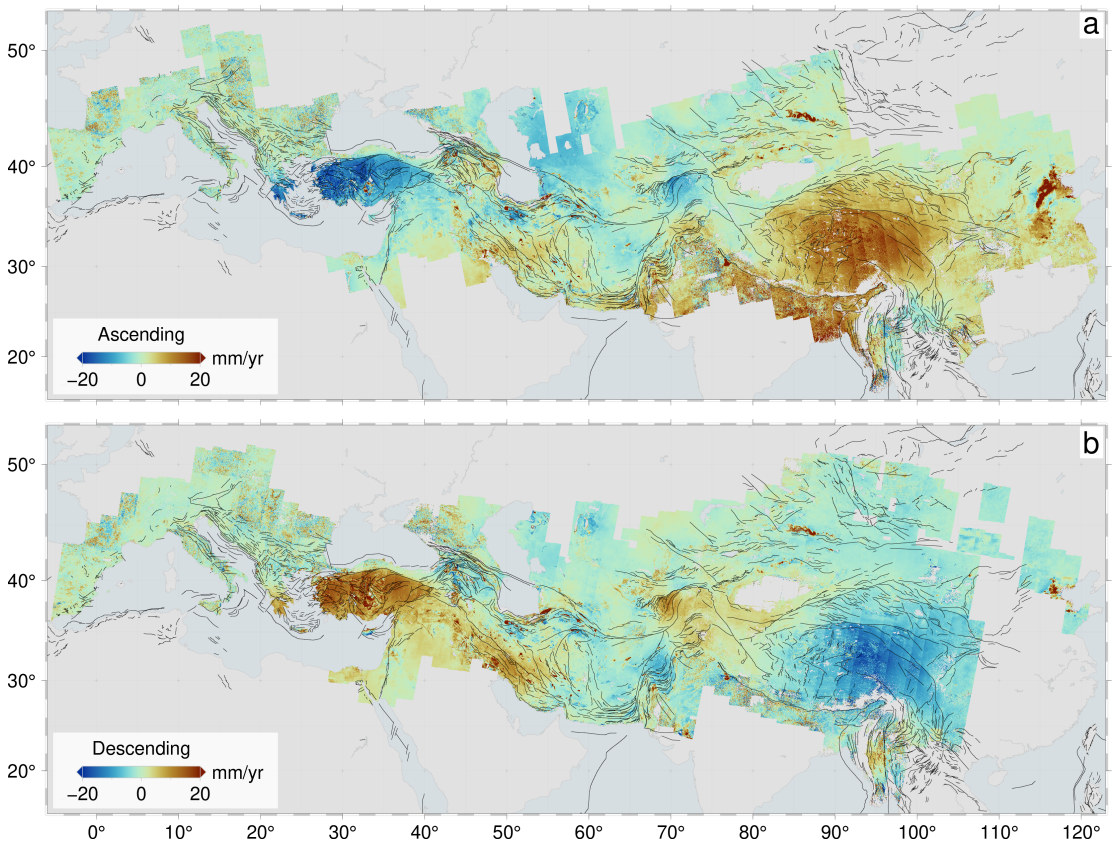


Figure 6: Mosaic of referenced line of sight average velocities for the Alpine Himalayan Belt on (a) ascending and (b) descending orbital heading directions, with positive values indicating motion away from the satellite. Active fault traces (black lines) are from Styron and Pagani (2020).

from the longer wavelength referencing from VELMAP (Figure SB21) of 2–3 mm/yr should be considered more realistic.

5.2. Strain Rates

Our strain rate fields of the AHB (Figure 9) shows two styles of deformation, with focused strain concentrated along major fault systems (Figure 9a-b) and more diffuse strain observed away from these large faults (Figure 9c). The major concentrations of strain rate lie along the centre of Greece, on the North and East Anatolian Faults (Figure S1), Caucasus, the Dead Sea Fault, the Makran and Sulaiman Ranges (Figure S3), the Pamirs (Figure S4), the parts of the Himalayas we can image, and the major strike-

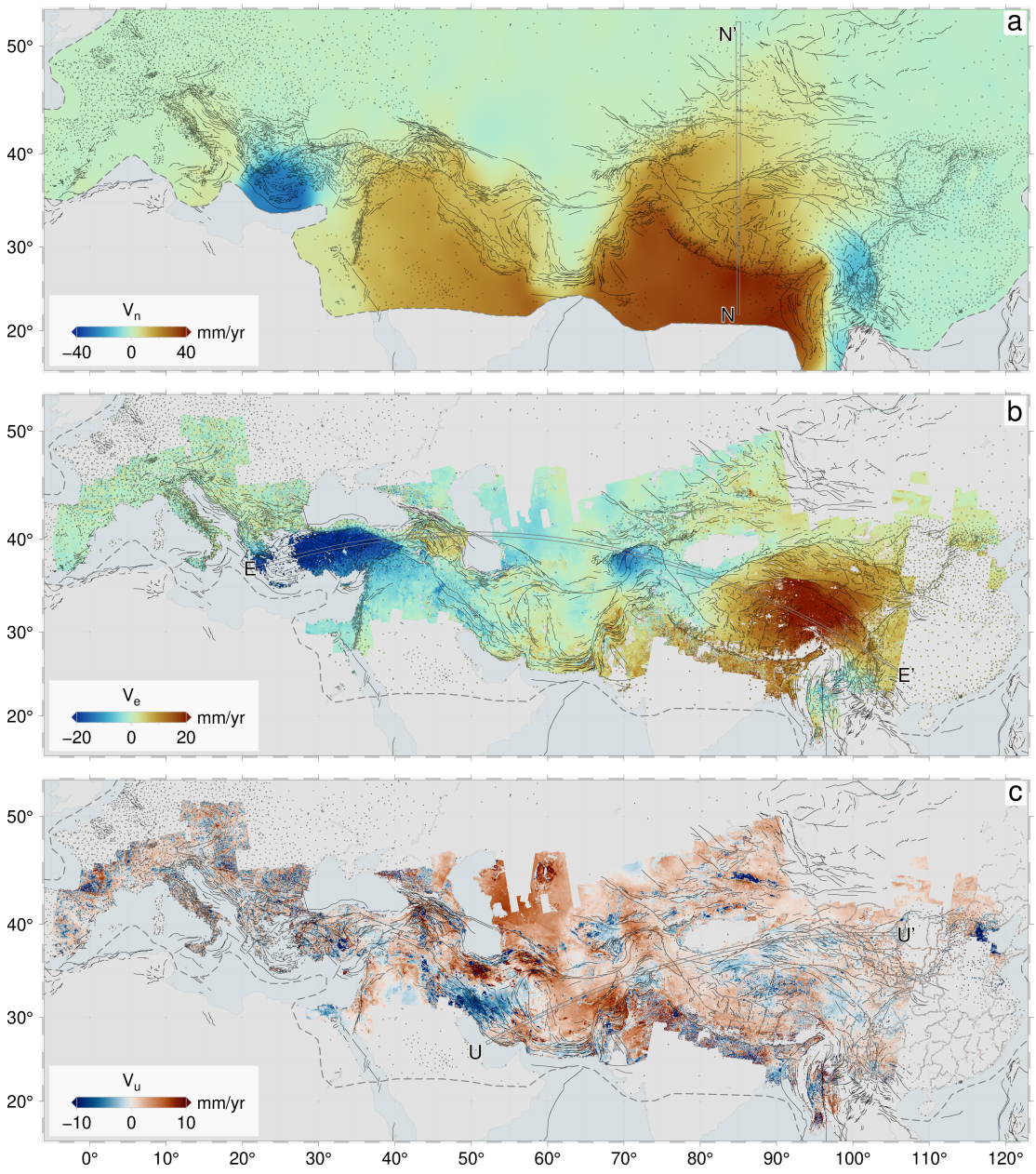


Figure 7: Three components of surface velocity: (a) North, (b) East, and (c) Vertical. GNSS sites are denoted by circles for 2D velocities, triangles for 3D velocities and coloured squares for levelling results. The dashed outline shows the extent of the mesh used to align the individual line-of-sight velocities. Gray polygons indicate the extent of the profiles (20 km bins) presented in Figure 8.

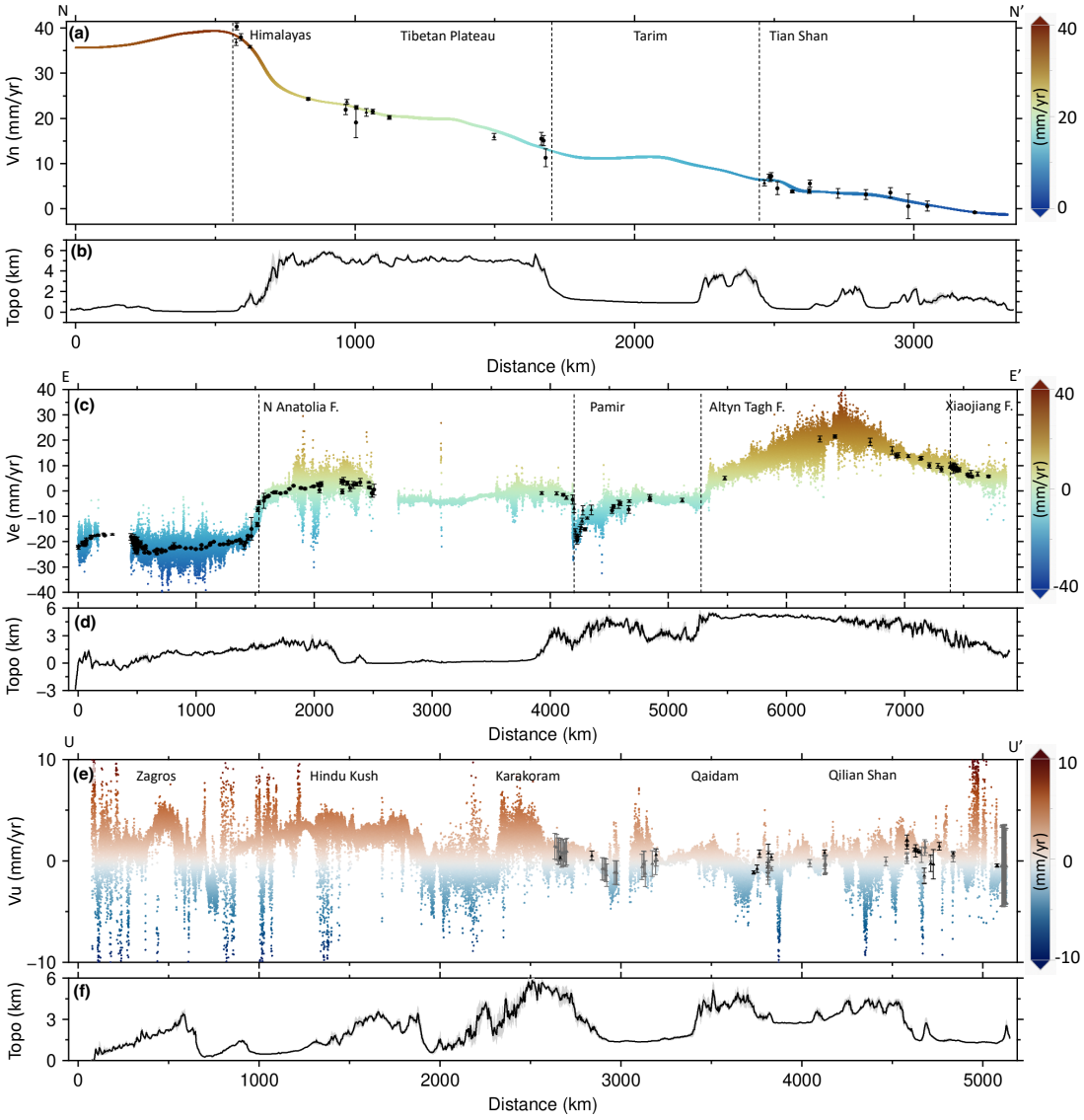


Figure 8: Profiles across the velocity fields of the Alpine Himalayan Belt with locations of mapped active faults from Styron and Pagani (2020) marked by dashed black lines. (a) Northward component of velocity along longitudinal line 85°E, with GNSS data and topography marked on. (b) Eastward component of velocity from Greece to southeastern Tibet along the Great Circle almost 8,000 km long (20% of the Earth's circumference). (c) Vertical component through Afghanistan to northeastern Tibet. The locations of the profiles are shown in Figure 7. InSAR data (coloured dots) are binned into 20 km wide profiles, while GNSS (black bars) and levelling (grey bars) data are binned into 40 km wide swaths.

slip faults of Tibet (Figures S6 & S7). Distributed strain occurs in regions such as Iran (Figure S2), and the interiors of western Anatolia and across the Tian Shan (Figure S5), as well as parts of the Tibetan Plateau away from the major faults. Whilst there is noise in these derivative fields, it is possible to discern low straining areas < 20 nstr/yr in western Europe, Northern Arabia, Central Iran, Afghanistan and much of the region between the Kopeh Dagh of Iran and the Pamirs, as well as North and East of the Tian Shan.

The horizontal dilatation strain rate field (Figure 9c) is particularly noisy, but viewed broadly, positive dilatation, indicating areal increase, supports known extension in Italy, through Greece and Western Türkiye (Figure S1), as well as across the bulk of the southern and central Tibetan Plateau and around the Eastern Syntaxis in Eastern Tibet. Negative dilatation associated with areal decrease and compression is pronounced across the converging regions of the Caucasus, Zagros mountains, Makran, Sulaiman ranges, Pamirs, Tian Shan, Himalayas, and Qilian Shan.

The rotation rates observed in the vorticity (Figure 9d) predominately reflect the horizontal motion caused by strain accumulation along the major faults, with the direction of rotation depending on the fault's sense of slip (Figure 9d). Left-lateral strike-slip faults are associated with anticlockwise rotation (e.g., East Anatolia, Chaman, Altyn Tagh, Haiyuan, Kunlun, and Xianshuihe Faults), while right-lateral strike-slip faults correspond to clockwise rotation (e.g., North Anatolian and Main Pamir Thrust Faults). These are likely not long-term rotations but reflect elastic interseismic strain accumulation around these faults. The vorticity also captures the long-term clockwise motion of Greece and south-east Tibet around the Eastern Syntaxis. The overall anticlockwise rotation of Anatolia, Northern Arabia, and the Sulaiman Ranges to Hindu Kush is also shown by the broad areas of positive rates of vorticity.

Comparison between GNSS-derived strain rate fields and those from the combined InSAR and GNSS solution shows that InSAR adds finer-scale details, typically localizing more strain onto the large fault systems such as the North Anatolian Fault and those across the Tibetan Plateau (Figures SB32 and SB29). However, in regions of low strain

856 ($<$ 20 nstr/yr), the InSAR can add noise, particularly where coherence is poor. The
857 InSAR strains also contain the contributions from postseismic deformation following past
858 major earthquakes that mostly predate our time series. This postseismic impact is most
859 clearly picked out in the difference of the two maximum strain rate fields (Figure SB32)
860 around Kokoxili on the Tibetan Plateau and the Baluchistan earthquake in the Eastern
861 Makran.

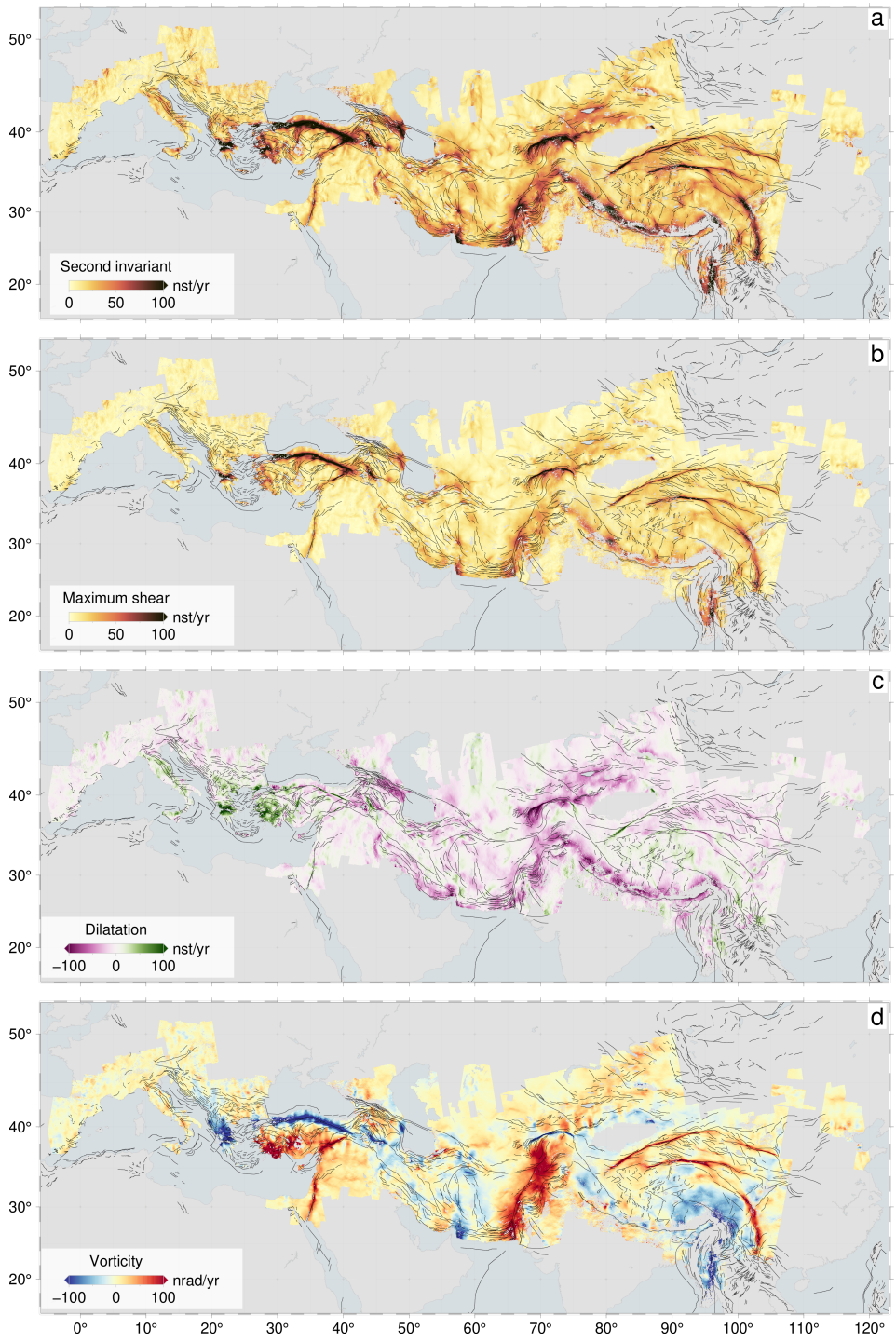


Figure 9: Measures of horizontal strain rates for the Alpine Himalayan Belt with mapped active faults from Styron and Pagani (2020) overlaid (black lines). (a) Second invariant of strain rate (nstr/yr), (b) Maximum shear strain rate (nstr/yr), (c) Horizontal Dilatation rate (nstr/yr), where positive indicates extension and negative contraction, and (d) Vorticity (nrad/yr), with positive values indicating anti-clockwise rotation.

5.3. Further Deformation

In addition to the large-scale horizontal velocities associated with long-wavelength continental deformation and the strain of interseismic accumulation across major faults, we also see sharp velocity gradients and high strain rates associated with individual creeping segments of strike-slip faults and also the elevated strains over regions with past earthquakes. We also observe the largest signals in the vertical associated with non-tectonic signals due to water subsidence across the belt and show a number of such examples, as well as the influence of permafrost on surface velocities across the Tibetan Plateau.

We have separated out these sources of deformation based upon visual inspection of the wavelength and magnitude of the signals, the dominance of horizontal motion, and whether they are associated with recent large earthquakes, or previously identified creeping faults. Conversely, those signals associated with subsidence due to water extraction are dominated by vertical deformation, are larger in magnitude (> 10 mm/yr), vary seasonally in the timeseries and are highly correlated with vegetated areas in arid regions close to population centres. We have not examined motion associated with events such as steady landsliding as our coarse velocity fields at 1 km would not be able to delineate short wavelength signals.

5.3.1. Creeping Faults

Earthquakes are not the only mechanism by which the crust releases its elastic strain. Many previous studies (Avouac, 2015; Harris, 2017; Jolivet and Frank, 2020) have shown that the elastic strain accumulated in the shallow crust can be released aseismically without producing huge seismic waves nor causing sudden movement of the shallow crust. Compared to most active faults, which are fully locked from the surface down to the seismogenic depth during the interseismic period (Reid, 1911), creeping faults are those that are not fully locked; instead, slow, aseismic slip occurs in the periods between earthquakes. Creeping faults are typically not well identified using GNSS datasets as the GNSS velocities are normally too sparse to distinguish shallow creeping and shallow locking depth and instead this is usually best captured with creepmeters (Bilham et al.,

2016). High-resolution InSAR velocities can capture the near-fault deformation pattern over wider areas to better identify whether a fault is creeping. Across the Alpine Himalayan Belt, previous InSAR studies have identified several creeping faults, including parts of the North Anatolian fault (e.g., Cakir et al., 2005; Hussain et al., 2016; Jolivet et al., 2023), Chaman fault (e.g., Fattahi and Amelung, 2016; Barnhart, 2017; Dalaison et al., 2021), Haiyuan fault (e.g., Jolivet et al., 2013), Xianshuihe fault (e.g., Qiao and Zhou, 2021) and Gozha Co fault (e.g., Huang et al., 2023).

By studying our velocity field and strain rates around some of these creeping faults, we observed obvious steps in our east velocity field and high shear strain rates running along them (Figure 10). The pattern of velocity steps and maximum shear strain rates indicates the spatial extent, creeping rates, and creeping depth. Taking velocity profiles perpendicular to the creeping section (Figure 10c,g,k,o), we can better understand the creeping rates and whether the fault is still partly locked (e.g., Hussain et al., 2016; Qiao and Zhou, 2021). The velocity profile across the North Anatolian creeping section shows that the tectonic loading rate (or the slip rate of the fault below the locking depth) on the fault is about 20 mm/yr, which is consistent with previous studies on this section (e.g., Jolivet et al., 2023). The localised offset on the fault (associated with shallow creep) is less than the tectonic loading rate, suggesting the fault is still partly locked, which is supported by previous studies (e.g., Hussain et al., 2016; Jolivet et al., 2023).

When compared with the North Anatolian creeping section, creep on the Chaman fault is much more obvious with a larger spatial extent along the fault (Figure 10e). Our east velocity profile across 31.7°N (Figure 10g) shows that the east component of the tectonic loading rate is about 3 mm/yr, from which we can estimate a fault-parallel loading rate of $\sim$ 7 mm/yr based on a strike of N25°E, consistent with the 6.6 $\pm$ 1.2 mm/yr estimated by Fattahi and Amelung (2016) and 7 $\pm$ 2 mm/yr from Dalaison et al. (2021).

Compared with other creeping faults, the spatial extent of the creeping section on the Haiyuan fault in northeastern Tibet is much smaller (Figure 10i). As the strike of the Haiyuan fault is nearly east-west, our velocity profile indicates that the overall

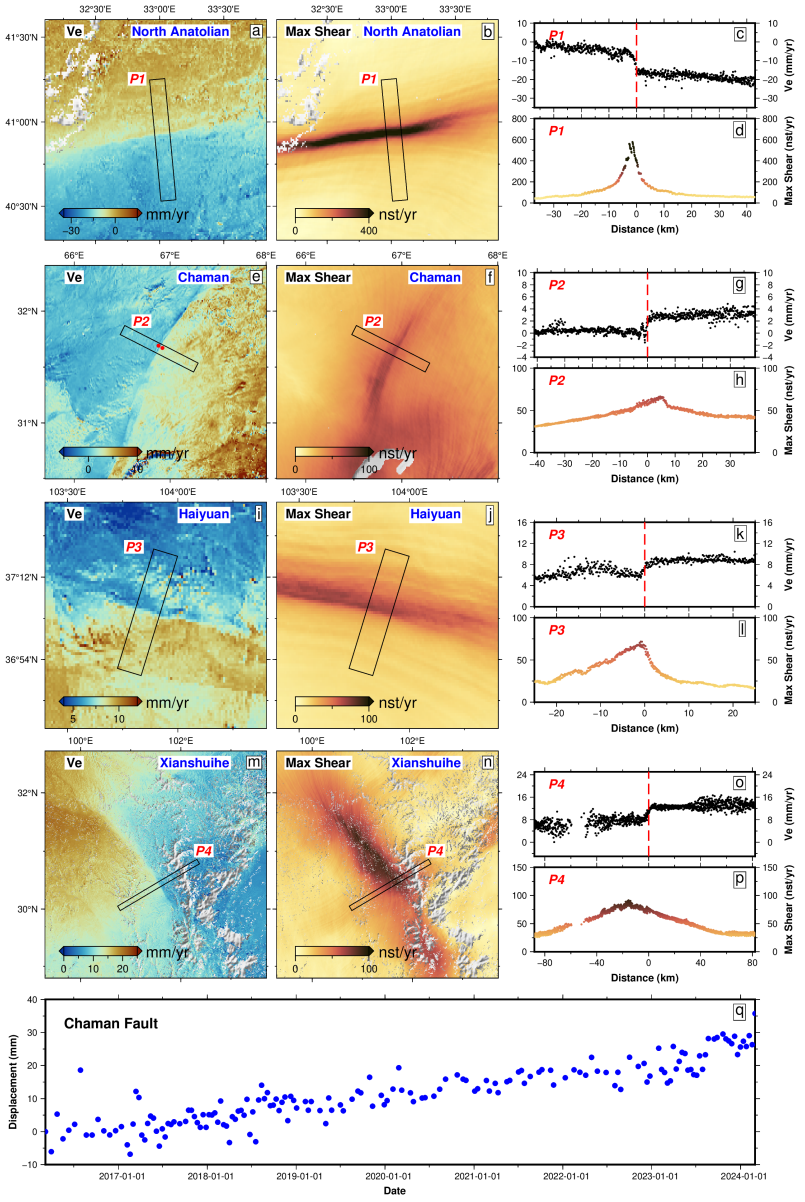


Figure 10: Examples of creeping fault signals observed in timeseries. Location of regions shown in Figure SB16. (a,e,i,m) East velocities around the North Anatolian fault, the Chaman fault, the Haiyuan fault and the Xianshuie fault. (b,f,j,n) Maximum shear strain rates around these active faults. (c,d,g,h,k,l,o,p) The velocity and Maximum shear strain rate profiles across these faults. The location of the profiles are shown in the left East velocity and Maximum shear strain rate maps. The width of the profiles is all 10 km. (q) A displacement time series of a pixel referred to a pixel at the other side of the fault based on LiCS frame 042A_05933_131313, and the location of these two pixels are shown by red points in (e).

tectonic rates of the Haiyuan fault should be near 4 mm/yr, which is consistent with previous studies (Huang et al., 2022). The velocity offset immediately across the fault suggests a creep rate that is slightly smaller than the loading rate in the location of our profile, suggesting a creep rate of $\sim$ 3 mm/yr, similar to Jolivet et al. (2023).

The Xianshuihe fault in Eastern Tibet also shows a clear step in the east velocity field (Figure 10m) and high maximum shear strain rates between 30°N and 32°N. The east velocity profiles indicate a loading rate of $\sim$ 12 mm/yr, assuming a strike of $\sim$60°, which is close to the 11.5 $\pm$ 1.5 mm/yr estimated by Qiao and Zhou (2021). The offset in the east velocity looks comparable with the far-field loading rate in our data indicating that the fault is fully creeping.

Our InSAR time series over the Alpine-Himalayan Belt not only provides a way to study the rate of creep but also allows for the investigation of its potential temporal variations. Figure 10q shows a displacement time series for the Chaman Fault for a pixel referenced to another pixel on the other side of the fault (two red points in Figure 10e); because the points are close to the fault, the displacement time series captures how the creep rate is changing temporally. The example time series suggests that creeping on the Chaman Fault is fairly steady in time ($\sim$ 3.8 mm/yr), with any variations from steady-state hard to distinguish from noise.

Although a systematic study of creeping faults is beyond the scope of this paper, our results have shown that our derived velocity field and time series can be used for further investigation and comparison of creeping faults within the Alpine-Himalayan Belt. Nevertheless, we can conclude that creep is relatively rare on continental faults.

5.3.2. Postseismic Deformation

During our InSAR data processing, we removed the impact of the coseismic signals that occurred during the acquisition timeframe by adding gaps or truncating the data (Table SA4). However, we did not attempt to correct for postseismic deformation resulting from earthquakes that occurred before the Sentinel-1 observation period nor which occurred within the observation window (although we did truncate time series before some earthquakes that occurred late in the observation window; Table SA4). Some sig-

nificant postseismic deformation signals are present in our velocity and strain rate data (Figure 11).

Postseismic deformation has been attributed to three primary processes: viscoelastic relaxation, poroelastic rebound, and afterslip (e.g., Ryder et al., 2007, 2011; Wright et al., 2013; McCormack et al., 2020; Zhao et al., 2021). Mapping how deformation varies in space and time following large earthquakes gives an opportunity for understanding the relative contributions of these mechanisms, and can act as a probe to determine lithospheric rheology and investigate the friction properties of faults (e.g., Barbot et al., 2009; Wright, 2016; Ingleby and Wright, 2017; Weiss et al., 2019). Ultimately, understanding postseismic deformation is required if we are to use short-term geodetic data to say anything meaningful about long-term hazard. Due to the variation in earthquake size, earthquake type, and structure of the Earth, the surface deformation pattern of the postseismic phase and its duration can vary significantly between events, although the largest velocities typically decay following a $1/t$ law (Ingleby and Wright, 2017).

Figure 11 shows several examples of signals due to postseismic deformation that we observe in our velocity field. From Figure 11a we could see that there is measurable and distributed postseismic deformation due to the 2013 M_w 7.7 Balochistan earthquake (Avouac et al., 2014) during our acquisition time (2016–2024). Previous research showed that the earthquake had a large strike-slip component (Avouac et al., 2014), which is consistent with the $\sim$ 20 mm/yr offset we see in the east velocity field (Figure 11g). The elevated shear strain rate of over 75 nst/yr around the fault (Figure 11h) suggests that the postseismic deformation on this fault is still dominated by strike-slip movement. The postseismic deformation associated with this fault is thought to be controlled mainly by widespread aseismic slip rather than viscoelastic relaxation (Lv et al., 2022), which is consistent with the deformation pattern we observed.

The 1997 M_w 7.5 Manyi earthquake was three decades before this dataset coverage, but the postseismic deformation related to it is still notable in the velocity field (Figure 11b). Previous studies based on the InSAR time series just after the earthquake suggest that both afterslip and viscoelastic relaxation can be plausible mechanisms for

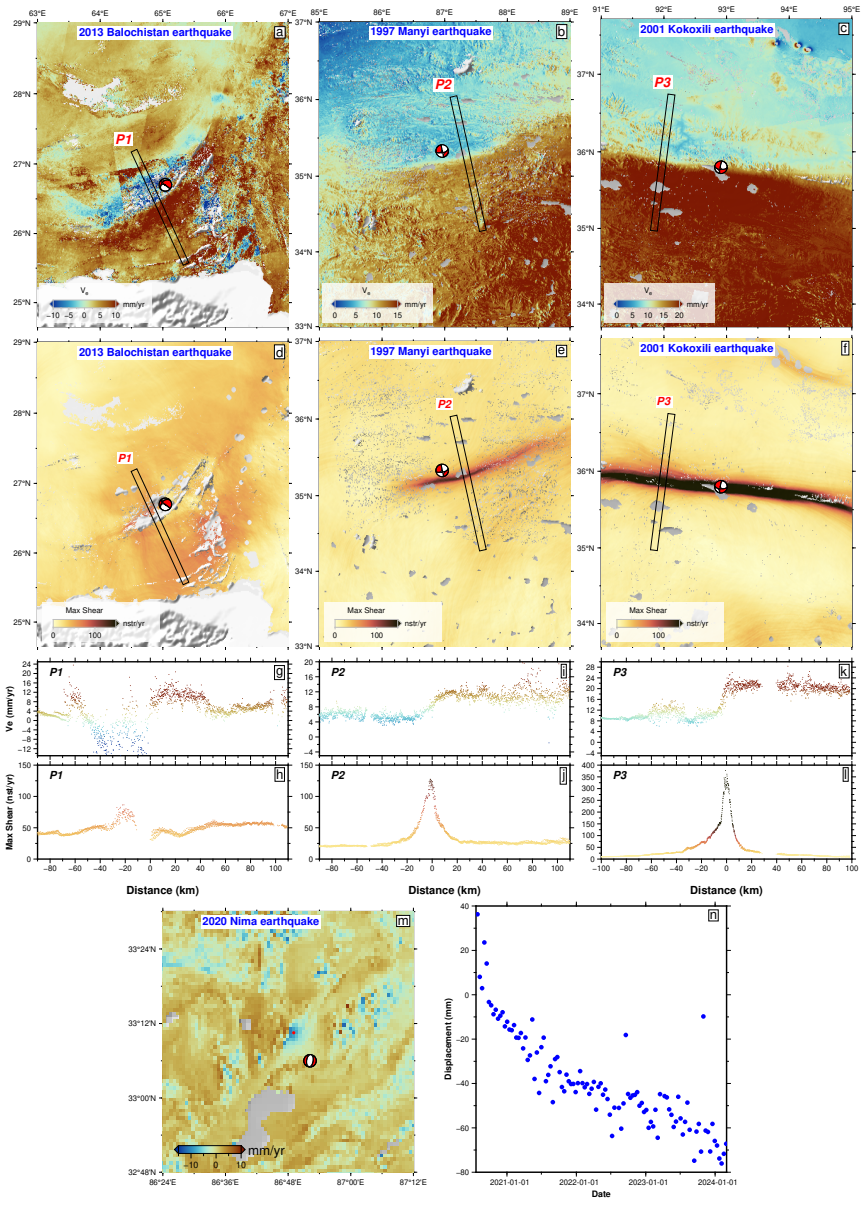


Figure 11: Examples of postseismic signals observed in timeseries. Location of regions shown in Figure SB16. (a,b,c) East velocities around the epicenter of the 2013 M_w 7.7 Balochistan earthquake, the 1997 M_w 7.5 Manyi Earthquake and the 2001 M_w 7.8 Kokoxili Earthquake. (d,e,f) Maximum shear strain rates around the epicenter of these earthquakes. (d-l) East velocity and maximum shear strain rate profiles across the postseismic deformation zones. The locations of the profiles are shown in (a-f). (m) LOS velocities around the 2020 Nima earthquake in the LiCS frame 012A_05642_131313. (n) The postseismic LOS displacement time series for the 2020 Nima earthquake based on the LiCS frame 012A_05642_131313. The location of the pixel is shown by red point in (m). The red focal mechanisms for the earthquakes in (a-f) and (m) are from Global Centroid Moment Tensor Catalog (Dziewonski et al., 1981; Ekström et al., 2012).

the postseismic deformation related to this earthquake (Ryder et al., 2007). Our velocity fields suggest the postseismic deformation related to this earthquake does not totally vanish even decades later. We consider the $\sim$ 7 mm/yr sharp step in the east velocity field (Figure 11i) to include postseismic deformation rather than purely interseismic based on a previous study that shows that the relative motion accommodated on this fault is only 3 ± 2 mm/yr before the earthquake (Bell et al., 2011).

Postseismic deformation related to the 2001 M_w 7.8 Kokoxili Earthquake is also particularly obvious and pronounced in our velocity field (Figure 11c). This earthquake occurred on the Kunlun fault, and its postseismic deformation generates high maximum shear strain rates of over 150 nst/yr along the fault (Figure 11f,l). Previous studies suggest the possible mechanism for the postseismic deformation of this earthquake to be viscoelastic relaxation and afterslip (e.g., Ryder et al., 2011; Wen et al., 2012), but separation of these two contributing sources is not well resolved. Moreover, the viscoelastic parameters for the deep crust given from previous studies show large variation (Lv and Shao, 2022). This variation not only comes from different models used in these studies, but also lies in the uncertainties and limitations of the observations themselves. Our derived velocity field, strain rates and time series can provide more constraints on such parameters in future studies.

Postseismic deformation of moderate earthquakes can also sometimes cause deformation that is observable in our velocity field, especially in the line-of-sight velocity results. Figure 11m shows the impact of the postseismic deformation of the 2020 M_w 6.3 Nima Earthquake (Hong et al., 2023) on our line-of-sight velocities. From the time series, the temporal decay in postseismic velocity is clear (Figure 11n).

We chose not to attempt to correct for postseismic signals to obtain "steady-state" velocities, as is often done during GNSS processing (Herring et al., 2016). However, a challenge is knowing what postseismic mechanism to correct for and which earthquakes to include, as we clearly document deformation from events such as the Manyi earthquake, which occurred 30 years prior to our data coverage (Figure 11i). By not correcting for the postseismic signals we see in our data, we provide an opportunity for

the community to use the deformation data to build improved models for the events we observe, rather than applying our prejudices on the functional form for the time series corrections.

5.3.3. Non-tectonic vertical signals

Sources that contributen to current measurements of vertical motions include those of tectonic, hydrologic, anthropogenic, and cryospheric signals. Those that are tectonic are associated with mapped active faults and the locations of recent earthquakes. Cryospheric signals are associate with glaciated areas and can be hard to separate out from tectonic uplift in these mountainous regions. However, the bulk of the significant vertical rates we are imaging are land subsidence, predominately due to water extraction.

In the vertical velocities, we observe non-tectonic deformation with distinct spatial patterns from tectonic deformation. For the most part, these incidences are large areas of rapid subsidence (faster than 10 mm/yr over areas larger than 4 km^2) located in valleys (Gambolati and Teatini, 2015; Herrera-García et al., 2021) associated with agriculture.

We observe this land surface subsidence in the Po Plain (Bonì et al., 2017), Po Delta (Da Lio and Tosi, 2019), and Tavoliere delle Puglie (Scardino et al., 2022) regions of Italy; several regions of Western and Central Türkiye (including the Konya Basin and the Küçük Menderes River Basin, Üstün et al., 2015; Yalvaç et al., 2023); Georgia and Azerbaijan; extensively across Iran (Motagh et al., 2008; Goorabi et al., 2020; Mirzadeh et al., 2021; Haghshenas Haghighi and Motagh, 2024); Afghanistan (Meldebekova et al., 2020; Kakar et al., 2025); Pakistan (Khan et al., 2022; Ahmad et al., 2019); and in the Junggar Basin (Wang et al., 2022a) and Beijing regions of China (Zhu et al., 2015; Hu et al., 2019; Chen et al., 2016; Ao et al., 2024).

Previous work has observed the correlation of subsidence rates in the Alpine Himalayan Belt with groundwater depletion, particularly across Iran (Motagh et al., 2008); Kabul, Afghanistan (Meldebekova et al., 2020; Kakar et al., 2025); and Beijing (Chen et al., 2016). However, more recent work derives a more complex picture of land subsidence across, for example, China (Ao et al., 2024), where the mass of cities, groundwater depletion, and hydrocarbon extraction all contribute to rapid land surface subsidence.

In this study, we find over ~227,000 km^2 is subsiding faster than 10 mm/yr in regions larger than 4 km^2. We choose this area threshold to discount isolated, noisy pixels. We choose this velocity threshold to discount apparently slowly subsiding regions which may instead represent non-deforming noise sources including phase bias (e.g. Ansari et al., 2021; Maghsoudi et al., 2022). Including the whole AHB, the largest region of continuous subsidence is in Eastern China, covering ~51,000 km^2 (Figure 12b). This region stretches from Beijing in the north, south through Tianjin, finishing in Puyang (Figure 12b). This region alone is similar to or larger than the total extent of land subsidence across the whole of Iran (Haghshenas Haghighi and Motagh, 2024; Payne et al., 2025). In northern China, there is a vast region of subsidence in the Junggar basin, north of the Tian Shan, covering ~13,000 km^2 (Figure 12a). This figure is similar to the 16,146 km^2 subsidence extent for this region reported by Wang et al. (2022a). Across the whole Tian Shan region, rapid subsidence covers ~18,000 km^2. Other subsidence regions of significant geographic extent include two regions around the Konya Basin, Türkiye, which total ~7,000 km^2 in extent (Figure 12c).

We find a total area of ~1,800 km^2 in which subsidence exceeds 100 mm/yr. The vast majority of these rapidly subsiding regions are located in Iran (1,580 km^2, 88.5 %), but also in Türkiye (123 km^2; near Ödemiş and in the Konya Basin), Pakistan (63 km^2; near Qila Saifullah and Quetta), western Azerbaijan (5 km^2), and in small areas of the Tian Shan (12 km^2).

For analysis of rapid subsidence in Eastern China (longitudes > 111°E), there are limited Sentinel-1 acquisitions in the descending direction, meaning velocity decomposition to retrieve vertical surface motion is not possible through our methodology across large sections of the main subsidence regions here (Figures 6 & 7). Instead, we use only ascending acquisitions and resulting surface velocities in the ascending direction to estimate ~100 km^2 is subsiding faster than 10 mm/yr in Eastern China. We therefore assume for this geographic region that 100% of the recorded ascending direction is vertical. We reproject our GNSS data (Figure 3) in this region into the ascending direction to compare to these ascending InSAR velocities (Figure 12b,e). We find rea-

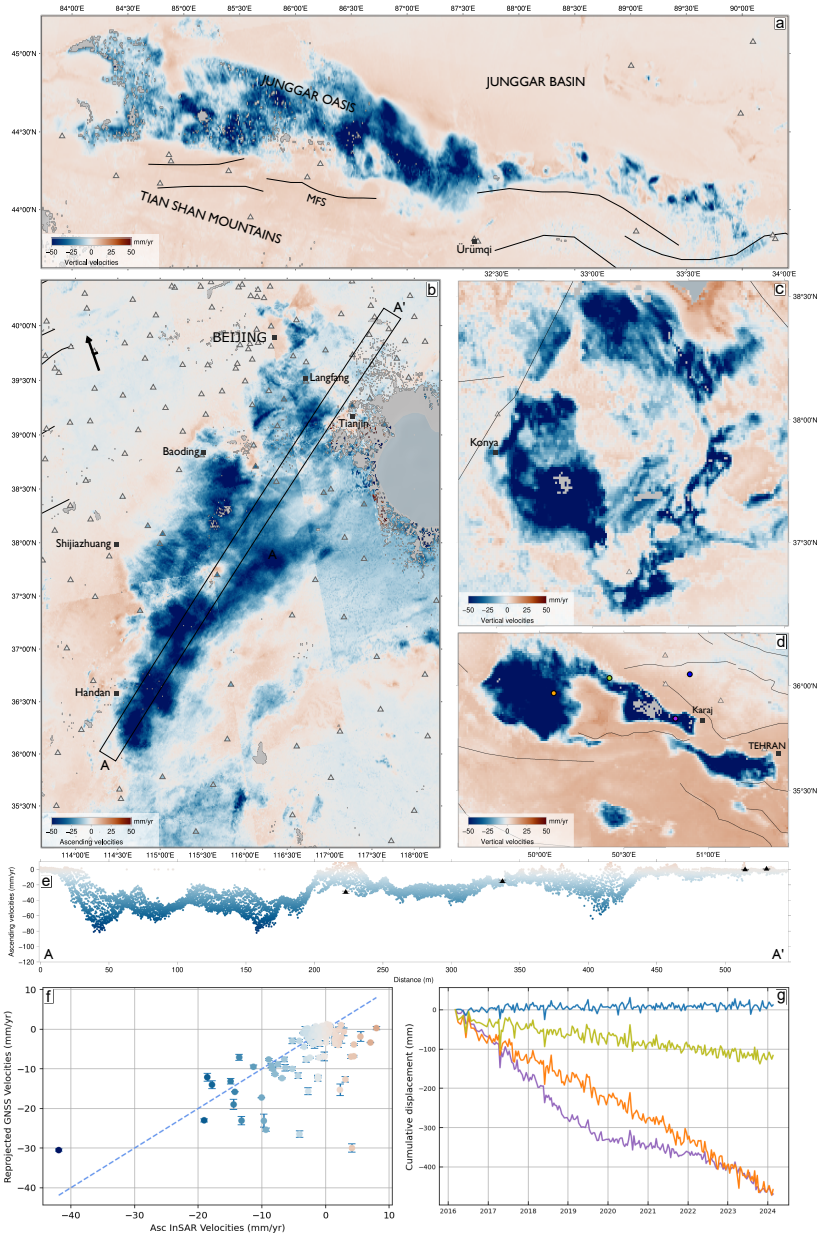


Figure 12: Case examples of rapid vertical subsidence signals associated (according to previous literature or hypothesised association) with groundwater depletion. Location of regions shown in Figure SB16. (a) Tianshan North Slope, China (Yi et al., 2025). (b) The largest continuous subsidence region in this study in Eastern China. Profiled velocities A–A' are in e) (e.g. Ao et al., 2024). (c) Konya Basin, Türkiye (e.g. Üstün et al., 2015)(d) Rapid subsidence near Tehran and Karaj in northern Iran (Haghshenas Haghighi and Motagh, 2024; Payne et al., 2025). (e) Ascending velocities in swath A–A' in b), Eastern China. Triangles = 3D GNSS, circles = 2D GNSS (both this study). (f) Comparison of ascending InSAR velocities from b) at locations of GNSS sites to GNSS velocities reprojected into Sentinel-1 ascending line-of-sight direction. (g) Line-of-sight cumulative displacement time series in the descending direction for frame 035D_05397_131013 at locations in d). Faults from (Styron and Pagani, 2020).

sonable agreement between these velocities ($r^2 = 0.63$), with the strongest disagreement between rapidly subsiding GNSS stations (20–30 mm/yr) and more apparently stable InSAR velocities. This discrepancy may be due to the GNSS instruments that recorded these more rapid velocities being mounted on monuments, for example, buildings, that are subsiding rapidly on a local spatial extent. Conversely, these InSAR results are posted to 1 km pixel widths, thus averaging to some extent deformation in the ascending direction across the pixel. Consequently, rapid subsidence of individual buildings or monuments would not be visible in our InSAR velocities. This discrepancy is additionally highlighted by uncertainties in both GNSS and InSAR velocities. For example, the GNSS site in Figure 12e at around 225 m along the profile has large uncertainties ($\pm$10 mm/yr). The spatial pattern of displacement varies significantly within this subsidence region, with the pattern of subsidence appearing like smaller, joined-up subsidence bowls (Figure 12b, e). This pattern suggests that perhaps the depth of aquifer sediments controls subsidence magnitude. Previously, more local work in this region does find that faulting has some control on the subsidence pattern in Beijing (Hu et al., 2019), but future work should investigate these spatial controls on a more regional scale.

Away from Beijing, the largest region of subsidence in the AHB is in the southern Junggar Basin – the Junggar Oasis – in China (Figure 12a). Previous work attributes this subsidence to over-exploitation of groundwater in this arid/semi-arid agricultural region (Wang et al., 2022a). Our results suggest maximum rates of subsidence in this oasis region reach $\sim$100 mm/yr, comparable to maximum rates estimated by Wang et al. (2022a) using Sentinel-1 over 2015–2020. In terms of spatial structure, the subsidence in this region appears to be bounded along part of its southern margin by the Manasi Fault system (Li et al., 2021b). Similar to the subsidence region south of Beijing, subsidence here is apparent as several smaller, joined-up subsidence bowls, perhaps suggesting a sedimentological rather than structural control on subsidence rate.

Land subsidence in Iran has been investigated thoroughly in previous work (Haghshenas Haghighi and Motagh, 2024; Payne et al., 2025), with the spatial pattern of several subsidence regions controlled by bedrock faults. However, there is a great need to investigate more

thoroughly land subsidence drivers, controls on spatial patterns of subsidence in these other critical regions of the Alpine-Himalayan Belt.

On a larger scale, another process that induces land surface subsidence is the thawing of permafrost under a warming climate. Comparing the spatial patterns of our vertical velocities and the model prediction of permafrost presence (Figure 13) reveals a spatial correlation between subsidence and regions with permafrost zonation index (PZI) greater than 0.5, indicating a high likelihood of permafrost presence (Gruber, 2012). In particular, the correlation is best observed in the Qilian Shan and the interior of the Tibetan Plateau, across almost the entire Qiangtang region, consistent with the result of Lemrabet et al. (2023).

At least 5 mm/yr of subsidence is measured across most of the permafrost zone, as averaged over 40 km wide profiles A-A' and B-B'. Up to 10 mm/yr of subsidence rates are measured on the low-relief valley slopes of the Qilian Shan, similar to results obtained by Daout et al. (2021). Up to 20 mm/yr of subsidence is captured within the Kokoxili region in the central Tibetan Plateau, consistent with values of Chen et al. (2022); Wang et al. (2022c); Lu et al. (2023). This is also where the permafrost zonation index indicates a transition from PZI=1 in northern Qiangtang, where permafrost presence occurs under all conditions, to PZI<0.5 in the southern Tibetan Plateau, where permafrost is only expected under very favorable conditions. We observe this characteristic across the whole region, where permafrost at the border of stability is the most susceptible to thawing and inducing the fastest subsidence. The co-location of sharp transitions in vertical velocity, topography, and permafrost zonation index at ∼300 km on Profile B-B' (Figure 13) is the best testament of this effect.

Our subsidence rates might be susceptible to the potential of underestimation due to unwrapping errors in long-temporal-baseline interferograms from C-band InSAR (Fan et al., 2025) and the potential of overestimation from phase biases due to multi-looking of especially short-temporal-baseline interferograms (Ansari et al., 2021). Despite uncertainties in the absolute subsidence rates measured by InSAR (Liu et al., 2025), we

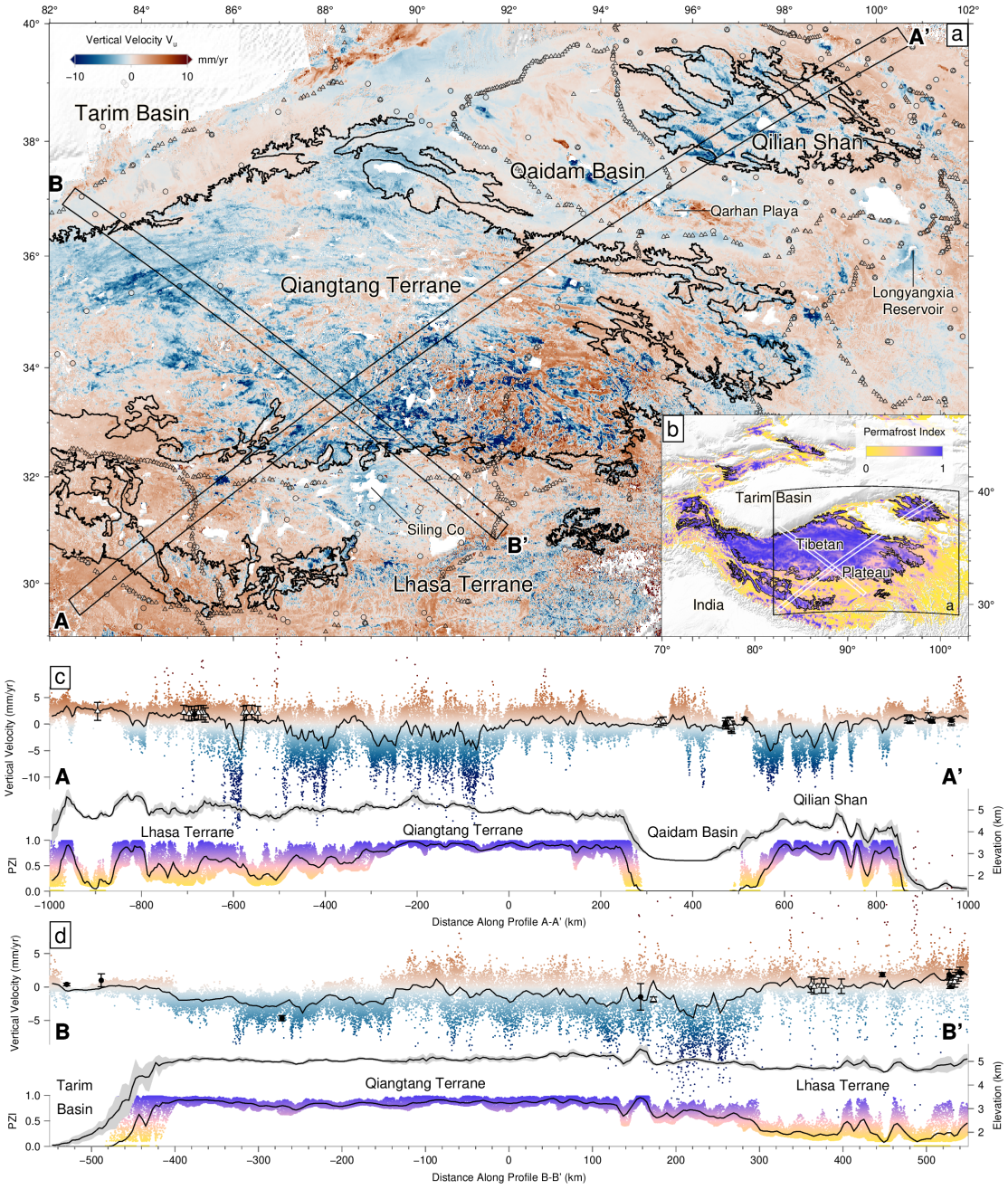


Figure 13: (a) Vertical velocity field with 3D GNSS stations shown in circles, levelling measurements in triangles, and contour line representing Permafrost Zonation Index of 0.5, above which there is a high likelihood of permafrost presence (Gruber, 2012). (b) Permafrost Zonation Index from Gruber (2012) with contours and profiles as in (a). (c,d) Profiles of vertical velocity, the Permafrost Zonation Index and topography. 3D GNSS and levelling vertical velocity measurements are shown as black circles and white triangles with error bars.

reveal a big picture of subsidence patterns over the most extensive high-altitude permafrost zone on Earth, highlighting the value of InSAR in improving our understanding of high-mountain permafrost dynamics.

We have not tried to distinguish the vertical rates associated with the ice unloading due to mass loss of glaciers in the Himalayas and the Tian Shan for instance. The rates would contribute to the overall tectonic uplift from crustal shortening (as observed elsewhere in InSAR results for example in New Zealand (Liu et al., 2024; McGrath et al., 2025)), but the noise in our vertical signals make it difficult currently to separate out the two relative contributions. In depth analysis and modelling is required to separate out Glacial Isostatic Adjustment (GIA) contribution and the impacts of hydrology to the vertical signal we measure.

Other interesting signals in the vertical velocity field include subsidence around the Siling Co and Longyangxia Reservoir, uplift on the Qarhan (Chaerhan) Playa in the Qaidam Basin and on various salt plains along the Hexi Corridor (northeast of Qilian Shan) and around the Tarim Basin, as well as localised subsidence on farmlands and mining and gas extraction sites (Figure 13).

6. Discussion

6.1. Validation of Velocity & Strain Rate Fields

The European Ground Motion Service (EGMS) provides detailed geodetic measurements across Europe and surrounding regions at a resolution of 100 m derived by tying PS InSAR results to a GNSS reference frame (Costantini et al., 2021). Both EGMS and our InSAR show similar eastward velocity patterns (Figure SB30), which is not a surprise given that both are tied to GNSS. Most of Europe exhibits stable velocities with deformation rates of less than ±2 mm/yr. However, in regions like Greece and Anatolia, a significant westward motion is observed at a rate of approximately 20 mm/yr. A comparison between EGMS velocities and our GNSS compilation (Figure 3) shows an RMS of 1.1 mm/yr for the eastward velocity and 1.5 mm/yr for the vertical velocity (Figure SB31). When comparing our InSAR-derived velocities with GNSS data in the European region, the RMS values are higher, with 2.5 mm/yr for eastward velocity and 3.3 mm/yr for vertical velocity (Figure SB24). Further work on some of our line-of-sight velocities should improve our noise levels, but some of this difference likely also reflects the difference in spatial resolution of the two processing strategies. We also note, however, that the EGMS time series can be misleading in terms of earthquakes – these create displacement steps in the EGMS time series that are then heavily smoothed, creating the dangerous false impression of pre-cursory deformation anomalies.

The Global Strain Rate Model (GSRM v.2.1) by Kreemer et al. (2014) and our GNSS-derived strain rates generally depict the same broad deformation patterns, with strain distributed over larger areas (Figures 9, SB28, SB29 and SB32). In regions with relatively sparse GNSS measurements, such as the Makran and Sulaiman Ranges, Pamirs, and major strike-slip faults of Tibet (Figure 3), the GNSS-derived strain rate models appear patchy and blurred due to limited data resolution, leading to less precise shear strain rate estimations and reduced clarity in deformation patterns. In contrast, our InSAR-resolution velocities provide higher spatial resolution, localizing more strain onto these structures and capturing finer-scale variations. It is also important to note, however, that our InSAR results also include contributions from postseismic deformation following

major earthquakes (Section 5.3.2; Figure SB32).

The GNSS-derived dilatation rate field exhibits smoother and more consistent trends. In contrast, extracting a clean dilatation field from InSAR is more challenging, as it often contains short-wavelength noise. Despite these differences, all models capture similar large-scale deformation patterns, including extension in Italy, Greece, western Türkiye, and central Tibet, and contraction across the Caucasus, Zagros Mountains, Makran, Sulaiman Ranges, Pamirs, Tian Shan, Himalayas, and Qilian Shan.

6.2. Sources of Deformation

By observing continental deformation at high spatial resolution at a trans-continental scale, our work reveals important insights into the variety of deformation styles that we see in the continents. Broadly speaking, our work confirms the emerging view that continental deformation occurs in two modes – strain is focused around major fault structures but is more distributed elsewhere (e.g., Wang and Barbot, 2023; Fang et al., 2024a,b). We see this most clearly by contrasting the elevated shear strains we observe around major strike-slip faults in Anatolia (Figure S1) and Tibet (Figures S6 & S7) with the more diffuse shear across regions such as the Iranian Plateau (Figure S2). Because we have uniform InSAR coverage across the entire region, this contrast in deformation style is much clearer than in the previous best strain map on this scale, the Global Strain Rate Model (Figure SB28). We see that the locations of past seismicity from the ISC-GEM catalogue of earthquakes (Storchak et al., 2013, 2015; Di Giacomo et al., 2018) aligns well with our strain rate field (Figure 14). Regions of current (120 year) aseismicity, such as northern Afghanistan and Turkmenistan, northern Arabia and north of the Tian Shan align with regions of very low strain rates in our data. Regions of notable high strain without recent seismicity are the northern Chaman Fault Zone up to the Eastern Syntaxis, and the Altyn Tagh Fault in northern Tibet. Zones of more distributed deformation across the Tian Shan and Makran have perhaps less recent seismicity than we might expect. Whilst the regions of concentrated strain have previously identified faults along them, many regions with active faults already mapped do not have significant strain rates across them in our results (Figure 14). This highlights the need to consider

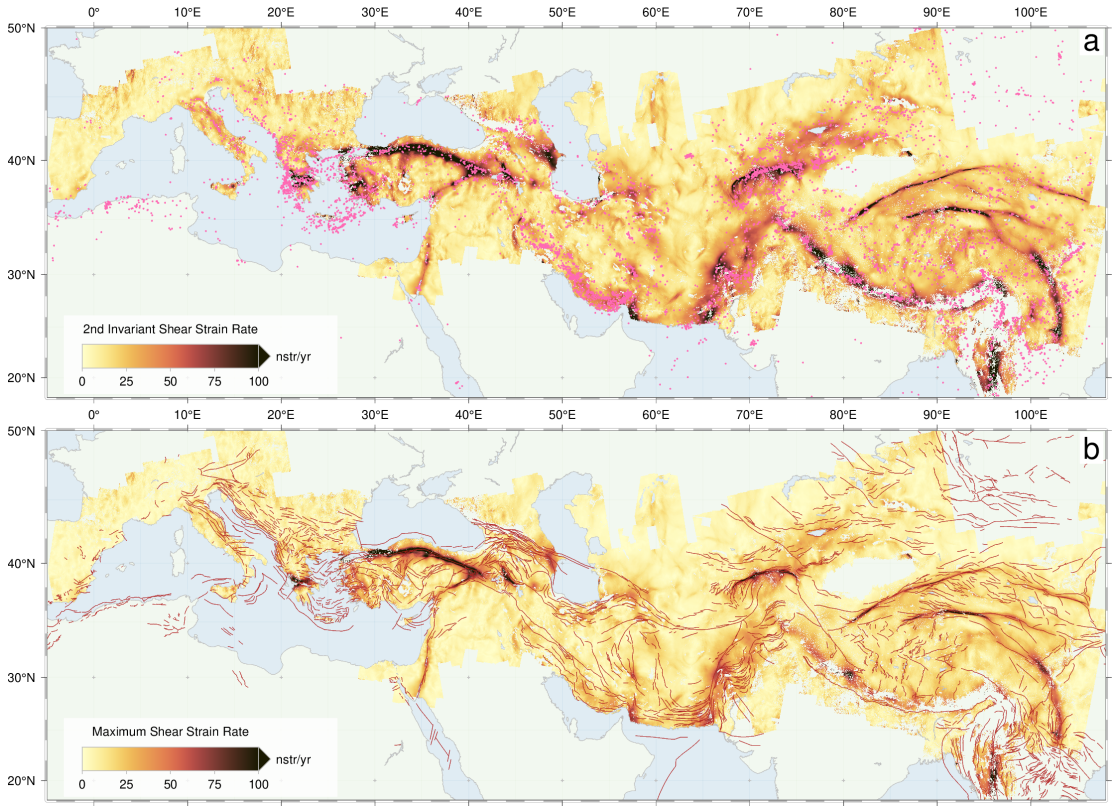


Figure 14: (a) Earthquakes from the ISC-GEM catalogue (Storchak et al., 2013, 2015; Di Giacomo et al., 2018) in pink overlaid on the 2nd invariant of the strain rate tensor. The earthquakes are from 1904 onwards, and selected for magnitudes (M> 5) at shallow depths (< 35 km). (b) Major active faults (red) from Styron and Pagani (2020) overlaid on maximum shear strain rate.

seismic potential even in relatively low straining areas.

It is clear that some of the focused strain we see today is long-lived postseismic deformation from past earthquakes (Section 5.3.2), which would need to be taken into account in any assessment of interseismic deformation. This transient deformation can last decades - for example, we still see elevated postseismic strain rates on the Manyi Fault in Tibet, which ruptured in 1997. However, it is worth noting that major faults such as the Altyn Tagh Fault, which have experienced long periods without earthquakes, still exhibit significant strain concentrations. Hussain et al. (2018) showed that the strain rate on the North Anatolian Fault is independent of time since the last earthquake, once a decadal postseismic period has ended. Ingleby and Wright (2017) showed that post-

seismic transients are measurable for up to 100 years, and that the largest postseismic velocities decay following a $1/t$ law (where t is the time since the last earthquake). Our results support the conclusion that, at least for the majority of major faults, rapid postseismic strain-rate transients decay to a steady-state interseismic rate (Meade et al., 2013), rather than varying throughout the earthquake cycle (Wang et al., 2021). One potential exception is the Karakoram Fault in western Tibet – it remains unclear whether the lack of a strain concentration on this fault is due to the low slip rate (Wright et al., 2004a) or because it is late in the earthquake cycle.

The major faults where we see strain concentrations are those that have accrued large geologic displacements. One hypothesis is that repeated earthquakes and significant displacements facilitate strain localisation, through mechanisms such as shear heating, grain size reduction, fabric development, and fluid infiltration. To explain the geodetic observations on major faults requires a weak component of the system (a low viscosity zone or weak fault) capable of producing rapid postseismic transients; this must be embedded within a relatively stronger substrate (relaxation time equal to or larger than the inter-event time) in order to give focused interseismic strain (Yamasaki et al., 2014; Elliott et al., 2016; Wright, 2016). Fang et al. (2024a) estimate a depth-averaged viscosity of 10^{22} Pa s for the lithosphere away from Tibetan faults, which would be consistent with this model.

Accruing significant (10s km) long-term displacements is only possible for long faults that remain in a favourable orientation. They are likely to be weak structures that cross the entire lithosphere (Vauchez et al., 2012). Smaller faults may behave differently, perhaps responding more passively to the overall regional strains, as proposed by Bourne et al. (1998). The interseismic strains associated with slow/small faults are still challenging for satellite geodetic approaches, but we expect future improvements in viewing geometries and coherence (Section 6) to help address whether small faults behave differently to the major structures.

The geodetic data are also capable of observing shallow interseismic creep on some fault structures. This seems to be a relatively rare phenomenon – most faults in the

continents are locked and capable of major earthquakes. Even for those faults that do exhibit shallow creep, most are creeping at rates significantly lower than the long-term fault slip rate. Aseismic shallow fault creep is not a significant mechanism for releasing elastic strain accumulation in continental interiors.

Geodetic data are now being increasingly used as inputs to seismic hazard models. One approach is to use the data to help constrain fault-based block models (e.g., Evans, 2022; Styron, 2022). In this approach, the "blocks" each behave as independent microplates; the continuous velocity fields we produce by combining GNSS and InSAR data ensure that there are sufficient data within each block to constrain the free parameters (coordinates of the pole of rotation and rotation rate). A major challenge with this approach is that each block has to be completely isolated by faults, even if such structures do not exist. Alternatively, Johnson et al. (2024) recently proposed a direct strain rate inversion approach; inverting strain rates directly removes the need to isolate "blocks" as the strain rates are independent of rotations. Fang et al. (2024b) showed that to match the observed strain in south-east Tibet required the addition of distributed strain sources, as strain on the mapped faults alone was insufficient. This approach relies on high-resolution strain rate data of the type we provide. Strain rate data can also be used directly to estimate moment deficit rates and hence seismicity rates (e.g., Bird et al., 2010, 2015). Our strain rates are significantly sharper than those derived from the Global Strain Rate Model and we would anticipate that they could be used to make a higher-resolution forecast of seismicity rates.

We note that deformation data are just one component of information required for managing and understanding seismic hazard and risk, alongside seismology, active fault mapping and geomorphology, historical earthquakes, and palaeoseismology (Abdrakhmatov et al., 2024). However, earth observation data and satellite geodesy feed into many aspects of the Disaster Risk Management cycle (Figure SB33). The Continental Strain Rate Fields from InSAR combined with GNSS are now emerging as potentially useful inputs into the preparedness of regions before earthquakes by highlighting the regions straining and providing constraints on models of seismic hazard.

6.3. Challenges & Future Improvements

Working at such a large spatial scale and aiming for millimetre per year accuracy in surface velocities has a number of challenges. The atmospheric noise contributions can be modelled and corrected to a significant degree, and mitigated against through time series analysis to better estimate average velocities. However, there are still some residual effects that could be improved by better and/or higher resolution tropospheric corrections (e.g., Yun et al., 2015), as the tropospheric correction does not always improve the noise in individual interferograms. Additional refinements to ionospheric corrections which take account of the seasonal and latitudinal variations in the vertical layering of the ionosphere would improve on our current simplifying assumption of a constant 85% of the total electron content being below the satellite.

The use of InSAR to estimate velocities does introduce finer resolution than that derived from the GNSS in most regions, but it does also introduce noise at short wavelengths in some locations. The InSAR data add the most information in areas which are highly coherent and where there is little existing GNSS coverage, such as across Iran and Central Asia, and within the Tibetan plateau (Figure 3). GNSS site velocities are typically more representative of the displacement of the earth's surface as they are often anchored in bedrock; InSAR is susceptible to the effects of vegetation, loss of coherence (Figure SB9) and phase biases (Ansari et al., 2021), as well as measuring other at, or near, surface displacements not representative of the deeper crustal tectonic motions. Identification of more representative pixels in the InSAR-derived velocity fields will help reduce the noise (as well as using longer time series to better estimate average velocities). Also, it may be possible to roll out corrections for the phase bias from using short period interferograms from individual frames to the whole AHB scale (Maghsoudi et al., 2022). In most cases, however, non-tectonic deformation and phase bias map to the vertical component; horizontal velocities at large scale can only be caused by tectonics.

The short wavelength variability in the surface velocities makes estimation of strain rates challenging. As strain rates are gradients in the velocity, this exacerbates any noise present. This means we have necessarily smoothed our velocities prior to strain-

rate calculation to average out some of this dispersion. Future methods could better adapt the filtering approach to account for levels of noise and thus capture the sharpness of velocity gradients expected. In addition, we do not have the north-south component of velocity in the InSAR, relying on the smoother GNSS-derived velocity field. This limitation could be improved in part by using the azimuth (predominantly north-south) motion from burst overlap interferometry (Li et al., 2021a). Of the various strain rates calculated, it has been particularly difficult to capture the dilatation rate sufficiently to make meaningful novel interpretations. This was also found using InSAR applied to the San Andreas Fault (Xu et al., 2021).

Our strain rates show that we are capturing the scars of old earthquakes in the postseismic deformation that is ongoing years and decades after these events. Whilst they are very much part of the velocity and strain rate field, we could choose to account for the postseismic contributions of earthquakes directly in velocity fields, as is done in the GNSS community (Herring et al., 2016; Sobrero et al., 2020), and separate their effects out from the even longer-term deformation. However, doing this in a systematic fashion without biasing the results by our prejudices is challenging – we have chosen to keep postseismic transients in our time series but provide the data that will allow others to make those corrections.

Whilst we are primarily concerned with capturing continental deformation at the scale of the whole AHB, the regions of greatest topography, in particular the Himalayas, are important as locations for major earthquakes. However, it has been very hard to reliably measure the velocities for the highest relief mountains of the Alps, Caucasus, and Himalayas with C-band SAR due to limited coherence at these wavelengths (Figure SB9). This is due to a mixture of environmental impacts including vegetation up to the tree line, and the impact of snow cover at high levels. There is also the challenge of the extreme overall relief, leading to layover and shadowing for radar viewing geometries, which is difficult for unwrapping phase; high relief also results in large gradients in tropospheric delays. It has also been challenging to capture deformation south of the Himalayas in northern India too due to extensive areas of agriculture, and vertical displacement

signals due to groundwater extraction.

The Sentinel-1 satellite radar data were processed continuously during the life span of the LiCS research project (over a 10–year timespan), using the JASMIN high performance computing facility (this involved continued development of the workflow routines, testing and smaller regional studies prior to a unified large scale effort culminating in the past 3 years focus). The total number of epochs for all descending and descending frames was about 222,000 dates, which approximated a similar number of SLC files each of about 4–7GB size (total volume 1PB) needed for generating all 1.2 million interferograms. The processing steps generated intermediate files of even greater volume, and the process is disk storage limited (as we only have access to hundreds of TerraBytes of disk space for the processing storage). This lack of larger data storage meant it was necessary to 1) proceed on a frame-by-frame basis rather than in parallel, and 2) multilook our data and downsample to 100 m to store over one million interferograms. To perform our subsequent analysis, it was again necessary to further downsample our average velocities to 1 km to make the time series inversion with LiCSBAS perform in reasonable time frames. We estimate at least 5 core-hours of processing time were spent per each epoch used starting from the original Sentinel-1 SLC download until generation of the final time series, totalling at least 1 million core-hours for the whole processed dataset. For curation of the interferogram dataset, we use the storage at the UK's Centre for Environmental Data Analysis (CEDA) in their long-term tape archive.

We expect we can also make general improvements by 1) widening the coverage further across the wider AHB into slower deforming areas, 2) lengthening the time series with more recent data from after March 2024, and 3) producing time series at higher spatial resolution than the current 1 km. There is relatively easy potential for 100 m as our catalogue of interferograms has been produced at that resolution, just not the time series and subsequent analysis for this study. By opening up the data set to the community, we give others the opportunity to apply different processing and correction algorithms to our very large observational data set.

6.4. Recommendations

Our results here show that whilst there are concentrations of strain associated with major faults and past earthquakes, an important fraction of the continental deformation occurs over long distances in a smooth, distributed fashion resulting in small strain rates. Ongoing acquisitions to lengthen the Sentinel-1 time series using Sentinel-1C and 1D will be crucial for lowering the threshold for capturing small strain. However, as highlighted with issues of maintaining coherence with C-band, it is important that there are no large data gaps in acquisitions as they break the time series, reducing the accuracy of the average velocities we derive.

Although we have benefited from an exceptionally large data set, some areas lack complete coverage in both ascending and descending viewing geometries, which prevents the retrieval of two components of the velocity field at InSAR resolution. We recommend that acquisitions in both look directions (i.e. including descending) are prioritised over eastern China around the Ordos. Additionally, the region that experienced amongst the largest continental earthquakes in the past century, the M8 Tsetserleg-Bulnay Strike-Slip Earthquake in 1905 in Mongolia (Choi et al., 2018), has a much less complete archive of data, and also should be targeted in the ongoing mission.

The open access data policy from the Copernicus ESA programme for Sentinels has not only been a great benefit in accomplishing a project at this scale, but a necessity. Systematic, regular acquisitions at broad scales are the only way to extract small strain rate signals over long wavelengths typical across the continents, and we recommend that such an approach be continued and adopted by other data providers.

6.5. Outlook for future satellite missions

The current Sentinel-1 mission is set to continue into the next decade (Miranda et al., 2023) with the recent successful launches of S1C and S1D. S1A will be deorbited once S1D becomes fully operational, but until that time, we anticipate the formation of interferograms between images acquired by S1A and S1C/D being possible, as has already been demonstrated (Figure SB34). The degradation of the S1A orbit will cause larger baselines between the two satellites than is ideal for deformation measurement,

leading to somewhat poorer coherence, but modelling of the degradation indicates that this will not become a significant issue before its end of life, although baselines of 700 m can be expected at higher latitudes (Pinjeiro, 2024).

Over the next decade, several planned ESA missions will lead to improvements in our ability to measure tectonic strain over large areas. The next generation of Sentinel-1 satellites (Sentinel-1 NG) will also have a repeat interval of 12 days but a wider swath and higher duty cycle, meaning that each patch of ground can be imaged more frequently on average.

The Copernicus expansion mission Rose-L will operate at L-band (Davidson and Furnell, 2021; Petrolati et al., 2023) in the same orbit as Sentinel-1 NG, expanding coherent InSAR coverage in vegetated areas. The longer wavelength will also be advantageous for measuring high-magnitude signals during earthquakes, which may be aliased in Sentinel-1 data.

The joint NASA and ISRO NISAR mission (Kellogg et al., 2020) launched in mid-2025 and will also acquire L-band with global coverage (Rosen and Kumar, 2021). As well as offering increased coverage in vegetated areas, the left-looking geometry of NISAR will allow for 3-D decomposition when combined with Sentinel-1 data.

The 10th ESA Earth Explorer Mission, Harmony, will consist of two receive-only SAR systems operating in constellation with Sentinel-1D. When combined with the data from Sentinel-1, this will enable the retrieval of a full 3-D deformation field (Prats et al., 2023). As an Earth Explorer mission designed for scientific research rather than an operational mission, it will not be possible to measure 3-D data globally, but Harmony could serve as a proof of concept for future operational missions.

The continuation of Sentinel-1 and future missions will also offer the potential to generate very long time series, by combining data from ERS, ENVISAT, Sentinel-1, Sentinel-1NG, ROSE-L and other missions. This will allow measurement of processes that vary over the long term such as time-varying slip, as was demonstrated for the Haiyuan Fault by combining 20 years of ERS and Envisat data (Jolivet et al., 2013). Ice loss in permafrost across the northeastern Tibetan Plateau was measured over nearly

two decades from combining Envisat and Sentinel-1 (Daout et al., 2020). Subsidence and uplift due to water extraction/replenishment in the Beijing Plain was measured spanning three decades from 1992 to 2023 by combining data from ERS, ENVISAT, Radarsat-2 and Sentinel-1 (Fu et al., 2025). The ability to measure changes in the Earth's surface environment over wide areas for decadal timescales will offer new insights into crustal and land surface processes.

7. Conclusion and outlook

We have compiled, aligned and quality controlled over 73,000 GNSS velocities collated from 171 recent studies into a Eurasia-fixed reference frame yielding over 21,000 consistent point velocities. We have produced the first transcontinental velocity and strain rate field for the Alpine Himalayan belt (20 million km^2), at a spatial sampling of 1 km and with levels of uncertainties in the horizontal ∼2–3 mm/yr and we are able to measure strain rates down to ∼ 10 nstr/yr, or better in some very coherent regions. We have achieved this by processing large volumes of Sentinel-1 data (222,000 epochs), applying a number of atmospheric corrections to reduce noise and combining it with the GNSS reference field.

We have found that horizontal velocities are dominated by tectonic processes. Our results show that whilst the horizontal strain rates are concentrated on major strike-slip faults of Anatolia and the Tibetan Plateau and major convergence zones of the Himalayas and Pamirs, the bulk of the Alpine Himalayan orogeny is undergoing diffuse deformation at relatively low strain rates. Significant regions of distributed deformation are found across Western Anatolia, Iran, the Makran, the whole of the Tian Shan and all of the Tibetan Plateau. We observe large-scale anti-clockwise rotations of northern Arabia and Anatolia, as well as along the Chaman Fault zone from the Makran through to the Hindu Kush and Eastern Syntaxis. We observe major broad clockwise rotations around the Western Syntaxis of the Himalayas. Regions of elevated strain are also found to be associated with creeping faults and postseismic deformation from recent major earthquakes. The results agree well with previously derived strain rate fields with

GNSS only, but the InSAR provides greater detail on short wavelengths for regions that lack very high densities of GNSS.

We find that the vertical rates are dominated by near-surface processes such ground subsidence due to water extraction from aquifers, and permafrost changes at high elevations, except in regions of rapid convergence such as the Pamirs and Himalayas where we observe tectonic uplift.

Improvements we can look forward to include, in the short term, lower uncertainties from increased data with the growing archive with Sentinel-1C/D, and higher-resolution time-series processing better than the 1 km provided here. In the medium term, better coverage from recently launched L-Band missions, will enable strain to be measured in areas with denser vegetation and higher relief, such as the Himalayas. NISAR's left-looking instrument, combined with the right-looking Sentinel-1, will provide some ability to recover full 3-component velocities.

Finally, one hundred years after Argand (1922)'s observations and tectonic map of the deformation of Eurasia, we look forward to the community developing, testing and applying new and improved algorithms to our open access data, and to the resulting improved understanding of continental tectonics.

CRediT authorship contribution statement

Conceptualization: J.R.E., A.J.H. & T.J.W.

Methodology: J.F., M.L. & C.R.

Software: M.L. & J.F.

Validation: J.F., M.L., C.R., Y.M., D.W. & J.R.E

Formal Analysis: J.F., C.R., Y.M., M.L., D.W., Q.O. & J.P.

Investigation: J.F., C.R., Y.M., M.L., Q.O., J.P. & D.W.

Resources: T.J.W., A.J.H & J.R.E.

Data Curation: M.L., C.R., Y.M., J.F., J.P., Q.O., D.W. & J.R.E.

Writing - Original Draft: J.R.E., J.F., C.R., M.L., D.W., Q.O., J.P. & Y.M.

Writing - Review & Editing: J.R.E., T.J.W. & A.J.H.

Visualization: J.F., J.R.E., D.W., C.R., M.L., J.P, Q.O & Y.M.

Supervision: J.R.E., A.J.H. & T.J.W.

Project Administration: J.R.E., A.J.H. & T.J.W.

Funding Acquisition: J.R.E., A.J.H. & T.J.W.

Declaration of competing interest

The authors declare that they have no known competing financial interests or personal relationships that could have appeared to influence the work reported in this paper.

Data availability

We thank the European Space Agency (ESA) for the open data policy on the Sentinel-1 mission. The InSAR data are copyrighted by ESA and are provided through the Copernicus Open Access Hub (https://scihub.copernicus.eu/). The Sentinel-1 InSAR data are also freely distributed by the Alaska Satellite Facility (https://asf.alaska.edu/). The GNSS compilation of 2D and 3D data in Eurasia and ITRF14 reference frames for this study are available here: https://github.com/earjcr1/AHB_GPS. The software *VELMAP* for referencing together InSAR line of sight data with GNSS is archived in Wang and Wright (2025) and continually maintained at https://github.com/eejf-leeds/velmap. The InSAR data were processed using LiCSAR System; time series inversion was performed using modified LiCSBAS, release version 1.17 archived in Lazecky et al. (2025) (from https://github.com/comet-licsar/LiCSBAS). The data files generated here will be made available in a zenodo data repository for download.

Declaration of Generative AI and AI-assisted technologies in the writing process

During the preparation of this work, the authors used ChatGPT for checking of grammar and for coding some algorithms. After using this tool, we reviewed and edited the content and take full responsibility for the content of the publication.

Acknowledgments and funding information

Research of this scale and scope would not have been possible without the systematic acquisitions and openness of the Sentinel-1 Archive by the ESA Copernicus Programme, for which we are very grateful. We also acknowledge the compilation of over 170 GNSS studies to form the velocity field here is only possible by the openness of that community to tabulate and share their velocities. This research is supported by the UK Research and Innovation (UKRI) Natural Environment Research Council (NERC) through the Centre for the Observation and Modelling of Earthquakes, Volcanoes and Tectonics (COMET, http://comet.nerc.ac.uk). This work is also supported by NERC through the Looking into the Continents from Space (LiCS) large Grant (NE/K010867/1). JRE acknowledges the Royal Society for their support through a University Research Fellowship (URF/R/211006 & UF150282) and grant (RF/ERE/210143). We acknowledge additional support from the European Plate Observing System (EPOS, https://www.epos-eu.org/). Some of the figures were generated using GMT versions 5 & 6 (Wessel et al., 2019) and pyGMT (Tian et al., 2025). Scientific colourmaps are from Crameri et al. (2020).

We gratefully acknowledge Barry Parsons for his early conceptualisation and leadership of the LiCS project. Barry's inspiration of the project and his motivation throughout have been important in fostering our community. We also thank Greg Houseman and Philip England for their discussions and thoughts on continental deformation. We thank Susanna Ebmeier, Scott Watson, Muhammet Nergizci, Richard Rigby, Yu Morishita, Chen Yu, Andrew Watson, Jack McGrath, Hua Wang, Jonathan Weiss, Pablo Gonzalez, Karsten Spaans, Richard Walters, Emma Hatton and previous LiCS staff, for their various contributions to this project over the many years of its development.

References

Abdrakhmatov, K., Arrowsmith, R., Elliott, J., Grutzner, C., Mukambayev, A., Rizza, M., Shnizai, Z., Walker, R., Weldon, R., Wilkinson, R., 2024. Urgent need for greater earthquake resilience in continental Asia. Nature Geoscience 17, 818–819. doi:10.1038/s41561-024-01531-0.

Abdrakhmatov, K.Y., Aldazhanov, S.A., Hager, B.H., Hamburger, M.W., Herring, T.A., Kalabaev, K.B., Makarov, V.I., Molnar, P., Panasyuk, S.V., Prilepin, M.T., Reilinger, R.E., Sadybakasov, I.S., Souter, B.J., Trapeznikov, Y.A., Tsurkov, V.Y., Zubovich, A.V., 1996. Relatively recent construction of the Tien Shan inferred from GPS measurements of present-day crustal deformation rates. Nature 384, 450–453. doi:10.1038/384450a0.

Ader, T., Avouac, J.P., Liu-Zeng, J., Lyon-Caen, H., Bollinger, L., Galetzka, J., Genrich, J., Thomas, M., Chanard, K., Sapkota, S.N., Rajaure, S., Shrestha, P., Ding, L., Flouzat, M., 2012. Convergence rate across the Nepal Himalaya and interseismic coupling on the Main Himalayan Thrust: Implications for seismic hazard. Journal of Geophysical Research: Solid Earth 117. doi:10.1029/2011JB009071.

Ahmad, W., Choi, M., Kim, S., Kim, D., 2019. Detection of land subsidence and its relationship with land cover types using ESA Sentinel satellite data: A case study of Quetta Valley, Pakistan. International Journal of Remote Sensing 40, 9572–9603. doi:10.1080/01431161.2019.1633704.

Altamimi, Z., Métivier, L., Rebischung, P., Rouby, H., Collilieux, X., 2017. ITRF2014 plate motion model. Geophysical Journal International 209, 1906–1912. doi:10.1093/gji/ggx136.

Ansari, H., De Zan, F., Parizzi, A., 2021. Study of Systematic Bias in Measuring Surface Deformation With SAR Interferometry. IEEE Transactions on Geoscience and Remote Sensing 59, 1285–1301. doi:10.1109/TGRS.2020.3003421.

Ao, Z., Hu, X., Tao, S., Hu, X., Wang, G., Li, M., Wang, F., Hu, L., Liang, X., Xiao, J., Yusup, A., Qi, W., Ran, Q., Fang, J., Chang, J., Zeng, Z., Fu, Y., Xue, B., Wang, P., Zhao, K., Li, L., Li, W., Li, Y., Jiang, M., Yang, Y., Shen, H., Zhao, X., Shi, Y., Wu, B., Yan, Z., Wang, M., Su, Y., Hu, T., Ma, Q., Bai, H., Wang, L., Yang, Z., Feng, Y., Zhang, D., Huang, E., Pan, J., Ye, H., Yang, C., Qin, Y., He, C., Guo, Y., Cheng, K., Ren, Y., Yang, H., Zheng, C., Zhu, J., Wang, S., Ji, C., Zhu, B., Liu, H., Tang, Z., Wang, Z., Zhao, S., Tang, Y., Xing, H., Guo, Q., Liu, Y., Fang, J., 2024. A national-scale assessment of land subsidence in China's major cities. Science 384, 301–306. doi:10.1126/science.adl4366.

Argand, E., 1922. La tectonique de l'Asie. Conférence faite á Bruxelles, le 10 août 1922, in: Congrès géologique international (XIIIe session)- Belgique 1922, p. 171.

Attema, E., Duchossois, G., Kohlhammer, G., 1998. ERS-1/2 SAR land applications: Overview and main results, in: IGARSS '98. Sensing and Managing the Environment. 1998 IEEE International Geoscience and Remote Sensing. Symposium Proceedings. (Cat. No.98CH36174), pp. 1796–1798 vol.4. doi:10.1109/IGARSS.1998.703655.

Avouac, J.P., 2015. From Geodetic Imaging of Seismic and Aseismic Fault Slip to Dynamic Modeling of the Seismic Cycle. Annual Review of Earth and Planetary Sciences 43, 233–271. doi:10.1146/annurev-earth-060614-105302.

Avouac, J.P., Ayoub, F., Wei, S., Ampuero, J.P., Meng, L., Leprince, S., Jolivet, R., Duputel, Z., Helmberger, D., 2014. The 2013, Mw 7.7 Balochistan earthquake, energetic strike-slip reactivation of a thrust fault. Earth and Planetary Science Letters 391, 128–134. doi:10.1016/j.epsl.2014.01.036.

Barbot, S., Fialko, Y., Bock, Y., 2009. Postseismic deformation due to the M 6.0 2004 Parkfield earthquake: Stress-driven creep on a fault with spatially variable rate-and-state friction parameters. Journal of Geophysical Research: Solid Earth 114. doi:10.1029/2008JB005748.

Barnhart, W.D., 2017. Fault creep rates of the Chaman fault (Afghanistan and Pakistan) inferred from InSAR. Journal of Geophysical Research: Solid Earth 122, 372–386. doi:10.1002/2016JB013656.

Beavan, J., Wallace, L.M., Palmer, N., Denys, P., Ellis, S., Fournier, N., Hreinsdottir, S., Pearson, C., Denham, M., 2016. New zealand GPS velocity field: 1995–2013. New Zealand journal of geology and geophysics 59, 5–14.

Bekaert, D., Arena, N., Bato, M.G., Buzzanga, B., Govorcin, M., Havazli, E., Hogenson, K., Hua, H., Johnston, A., Karim, M., Kennedy, J.H., Lu, Z., Marshak, C.Z., Meyer, F., Owen, S., Sangha, S., Short, G., Wang, J., Zinke, R., 2023. The Aria-S1-Gunw: The ARIA Sentinel-1 Geocoded Unwrapped Phase Product for Open Insar Science and Disaster Response, in: IGARSS 2023 - 2023 IEEE International Geoscience and Remote Sensing Symposium, pp. 2850–2853. doi:10.1109/IGARSS52108.2023.10282671.

Bekaert, D.P.S., Walters, R.J., Wright, T.J., Hooper, A.J., Parker, D.J., 2015. Statistical comparison of InSAR tropospheric correction techniques. Remote Sensing of Environment 170, 40–47. doi:10.1016/j.rse.2015.08.035.

Bell, M.A., Elliott, J.R., Parsons, B.E., 2011. Interseismic strain accumulation across the Manyi fault (Tibet) prior to the 1997 M $_w$ 7.6 earthquake. Geophysical Research Letters 38. doi:10.1029/2011GL049762.

Bilham, R., 2019. Himalayan earthquakes: A review of historical seismicity and early 21st century slip potential. Geological Society, London, Special Publications 483, 423–482. doi:10.1144/SP483.16.

Bilham, R., Ozener, H., Mencin, D., Dogru, A., Ergintav, S., Cakir, Z., Aytun, A., Aktug, B., Yilmaz, O., Johnson, W., Mattioli, G., 2016. Surface creep on the North Anatolian Fault at Ismetpasa, Turkey, 1944–2016. Journal of Geophysical Research: Solid Earth 121, 7409–7431. doi:10.1002/2016JB013394.

Bilitza, D., Altadill, D., Truhlik, V., Shubin, V., Galkin, I., Reinisch, B., Huang, X., 2017. International Reference Ionosphere 2016: From ionospheric climate to real-time weather predictions. Space Weather 15, 418–429. doi:10.1002/2016SW001593.

Bird, P., 2003. An updated digital model of plate boundaries. Geochemistry, Geophysics, Geosystems 4. doi:10.1029/2001GC000252.

Bird, P., Jackson, D.D., Kagan, Y.Y., Kreemer, C., Stein, R.S., 2015. GEAR1: A Global Earthquake Activity Rate Model Constructed from Geodetic Strain Rates and Smoothed Seismicity. Bulletin of the Seismological Society of America 105, 2538–2554. doi:10.1785/0120150058.

Bird, P., Kreemer, C., Holt, W.E., 2010. A Long-term Forecast of Shallow Seismicity Based on the Global Strain Rate Map. Seismological Research Letters 81, 184–194. doi:10.1785/gssrl.81.2.184.

Blewitt, G., Lavallée, D., 2002. Effect of annual signals on geodetic velocity. Journal of Geophysical Research: Solid Earth 107, ETG–9.

Bonì, R., Meisina, C., Cigna, F., Herrera, G., Notti, D., Bricker, S., McCormack, H., Tomás, R., Béjar-Pizarro, M., Mulas, J., Ezquerro, P., 2017. Exploitation of Satellite A-DInSAR Time Series for Detection, Characterization and Modelling of Land Subsidence. Geosciences 7, 25. doi:10.3390/geosciences7020025.

Bos, MS., Fernandes, RMS., Williams, SDP., Bastos, L., 2008. Fast error analysis of continuous GPS observations. Journal of Geodesy 82, 157–166.

Bourne, S.J., England, P.C., Parsons, B., 1998. The motion of crustal blocks driven by flow of the lower lithosphere and implications for slip rates of continental strike-slip faults. Nature 391, 655–659. doi:10.1038/35556.

Bürgmann, R., Rosen, P.A., Fielding, E.J., 2000. Synthetic Aperture Radar Interferometry to Measure Earth's Surface Topography and Its Deformation. Annual Review of Earth and Planetary Sciences 28, 169–209. doi:10.1146/annurev.earth.28.1.169.

Cakir, Z., Akoglu, A.M., Belabbes, S., Ergintav, S., Meghraoui, M., 2005. Creeping along the Ismetpasa section of the North Anatolian fault (Western Turkey): Rate and extent from InSAR. Earth and Planetary Science Letters 238, 225–234. doi:10.1016/j.epsl.2005.06.044.

Calais, E., Vergnolle, M., San'kov, V., Lukhnev, A., Miroshnitchenko, A., Amarjargal, S., Déverchère, J., 2003. GPS measurements of crustal deformation in the Baikal-Mongolia area (1994–2002): Implications for current kinematics of Asia. Journal of Geophysical Research: Solid Earth 108. doi:10.1029/2002JB002373.

Castro-Perdomo, N., Viltres, R., Masson, F., Klinger, Y., Liu, S., Dhahry, M., Ulrich, P., Bernard, J.D., Matrau, R., Alothman, A., et al., 2022. Interseismic deformation in the Gulf of Aqaba from GPS measurements. Geophysical Journal International 228, 477–492.

Chen, C., Zebker, H., 2002. Phase unwrapping for large SAR interferograms: Statistical segmentation and generalized network models. IEEE Transactions on Geoscience and Remote Sensing 40, 1709–1719. doi:10.1109/TGRS.2002.802453.

Chen, J., Wu, T., Zou, D., Liu, L., Wu, X., Gong, W., Zhu, X., Li, R., Hao, J., Hu, G., Pang, Q., Zhang, J., Yang, S., 2022. Magnitudes and patterns of large-scale permafrost ground deformation revealed by Sentinel-1 InSAR on the central Qinghai-Tibet Plateau. Remote Sensing of Environment 268, 112778. doi:10.1016/j.rse.2021.112778.

Chen, M., Tomás, R., Li, Z., Motagh, M., Li, T., Hu, L., Gong, H., Li, X., Yu, J., Gong, X., 2016. Imaging Land Subsidence Induced by Groundwater Extraction in Beijing (China) Using Satellite Radar Interferometry. Remote Sensing 8, 468. doi:10.3390/rs8060468.

Choi, J.H., Klinger, Y., Ferry, M., Ritz, J.F., Kurtz, R., Rizza, M., Bollinger, L., Davaasambuu, B., Tsend-Ayush, N., Demberel, S., 2018. Geologic Inheritance and Earthquake Rupture Processes: The 1905 M $\geq$ 8 Tsetserleg-Bulnay Strike-Slip Earthquake Sequence, Mongolia. Journal of Geophysical Research: Solid Earth 123, 1925–1953. doi:10.1002/2017JB013962.

Costantini, M., Minati, F., Trillo, F., Ferretti, A., Novali, F., Passera, E., Dehls, J., Larsen, Y., Marinkovic, P., Eineder, M., Brcic, R., Siegmund, R., Kotzerke, P., Probeck, M., Kenyeres, A., Proietti, S., Solari, L., Andersen, H.S., 2021. European Ground Motion Service (EGMS), in: 2021 IEEE International Geoscience and Remote Sensing Symposium IGARSS, pp. 3293–3296. doi:10.1109/IGARSS47720.2021.9553562.

Crameri, F., Shephard, G.E., Heron, P.J., 2020. The misuse of colour in science communication. Nature Communications 11, 5444. doi:10.1038/s41467-020-19160-7.

Da Lio, C., Tosi, L., 2019. Vulnerability to relative sea-level rise in the Po river delta (Italy). Estuarine, Coastal and Shelf Science 228, 106379. doi:10.1016/j.ecss.2019.106379.

Dalaison, M., Jolivet, R., van Rijsingen, E.M., Michel, S., 2021. The Interplay Between Seismic and Aseismic Slip Along the Chaman Fault Illuminated by InSAR. Journal of Geophysical Research: Solid Earth 126, e2021JB021935. doi:10.1029/2021JB021935.

Daout, S., Dini, B., Haeberli, W., Doin, M.P., Parsons, B., 2020. Ice loss in the Northeastern Tibetan Plateau permafrost as seen by 16 yr of ESA SAR missions. Earth and Planetary Science Letters 545, 116404. doi:10.1016/j.epsl.2020.116404.

Daout, S., Parsons, B., Walker, R., 2021. Post-Earthquake Fold Growth Imaged in the Qaidam Basin, China, With Interferometric Synthetic Aperture Radar. Journal of Geophysical Research: Solid Earth 126, e2020JB021241. doi:10.1029/2020JB021241.

Davidson, M.W.J., Furnell, R., 2021. ROSE-L: Copernicus L-Band Sar Mission, in: 2021 IEEE International Geoscience and Remote Sensing Symposium IGARSS, pp. 872–873. doi:10.1109/IGARSS47720.2021.9554018.

De Zan, F., Gomba, G., 2018. Vegetation and soil moisture inversion from SAR closure phases: First experiments and results. Remote Sensing of Environment 217, 562–572. doi:10.1016/j.rse.2018.08.034.

De Zan, F., Parizzi, A., Prats-Iraola, P., López-Dekker, P., 2014. A SAR Interferometric Model for Soil Moisture. IEEE Transactions on Geoscience and Remote Sensing 52, 418–425. doi:10.1109/TGRS.2013.2241069.

De Zan, F., Zonno, M., López-Dekker, P., 2015. Phase Inconsistencies and Multiple Scattering in SAR Interferometry. IEEE Transactions on Geoscience and Remote Sensing 53, 6608–6616. doi:10.1109/TGRS.2015.2444431.

Dehls, J.F., Larsen, Y., Marinkovic, P., Lauknes, T.R., Stødle, D., Moldestad, D.A., 2019. INSAR.No: A National Insar Deformation Mapping/Monitoring Service In Norway – From Concept To Operations, in: IGARSS 2019 - 2019 IEEE International Geoscience and Remote Sensing Symposium, pp. 5461–5464. doi:10.1109/IGARSS.2019.8898614.

Desnos, Y.L., Buck, C., Guijarro, J., Levrini, G., Suchail, J.L., Torres, R., Laur, H., Closa, J., Rosich, B., 2000. The ENVISAT advanced synthetic aperture radar system, in: IGARSS 2000. IEEE 2000 International Geoscience and Remote Sensing Symposium. Taking the Pulse of the Planet: The Role of Remote Sensing in Managing the Environment. Proceedings (Cat. No.00CH37120), pp. 1171–1173 vol.3. doi:10.1109/IGARSS.2000.858057.

Di Giacomo, D., Engdahl, E.R., Storchak, D.A., 2018. The ISC-GEM Earthquake Catalogue (1904–2014): Status after the Extension Project. Earth System Science Data 10, 1877–1899. doi:10.5194/essd-10-1877-2018.

DiCaprio, C.J., Simons, M., 2008. Importance of ocean tidal load corrections for differential InSAR. Geophysical Research Letters 35. doi:10.1029/2008GL035806.

Doin, M.P., Lodge, F., Guillaso, S., Jolivet, R., Lasserre, C., Ducret, G., Grandin, R., Pathier, E., Pinel, V., 2011. Presentation of the Small Baselin NSBAS Processing Chain on a Case Example : The Etan Deformation Monitoring from 2003 to 2010 Using Envisat Data, in: Fringe Symposium, pp. 1–7.

Drouin, V., Sigmundsson, F., 2019. Countrywide Observations of Plate Spreading and Glacial Isostatic Adjustment in Iceland Inferred by Sentinel-1 Radar Interferometry, 2015–2018. Geophysical Research Letters 46, 8046–8055. doi:10.1029/2019GL082629.

Dziewonski, A.M., Chou, T.A., Woodhouse, J.H., 1981. Determination of earthquake source parameters from waveform data for studies of global and regional seismicity. Journal of Geophysical Research: Solid Earth 86, 2825–2852. doi:10.1029/JB086iB04p02825.

Efron, B., Tibshirani, R., 1986. Bootstrap Methods for Standard Errors, Confidence Intervals, and Other Measures of Statistical Accuracy. Statistical Science 1, 54–75. doi:10.1214/ss/1177013815.

Ekström, G., Nettles, M., Dziewoński, A.M., 2012. The global CMT project 2004–2010: Centroid-moment tensors for 13,017 earthquakes. Physics of the Earth and Planetary Interiors 200–201, 1–9. doi:10.1016/j.pepi.2012.04.002.

Elliott, J., Walters, R., Wright, T., 2016. The role of space-based observation in understanding and responding to active tectonics and earthquakes. Nature Communications 7, 13844. doi:10.1038/ncomms13844.

England, P., Jackson, J., 1989. Active Deformation of the Continents. Annual Review of Earth and Planetary Sciences 17, 197–226. doi:10.1146/annurev.ea.17.050189.001213.

England, P., Jackson, J., 2011. Uncharted seismic risk. Nature Geoscience 4, 348–349. doi:10.1038/ngeo1168.

England, P., Molnar, P., 1997. Active Deformation of Asia: From Kinematics to Dynamics. Science 278, 647–650. doi:10.1126/science.278.5338.647.

Evans, E.L., 2022. A Dense Block Model Representing Western Continental United States Deformation for the 2023 Update to the National Seismic Hazard Model. Seismological Research Letters 93, 3024–3036. doi:10.1785/0220220141.

Fan, C., Liu, L., Zhao, Z., Mu, C., 2025. Pronounced Underestimation of Surface Deformation Due To Unwrapping Errors Over Tibetan Plateau Permafrost by Sentinel-1 InSAR: Identification and Correction. Journal of Geophysical Research: Earth Surface 130, e2024JF007854. doi:10.1029/2024JF007854.

Fang, J., Houseman, G.A., Wright, T.J., Evans, L.A., Craig, T.J., Elliott, J.R., Hooper, A., 2024a. The Dynamics of the India-Eurasia Collision: Faulted Viscous Continuum Models Constrained by High-Resolution Sentinel-1 InSAR and GNSS Velocities. Journal of Geophysical Research: Solid Earth 129, e2023JB028571. doi:10.1029/2023JB028571.

Fang, J., Wright, T.J., Johnson, K.M., Ou, Q., Styron, R., Craig, T.J., Elliott, J.R., Hooper, A., Zheng, G., 2024b. Strain Partitioning in the Southeastern Tibetan Plateau From Kinematic Modeling of High-Resolution Sentinel-1 InSAR and GNSS. Geophysical Research Letters 51, e2024GL111199. doi:10.1029/2024GL111199.

Farr, T.G., Rosen, P.A., Caro, E., Crippen, R., Duren, R., Hensley, S., Kobrick, M., Paller, M., Rodriguez, E., Roth, L., Seal, D., Shaffer, S., Shimada, J., Umland, J., Werner, M., Oskin, M., Burbank, D., Alsdorf, D., 2007. The Shuttle Radar Topography Mission. Reviews of Geophysics 45. doi:10.1029/2005RG000183.

Fattahi, H., Amelung, F., 2016. InSAR observations of strain accumulation and fault creep along the Chaman Fault system, Pakistan and Afghanistan. Geophysical Research Letters 43, 8399–8406. doi:10.1002/2016GL070121.

Feigl, K.L., Agnew, D.C., Bock, Y., Dong, D., Donnellan, A., Hager, B.H., Herring, T.A., Jackson, D.D., Jordan, T.H., King, R.W., Larsen, S., Larson, K.M., Murray, M.H., Shen, Z., Webb, F.H., 1993. Space geodetic measurement of crustal deformation in central and southern California, 1984–1992. Journal of Geophysical Research: Solid Earth 98, 21677–21712. doi:10.1029/93JB02405.

Feigl, K.L., Thatcher, W., 2006. Geodetic observations of post-seismic transients in the context of the earthquake deformation cycle. Comptes Rendus. Géoscience 338, 1012–1028. doi:10.1016/j.crte.2006.06.006.

Fernández, J., Peter, H., Fernández, C., Berzosa, J., Fernández, M., Bao, L., Muñoz, M.Á., Lara, S., Terradillos, E., Féménias, P., Nogueira, C., 2024. The Copernicus POD Service. Advances in Space Research 74, 2615–2648. doi:10.1016/j.asr.2024.02.056.

Festa, D., Bonano, M., Casagli, N., Confuorto, P., De Luca, C., Del Soldato, M., Lanari, R., Lu, P., Manunta, M., Manzo, M., Onorato, G., Raspini, F., Zinno, I., Casu, F., 2022. Nation-wide mapping and classification of ground deformation phenomena through the spatial clustering of P-SBAS InSAR measurements: Italy case study. ISPRS Journal of Photogrammetry and Remote Sensing 189, 1–22. doi:10.1016/j.isprsjprs.2022.04.022.

Field, E.H., Biasi, G.P., Bird, P., Dawson, T.E., Felzer, K.R., Jackson, D.D., Johnson, K.M., Jordan, T.H., Madden, C., Michael, A.J., Milner, K.R., Page, M.T., Parsons, T., Powers, P.M., Shaw, B.E., Thatcher, W.R., Weldon, II, R.J., Zeng, Y., 2015. Long-Term Time-Dependent Probabilities for the Third Uniform California Earthquake Rupture Forecast (UCERF3). Bulletin of the Seismological Society of America 105, 511–543. doi:10.1785/0120140093.

Flesch, L.M., Haines, A.J., Holt, W.E., 2001. Dynamics of the India-Eurasia collision zone. Journal of Geophysical Research: Solid Earth 106, 16435–16460. doi:10.1029/2001JB000208.

Fu, Y., Wang, J., Zhang, Y., Yang, H., Li, L., Ren, Z., 2025. Spatiotemporal evolution characteristics of ground deformation in the Beijing Plain from 1992 to 2023 derived from a novel multi-sensor InSAR fusion method. Remote Sensing of Environment 319, 114635. doi:10.1016/j.rse.2025.114635.

Funning, G.J., Garcia, A., 2019. A systematic study of earthquake detectability using Sentinel-1 Interferometric Wide-Swath data. Geophysical Journal International 216, 332–349. doi:10.1093/gji/ggy426.

Gabriel, A.K., Goldstein, R.M., Zebker, H.A., 1989. Mapping small elevation changes over large areas: Differential radar interferometry. Journal of Geophysical Research: Solid Earth 94, 9183–9191. doi:10.1029/JB094iB07p09183.

Gambolati, G., Teatini, P., 2015. Geomechanics of subsurface water withdrawal and injection: GROUNDWATER GEOMECHANICS. Water Resources Research 51, 3922–3955. doi:10.1002/2014WR016841.

Geary, R.C., 1935. The ratio of the mean deviation to the standard deviation as a test of normality. Biometrika 27, 310–332.

Geudtner, D., Torres, R., Snoeij, P., Davidson, M., Rommen, B., 2014. Sentinel-1 System capabilities and applications, in: 2014 IEEE Geoscience and Remote Sensing Symposium, pp. 1457–1460. doi:10.1109/IGARSS.2014.6946711.

Goldstein, R.M., Werner, C.L., 1998. Radar interferogram filtering for geophysical applications. Geophysical Research Letters 25, 4035–4038. doi:10.1029/1998GL900033.

Gomba, G., De Zan, F., Brcic, R., Eineder, M., 2024. Mapping Worldwide Ground Deformation in High-Strain Areas with SAR PS/DS Interferometry and Sentinel-1 Imagery, in: EGU Conference Abstracts, p. 8645. doi:10.5194/egusphere-egu24-8645.

Goorabi, A., Karimi, M., Yamani, M., Perissin, D., 2020. Land subsidence in Isfahan metropolitan and its relationship with geological and geomorphological settings revealed by Sentinel-1A InSAR observations. Journal of Arid Environments 181, 104238. doi:10.1016/j.jaridenv.2020.104238.

Grafarend, E., 1984. Variance-covariance components estimation, theoretical results and geodetic applications, in: 16th European meeting of statisticians.

Grandin, R., Doin, M.P., Bollinger, L., Pinel-Puysségur, B., Ducret, G., Jolivet, R., Sapkota, S.N., 2012. Long-term growth of the Himalaya inferred from interseismic InSAR measurement. Geology 40, 1059–1062. doi:10.1130/G33154.1.

Gruber, S., 2012. Derivation and analysis of a high-resolution estimate of global permafrost zonation. The Cryosphere 6, 221–233. doi:10.5194/tc-6-221-2012.

Guns, K., Sandwell, D., Xu, X., Bock, Y., Yong, L.W., Smith-Konter, B., 2024. Seismic Moment Accumulation Rate From Geodesy: Constraining Kostrov Thickness in Southern California. Journal of Geophysical Research: Solid Earth 129, e2023JB027939. doi:10.1029/2023JB027939.

Haghshenas Haghighi, M., Motagh, M., 2024. Uncovering the impacts of depleting aquifers: A remote sensing analysis of land subsidence in Iran. Science Advances 10, eadk3039. doi:10.1126/sciadv.adk3039.

Harris, R.A., 2017. Large earthquakes and creeping faults. Reviews of Geophysics 55, 169–198. doi:10.1002/2016RG000539.

Hathaway, D.H., 2015. The Solar Cycle. Living Reviews in Solar Physics 12, 4. doi:10.1007/lrsp-2015-4.

Hearn, E.H., 2003. What can GPS data tell us about the dynamics of post-seismic deformation? Geophysical Journal International 155, 753–777. doi:10.1111/j.1365-246X.2003.02030.x.

Herrera-García, G., Ezquerro, P., Tomás, R., Béjar-Pizarro, M., López-Vinielles, J., Rossi, M., Mateos, R.M., Carreón-Freyre, D., Lambert, J., Teatini, P., Cabral-Cano, E., Erkens, G., Galloway, D., Hung, W.C., Kakar, N., Sneed, M., Tosi, L., Wang, H., Ye, S., 2021. Mapping the global threat of land subsidence. Science 371, 34–36. doi:10.1126/science.abb8549.

Herring, T.A., Melbourne, T.I., Murray, M.H., Floyd, M.A., Szeliga, W.M., King, R.W., Phillips, D.A., Puskas, C.M., Santillan, M., Wang, L., 2016. Plate Boundary Observatory and related networks: GPS data analysis methods and geodetic products. Reviews of Geophysics 54, 759–808. doi:10.1002/2016RG000529.

Hetland, E.A., Musé, P., Simons, M., Lin, Y.N., Agram, P.S., DiCaprio, C.J., 2012. Multiscale InSAR Time Series (MInTS) analysis of surface deformation. Journal of Geophysical Research: Solid Earth 117. doi:10.1029/2011JB008731.

Hilley, G.E., Johnson, K., Wang, M., Shen, Z.K., Bürgmann, R., 2009. Earthquake-cycle deformation and fault slip rates in northern Tibet. Geology 37, 31–34. doi:10.1130/G25157A.1.

Hong, S., Liu, M., Zhou, X., Meng, G., Dong, Y., 2023. Afterslip on Conjugate Faults of the 2020 Mw 6.3 Nima Earthquake in the Central Tibetan Plateau: Evidence from InSAR Measurements. Bulletin of the Seismological Society of America 113, 2026–2040. doi:10.1785/0120220247.

Hooper, A., Segall, P., Zebker, H., 2007. Persistent scatterer interferometric synthetic aperture radar for crustal deformation analysis, with application to Volcán Alcedo, Galápagos. Journal of Geophysical Research: Solid Earth 112. doi:10.1029/2006JB004763.

Hooper, A., Zebker, H., Segall, P., Kampes, B., 2004. A new method for measuring deformation on volcanoes and other natural terrains using InSAR persistent scatterers. Geophysical Research Letters 31. doi:10.1029/2004GL021737.

Houseman, G., England, P., 1986. Finite strain calculations of continental deformation: 1. Method and general results for convergent zones. Journal of Geophysical Research: Solid Earth 91, 3651–3663. doi:10.1029/JB091iB03p03651.

Hu, J., Li, Z.W., Ding, X.L., Zhu, J.J., Zhang, L., Sun, Q., 2014. Resolving three-dimensional surface displacements from InSAR measurements: A review. Earth-Science Reviews 133, 1–17. doi:10.1016/j.earscirev.2014.02.005.

Hu, L., Dai, K., Xing, C., Li, Z., Tomás, R., Clark, B., Shi, X., Chen, M., Zhang, R., Qiu, Q., Lu, Y., 2019. Land subsidence in Beijing and its relationship with geological faults revealed by Sentinel-1 InSAR observations. International Journal of Applied Earth Observation and Geoinformation 82, 101886. doi:10.1016/j.jag.2019.05.019.

Huang, Z., Zhou, Y., Qiao, X., Zhang, P., Cheng, X., 2022. Kinematics of the ∼1000 km Haiyuan fault system in northeastern Tibet from high-resolution Sentinel-1 InSAR velocities: Fault architecture, slip rates, and partitioning. Earth and Planetary Science Letters 583, 117450. doi:10.1016/j.epsl.2022.117450.

Huang, Z., Zhou, Y., Zhang, P., 2023. Newly discovered shallow creep along the Gozha Co fault in northwestern Tibet: Spatial extent, rate and temporal evolution. Earth and Planetary Science Letters 621, 118388. doi:10.1016/j.epsl.2023.118388.

Hussain, E., Hooper, A., Wright, T.J., Walters, R.J., Bekaert, D.P.S., 2016. Interseismic strain accumulation across the central North Anatolian Fault from iteratively unwrapped InSAR measurements. Journal of Geophysical Research: Solid Earth 121, 9000–9019. doi:10.1002/2016JB013108.

Hussain, E., Wright, T.J., Walters, R.J., Bekaert, D.P.S., Lloyd, R., Hooper, A., 2018. Constant strain accumulation rate between major earthquakes on the North Anatolian Fault. Nature Communications 9, 1392. doi:10.1038/s41467-018-03739-2.

Ingleby, T., Wright, T.J., 2017. Omori-like decay of postseismic velocities following continental earthquakes. Geophysical Research Letters 44, 3119–3130. doi:10.1002/2017GL072865.

Jackson, J., McKenzie, D., 1984. Active tectonics of the Alpine—Himalayan Belt between western Turkey and Pakistan. Geophysical Journal International 77, 185–264. doi:10.1111/j.1365-246X.1984.tb01931.x.

Jiang, J., Lohman, R.B., 2021. Coherence-guided InSAR deformation analysis in the presence of ongoing land surface changes in the Imperial Valley, California. Remote Sensing of Environment 253, 112160. doi:10.1016/j.rse.2020.112160.

Johnson, K.M., Wallace, L.M., Maurer, J., Hamling, I., Williams, C., Rollins, C., Gerstenberger, M., Van Dissen, R., 2024. Inverting Geodetic Strain Rates for Slip Deficit Rate in Complex Deforming Zones: An Application to the New Zealand Plate Boundary. Journal of Geophysical Research: Solid Earth 129, e2023JB027565. doi:10.1029/2023JB027565.

Jolivet, R., Agram, P.S., Lin, N.Y., Simons, M., Doin, M.P., Peltzer, G., Li, Z., 2014. Improving InSAR geodesy using Global Atmospheric Models. Journal of Geophysical Research: Solid Earth 119, 2324–2341. doi:10.1002/2013JB010588.

Jolivet, R., Frank, W.B., 2020. The Transient and Intermittent Nature of Slow Slip. AGU Advances 1, e2019AV000126. doi:10.1029/2019AV000126.

Jolivet, R., Grandin, R., Lasserre, C., Doin, M.P., Peltzer, G., 2011. Systematic InSAR tropospheric phase delay corrections from global meteorological reanalysis data. Geophysical Research Letters 38. doi:10.1029/2011GL048757.

Jolivet, R., Jara, J., Dalaison, M., Rouet-Leduc, B., Özdemir, A., Dogan, U., Çakir, Z., Ergintav, S., Dubernet, P., 2023. Daily to centennial behavior of aseismic slip along the central section of the North Anatolian Fault. Journal of Geophysical Research: Solid Earth 128, e2022JB026018.

Jolivet, R., Lasserre, C., Doin, M.P., Peltzer, G., Avouac, J.P., Sun, J., Dailu, R., 2013. Spatio-temporal evolution of aseismic slip along the Haiyuan fault, China: Implications for fault frictional properties. Earth and Planetary Science Letters 377–378, 23–33. doi:10.1016/j.epsl.2013.07.020.

Kääb, A., Mouginot, J., Prats-Iraola, P., Rignot, E., Rabus, B., Benedikter, A., Rott, H., Nagler, T., Rommen, B., Lopez-Dekker, P., 2024. Potential of the Bi-Static SAR Satellite Companion Mission Harmony for Land-Ice Observations. Remote Sensing 16, 2918. doi:10.3390/rs16162918.

Kakar, N., Metzger, S., Schöne, T., Motagh, M., Waizy, H., Nasrat, N.A., Lazecký, M., Amelung, F., Bookhagen, B., 2025. Interferometric Radar Satellite and In-Situ Well Time-Series Reveal Groundwater Extraction Rate Changes in Urban and Rural Afghanistan. Water Resources Research 61, e2023WR036626. doi:10.1029/2023WR036626.

Kellndorfer, J., Cartus, O., Lavalle, M., Magnard, C., Milillo, P., Oveisgharan, S., Osmanoglu, B., Rosen, P.A., Wegmüller, U., 2022. Global seasonal Sentinel-1 interferometric coherence and backscatter data set. Scientific Data 9, 73. doi:10.1038/s41597-022-01189-6.

Kellogg, K., Hoffman, P., Standley, S., Shaffer, S., Rosen, P., Edelstein, W., Dunn, C., Baker, C., Barela, P., Shen, Y., Guerrero, A.M., Xaypraseuth, P., Sagi, V.R., Sreekantha, C.V., Harinath, N., Kumar, R., Bhan, R., Sarma, C.V.H.S., 2020. NASA-ISRO Synthetic Aperture Radar (NISAR) Mission, in: 2020 IEEE Aerospace Conference, pp. 1–21. doi:10.1109/AERO47225.2020.9172638.

Khan, J., Ren, X., Hussain, M.A., Jan, M.Q., 2022. Monitoring Land Subsidence Using PS-InSAR Technique in Rawalpindi and Islamabad, Pakistan. Remote Sensing 14, 3722. doi:10.3390/rs14153722.

Khorrami, F., Vernant, P., Masson, F., Nilfouroushan, F., Mousavi, Z., Nankali, H., Saadat, S.A., Walpersdorf, A., Hosseini, S., Tavakoli, P., et al., 2019. An up-to-date crustal deformation map of Iran using integrated campaign-mode and permanent GPS velocities. Geophysical Journal International 217, 832–843.

Kreemer, C., Blewitt, G., Klein, E.C., 2014. A geodetic plate motion and Global Strain Rate Model. Geochemistry, Geophysics, Geosystems 15, 3849–3889. doi:10.1002/2014GC005407.

Kreemer, C., Holt, W.E., Haines, A.J., 2003. An integrated global model of present-day plate motions and plate boundary deformation. Geophysical Journal International 154, 8–34. doi:10.1046/j.1365-246X.2003.01917.x.

Lazecky, M., Fang, J., Hooper, A., Wright, T., 2022. Improved Phase Unwrapping Algorithm Based on Standard Methods, in: IGARSS 2022 - 2022 IEEE International Geoscience and Remote Sensing Symposium, pp. 743–746. doi:10.1109/IGARSS46834.2022.9884337.

Lazecký, M., Hooper, A.J., Piromthong, P., 2023. InSAR-Derived Horizontal Velocities in a Global Reference Frame. Geophysical Research Letters 50, e2022GL101173. doi:10.1029/2022GL101173.

Lazecky, M., Morishita, Y., Shen, L., Espín, P., Ou, Q., Hooper, A., McGrath, J., Fang, J., Wang, D., Nergizci, M., Gao, Y., Watson, A., Wright, T., 2025. LiCSAR Extra & LiCSBAS. Zenodo doi:10.5281/zenodo.17734804.

Lazecký, M., Ou, Q., Shen, L., McGrath, J., Payne, J., Espín, P., Hooper, A., Wright, T., 2024. Strategies for improving and correcting unwrapped interferograms implemented in LiCSBAS. Procedia Computer Science 239, 2408–2412. doi:10.1016/j.procs.2024.06.435.

Lazecký, M., Spaans, K., González, P.J., Maghsoudi, Y., Morishita, Y., Albino, F., Elliott, J., Greenall, N., Hatton, E., Hooper, A., Juncu, D., McDougall, A., Walters, R.J., Watson, C.S., Weiss, J.R., Wright, T.J., 2020. LiCSAR: An Automatic InSAR Tool for Measuring and Monitoring Tectonic and Volcanic Activity. Remote Sensing 12, 2430. doi:10.3390/rs12152430.

Lemrabet, L., Doin, M.P., Lasserre, C., Durand, P., 2023. Referencing of Continental-Scale InSAR-Derived Velocity Fields: Case Study of the Eastern Tibetan Plateau. Journal of Geophysical Research: Solid Earth 128, e2022JB026251. doi:10.1029/2022JB026251.

Li, S., Xu, W., Li, Z., 2022. Review of the SBAS InSAR Time-series algorithms, applications, and challenges. Geodesy and Geodynamics 13, 114–126. doi:10.1016/j.geog.2021.09.007.

Li, X., Jónsson, S., Cao, Y., 2021a. Interseismic Deformation From Sentinel-1 Burst-Overlap Interferometry: Application to the Southern Dead Sea Fault. Geophysical Research Letters 48, e2021GL093481. doi:10.1029/2021GL093481.

Li, Y., Liu, M., Hao, M., Zhu, L., Cui, D., Wang, Q., 2021b. Active crustal deformation in the Tian Shan region, central Asia. Tectonophysics 811, 228868. doi:10.1016/j.tecto.2021.228868.

Li, Z., Muller, J.P., Cross, P., Fielding, E.J., 2005. Interferometric synthetic aperture radar (InSAR) atmospheric correction: GPS, Moderate Resolution Imaging Spectroradiometer (MODIS), and InSAR integration. Journal of Geophysical Research: Solid Earth 110. doi:10.1029/2004JB003446.

Liang, C., Agram, P., Simons, M., Fielding, E.J., 2019. Ionospheric Correction of InSAR Time Series Analysis of C-band Sentinel-1 TOPS Data. IEEE Transactions on Geoscience and Remote Sensing 57, 6755–6773. doi:10.1109/TGRS.2019.2908494.

Liu, C., Gao, Y., Tian, S., Dong, X., 2018. Rortex—A new vortex vector definition and vorticity tensor and vector decompositions. Physics of Fluids 30, 035103. doi:10.1063/1.5023001.

Liu, M., Stein, S., 2016. Mid-continental earthquakes: Spatiotemporal occurrences, causes, and hazards. Earth-Science Reviews 162, 364–386. doi:10.1016/j.earscirev.2016.09.016.

Liu, S., Moulin, A., Jónsson, S., 2024. Unloading uplift caused by surface processes in new zealand's southern alps. Geophysical Research Letters 51, e2024GL109019. doi:10.1029/2024GL109019.

Liu, S., Zhao, L., Wang, L., Liu, L., Zou, D., Hu, G., Sun, Z., Zhang, Y., Chen, W., Wang, X., Wang, M., Zhou, H., Qiao, Y., 2025. Ground surface deformation in permafrost region on the Qinghai-Tibet Plateau: A review. Earth-Science Reviews 265, 105109. doi:10.1016/j.earscirev.2025.105109.

Lohman, R.B., Bürgi, P.M., 2023. Soil moisture effects on InSAR - A correction approach and example from a hyper-arid region. Remote Sensing of Environment 297, 113766. doi:10.1016/j.rse.2023.113766.

Lohman, R.B., Simons, M., 2005. Some thoughts on the use of InSAR data to constrain models of surface deformation: Noise structure and data downsampling. Geochemistry, Geophysics, Geosystems 6. doi:10.1029/2004GC000841.

Lu, P., Han, J., Yi, Y., Hao, T., Zhou, F., Meng, X., Zhang, Y., Li, R., 2023. MT-InSAR Unveils Dynamic Permafrost Disturbances in Hoh Xil (Kekexili) on the Tibetan Plateau Hinterland. IEEE Transactions on Geoscience and Remote Sensing 61, 1–16. doi:10.1109/TGRS.2023.3253937.

Lv, X., Amelung, F., Shao, Y., 2022. Widespread Aseismic Slip Along the Makran Megathrust Triggered by the 2013 Mw 7.7 Balochistan Earthquake. Geophysical Research Letters 49, e2021GL097411. doi:10.1029/2021GL097411.

Lv, X., Shao, Y., 2022. Rheology of the Northern Tibetan Plateau Lithosphere Inferred from the Post-Seismic Deformation Resulting from the 2001 Mw 7.8 Kokoxili Earthquake. Remote Sensing 14, 1207. doi:10.3390/rs14051207.

Maghsoudi, Y., Hooper, A.J., Wright, T.J., Lazecky, M., Ansari, H., 2022. Characterizing and correcting phase biases in short-term, multilooked interferograms. Remote Sensing of Environment 275, 113022. doi:10.1016/j.rse.2022.113022.

McCormack, K., Hesse, M.A., Dixon, T., Malservisi, R., 2020. Modeling the Contribution of Poroelastic Deformation to Postseismic Geodetic Signals. Geophysical Research Letters 47, e2020GL086945. doi:10.1029/2020GL086945.

McGrath, J.D., Elliott, J.R., Watson, A.R., Wright, T.J., Piazolo, S., Hamling, I.J., 2025. Linking geodetically resolved uplift to long-term orogenic exhumation in the southern alps, new zealand. Journal of Geophysical Research: Solid Earth 130, e2024JB030625. doi:10.1029/2024JB030625.

McKenzie, D., 1972. Active Tectonics of the Mediterranean Region. Geophysical Journal International 30, 109–185. doi:10.1111/j.1365-246X.1972.tb02351.x.

McKenzie, D., 2025. The past and future geography of the Eastern Mediterranean constructed from GNSS observations. Earth and Planetary Science Letters 658, 119313. doi:10.1016/j.epsl.2025.119313.

Meade, B.J., Klinger, Y., Hetland, E.A., 2013. Inference of Multiple Earthquake-Cycle Relaxation Timescales from Irregular Geodetic Sampling of Interseismic Deformation. Bulletin of the Seismological Society of America 103, 2824–2835. doi:10.1785/0120130006.

Meldebekova, G., Yu, C., Li, Z., Song, C., 2020. Quantifying Ground Subsidence Associated with Aquifer Overexploitation Using Space-Borne Radar Interferometry in Kabul, Afghanistan. Remote Sensing 12, 2461. doi:10.3390/rs12152461.

Meyer, F.J., Hogenson, K., Kennedy, J.H., Lewandowski, A.F., Albright, R.W., Short, G., Flores-Anderson, A.I., Rosen, P.A., 2025. Facilitating the Golden Age of Synthetic Aperture Radar: New tools, services, and training to make synthetic aperture radar data more accessible. IEEE Geoscience and Remote Sensing Magazine , 2–13doi:10.1109/MGRS.2025.3526588.

Miranda, N., Meadows, P., Piantanida, R., Recchia, A., Small, D., Schubert, A., Vincent, P., Geudtner, D., Navas-Traver, I., Vega, F.C., 2017. The Sentinel-1 constellation mission performance, in: 2017 IEEE International Geoscience and Remote Sensing Symposium (IGARSS), pp. 5541–5544. doi:10.1109/IGARSS.2017.8128259.

Miranda, N., Torres, R., Geudtner, D., Pinheiro, M., Potin, P., Gratadour, J.B., O'Connell, A., Bibby, D., Navas-Traver, I., Cossu, M., 2023. Sentinel-1 First Generation Status, Past and Future, in: IGARSS 2023 - 2023 IEEE International Geoscience and Remote Sensing Symposium, pp. 4560–4563. doi:10.1109/IGARSS52108.2023.10281990.

Mirzadeh, S.M.J., Jin, S., Parizi, E., Chaussard, E., Bürgmann, R., Delgado Blasco, J.M., Amani, M., Bao, H., Mirzadeh, S.H., 2021. Characterization of Irreversible Land Subsidence in the Yazd-Ardakan Plain, Iran From 2003 to 2020 InSAR Time Series. Journal of Geophysical Research: Solid Earth 126, e2021JB022258. doi:10.1029/2021JB022258.

Molnar, P., Tapponnier, P., 1975. Cenozoic Tectonics of Asia: Effects of a Continental Collision. Science 189, 419–426. doi:10.1126/science.189.4201.419.

Molnar, P., Tapponnier, P., 1978. Active tectonics of Tibet. Journal of Geophysical Research: Solid Earth 83, 5361–5375. doi:10.1029/JB083iB11p05361.

Morishita, Y., 2021. Nationwide urban ground deformation monitoring in Japan using Sentinel-1 LiCSAR products and LiCSBAS. Progress in Earth and Planetary Science 8, 6. doi:10.1186/s40645-020-00402-7.

Morishita, Y., Lazecky, M., Wright, T., Weiss, J., Elliott, J., Hooper, A., 2020. LiCSBAS: An Open-Source InSAR Time Series Analysis Package Integrated with the LiCSAR Automated Sentinel-1 InSAR Processor. Remote Sensing 12, 424. doi:10.3390/rs12030424.

Motagh, M., Walter, T.R., Sharifi, M.A., Fielding, E., Schenk, A., Anderssohn, J., Zschau, J., 2008. Land subsidence in Iran caused by widespread water reservoir overexploitation. Geophysical Research Letters 35. doi:10.1029/2008GL033814.

Murray, K.D., Bekaert, D.P.S., Lohman, R.B., 2019. Tropospheric corrections for InSAR: Statistical assessments and applications to the Central United States and Mexico. Remote Sensing of Environment 232, 111326. doi:10.1016/j.rse.2019.111326.

Nocquet, J.M., Calais, E., 2003. Crustal velocity field of western Europe from permanent GPS array solutions, 1996–2001. Geophysical Journal International 154, 72–88. doi:10.1046/j.1365-246X.2003.01935.x.

Ou, Q., Daout, S., Weiss, J.R., Shen, L., Lazecký, M., Wright, T.J., Parsons, B.E., 2022. Large-Scale Interseismic Strain Mapping of the NE Tibetan Plateau From Sentinel-1 Interferometry. Journal of Geophysical Research: Solid Earth 127, e2022JB024176. doi:10.1029/2022JB024176.

Palano, M., Imprescia, P., Agnon, A., Gresta, S., 2018. An improved evaluation of the seismic/geodetic deformation-rate ratio for the Zagros Fold-and-Thrust collisional belt. Geophysical Journal International 213, 194–209.

Payne, J.A., Watson, A., Maghsoudi, Y., Ebmeier, S., Rigby, R., Lazeckỳ, M., Thomas, M., Elliott, J., 2025. Widespread extent of irrecoverable aquifer depletion revealed by country-wide analysis of land surface subsidence hazard in iran. Journal of Geophysical Research: Solid Earth 130, e2024JB030367. doi:10.1029/2024JB030367.

Peltzer, G., Crampé, F., Hensley, S., Rosen, P., 2001. Transient strain accumulation and fault interaction in the Eastern California shear zone. Geology 29, 975–978. doi:10.1130/0091-7613(2001)029<0975:TSAAFI>2.0.CO;2.

Petrolati, D., Gebert, N., Geudtner, D., Bollian, T., Osborne, S., Cesa, M., Simonini, A., Davidson, M., Iannini, L., Cosimo, G.D., 2023. An Overview of the Copernicus Rose-L SAR Instrument, in: IGARSS 2023 - 2023 IEEE International Geoscience and Remote Sensing Symposium, pp. 4310–4313. doi:10.1109/IGARSS52108.2023.10281670.

Piña-Valdés, J., Socquet, A., Beauval, C., Doin, M.P., D'Agostino, N., Shen, Z.K., 2022. 3D GNSS Velocity Field Sheds Light on the Deformation Mechanisms in Europe: Effects of the Vertical Crustal Motion on the Distribution of Seismicity. Journal of Geophysical Research: Solid Earth 127, e2021JB023451. doi:10.1029/2021JB023451.

Pinjeiro, M., 2024. Increase of Sentinel-1A Orbital Tube: Impact on Interferometry. TN - Technical Note. ESA. Esri, Italy.

Pintori, F., Serpelloni, E., Gualandi, A., 2022. Common-mode signals and vertical velocities in the greater Alpine area from GNSS data. Solid Earth Sciences Library 13, 1541–1567.

Potin, P., Rosich, B., Grimont, P., Miranda, N., Shurmer, I., O'Connell, A., Torres, R., Krassenburg, M., 2016. Sentinel-1 Mission Status, in: Proceedings of EUSAR 2016: 11th European Conference on Synthetic Aperture Radar, pp. 1–6.

Prats, P., Pulella, A., Benedikter, A., Hooper, A., Biggs, J., Kääb, A., Rabus, B., Nagler, T., Rott, H., Pappas, O., et al., 2023. Performance analysis of the Harmony Mission for land applications: Results from the Phase A study. FRINGE Online Abstracts , 1–4.

Prats-Iraola, P., Rodriguez-Cassola, M., De Zan, F., Scheiber, R., López-Dekker, P., Barat, I., Geudtner, D., 2015. Role of the Orbital Tube in Interferometric Spaceborne SAR Missions. IEEE Geoscience and Remote Sensing Letters 12, 1486–1490. doi:10.1109/LGRS.2015.2409885.

Qiao, X., Zhou, Y., 2021. Geodetic imaging of shallow creep along the Xianshuihe fault and its frictional properties. Earth and Planetary Science Letters 567, 117001. doi:10.1016/j.epsl.2021.117001.

Reid, H.F., 1911. The elastic-rebound theory of earthquakes. Bulletin of the Department of Geology 6.

Reilinger, R., McClusky, S., Vernant, P., Lawrence, S., Ergintav, S., Cakmak, R., Ozener, H., Kadirov, F., Guliev, I., Stepanyan, R., Nadariya, M., Hahubia, G., Mahmoud, S., Sakr, K., ArRajehi, A., Paradissis, D., Al-Aydrus, A., Prilepin, M., Guseva, T., Evren, E., Dmitrotsa, A., Filikov, S.V., Gomez, F., Al-Ghazzi, R., Karam, G., 2006. GPS constraints on continental deformation in the Africa-Arabia-Eurasia continental

collision zone and implications for the dynamics of plate interactions. Journal of Geophysical Research: Solid Earth 111. doi:10.1029/2005JB004051.

Reilinger, R.E., McClusky, S.C., Oral, M.B., King, R.W., Toksoz, M.N., Barka, A.A., Kinik, I., Lenk, O., Sanli, I., 1997. Global Positioning System measurements of present-day crustal movements in the Arabia-Africa-Eurasia plate collision zone. Journal of Geophysical Research: Solid Earth 102, 9983–9999. doi:10.1029/96JB03736.

Rizzoli, P., Martone, M., Gonzalez, C., Wecklich, C., Borla Tridon, D., Bräutigam, B., Bachmann, M., Schulze, D., Fritz, T., Huber, M., Wessel, B., Krieger, G., Zink, M., Moreira, A., 2017. Generation and performance assessment of the global TanDEM-X digital elevation model. ISPRS Journal of Photogrammetry and Remote Sensing 132, 119–139. doi:10.1016/j.isprsjprs.2017.08.008.

Roma-Dollase, D., Hernández-Pajares, M., Krankowski, A., Kotulak, K., Ghoddousi-Fard, R., Yuan, Y., Li, Z., Zhang, H., Shi, C., Wang, C., Feltens, J., Vergados, P., Komjathy, A., Schaer, S., García-Rigo, A., Gómez-Cama, J.M., 2018. Consistency of seven different GNSS global ionospheric mapping techniques during one solar cycle. Journal of Geodesy 92, 691–706. doi:10.1007/s00190-017-1088-9.

Rosen, P.A., Gurrola, E., Sacco, G.F., Zebker, H., 2012. The InSAR scientific computing environment, in: EUSAR 2012; 9th European Conference on Synthetic Aperture Radar, pp. 730–733.

Rosen, P.A., Kumar, R., 2021. NASA-ISRO SAR (NISAR) Mission Status, in: 2021 IEEE Radar Conference (RadarConf21), pp. 1–6. doi:10.1109/RadarConf2147009.2021.9455211.

Rui, X., Stamps, D.S., 2019. A geodetic strain rate and tectonic velocity model for China. Geochemistry, Geophysics, Geosystems 20, 1280–1297.

Ryder, I., Bürgmann, R., Pollitz, F., 2011. Lower crustal relaxation beneath the Tibetan Plateau and Qaidam Basin following the 2001 Kokoxili earthquake. Geophysical Journal International 187, 613–630. doi:10.1111/j.1365-246X.2011.05179.x.

Ryder, I., Parsons, B., Wright, T.J., Funning, G.J., 2007. Post-seismic motion following the 1997 Manyi (Tibet) earthquake: InSAR observations and modelling. Geophysical Journal International 169, 1009–1027. doi:10.1111/j.1365-246X.2006.03312.x.

Salvi, S., Stramondo, S., Funning, G.J., Ferretti, A., Sarti, F., Mouratidis, A., 2012. The Sentinel-1 mission for the improvement of the scientific understanding and the operational monitoring of the seismic cycle. Remote Sensing of Environment 120, 164–174. doi:10.1016/j.rse.2011.09.029.

Sandwell, D., Mellors, R., Tong, X., Wei, M., Wessel, P., 2011. Open radar interferometry software for mapping surface Deformation. Eos, Transactions American Geophysical Union 92, 234–234. doi:10.1029/2011EO280002.

Sandwell, D.T., Wessel, P., 2016. Interpolation of 2-D vector data using constraints from elasticity. Geophysical Research Letters 43, 10,703–10,709. doi:10.1002/2016GL070340.

Savage, J.C., Gan, W., Svarc, J.L., 2001. Strain accumulation and rotation in the Eastern California Shear Zone. Journal of Geophysical Research: Solid Earth 106, 21995–22007. doi:10.1029/2000JB000127.

Savage, J.C., Prescott, W.H., 1978. Asthenosphere readjustment and the earthquake cycle. Journal of Geophysical Research: Solid Earth 83, 3369–3376. doi:10.1029/JB083iB07p03369.

Scardino, G., Anzidei, M., Petio, P., Serpelloni, E., De Santis, V., Rizzo, A., Liso, S.I., Zingaro, M., Capolongo, D., Vecchio, A., Refice, A., Scicchitano, G., 2022. The Impact of Future Sea-Level Rise on Low-Lying Subsiding Coasts: A Case Study of Tavoliere Delle Puglie (Southern Italy). Remote Sensing 14, 4936. doi:10.3390/rs14194936.

Serpelloni, E., Cavaliere, A., Martelli, L., Pintori, F., Anderlini, L., Borghi, A., Randazzo, D., Bruni, S., Devoti, R., Perfetti, P., et al., 2022. Surface velocities and strain-rates in the Euro-Mediterranean region from massive GPS data processing. Frontiers in Earth Science 10, 907897.

Serpelloni, E., Faccenna, C., Spada, G., Dong, D., Williams, S.D., 2013. Vertical GPS ground motion rates in the Euro-Mediterranean region: New evidence of velocity gradients at different spatial scales along the Nubia-Eurasia plate boundary. Journal of Geophysical Research: Solid Earth 118, 6003–6024.

Shen, L., Hooper, A., Elliott, J.R., Wright, T.J., 2024a. Variability in interseismic strain accumulation rate and style along the Altyn Tagh Fault. Nature Communications 15, 6876. doi:10.1038/s41467-024-51116-z.

Shen, L., Steckler, M., Lindsey, E., Oryan, B., Chong, J.H., 2024b. Large-Scale Geodetic Deformation Measurements of the Indo-Burma Subduction Zone from Multi-Sensor InSAR and GNSS: Implications for Strain Partitioning and Earthquake Hazard. Technical Report EGU24-11641. Copernicus Meetings. doi:10.5194/egusphere-egu24-11641.

Sobrero, F.S., Bevis, M., Gómez, D.D., Wang, F., 2020. Logarithmic and exponential transients in GNSS trajectory models as indicators of dominant processes in postseismic deformation. Journal of Geodesy 94, 84. doi:10.1007/s00190-020-01413-4.

Socquet, A., Janex, G., 2019. GNSS position and velocity solutions calculated in the framework of the EPOS initiative with GAMIT-GLOBK. doi:10.17178/GNSS.products.EPOS.2019.

Stamps, D.S., Kreemer, C., 2024. Open Access GNSS Data for Studies of the Lithosphere. Geochemistry, Geophysics, Geosystems 25, e2024GC011567. doi:10.1029/2024GC011567.

Steffen, R., Steffen, H., Kenyeres, A., Nilsson, T., Lidberg, M., 2025. EuVeM2022—a European three-dimensional GNSS velocity model based on least-squares collocation. Geophysical Journal International 241, 437–453. doi:10.1093/gji/ggaf052.

Stephenson, O.L., Liu, Y.K., Yunjun, Z., Simons, M., Rosen, P., Xu, X., 2022. The Impact of Plate Motions on Long-Wavelength InSAR-Derived Velocity Fields. Geophysical Research Letters 49, e2022GL099835. doi:10.1029/2022GL099835.

Stevens, V.L., Avouac, J.P., 2021. On the relationship between strain rate and seismicity in the India–Asia collision zone: Implications for probabilistic seismic hazard. Geophysical Journal International 226, 220–245. doi:10.1093/gji/ggab098.

Storchak, D.A., Di Giacomo, D., Bondár, I., Engdahl, E.R., Harris, J., Lee, W.H.K., Villaseñor, A., Bormann, P., 2013. Public Release of the ISC–GEM Global Instrumental Earthquake Catalogue (1900–2009). Seismological Research Letters 84, 810–815. doi:10.1785/0220130034.

Storchak, D.A., Di Giacomo, D., Engdahl, E.R., Harris, J., Bondár, I., Lee, W.H.K., Bormann, P., Villaseñor, A., 2015. The ISC-GEM Global Instrumental Earthquake Catalogue (1900–2009): Introduction. Physics of the Earth and Planetary Interiors 239, 48–63. doi:10.1016/j.pepi.2014.06.009.

Styron, R., 2022. Contemporary Slip Rates of All Active Faults in the Indo-Asian Collision Zone. doi:10.1002/essoar.10512747.1.

Styron, R., Pagani, M., 2020. The GEM Global Active Faults Database. Earthquake Spectra 36, 160–180. doi:10.1177/8755293020944182.

Thatcher, W., 2007. Microplate model for the present-day deformation of Tibet. Journal of Geophysical Research: Solid Earth 112. doi:10.1029/2005JB004244.

Thatcher, W., 2009. How the Continents Deform: The Evidence From Tectonic Geodesy*. Annual Review of Earth and Planetary Sciences 37, 237–262. doi:10.1146/annurev.earth.031208.100035.

Tian, D., Uieda, L., Leong, W.J., Fröhlich, Y., Schlitzer, W., Grund, M., Jones, M., Toney, L., Yao, J., Tong, J.H., Magen, Y., Materna, K., Belem, A., Newton, T., Anant, A., Ziebarth, M., Quinn, J., Wessel, P., 2025. PyGMT: A Python interface for the Generic Mapping Tools. Zenodo. doi:10.5281/zenodo.14868324.

Tong, X., Sandwell, D.T., Smith-Konter, B., 2013. High-resolution interseismic velocity data along the San Andreas Fault from GPS and InSAR. Journal of Geophysical Research: Solid Earth 118, 369–389. doi:10.1029/2012JB009442.

Torres, R., Geudtner, D., Davidson, M., Bibby, D., Navas-Traver, I., Garcia Hernandez, A.I., Laduree, G., Poupaert, J., Bollian, T., Graham, S., 2024. Sentinel-1 Next Generation: Enhanced C-band Data Continuity, in: EUSAR 2024; 15th European Conference on Synthetic Aperture Radar, pp. 1–4.

Torres, R., Navas-Traver, I., Bibby, D., Lokas, S., Snoeij, P., Rommen, B., Osborne, S., Ceba-Vega, F., Potin, P., Geudtner, D., 2017. Sentinel-1 SAR system and mission, in: 2017 IEEE Radar Conference (RadarConf), pp. 1582–1585. doi:10.1109/RADAR.2017.7944460.

Torres, R., Snoeij, P., Geudtner, D., Bibby, D., Davidson, M., Attema, E., Potin, P., Rommen, B., Floury, N., Brown, M., Traver, I.N., Deghaye, P., Duesmann, B., Rosich, B., Miranda, N., Bruno, C., L'Abbate, M., Croci, R., Pietropaolo, A., Huchler, M., Rostan, F., 2012. GMES Sentinel-1 mission. Remote Sensing of Environment 120, 9–24. doi:10.1016/j.rse.2011.05.028.

Üstün, A., Tuşat, E., Yalvaç, S., Özkan, İ., Eren, Y., Özdemir, A., Bildirici, İ.Ö., Üstüntaş, T., Kırtıloğlu, O.S., Mesutoğlu, M., Doğanalp, S., Canaslan, F., Abbak, R.A., Avşar, N.B., Şimşek, F.F., 2015. Land subsidence in Konya Closed Basin and its spatio-temporal detection by GPS and DInSAR. Environmental Earth Sciences 73, 6691–6703. doi:10.1007/s12665-014-3890-5.

Vauchez, A., Tommasi, A., Mainprice, D., 2012. Faults (shear zones) in the Earth's mantle. Tectonophysics 558–559, 1–27. doi:10.1016/j.tecto.2012.06.006.

Vergnolle, M., Calais, E., Dong, L., 2007. Dynamics of continental deformation in Asia. Journal of Geophysical Research: Solid Earth 112. doi:10.1029/2006JB004807.

Wang, D., Elliott, J.R., Zheng, G., Wright, T.J., Watson, A.R., McGrath, J.D., 2024. Deciphering interseismic strain accumulation and its termination on the central-eastern Altyn Tagh fault from high-resolution velocity fields. Earth and Planetary Science Letters 644, 118919. doi:10.1016/j.epsl.2024.118919.

Wang, H., Wright, T.J., 2012. Satellite geodetic imaging reveals internal deformation of western Tibet. Geophysical Research Letters 39. doi:10.1029/2012GL051222.

Wang, H., Wright, T.J., 2025. velmap (v1.1). Zenodo doi:10.5281/zenodo.17713962.

Wang, K., Zhu, Y., Nissen, E., Shen, Z.K., 2021. On the Relevance of Geodetic Deformation Rates to Earthquake Potential. Geophysical Research Letters 48, e2021GL093231. doi:10.1029/2021GL093231.

Wang, L., Barbot, S., 2023. Three-dimensional kinematics of the India–Eurasia collision. Communications Earth & Environment 4, 1–12. doi:10.1038/s43247-023-00815-4.

Wang, L., Zhao, L., Zhou, H., Liu, S., Du, E., Zou, D., Liu, G., Xiao, Y., Hu, G., Wang, C., Sun, Z., Li, Z., Qiao, Y., Wu, T., Li, C., Li, X., 2022a. Contribution of ground ice melting to the expansion of Selin Co (lake) on the Tibetan Plateau. The Cryosphere 16, 2745–2767. doi:10.5194/tc-16-2745-2022.

Wang, L.W., Garthwaite, M., Du, Z., Deane, A., McCubbine, J., Wheeler, M., O'Hehir, A., Davies, B., 2022b. InSAR Analysis Ready Data, in: IGARSS 2022 - 2022 IEEE International Geoscience and Remote Sensing Symposium, pp. 2920–2923. doi:10.1109/IGARSS46834.2022.9884464.

Wang, M., Shen, Z.K., 2020. Present-day crustal deformation of continental China derived from GPS and its tectonic implications. Journal of Geophysical Research: Solid Earth 125, e2019JB018774.

Wang, Q., Zhang, P.Z., Freymueller, J.T., Bilham, R., Larson, K.M., Lai, X., You, X., Niu, Z., Wu, J., Li, Y., Liu, J., Yang, Z., Chen, Q., 2001. Present-Day Crustal Deformation in China Constrained by Global Positioning System Measurements. Science 294, 574–577. doi:10.1126/science.1063647.

Wang, W., Zhao, B., Wang, Q., Yang, S., 2012. Noise analysis of continuous GPS coordinate time series for CMONOC. Advances in space research 49, 943–956.

Wang, Y., Feng, G., Li, Z., Xu, W., Wang, H., Hu, J., Liu, S., He, L., 2022c. Estimating the long-term deformation and permanent loss of aquifer in the southern Junggar Basin, China, using InSAR. Journal of Hydrology 614, 128604. doi:10.1016/j.jhydrol.2022.128604.

Ward, S.N., 1998. On the consistency of earthquake moment rates, geological fault data, and space geodetic strain: The United States. Geophysical Journal International 134, 172–186. doi:10.1046/j.1365-246x.1998.00556.x.

Wasmeier, P., 2025. Geodetic transformations (matlab central file exchange). https://mathworks.com/matlabcentral/fileexchange/9696-geodetic-transformations. Accessed: 2025-12-12.

Watson, A.R., Elliott, J.R., Lazecký, M., Maghsoudi, Y., McGrath, J.D., Walters, R.J., 2024. An InSAR-GNSS Velocity Field for Iran. Geophysical Research Letters 51, e2024GL108440. doi:10.1029/2024GL108440.

Weiss, J.R., Qiu, Q., Barbot, S., Wright, T.J., Foster, J.H., Saunders, A., Brooks, B.A., Bevis, M., Kendrick, E., Ericksen, T.L., Avery, J., SmalleyJr, R., Cimbaro, S.R., Lenzano, L.E., Barón, J., Báez, J.C., Echalar, A., 2019. Illuminating subduction zone rheological properties in the wake of a giant earthquake. Science Advances doi:10.1126/sciadv.aax6720.

Weiss, J.R., Walters, R.J., Morishita, Y., Wright, T.J., Lazecky, M., Wang, H., Hussain, E., Hooper, A.J., Elliott, J.R., Rollins, C., Yu, C., González, P.J., Spaans, K., Li, Z., Parsons, B., 2020. High-Resolution Surface Velocities and Strain for Anatolia From Sentinel-1 InSAR and GNSS Data. Geophysical Research Letters 47, e2020GL087376. doi:10.1029/2020GL087376.

Wen, Y., Li, Z., Xu, C., Ryder, I., Bürgmann, R., 2012. Postseismic motion after the 2001 MW 7.8 Kokoxili earthquake in Tibet observed by InSAR time series. Journal of Geophysical Research: Solid Earth 117. doi:10.1029/2011JB009043.

Wessel, P., Luis, J.F., Uieda, L., Scharroo, R., Wobbe, F., Smith, W.H.F., Tian, D., 2019. The Generic Mapping Tools Version 6. Geochemistry, Geophysics, Geosystems 20, 5556–5564. doi:10.1029/2019GC008515.

Williams, S.D., Bock, Y., Fang, P., Jamason, P., Nikolaidis, R.M., Prawirodirdjo, L., Miller, M., Johnson, D.J., 2004. Error analysis of continuous GPS position time series. Journal of Geophysical Research: Solid Earth 109.

Williams, SDP., 2003. The effect of coloured noise on the uncertainties of rates estimated from geodetic time series. Journal of Geodesy 76, 483–494.

Wright, T., Parsons, B., Fielding, E., 2001. Measurement of interseismic strain accumulation across the North Anatolian Fault by satellite radar interferometry. Geophysical Research Letters 28, 2117–2120. doi:10.1029/2000GL012850.

Wright, T.J., 2002. Remote monitoring of the earthquake cycle using satellite radar interferometry. Philosophical Transactions of the Royal Society of London. Series A: Mathematical, Physical and Engineering Sciences 360, 2873–2888. doi:10.1098/rsta.2002.1094.

Wright, T.J., 2016. The earthquake deformation cycle. Astronomy & Geophysics 57, 4.20–4.26. doi:10.1093/astrogeo/atw148.

Wright, T.J., Elliott, J.R., Wang, H., Ryder, I., 2013. Earthquake cycle deformation and the Moho: Implications for the rheology of continental lithosphere. Tectonophysics 609, 504–523. doi:10.1016/j.tecto.2013.07.029.

Wright, T.J., Houseman, G.A., Fang, J., Maghsoudi, Y., Hooper, A.J., Elliott, J.R., Lazecký, M., Ou, Q., Parsons, B.E., Rollins, C., Shen, L., Wang, H., Wang, D., 2026. High-resolution geodetic velocities reveal role of weak faults in deformation of Tibetan Plateau. Science .

Wright, T.J., Parsons, B., England, P.C., Fielding, E.J., 2004a. InSAR Observations of Low Slip Rates on the Major Faults of Western Tibet. Science 305, 236–239. doi:10.1126/science.1096388.

Wright, T.J., Parsons, B.E., Lu, Z., 2004b. Toward mapping surface deformation in three dimensions using InSAR. Geophysical Research Letters 31. doi:10.1029/2003GL018827.

Wu, P.C., Wei, M.M., D'Hondt, S., 2022. Subsidence in Coastal Cities Throughout the World Observed by InSAR. Geophysical Research Letters 49, e2022GL098477. doi:10.1029/2022GL098477.

Wu, Z., Xiao, R., Jiang, M., Ferreira, V.G., 2024. Characterizing the spatial structure and aliasing effect of ocean tide loading on InSAR measurements. Remote Sensing of Environment 311, 114297. doi:10.1016/j.rse.2024.114297.

Xu, X., Sandwell, D.T., 2020. Toward Absolute Phase Change Recovery With InSAR: Correcting for Earth Tides and Phase Unwrapping Ambiguities. IEEE Transactions on Geoscience and Remote Sensing 58, 726–733. doi:10.1109/TGRS.2019.2940207.

Xu, X., Sandwell, D.T., Klein, E., Bock, Y., 2021. Integrated Sentinel-1 InSAR and GNSS time-series along the San Andreas fault system. Journal of Geophysical Research: Solid Earth n/a, e2021JB022579. doi:10.1029/2021JB022579.

Yagüe-Martínez, N., Prats-Iraola, P., Rodríguez González, F., Brcic, R., Shau, R., Geudtner, D., Eineder, M., Bamler, R., 2016. Interferometric Processing of Sentinel-1 TOPS Data. IEEE Transactions on Geoscience and Remote Sensing 54, 2220–2234. doi:10.1109/TGRS.2015.2497902.

Yalvaç, S., Alemdağ, S., Zeybek, H.İ., Yalvaç, M., 2023. Excessive groundwater withdrawal and resultant land subsidence in the Küçük Menderes River Basin, Turkey as estimated from InSAR-SBAS and GNSS measurements. Advances in Space Research 72, 4282–4297. doi:10.1016/j.asr.2023.08.001.

Yamasaki, T., Wright, T.J., Houseman, G.A., 2014. Weak ductile shear zone beneath a major strike-slip fault: Inferences from earthquake cycle model constrained by geodetic observations of the western North Anatolian Fault Zone. Journal of Geophysical Research: Solid Earth 119, 3678–3699. doi:10.1002/2013JB010347.

Yi, X., Wang, L., Ci, H., Wang, R., Yang, H., Yan, Z., 2025. Monitoring of Land Subsidence and Analysis of Impact Factors in the Tianshan North Slope Urban Agglomeration. Land 14, 202. doi:10.3390/land14010202.

Yin, A., 2010. Cenozoic tectonic evolution of Asia: A preliminary synthesis. Tectonophysics 488, 293–325. doi:10.1016/j.tecto.2009.06.002.

Yu, C., Li, Z., Penna, N.T., 2018a. Interferometric synthetic aperture radar atmospheric correction using a GPS-based iterative tropospheric decomposition model. Remote Sensing of Environment 204, 109–121. doi:10.1016/j.rse.2017.10.038.

Yu, C., Li, Z., Penna, N.T., Crippa, P., 2018b. Generic Atmospheric Correction Model for Interferometric Synthetic Aperture Radar Observations. Journal of Geophysical Research: Solid Earth 123, 9202–9222. doi:10.1029/2017JB015305.

Yun, Y., Zeng, Q., Green, B.W., Zhang, F., 2015. Mitigating atmospheric effects in InSAR measurements through high-resolution data assimilation and numerical simulations with a weather prediction model. International Journal of Remote Sensing 36, 2129–2147. doi:10.1080/01431161.2015.1034894.

Yunjun, Z., Fattahi, H., Pi, X., Rosen, P., Simons, M., Agram, P., Aoki, Y., 2022. Range Geolocation Accuracy of C-/L-Band SAR and its Implications for Operational Stack Coregistration. IEEE Transactions on Geoscience and Remote Sensing 60, 1–19. doi:10.1109/TGRS.2022.3168509.

Zeng, Y., Shen, Z.K., 2016. A Fault-Based Model for Crustal Deformation, Fault Slip Rates, and Off-Fault Strain Rate in California. Bulletin of the Seismological Society of America 106, 766–784. doi:10.1785/0120140250.

Zhang, G., Xu, Z., Chen, Z., Wang, S., Liu, Y., Gong, X., 2024. Analyzing surface deformation throughout China's territory using multi-temporal InSAR processing of Sentinel-1 radar data. Remote Sensing of Environment 305, 114105. doi:10.1016/j.rse.2024.114105.

Zhao, D., Qu, C., Bürgmann, R., Gong, W., Shan, X., 2021. Relaxation of Tibetan Lower Crust and Afterslip Driven by the 2001 Mw7.8 Kokoxili, China, Earthquake Constrained by a Decade of Geodetic Measurements. Journal of Geophysical Research: Solid Earth 126, e2020JB021314. doi:10.1029/2020JB021314.

Zhu, L., Gong, H., Li, X., Wang, R., Chen, B., Dai, Z., Teatini, P., 2015. Land subsidence due to groundwater withdrawal in the northern Beijing plain, China. Engineering Geology 193, 243–255. doi:10.1016/j.enggeo.2015.04.020.

Figure 1: (a) Major active faults of the Alpine Himalayan orogeny (Styron and Pagani, 2020) with the tectonic plates of the region outlined from Bird (2003) and the major faults (F.) named in the text marked. (b) Topographic map of the belt with major mountain zones marked in brown and capital cities denoted by squares. (c) Compiled and aligned GNSS locations used in this study (Tables SA1–SA2) with velocities shown with respect to a fixed Eurasia reference frame (velocities with respect to the ITRF14 are shown in Figure SB1). The combined InSAR-GNSS velocity field coverage is denoted by the dark grey polygon.

Figure 2: Workflow for (a) InSAR processing chain and (b) correction and time series calculation, (c) GNSS compilation, quality control and alignment, (d) unified velocity generation and (e) final strain rate field calculations and outputs. InSAR - Interferometric Synthetic Aperture Radar, NLA - Near-Line Archive, ASF - Alaska SAR Facility, POE - Precise Orbital Ephemerides, DEM - Digital Elevation Model, COP30 - Copernicus 30 m, SRTM - Shuttle Radar Topography Mission, SLC - Single Look Complex, VV - Vertical Transmit–Vertical Receive Single Polarisation, LiCSAR - Looking inside the Continents from Space SAR, LOS - Line-of-Sight, LiCSBAS - Looking inside the Continents from Space Small Baseline Subset, GACOS - Generic Atmospheric Correction Online Service, GNSS - Global Navigation Satellite System, ITRF2014 - International Terrestrial Reference Frame, E, N, U - East North, Up. $\dot{\varepsilon}_{II_h}$ = second invariant of strain rate, $\dot{\varepsilon}_{shear}$ = maximum shear strain rate, $\dot{\varepsilon}_{dil}$ = horizontal dilatation rate, ω = vorticity, (Savage et al., 2001).

Figure 3: The prepared 3D combination of GNSS and point velocities used to reference and align the InSAR data, in the western AHB (top) and central/eastern AHB (bottom). Arrows show horizontal motions with respect to the ITRF2014 Eurasia-fixed reference frame (Altamimi et al., 2017); coloured circles show vertical motion rates.

Figure 4: Application of corrections on example frame 130A_06248_212118 over the Zagros mountains of southern Iran: a) LOS average velocity from original time series of uncorrected interferograms; b-d) velocity inverted from time series corrections on troposphere, ionosphere and solid earth tides, respectively; e) plate motion velocity correction (Figure SB14); f) normalized frequency histogram of the b–e correction velocities; g) final LOS velocity with all corrections applied; h) relative LOS displacement time series between locations A and B (reference), locations shown in subpanels a,f, from both datasets before and after b–d corrections. i) Inset map of Iran with location of frame coverage extents denoted in purple.

Figure 5: LOS uncertainty analysis through the differences between observed and reconstructed LOS velocities at track overlaps. The observed LOS velocities in Figure 6 are split into four non-overlapping groups of ascending and descending tracks, A1, A2, D1, and D2. (a-b) A1 represents the differences between the observed LOS velocities in A1 and the reconstructed LOS velocities at A1's pixel locations using LOS velocities in A2, D1, and D2. The same applies to D1, A2, and D2, respectively. (c-f) Residual and Root-mean-square (RMS) differences between the corresponding observed and reconstructed LOS velocities. The differences are reported first as RMS of 1-99 percentiles, and then of all pixels.

Figure 6: Mosaic of referenced line of sight average velocities for the Alpine Himalayan Belt on (a) ascending and (b) descending orbital heading directions, with positive values indicating motion away from the satellite. Active fault traces (black lines) are from Styron and Pagani (2020).

Figure 7: Three components of surface velocity: (a) North, (b) East, and (c) Vertical. GNSS sites are denoted by circles for 2D velocities, triangles for 3D velocities and coloured squares for levelling results. The dashed outline shows the extent of the mesh used to align the individual line-of-sight velocities. Gray polygons indicate the extent of the profiles (20 km bins) presented in Figure 8.

Figure 8: Profiles across the velocity fields of the Alpine Himalayan Belt with locations of mapped active faults from Styron and Pagani (2020) marked by dashed black lines. (a) Northward component of velocity along longitudinal line 85°E, with GNSS data and topography marked on. (b) Eastward component of velocity from Greece to southeastern Tibet along the Great Circle almost 8,000 km long (20% of the Earth's circumference). (c) Vertical component through Afghanistan to northeastern Tibet. The locations of the profiles are shown in Figure 7. InSAR data (coloured dots) are binned into 20 km wide profiles, while GNSS (black bars) and levelling (grey bars) data are binned into 40 km wide swaths.

Figure 9: Measures of horizontal strain rates for the Alpine Himalayan Belt with mapped active faults from Styron and Pagani (2020) overlaid (black lines). (a) Second invariant of strain rate (nstr/yr), (b) Maximum shear strain rate (nstr/yr), (c) Horizontal Dilatation rate (nstr/yr), where positive indicates extension and negative contraction, and (d) Vorticity (nrad/yr), with positive values indicating anti-clockwise rotation.

Figure 10: Examples of creeping fault signals observed in timeseries. Location of regions shown in Figure SB16. (a,e,i,m) East velocities around the North Anatolian fault, the Chaman fault, the Haiyuan fault and the Xianshuie fault. (b,f,j,n) Maximum shear strain rates around these active faults. (c,d,g,h,k,l,o,p) The velocity and Maximum shear strain rate profiles across these faults. The location of the profiles are shown in the left East velocity and Maximum shear strain rate maps. The width of the profiles is all 10 km. (q) A displacement time series of a pixel referred to a pixel at the other side of the fault based on LiCS frame 042A_05933_131313, and the location of these two pixels are shown by red points in (e).

Figure 11: Examples of postseismic signals observed in timeseries. Location of regions shown in Figure SB16. (a,b,c) East velocities around the epicenter of the 2013 M_w 7.7 Balochistan earthquake, the 1997 M_w 7.5 Manyi Earthquake and the 2001 M_w 7.8 Kokoxili Earthquake. (d,e,f) Maximum shear strain rates around the epicenter of these earthquakes. (d-l) East velocity and maximum shear strain rate profiles across the postseismic deformation zones. The locations of the profiles are shown in (a-f). (m) LOS velocities around the 2020 Nima earthquake in the LiCS frame 012A_05642_131313. (n) The postseismic LOS displacement time series for the 2020 Nima earthquake based on the LiCS frame 012A_05642_131313. The location of the pixel is shown by red point in (m). The red focal mechanisms for the earthquakes in (a-f) and (m) are from Global Centroid Moment Tensor Catalog (Dziewonski et al., 1981; Ekström et al., 2012).

Figure 12: Case examples of rapid vertical subsidence signals associated— according to previous literature or hypothesised association— with groundwater depletion. Location of regions shown in Figure SB16. (a) Tianshan North Slope, China (Yi et al., 2025). (b) The largest continuous subsidence region in this study in Eastern China. Profiled velocities A–A' are in e) (e.g. Ao et al., 2024). (c) Konya Basin, Türkiye (e.g. Üstün et al., 2015)(d) Rapid subsidence near Tehran and Karaj in northern Iran (Haghshenas Haghighi and Motagh, 2024; Payne et al., 2025). (e) Ascending velocities in swath A–A' in b), Eastern China. Triangles = 3D GNSS, circles

= 2D GNSS (both this study). (f) Comparison of ascending InSAR velocities from b) at locations of GNSS sites to GNSS velocities reprojected into Sentinel-1 ascending line-of-sight direction. (g) Line-of-sight cumulative displacement time series in the descending direction for frame 035D_05397_131013 at locations in d). Faults from (Styron and Pagani, 2020).

Figure 13: (a) Vertical velocity field with 3D GNSS stations shown in circles, levelling measurements in triangles, and contour line representing Permafrost Zonation Index of 0.5, above which there is a high likelihood of permafrost presence (Gruber, 2012). (b) Permafrost Zonation Index from Gruber (2012) with contours and profiles as in (a). (c,d) Profiles of vertical velocity, the Permafrost Zonation Index and topography. 3D GNSS and levelling vertical velocity measurements are shown as black circles and white triangles with error bars.

Figure 14: (a) Earthquakes from the ISC-GEM catalogue (Storchak et al., 2013, 2015; Di Giacomo et al., 2018) in pink overlaid on the 2nd invariant of the strain rate tensor. The earthquakes are from 1904 onwards, and selected for magnitudes (M$>$ 5) at shallow depths ($<$ 35 km). (b) Major active faults (red) from Styron and Pagani (2020) overlaid on maximum shear strain rate.

Figure S1:

Figure S2:

Appendix A. Supplementary Tables

Appendix B. Supplementary Figures

Appendix C. Supplementary Data

Figure S3:

Figure S4:

Figure S5:

Figure S6:

Figure S7:

Table SA1:

Table SA2:

Table SA3:

Table SA4:

Figure SB1:

Figure SB2:

Figure SB3:

Figure SB4:

Figure SB5:

Figure SB6:

Figure SB7:

Figure SB8:

Figure SB9:

Figure SB10:

Figure SB11:

Figure SB12:

Figure SB13:

Figure SB14:

Figure SB15:

Figure SB16:

Figure SB17:

Figure SB18:

Figure SB19:

Figure SB20:

Figure SB21:

Figure SB22:

Figure SB23:

Figure SB24:

Figure SB25:

Figure SB26:

Figure SB27:

Figure SB28:

Figure SB29:

Figure SB30:

Figure SB31:

Figure SB32:

Figure SB33:

Figure SB34:

Supplementary Information — Deformation, Strains and Velocities for the Alpine Himalayan Belt from trans-continental Sentinel-1 InSAR & GNSS

J. R. Elliott[a], J. Fang[a], M. Lazecký[a], Y. Maghsoudi[b], Q. Ou[c], J. A. Payne[a], C. Rollins[d], D. Wang[a], A. Hooper[a], T, J. Wright[a]

[a]*COMET, School of Earth & Environment, University of Leeds, Woodhouse Lane, Leeds, LS2 9JT, West Yorkshire, UK*
[b]*Centre for Environmental Mathematics, University of Exeter, Penryn Campus, Nr Falmouth, TR10 9FE, Cornwall, UK*
[c]*School of GeoSciences, University of Edinburgh, Drummond Street, Edinburgh, EH8 9XP, West Lothian, UK*
[d]*Earthquake Physics and Statistics, GNS Science, 1 Fairway Drive, Avalon, 5011, Lower Hutt, New Zealand*

1. Introduction

Using surface deformation over wide areas, we aim to understand processes occurring at depth in the lithosphere, where we cannot make direct observations. We can make sensible inferences of the behaviour of crustal material at depth in terms of the rock rheology (Bürgmann and Dresen, 2008) by examining time-dependent processes and testing possible spatial variabilities in strength and weaknesses of the lithosphere. We want to determine the forces involved in the collision of continents and during mountain building (Copley et al., 2010; Warners-Ruckstuhl et al., 2013; England et al., 2016; Fang et al., 2024a) and their evolution, erosion (Avouac and Burov, 1996) and subsequent gravitational collapse (Rey et al., 2001). Determining what level of influence the convecting mantle has on controlling the scale and pattern of surface deformation we observe today has also been a focus of research (Houseman and Molnar, 1997; Faccenna et al., 2021). We want to explain the patterns of fault frictional behaviour, and what promotes shallow aseismic creeping of active faults versus locking and strain accumulating (Harris, 2017; Jolivet and Frank, 2020). Finally, knowing whether the decadal geodetic rates of strain accumulation we measure today are consistent with the longer-term geological rates is important for understanding the evolution of fault zones, building models of the earthquake deformation cycle, and for enabling the use of short-term geodesy in assessing longer-term hazard (Thatcher, 2009; Meade et al., 2013; Elliott et al., 2016; Wright, 2016; Hussain et al., 2018; Mousavi et al., 2025).

There are also broader implications of our new data in terms of probing the link of tectonics to climate (Molnar and England, 1990), in particular understanding the growth of topography and evolution of geomorphology of mountains (Wolf et al., 2022) and the relative importance of surface processes and rheology. Also important is measuring and accounting for Glacial Isostatic Adjustment (Whitehouse, 2018), as well as constraining the distribution and behaviour of permafrost (Zwieback et al., 2024). Displacement time series of surface observations can provide information on water resources from the measurements of the widespread land subsidence and coastal subsidence (Galloway and Burbey, 2011), the latter of which has implications for relative sea-level rise (Wu et al., 2022). Additionally, such measurements, when at sufficiently high resolution, can be useful for volcano deformation monitoring (Ebmeier et al., 2018; Poland and Zebker, 2022), determining landslide stability (Cohen-Waeber et al., 2018; Bekaert et al., 2020) and for monitoring mining activities (Yang et al., 2020) and critical infrastructure (Wu et al., 2020).

2. Tectonic Background

The Alpine Himalayan orogenic belt formed from the ongoing collision of Eurasia with the Nubian (African) (Jolivet and Faccenna, 2000; Billi et al., 2023; Nocquet, 2012), Arabian (Reilinger and McClusky, 2011; Allen, 2021; Viltres et al., 2022) and Indian plates (Molnar and Stock, 2009; DeMets et al., 2020). These relative plate motions narrowed and then closed the Tethys Ocean through the process of subduction (Storetvedt, 1990), suturing crustal material with the Eurasian continent over the past few tens of millions of years (Yin, 2010; Parsons et al., 2020; Allen, 2021). Sustained plate convergence uplifted large mountain chains (Ding et al., 2022) and created high peaks such as Everest in the Himalayas at 8,849 m and Jengish Chokusu in the Tian Shan at 7,439 m. The consequent thickening of the crust and the creation of topography generates gravitational potential energy that resists the tectonic driving forces and, along-with the reduction in slab-pull forces (Collins, 2003), results in a rapid slowdown of the rate of northward convergence of the plates with Eurasia (England and Molnar, 2022).

The tectonics of the Mediterranean are dominated by the relative motion of Africa (Nubia Plate) and the rate of convergence has slowed over the past few tens of millions of years from > 30 mm/yr before 25 Ma to 13 mm/yr for 11–25 Ma and most recently < 7 mm/yr in the last 11 Ma (McQuarrie et al., 2003; Reilinger and McClusky, 2011). The deformation of the Turkish Iranian Plateau, Iran and the Makran is controlled by the Arabian plate with its northward motion (and anticlockwise rotation). The rates of relative convergence have slowed less significantly than for the case of Nubia-Eurasia, from the same > 30 mm/yr before 25 Ma to 21 mm/yr for the past 25 million years (Reilinger and McClusky, 2011). Finally, in the East, the Himalayas, Pamirs, Tibetan Plateau and Tian Shan are

all controlled by the relatively rapid northward motion of India which has slowed from 58–83 mm/yr between 45–20 Ma to 44–57 mm/yr for the period 11–20 Ma and now to a rate of 34–44 mm/yr for the past 11 Ma (Molnar and Stock, 2009). In each of these, the distribution of gravitational potential energy of the regions modifies the pattern of deformation imposed by the boundary forces (England and Houseman, 1989; England and Molnar, 2015; England et al., 2016; Walters et al., 2017; Fang et al., 2024a).

The European Alps are a region of shortening and uplift (Sánchez et al., 2018), whilst the Apennine Mountains running down the length of Italy currently experience extension (Daout et al., 2023; Nucci et al., 2025). Whilst east-west extension is also occurring in east Albania, convergence and thrust faulting along the Adriatic occurs in the western part of the country (Copley et al., 2009). The Southwestern Balkans, north of the Aegean, are at the transition from collision to subduction (d'Agostino et al., 2020), whilst across Greece there is a large velocity gradient associated with the Hellenic Arc and extension within Greece (Taymaz et al., 1991; Chousianitis et al., 2024).

Anatolia similarly exhibits extensional tectonics, particularly in the west; the rapid rotation and westward motion of Anatolia with respect to Eurasia is accommodated along the North and East Anatolian Faults (Weiss et al., 2020; Barbot and Weiss, 2021). Whilst the westerly part of the AHB is most strongly influenced by the relative motion of the Nubian Plate, Anatolia's motion is controlled as well by the northward motion of the Arabian Plate and lateral variations in gravitational potential energy (England et al., 2016).

The Turkish Iranian Plateau (Copley and Jackson, 2006) and Caucasus's active tectonics (Sokhadze et al., 2018; Ismail-Zadeh et al., 2020) are also a result of Arabia moving ~20 mm/yr northward, resulting in a high mountain chain running from the Caspian to the Black Sea. The Turkish Iranian Plateau grows laterally by incorporating the western edge of the Zagros Fold and Thrust Belt (Allen et al., 2013), which runs along the southern margin of Iran and the Persian Gulf. The Zagros is a region of active shortening and seismicity, comprising large scale folds that result in characteristic "whale-back" anticlines (Nissen et al., 2011). The active deformation across Iran is relatively diffuse (Khorrami et al., 2019; Watson et al., 2024) with the Alborz mountains lying along the northern edge with the Caspian Sea as an example of an actively uplifting intercontinental orogen (Ballato et al., 2015). At the eastern end of the country, the tectonics changes from right-lateral shear (Walker and Jackson, 2004) to shortening along the Makran, a region of subduction which is currently accumulating strain and has the potential for megathrust earthquakes (Smith et al., 2013; Penney et al., 2017).

To the north of this lies the complex zone of the Hindu Kush, Afghan-Tajik depression and the Pamirs which are shortening and shearing as a result of the northward motion of India (Schurr et al., 2014; Metzger et al., 2021). The Himalayas run along the southern margin of the Tibetan Plateau and are the arcuate interface between India and Eurasia, accommodating about half of the overall ~40 mm/yr shortening between the two (Ader et al., 2012). With the largest earthquake potential and some of the greatest density of human populations, this stretch of the AHB presents some of the biggest earthquake risk (Bilham, 2019).

The Tibetan Plateau has grown to 5 km elevation from the sustained collision, shortening, and thickening of the crust (Yin and Harrison, 2000; Royden et al., 2008), and, apart from thrust faulting in the north-east and east, it is now dominated by strike-slip and extensional faulting within it. Beyond all of these mountain ranges, deeper within Eurasia, the Indian plate's most northerly significant tectonic impact is in shortening occurring within the Tian Shan (Jolivet et al., 2010; Zubovich et al., 2010).

3. Results - Active Tectonic Regions of Interest

We consider each of the main tectonic areas of significant deformation in turn, running from west to east, highlighting the general kinematics we see and the significant localisation of strain that we calculate.

3.1. Türkiye

Türkiye, located at the intersection of the Eurasian, African, and Arabian plates (Figure 1), is characterized by complex and high magnitude tectonic deformation. Anatolia experiences a push from the west, where Arabia is colliding with Eurasia, and a pull from the west, where subduction occurs beneath the Hellenic Arc (Barka and Reilinger, 1997; Taymaz et al., 2007; England et al., 2016). The motion is accommodated in part by motion on two major strike-slip faults - the right-lateral North Anatolian and left-lateral East Anatolian Faults (Şengör et al., 2005; Güvercin et al., 2022), with extensional faulting dominating in western Anatolia (Yilmaz and Gürer, 2024). Although Anatolia has often been described as a microplate (e.g., McKenzie, 1972), geodetic studies from GNSS show non-negligible internal deformation (e.g., Aktug et al., 2009).

Türkiye has experienced a large number of damaging recent and historical earthquakes, which have impacted all the tectonic zones described above. The North Anatolia experienced a westward progression of $M_w > 7$ earthquakes in the 20th century (Barka, 1996), culminating in two large earthquakes in 1999 (e.g., Özalaybey et al., 2002; Bürgmann et al., 2002). In the last few years, the East Anatolian fault experienced several major earthquakes, including the 2020 M*w* 6.8 Elazĭg earthquake (Tatar et al., 2020), and the two devastating earthquakes (M*w* 7.8 and 7.6) of the 6 February 2023 Kahramanmaraş sequence (e.g. Hussain et al., 2023; Ergintav et al., 2024). Western Anatolia has experienced smaller but nevertheless damaging earthquakes, including the normal-faulting 1995 Dinar earthquake (Eyidoğan and Barka, 1996; Wright et al., 1999).

A large number of previous studies have used InSAR and GNSS to study velocity and strain rate in different parts of Türkiye, and we do not attempt to provide a comprehensive review here. We focus on those studies that have attempted to map deformation across the whole of Türkiye. The most recent GNSS compilation from (Kurt et al., 2023) contains velocities

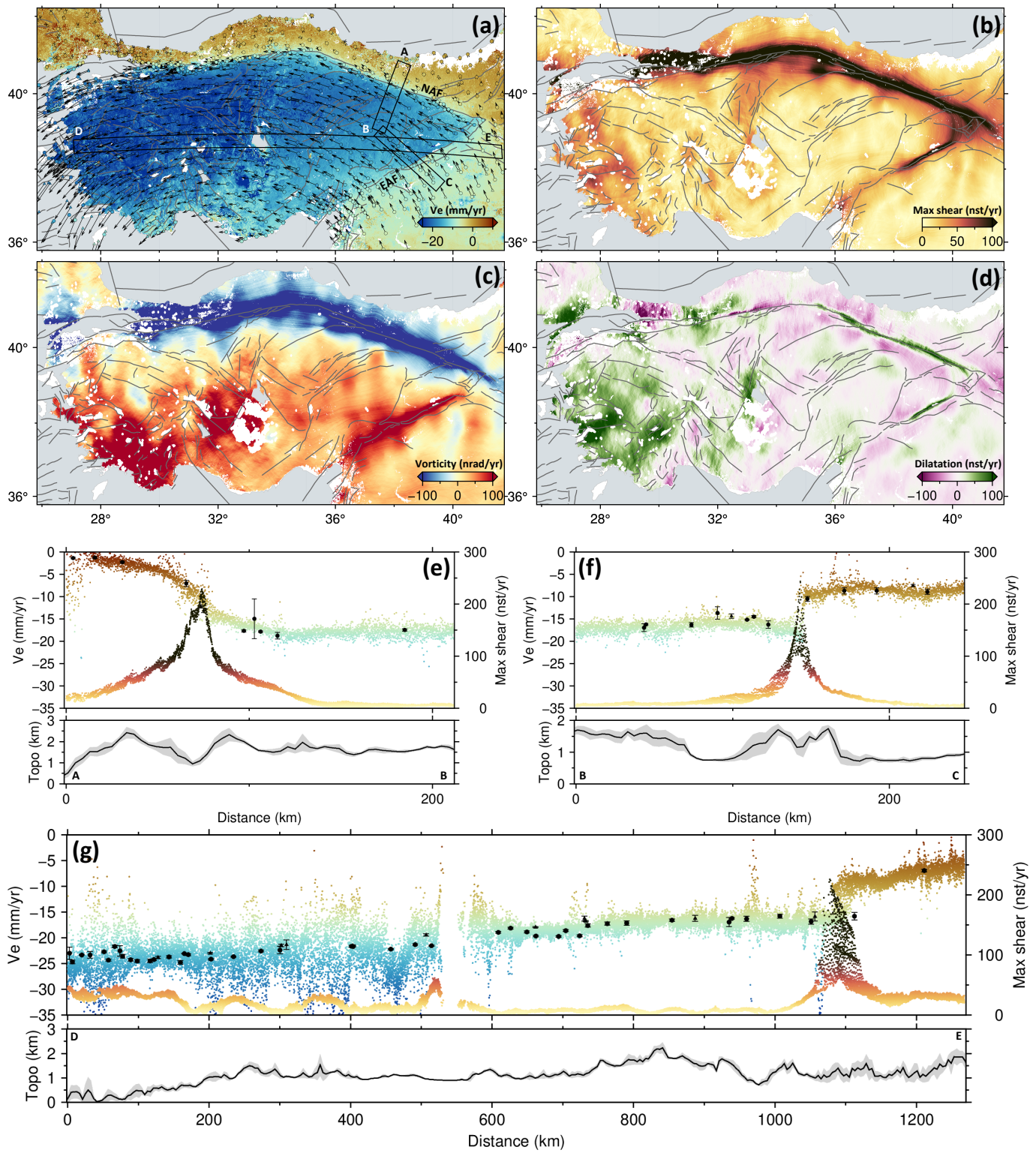


Figure S1: Velocity and strain rate maps and profiles for the region of Anatolia, Türkiye. (a) Eastward velocity; (b) Maximum shear strain rate; (c) Vorticity, where positive values indicate anti-clockwise rotation; (d) Dilatation, where positive values indicate extension. (e) Profile A–B showing eastward velocity across the North Anatolian Fault (NAF) and corresponding maximum shear strain rate; (f) Profile B–C showing eastward velocity across the East Anatolian Fault (EAF) and corresponding maximum shear strain rate; (g) Profile D–E showing eastward velocity from west to east and corresponding maximum shear strain rate.

from 836 stations. The InSAR velocity field from Weiss et al. (2020) uses the first ~5 years of data from Sentinel-1 to derive east-west and vertical velocity fields. Both of these studies capture the large-scale features expected from the tectonics of the region, and Weiss et al. (2020) also shows significant non-tectonic vertical deformation, particularly associated with the Konya basin in Central Anatolia. Other studies have focused on specific aspects of the deformation field, such as the dynamics of the creeping section of the North Anatolian Fault (e.g., Cetin et al., 2014; Jolivet et al., 2023)

Our velocity field (Figure S1) improves on the results of Weiss et al. (2020), using more sophisticated processing and a longer time series. The shear strain rates associated with the North and East Anatolian Faults are sharper, being derived directly from gradients of the referenced InSAR velocities. This is also seen very clearly in the profiles crossing the faults (Figure S1). The cleaner velocity fields show that creep is occurring on parts of the East Anatolian Fault as well as on the well-known sections of the North Anatolian Fault – further work is needed to understand how the creep rate was influenced by the 2020 earthquake.

Our results corroborate previous studies that show all of the North and East Anatolian Faults having focused, elevated strain rates, which appear to be independent of the time since the last earthquake. This suggests that these major faults reach a steady state interseismic strain rate (Hussain et al., 2018). A possible exception is the south-western end of the East Anatolian Fault, which ruptured in the Kahramanmaraş sequence. While there is elevated strain in this region, seen both in the shear strains and rotations (Figure S1), the strain rate is lower than on the north-eastern part of the East Anatolian Fault. This may simply reflect the fact that the fault splits here into multiple strands, so the strain is more distributed (although the strain measurements for the north-eastern half of the EAF are largely due to the postseismic effects of the 2020 earthquake there, as whilst we mitigate against the coseismic effects, the postseismic remains in our time series).

The horizontal dilatation field shows very clearly the high rates of extension in Western Anatolia, associated with normal faulting there. A long profile through our data crossing all of Anatolia (Figure S1) also shows clearly the steadily increasing eastward velocities as you go from east to west across the region - demonstrating that Anatolia does not behave as a rigid microplate.

While the east-west and north-south velocities are well constrained by both InSAR and GNSS data, the vertical component is less certain due to phase biases and potential land subsidence effects. The 3D GNSS data, which could provide better constraints on the vertical velocity, also show higher uncertainty in these regions, which necessitates a more cautious interpretation. Nevertheless, we see high rates of subsidence in the Konya basin (Figure 12) confirming the result of Weiss et al. (2020).

3.2. Iran

Much of Iran's active tectonic deformation is driven by the northward and anti-clockwise motion of the Arabian plate colliding with the south-west of the country. This collision contributes to the active shortening of the Zagros Fold and Thrust Belt in south-west Iran (Nissen et al., 2011), which accommodates about half of Arabia's northward motion (Hollingsworth et al., 2006). Previous research finds deformation in much of the rest of Iran is concentrated in the Alborz and Kopeh Dagh mountains, with Central Iran and the Lut desert behaving near to aseismically (Hollingsworth et al., 2006).

Overall, we find, in agreement with previous studies, that active deformation and subsequent strain are relatively diffuse across Iran (Khorrami et al., 2019; Dodds et al., 2022; Watson et al., 2024). Where there is elevated shear strain (Figure S2b, c), this strain forms wide bands and is apparently not tightly localised to single faults but wider deforming fault belts. This is particularly true in the Zagros belt. Strain in this fold-thrust belt does not exceed ~50 nanostrain/year and is spread diffusely across much of the entire width of the Zagros (~300 km^2).

Stronger strain localisation is evident in north-east Iran on the margins of the Turan platform. Our results indicate this platform is moving to the west, with the rate of westward motion increasing from east to west to a maximum of ~8 mm/yr. This westwards motion is accommodated by the north-west south-east striking Main Kopeh Dagh and Ashkabad right lateral strike-slip faults on the platform's northern extent (Hollingsworth et al., 2006; Walker et al., 2021), and a series of smaller faults to the south, including the Robet-e Qarabil Fault (Figure S2). Strain on these southern faults reaches ~70 nanostrain/year.

In north-west Iran, we observe right-lateral strike slip motion across the North Tabriz fault (Figure S2e, Copley and Jackson, 2006). Our results indicate that, in the far field, areas north and south of the Tabriz fault are moving ~3-4 mm/yr, towards the east on the north and to the west on the south. On the fault itself, we find some elevated strain compared to neighbouring regions at ~45 nanostrain/year (Figure S2). Some of this shear strain motion may be post-seismic deformation associated with two series of M_W4–6 earthquakes in February 2020 and late 2023 (near Khovy on the Iran-Türkiye border). Overall, however, the strain and east-west motion across this fault is still quite diffuse (reaching 40 nst/yr over 100 km, Figure S2e) despite the influence of post-seismic signals. This diffuse strain provides evidence for strong strain partitioning in this part of the Alpine-Himalayan Belt (Copley and Jackson, 2006).

Finally, we observe significant post-seismic deformation in north-west Iran associated with the November 2017 Sarpol-e Zahab earthquake in the north-west Zagros mountains (Figure S2e, 300 m). We have removed all co-seismic interferograms associated with this earthquake, so any residual deformation around this rupture site is due to post-seismic relaxation. Overall, the wider region of this earthquake is moving ~4-5 mm/yr to the west, meaning post-seismic velocities in the east component direction since November 2017 are ~10 mm/yr for both post-seismic lobes. Previous work has attributed this post-seismic deformation to afterslip (Fathian et al., 2021). We note that this elevated deformation is associated with elevated shear strain around deforming lobes, reaching ~60 nstr/yr at this location.

Overall there is good coverage in our Iran-wide velocity field due to high coherence (Figure SB9), in part due to the lack

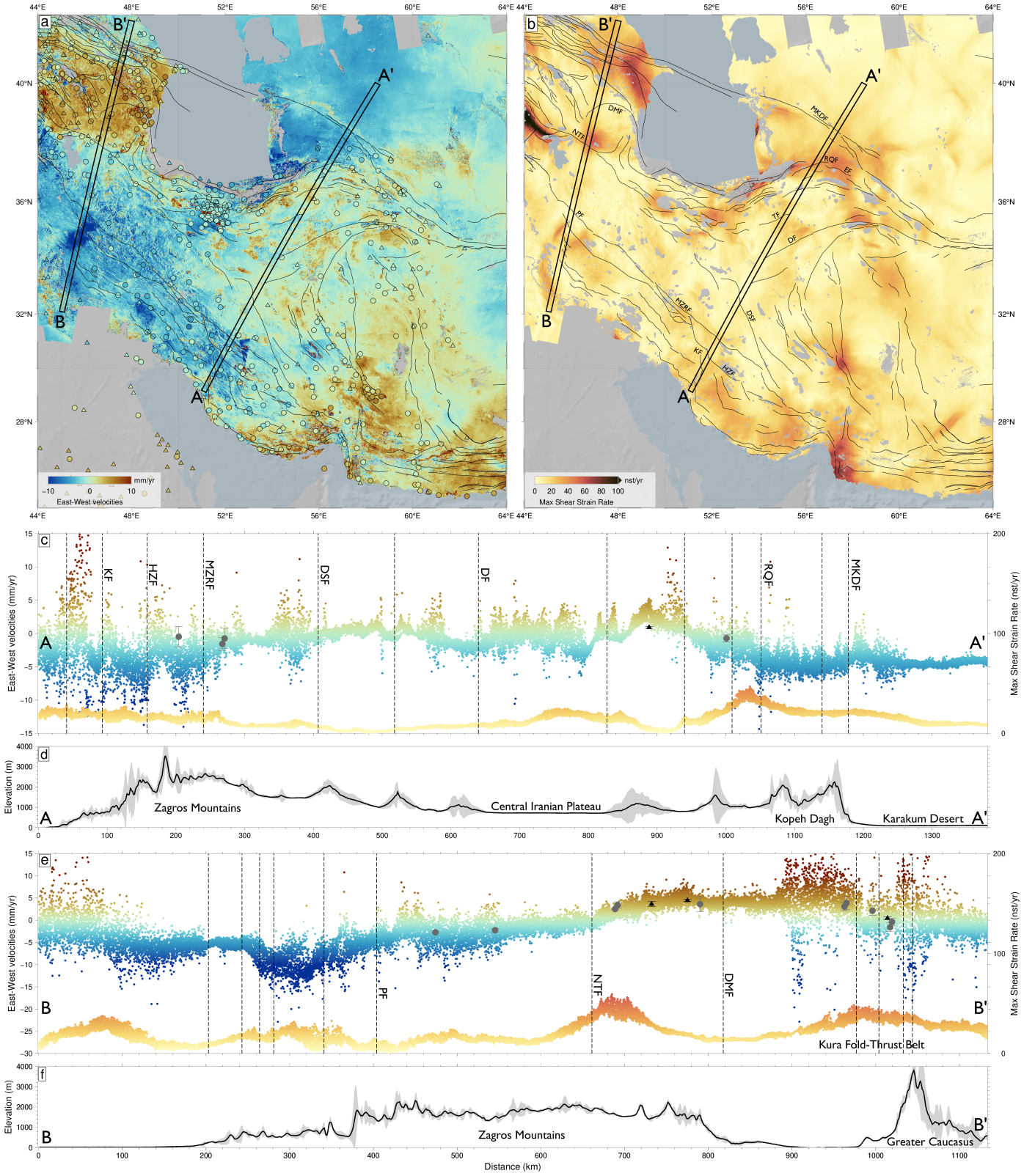


Figure S2: Velocity and strain rate maps and profiles for the region of Iran. (a) Surface velocities of Iran in the East-West direction. Blue, negative velocities indicate motion towards the west; brown to the east (Watson et al., 2024). Circles indicate East-West GNSS velocities compiled in this study. Triangles = 3D velocities; circles = 2D velocities. Fault names from (Hessami and Jamali, 2006); fault locations from (Styron and Pagani, 2020) (KF = Kazerun Fault, HZF = High Zagros Fault, MZRF = Main Zagros Reverse Fault, DSF = Deh Shir Fault, DF = Doruneh Fault, TF = Torud Fault, RQF = Robat-e Qarabil Fault, EF = Esfarayen Fault, MKDF = Main Kopeh Dagh Fault; NTF = North Tabriz Fault; PF = Piranshahr Fault; DMF = Dasht-e Moghan Fault). (b) Maximum shear strain: sig15, window 100. (c) East-West velocities and maximum shear strain in swath A–A' in a) and b). Black dashed lines denote faults mapped in a) and b). (d) Topography in swath A–A' in a) and b). Triangles = 3D velocities; circles = 2D velocities. (e) Profiled East-West velocities and maximum shear strain in B–B' swath. (f) Topography in B–B'.

of extensive vegetation towards inland regions of the country. This lack of vegetation additionally contributes to a low level of noise in the velocities (Figure S2a). This is particularly evident in velocity profiles of desert regions in the north-east of the country at the border with Turkmenistan (Figure S2c) where the spread of values is 2 mm/yr and the retrieved strain rates are very low (< 10 nstr/yr).

3.3. Makran & Hindu Kush

The Eastern Makran, Sulaiman Ranges, and Hindu Kush are a tectonically complex region at the western edge of the Indian plate (Figure 1). The Chaman fault and associated sub-parallel fault systems runs along much of this boundary accommodating the fast relative motion of India with Eurasia of ~ 30 mm/yr (Szeliga et al., 2012). The Chaman fault is unusual in that it has not experienced any major historical earthquakes, despite being a major strike-slip zone, although parts of it are creeping (Dalaison et al., 2021). The Hindu Kush region represents an unusual tectonic setting characterized by ongoing slab break-off processes, as evidenced by intermediate-depth seismicity. The Indian lithospheric slab is subducting northward beneath the Hindu Kush, with the slab's penetration depth increasing along its strike (Kufner et al., 2021; Metzger et al., 2021). The Sulaiman Ranges in western Pakistan are a fold and thrust belt that experience a style of shallow crustal faulting that suggests it is deforming out over the Indian foreland with shear along its edges (Reynolds et al., 2015). The Makran region is a wide accretionary prism (Smith et al., 2012) that results from the subduction of the Arabian plate beneath eastern Iran and Pakistan that has the potential for major earthquakes along its interface (Penney et al., 2017). At the eastern end of the Makran, the 2013 M_w 7.7 Baluchistan earthquake ruptured the arcuate Hoshab fault (Avouac et al., 2014).

The coherence in this region (Figure SB9) is amongst the best seen across the AHB in the area in the north-west in Afghanistan, and amongst the worst in south-east Pakistan where agriculture around the Indus river is challenging for C-band to maintain coherence. It is also the region with the least number of GNSS sites (Figure SB1), leading to some large estimates of uncertainty in the derived 3-component velocity (Figures SB15 & SB21), but it is where InSAR offers the potential to improve estimates of velocity and strain rates the most (Figure S3).

In our results, the bulk of Afghanistan is not moving east-west with respect to Eurasia, but along the Makran and Sulaiman Ranges we see eastward velocities of ~ 10 mm/yr. The shorter wavelength change in velocities from east to west in the Eastern Makran is due to postseismic deformation following the 2013 M_w 7.7.Baluchistan earthquake (Lv et al., 2022). The near-zero east velocities at the north-western edge of the area in Figure S3a illustrate the low level of noise possible under the most ideal circumstances, with spreads in the velocities of < 1 mm/yr (Figure S3c). The vertical competent of velocity is much more difficult to reliable interpret, especially with the lack of GNSS constraints (Figures S3d & 7c) which possible leads to some long wavelength errors.

The maximum shear strain rate is dominated by the earthquake postseismic in Baluchistan, but also broadly aligns with the Chaman Fault zone. Due to its strike running almost north-south, we poorly resolve the expected concentration of shear here despite the overall relative motion > 30 mm/yr, as our northward velocities are relatively smooth (Figure 7) having come largely from the very sparse GNSS. Across Afghanistan, we observe very low strain rates < 20 nstr/yr and north of the Herat Fault, we observe near-zero strain in our data indicating the level of our noise floor for this region.

The whole region running along the Chaman Fault Zone experiences a very broad area of anticlockwise rotation, as viewed in the vorticity for the belt (Figure 9), as a result of the northward motion of India.

3.4. Pamirs

The Pamirs lie between the Afghan-Tajik Depression (McNab et al., 2019) in the west and the Tarim basin in the east, and they have formed northwards of the western syntaxis of the Himalayas as a result of the northward motion of India. In addition to a large degree of crustal shortening and associated seismicity, this region is also unusual along the Alpine Himalayan Belt in having intermediate depth earthquakes as well (Schurr et al., 2014). The current shortening across the Pamirs is known to be largely accommodated on the Pamir Thrust system (Ischuk et al., 2013) and north of this major fault zone lies the Tian Shan (Section 3.5).

Major earthquakes have recently struck the region including the 2015 M_w 7.2 earthquake in the Central Pamir, Tajikistan, which was a strike-slip rupture of the Sarez-Karakul fault (Metzger et al., 2017; Zubovich et al., 2022) that was part of a sequence of earthquakes that continued around the Pamirs (Bloch et al., 2023). Previous InSAR studies have measured the deformation field (Metzger et al., 2021), but the coherence in the mountainous and snow-covered region is challenging, resulting in largely the Afghan-Tajik Depression being retrieved in their velocity fields.

In terms of our results, the coherence in both the ascending and descending is fairly good (Figure SB9) except for the highest peaks in the Pamirs and to the south towards the Eastern Syntaxis resulting in some gaps in the velocities (Figure 6). The formal uncertainties calculated from the time series and velocity decomposition indicate that the line-of-sight and 3-component rates are around a 1σ level of 1 mm/yr (Figure 5 & SB15). The eastward velocity with respect to Eurasia shows, in agreement with the sparse GNSS velocities, that most of the immediate region outside of the Pamir is moving only in the north-south direction, with little east-west component (Figure S4a). However, within the Pamirs, there is a significant amount of westward motion from the Pamirs into the Afghan-Tajik Depression where the dilatation (Figure S4d) shows a large amount of contraction ($> 100 \times 10^{-9}$ strain/yr) associated with shortening across the thrust faults in this region (McNab et al., 2019).

There is a sharp gradient in this relative westward motion of the Pamirs (right-lateral shear) at the Pamir Thrust where we see the maximum shear strain rate is co-located with the

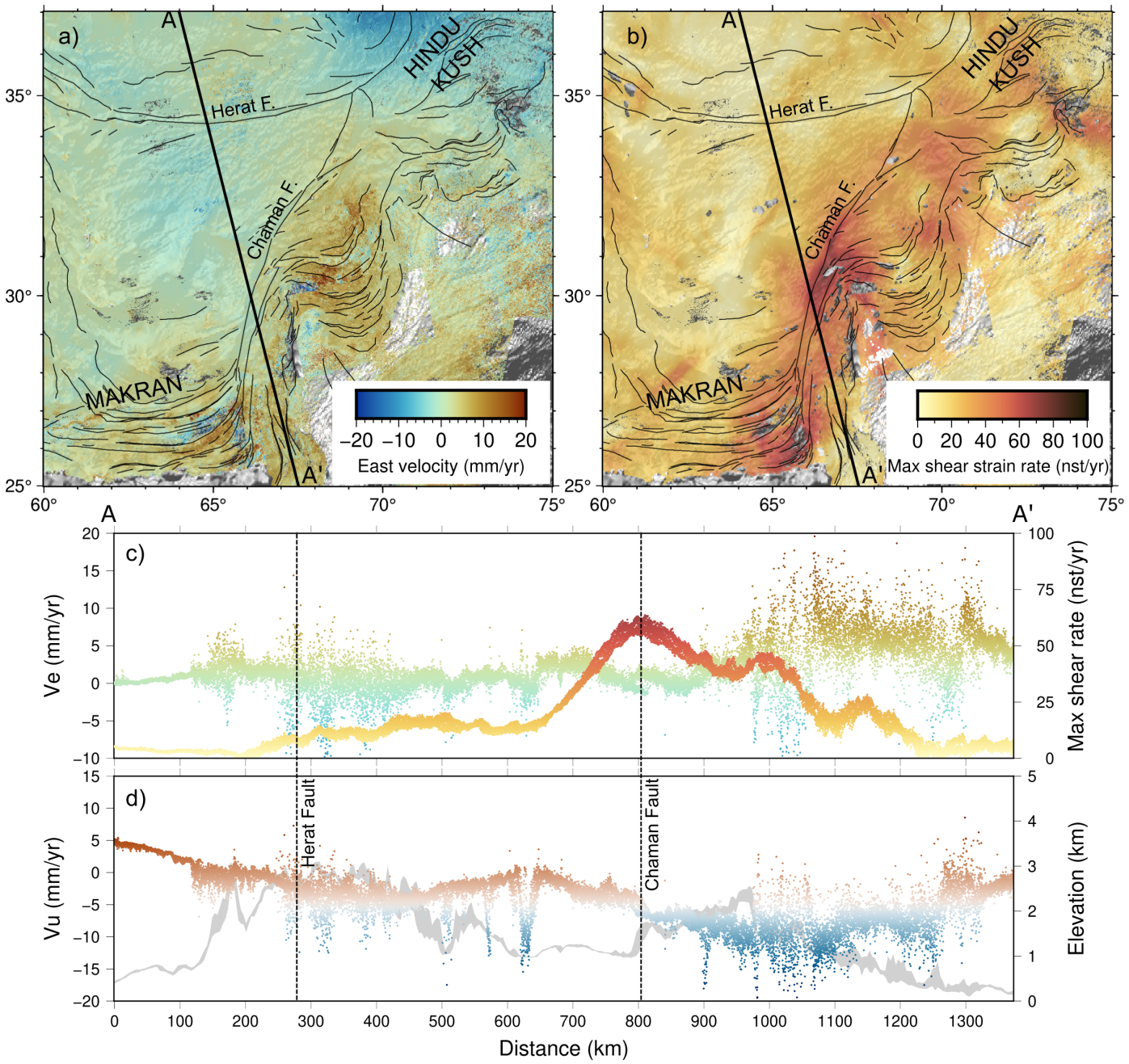


Figure S3: Velocity and strain rate maps and profiles for the region of the Chaman Fault Zone form the Makran, though the Sulaiman Ranges to the Hindu Kush: a) East Velocity; b) Maximum Shear Strain Rate; c) profile through eastwards velocity and maximum shear strain rate fields between points A and B; d) profile from vertical velocity and elevation between A and B.

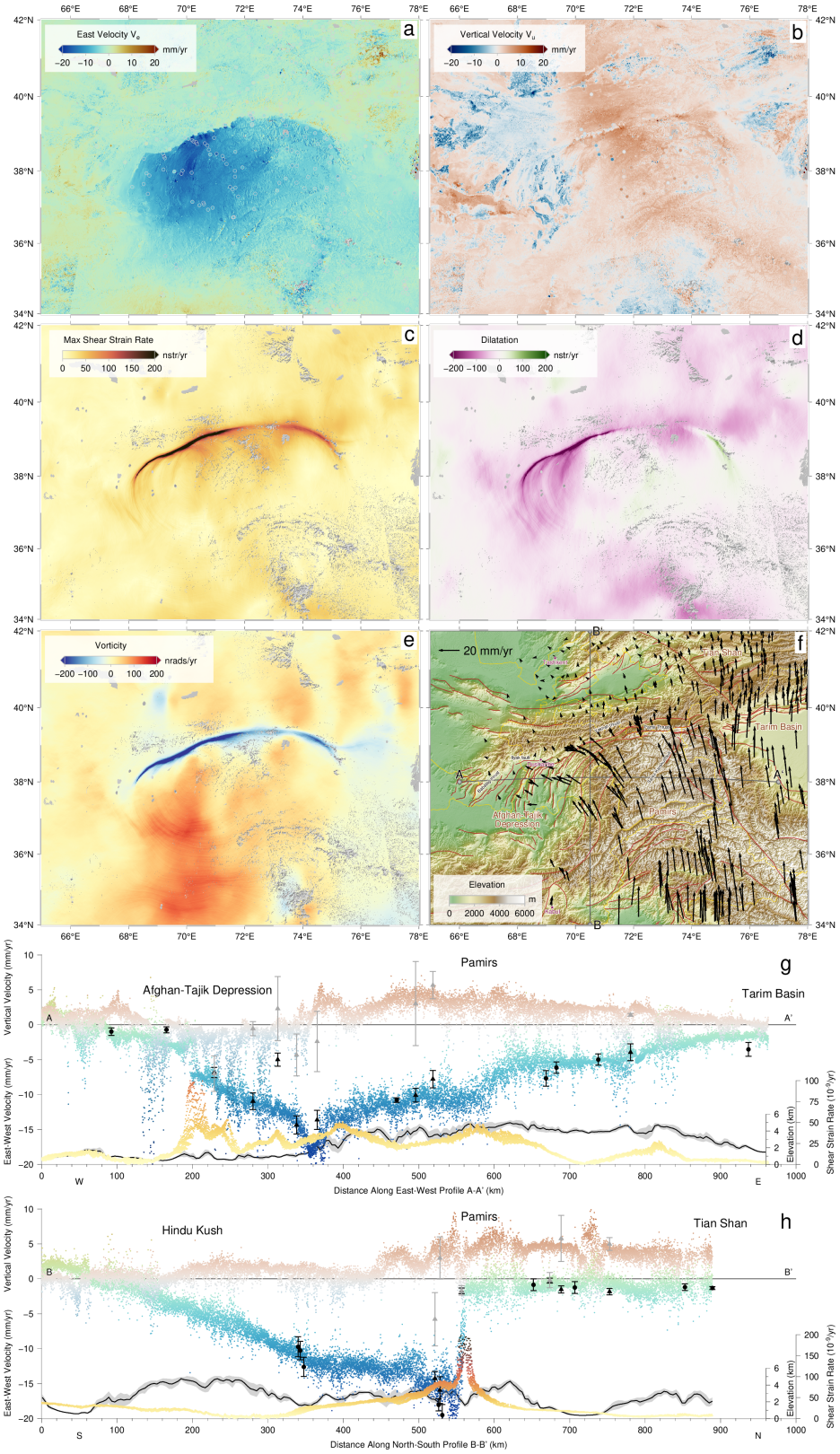


Figure S4: Velocity and strain rate maps and profiles for the region of the Pamirs. (a) Component of Eastward Velocity with GNSS eastwrad velocities as coloured circles, (b) Component of Vertical Velocity with 3D GNSS vertical component as coloured circles, (c) Maximum Shear Strain Rate, (d) Horizontal Dilatation Rate (positive is extension), (e) Vorticity (positive is anticlockwise rotation), (f) Elevation map of the Pamirs with GNSS velocities overlaid (black arrows), active faults from (Styron and Pagani, 2020) and location of profiles in grey, (g) East-west profile A–A' through velocity and strain rate fields (with GNSS and topography marked). (h) North-south profile B–B'.

large gradient in north-south GNSS velocities across the Pamir Thrust system. This strain peaks at $> 200 \times 10^{-9}$strain/yr although our velocity pixel spacing at ~1 km and smoothing of the strains means this peak is somewhat subdued and broadened (and made arcuate with a additional artefact of a Gibbs ringing effect). An anticipated steeper gradient is suggested by the sharp transition in the east-west velocities seen in the north-south transect in Figure S4h that is almost step-like in profile. However, there is also the potential for unwrapping errors in the interferograms along this steep margin where there is a topographic step of almost 4 km kilometres over a distance of less than 20 km. Following the trace of the east-west velocity step and maximum shear westwards towards Dushanbe, the sharp step in velocity follows the Vakhsh thrust confirming this is a region of active fault creep (Metzger et al., 2021), as is the along-strike continuation to the Ilyak fault immediately north of Dushanbe. Continuing around onto the north-south striking Babatag thrust, there is another sharp gradient in velocity imaged across it with a step of 5 mm/yr observed (Figure S4g).

Our uplift results carry much greater uncertainty in terms of interpreting tectonic contributions (rather than formal uncertainties themselves Figure SB15), but we do see systematic patterns of broad uplift in the south and western Pamir of ~ 5 mm/yr (Figure S4b,g,h), which agree with the few 3-component GNSS rates available (albeit with large uncertainties themselves). Regions of apparent subsidence in the Afghan-Tajik Depression are likely associated with agriculture and therefore are probably artefacts due to phase bias (Ansari et al., 2021). The non-agricultural areas within this region associated with folds and exposed bedrock show negligible uplift rates around 0 mm/yr except west of Dushanbe where we see some potential tectonic uplift associated with the folds. Further westwards even stronger values of apparent uplift > 10 mm/yr also closely follow the desert land cover of Western Turkmenistan and it is not possible to discern if these relate to tectonic or near surface processes, or are in fact long wavelength errors in our velocity fields due to a lack of GNSS constraints for this area (Figures SB15 and SB21).

Whilst our time series starts after (Table SA4) the 2015 November Sarez earthquake (Metzger et al., 2017; Elliott et al., 2020), the postseismic motion following this event (Jin et al., 2022) is also visible within our results, in particular the NE-SW orientated maximum shear strain located south of the Pamir Thrust System. Whilst much smaller in magnitude, some of the maximum shear along the eastern end of the Pamir thrust system will also be attributable to the postseismic motion from the June 2016 M_w 6.4 Sary-Tash and November 2016 M_w 6.6 Muji earthquakes.

3.5. Tian Shan

The Tian Shan is a relatively young mountain belt reactivated as a far-field response to the ongoing collision between India and Eurasia (Jolivet et al., 2010). It is bounded between the Tarim Basin in the south, the Pamir in the southwest, and the Kazakh Platform in the north, which represents the Stable Eurasia. Absorbing over half of the shortening between India and Eurasia (Zubovich et al., 2010), the Tian Shan is seismically active, with over ten magnitude greater than 7 earthquakes that occurred in the mountain range over the past just over a century (Kulikova, 2016), including the 1889 M8 Chilik Earthquake (Krüger et al., 2017), the 1911 M8 Chon-Kemin Earthquake (Kulikova and Krüger, 2015), and the recent 2024 M_w 7.0 Wushi Earthquake that happened on the southern range front (Zheng et al., 2024).

However, unlike the Pamir which concentrates most of its strain on a single structure, the deformation in Tian Shan is largely distributed, as evident in the gentle gradients and almost linear east velocity profiles both perpendicular and parallel to the range (Figure S5a,e,f). In terms of strain, the negative dilatation (contraction) rates are up to twice in magnitude as the maximum shear, consistent with the compressional regime that dominates Tian Shan's deformation. The spatial patterns of the maximum shear and the dilatation strains are rather similar (Figure S5c,d), and are all slightly more concentrated in the western Tian Shan. However, within this region they are still fairly evenly distributed and rarely exceed 50 nstr/yr. This is consistent with geological observations that show the shortening in the western Tian Shan being partitioned between slip rates on the range-frontal folds-and-thrust belts, basin-bounding faults and basin-interior folds (Thompson et al., 2002). Hence, the deformation in Tian Shan is more similar to that described by a continuum model (England and Molnar, 2015). Elsewhere in the Tian Shan, the strain rates are mostly below 30 nstr/yr, which is getting towards the noise level of our measurements for this area (Section 3.3).

Apart from the range-parallel thrusts and folds, the Tian Shan is thought to accommodate shortening via the northwest-trending right-lateral strike-slip faults that extend into the crystalline Kazakh Platform. The Talas-Fergana fault and the Dzhungarian fault, in particular, have pronounced geomorphological features that suggest they have ruptured in very large earthquakes (Burtman et al., 1996; Campbell et al., 2015). However, in our datasets, we do not observe significant east velocity steps across these two structures, or any of the northwest-trending strike-slip faults. The only signal that might suggest the role played by the strike-slip faulting is the slightly higher shear strain along the segment of the Talas Fergana fault dividing the Fergana Basin and the western Tian Shan (Figure S5c). However, the magnitude of shear rate on this fault is not higher than that in the interior western Tian Shan, suggesting that its role is minor. This is consistent with published geodetic slip rates on the slow end (Zubovich et al., 2010; Wu et al., 2023), in contrast to the often fast slip rates derived from geological methods (Rizza et al., 2019; Rust et al., 2018).

The vertical velocity field shows gentle uplift across the Tian Shan, punctuated by subsidence signals from agriculture, mining, oil and gas exploitation, and groundwater extraction with likely impact from phase bias (Ansari et al., 2021). The rapid subsidence might also have introduced artifacts into the vertical velocities in regions with sparse vertical GNSS control, as VELMAP inherently assumes zero average vertical velocities at mesh nodes during the inversion for referencing the LOS velocities (Wang and Wright, 2012). This might have implications

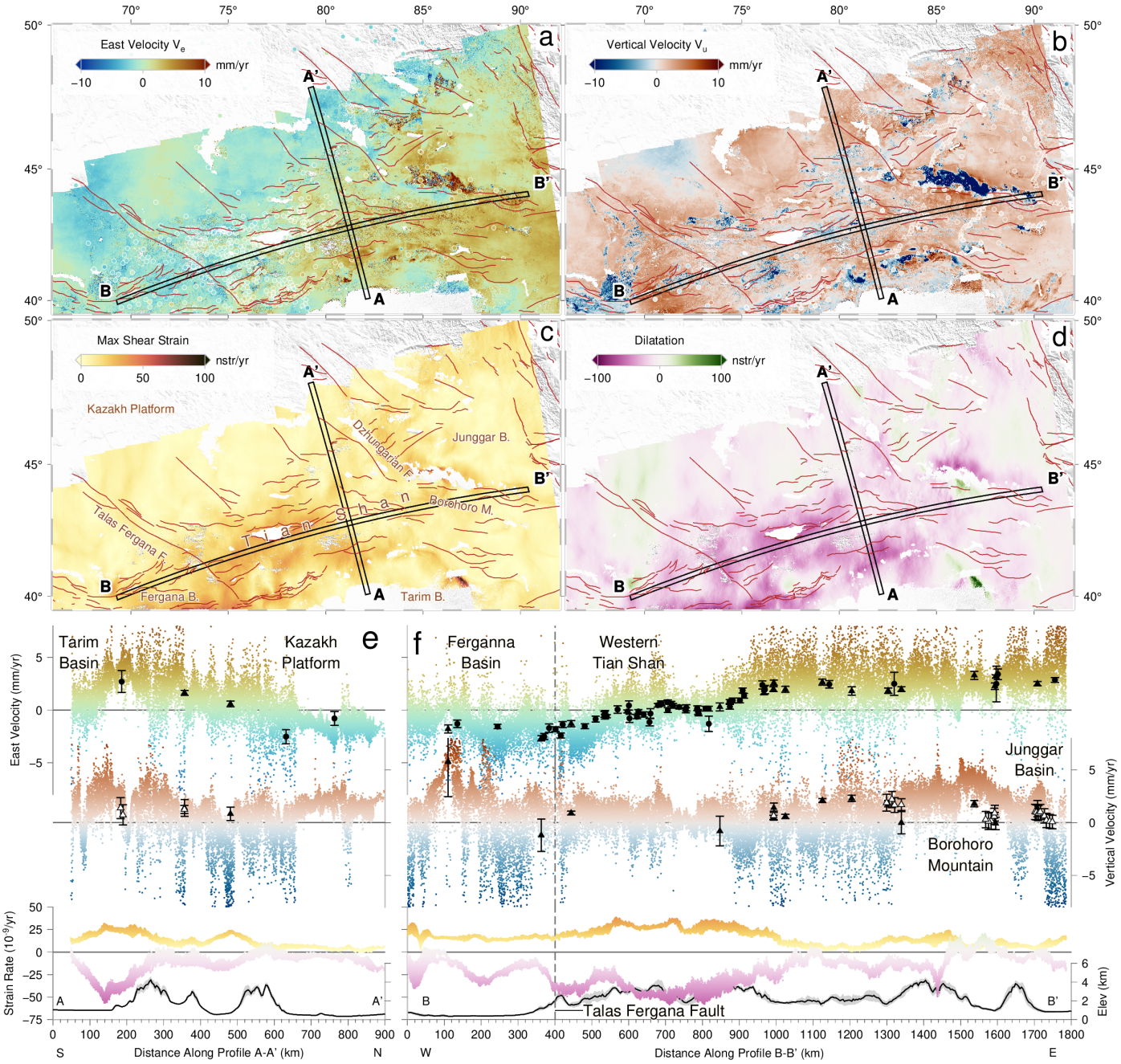


Figure S5: Velocity and strain rate maps and profiles for the region of the Tian Shan. (a) Component of Eastward Velocity with GNSS eastward velocities as coloured circles, (b) Component of Vertical Velocity with 3D GNSS vertical component as coloured circles and levelling data as coloured triangles, (c) Maximum Shear Strain Rate, (d) Horizontal Dilatation Rate (positive is extension), (e) North-south profile A–A' through velocity and strain rate fields (with GNSS, levelling and topography marked). (f) East-west Profile B-B'. B.=Basin. F.=Fault. M.=Mountain. Active faults from Styron and Pagani (2020).

for interpreting the ~5 mm/yr uplift along the Borohoro Mountain, and into the Kazakh Platform, for example. It is likely that the high uplift rates between 1200 and 1600 km along the profile B–B' are overestimated.

The circle of gentle subsidence around the Lake Issyk-Kul might be real. This subsidence could be due to permafrost thaw, or the delamination of the lithosphere underneath (Pan et al., 2019), or a combination of both. Just to the east of the Issyk-Kul lake is the Karkara Range front Fault which is thought to be creeping at rates up to 3 mm/yr (Mackenzie et al., 2018). However, no obvious contraction nor uplift was resolved from our data sets, possibly because the motion is largely north-south oriented, or because it is creeping at a rate lower than the noise level of our velocities.

3.6. Western Tibet

Taking 98°E as a boundary, we can subdivide the Tibetan Plateau into Western Tibet and Eastern Tibet. Northwest of Western Tibet lies the Tarim basin, a relatively rigid block with low topography, little internal crust deformation and minimal seismic activity (Avouac and Tapponnier, 1993). To accommodate ~50 mm/yr of collision between India and Eurasia (Molnar and Tapponnier, 1975), numerous active faults have formed in Western Tibet, with the Altyn Tagh Fault being the most significant. This fault is one of the longest active strike-slip faults in the world, with a length of ~1500 km (Tapponnier and Molnar, 1977), and acts as the boundary between Tibet and the Tarim basin (Molnar and Dayem, 2010). Besides the Altyn Tagh fault, other major active faults in Western Tibet include the Karakoram fault (e.g. Avouac and Tapponnier (1993); Wright et al. (2004)), the Karakax fault (e.g., Peltzer et al., 2020), the Kunlun fault (e.g., Kirby et al., 2007; Harkins et al., 2010; Diao et al., 2019) and the Manyi fault (e.g., Bell et al., 2011). Several active faults are also found both inside and around the Qaidam basin (e.g., Daout et al., 2019), as well as in the Qilian Shan - Nan Shan thrust belt (e.g., Hao et al., 2015; Xu et al., 2021; Wang et al., 2024a).

Strong earthquakes within the Western Tibet during the last 100 years include the 1932 M_w 7.6 Changma Earthquake on the Changma Fault (Du et al., 2019), the 2008 M_w 7.2 Yutian Earthquake and the 2014 M_w 6.9 Yutian Earthquake on the Longmu-Gozha Co fault system (Li et al., 2015, 2016, 2020), the 1997 M_w 7.5 Manyi Earthquake on the Manyi fault (Funning et al., 2007; Wang et al., 2007) and the 2001 M_w 7.8 Kokoxili Earthquake on the Kunlun fault (Lasserre et al., 2005). It should be noted that there has been an absence of major earthquakes for over 300 years on the central Altyn Tagh Fault (between ~ 84°E and ~ 94°E (Yuan et al., 2020).

Previous GNSS and InSAR studies over the Western Tibet are mainly focused on fault kinematic parameter estimation, especially the slip rate of the Altyn Tagh fault (e.g., Bendick et al., 2000; Mériaux et al., 2004; Wallace et al., 2004; Zhang et al., 2007; Elliott et al., 2008; Li et al., 2018; Shen et al., 2019), as this can help us better understand how the Tibet Plateau accommodates the strain generated by the collision between India and Eurasia (e.g., Tapponnier et al., 2001; England and Molnar, 2005). The GNSS velocity field has short comings in determining the locking depth of faults and sources of strain as it is normally too sparse in this region; however, the InSAR velocities, especially the large-scale InSAR velocities that merge several tracks (e.g., Shen et al., 2024; Wang et al., 2024a), can provide a good opportunity to study strain localization and spatial variation of fault kinematic parameters in the Western Tibet.

Due to the good coherence in this region (Figure SB9), the velocity field and strain rate results (Figure 6, Figure 7) show a good extent of coverage over Western Tibet, and as we obtained our LOS velocities based on ~8-year time series, the uncertainties of the long-term rates are at a relatively low level, with most of them smaller than 1 mm/yr based on the LiCSBAS time-series analysis (Figure 5). The north velocities of Western Tibet show relatively low uncertainty in most of the region, and only show large uncertainties of over 2 mm/yr around the western Kunlun fault and the north side of the Altyn Tagh fault due to the missing of GPS velocities (Figure 5).

The results we obtained revealed some key surface deformation characteristics of this region. By zooming in on this area (Figure S6), we could see that our decomposed east velocities fit the GNSS east velocities (the coloured circles in Figure S6a) very well. We found the east-west velocity field pattern is mainly controlled by the left-lateral strike-slip motion along the active strike-slip faults (e.g., the Altyn Tagh Fault, the Kunlun Fault, and the Manyi Fault) in this region (Figure S6a) and that high strain rates mainly focus on these major active faults (Figure S6b).

We see maximum shear strain rates of well over 60 nst/yr along the Altyn Tagh fault between 84°E and 91°E and relatively decreasing maximum shear strain rate between 92°E and 95°E (Figure S6b), which is consistent with previous research and can be explained by a strike-slip rate of near 8 mm/yr on the deep shearing part of the fault between 84°E and 91°E and a lower strike-slip rate of near 5 mm/yr between 92°E and 95°E (Wang et al., 2024a). The high maximum shear strain rates on the Altyn Tagh Fault do not continue further east than 95°E, supporting the view that the strain accumulation on the Altyn Tagh Fault is terminated around this area (Wang et al., 2024a). The Altyn Tagh fault shows relatively higher shear rates at 90.5°E (around the Pingding Shan bend), which may be related to shallow creeping indicated by previous studies (e.g. Wang et al. (2024a)).

We also found very high maximum shear strain rates of over 100 nst/yr along the western Altyn Tagh Fault (or the Longmu-Gozha Co fault system), the Kunlun Fault and the Manyi Fault (Figure S6b,e,f,h,i). Previous studies (Li et al., 2015, 2016, 2020; Funning et al., 2007; Wang et al., 2007; Lasserre et al., 2005) show that all these areas experienced strong earthquakes with a magnitude of over 6.5 during the last 30 years, which include the 2008 M_w 7.2 Yutian Earthquake, the 2014 M_w 6.9 Yutian Earthquake, the 1997 M_w 7.5 Manyi Earthquake and the 2001 M_w 7.8 Kokoxili Earthquake. Therefore, the high strain rates we observe around these places are at least in part due to postseismic deformation related to these strong earthquakes (e.g., Huang et al., 2023; Ryder et al., 2007; Yamasaki and Houseman, 2012; Ryder et al., 2011; Wen et al., 2012).

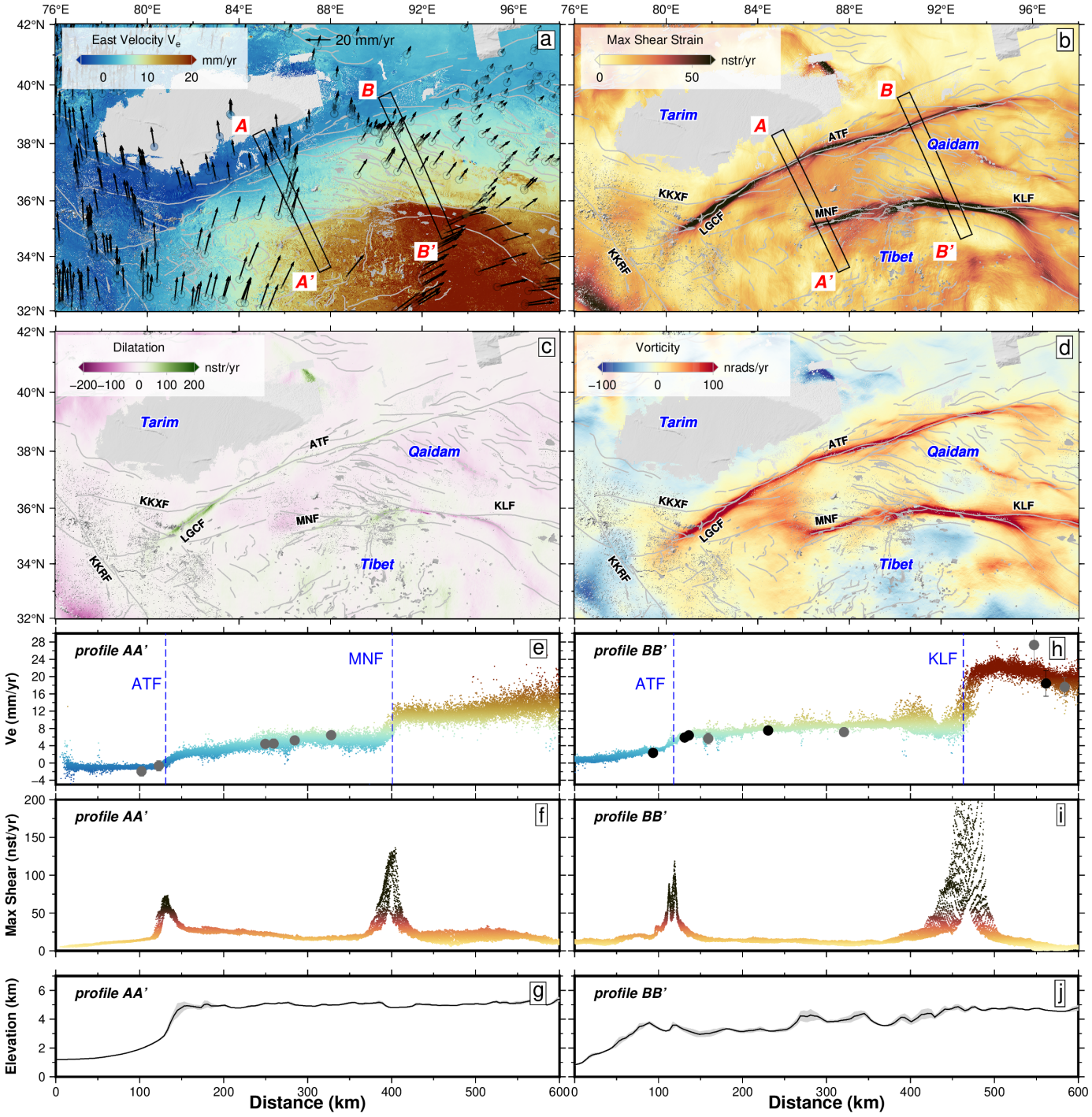


Figure S6: Velocity and strain rate maps and profiles for the region of Northern and West Tibet. (a) East Velocity. The GNSS east velocities are shown by coloured circles, and the GNSS horizontal velocities are shown by black arrows. (b) Maximum Shear strain rates. (c) Dilatation, with positive values indicating extension. (d) Vorticity, with positive indicating anti-clockwise rotation. (e–g) The eastward velocities, maximum shear strain rates and elevation for profile A–A' in (a), black and gray circles in (e) represent the east components of 3D and 2D GNSS velocities, respectively. (h-j) The eastward velocities, maximum shear strain rates and elevation for profile B–B' in (a), black and gray circles in (h) represent the east components of 3D and 2D GNSS velocities, respectively. ATF: Altyn Tagh Fault, MNF: Manyi Fault, KKXF: Karakax fault, KKRF: Karakoram fault, LGCF: Longmu-Gozha Co fault.

The dilatation rates (Figure S6c) indicate that there is distributed compression around the Altyn Tagh fault. Other regions such as the Himalayas, the Qaidam basin and the Qilian Shan–Nan Shan Thrust belt also exhibit distributed compression. This pattern is consistent with previous studies (e.g., Avouac and Tapponnier, 1993; Yin et al., 2008; Wang et al., 2024a), suggesting that these areas are the main thrust zones in western Tibet. Distributed extension (positive dilatation rates) is observed in Central Tibet (Figure S6c), which is consistent with the widely distributed N-S trending normal faults present in this region (Tapponnier et al., 1981; Wang et al., 2010). The Vorticity map (Figure S6d) can be used to show the rotation direction and rates of the crust in Western Tibet, but it will also capture the strike-slip motion along the faults. The Altyn Tagh fault and the Kunlun fault show positive vorticity rates due to the left-lateral motion of crust along them. Central Tibet exhibits a noisy pattern in the vorticity map, which may be due to the widely distributed faults and sub-blocks within the region. We can observe negative vorticity rates around the Tarim basin, supporting a clockwise rotation of the rigid Tarim that indicated by previous studies (e.g., Wang and Shen, 2020).

Vertical velocities are also given in our studies (Figure 7). Unlike the East velocities which are dominantly controlled by tectonic motion, the vertical velocities are more sensitive to non-tectonic activities such as permafrost, hydrology and anthropogenic activities (e.g., Gruber, 2012; Ou et al., 2022; Wang et al., 2024a). Moreover, the remaining phase bias (e.g., Ansari et al., 2021; Maghsoudi et al., 2022) also maps primarily into the vertical velocity field. Although the vertical velocity field is influenced by various non-tectonic sources, the long-wavelength signals in it can still reflects some tectonic activities within Western Tibet. Strong shortening and thrust motion due to India-Eurasia collision generates rapid uplift rates that we observe around Himalayas. Distributed uplifts are also observed within the Qaidam basin and the Qilian Shan–Nan Shan thrust belts, which may be controlled by the thrust motion along the active faults within them (Wang et al., 2024a).

3.7. Eastern Tibet

Eastern Tibet is a key region within the AHB, situated between the high-relief plateau interior to the west and the stable Sichuan Basin to the east, with the eastern Himalayan syntaxis and the Indo-Burma subduction zone to the south. This region is a transition zone where the internal deformation of the Tibetan Plateau is accommodated by large-scale strike-slip faulting along major faults (i.e., Haiyuan, Kunlun, and Xianshuihe Faults) and distributed off-fault deformation (Fang et al., 2024b). The driving forces behind the deformation include the ongoing convergence of India and Eurasia, active faulting resistant to deformation, and gravitational potential energy (GPE) from the high plateau topography (Houseman and England, 1986; Flesch et al., 2001; Fang et al., 2024a).

Eastern Tibet has experienced several large earthquakes, highlighting its active tectonics. Notable events include the 2008 M_w 7.9 Wenchuan (Qi et al., 2011), 2013 M_w 6.6 Lushan (Xu et al., 2013), 2017 M_w 6.5 Jiuzhaigou (Sun et al., 2018), 2021 M_w 7.4 Maduo (Fang et al., 2022a), 2021 M_w 6.1 Yangbi (Zhou et al., 2022), 2022 M_w 6.6 Menyuan (Yang et al., 2023), 2022 M_w 6.7 Luding (Guo et al., 2023), and 2025 M_w 7.9 Myanmar earthquakes.

Previous studies have quantified surface deformation and strain partitioning in eastern Tibet using GNSS and InSAR. Shen et al. (2005) derived a detailed horizontal velocity field for southeastern Tibet from GNSS. Wang and Shen (2020) updated the deformation field with higher-density GNSS networks, refining strain rate estimates. Wang et al. (2021) analyzed fault slip rates and regional kinematics from GNSS observations. More recently, InSAR time series analysis has been used to resolve interseismic strain accumulation (Qiao and Zhou, 2021; Huang and Zhou, 2022; Zhao et al., 2024; Fang et al., 2024b).

Our analysis benefits from extensive Sentinel-1 InSAR coverage in eastern Tibet. The coherence of the interferograms varies spatially, influenced by surface properties and temporal decorrelation effects. Coherence is lower in the southern part of the study area, where dense vegetation causes significant temporal decorrelation (Figure SB9), leading to relatively higher uncertainties (3-5 mm/yr) in the velocities (Figure SB15). Overall, the InSAR-derived velocities show a good fit to GNSS data, with a root mean square (RMS) difference of approximately 2 mm/yr.

The E-W velocity field reveals clear contrasts across major faults, especially creeping segments of the Haiyuan and Xianshuihe Faults, where strain localization is observed, with a peak of approximately 100 nanostrain/yr (Figure S7). This value is likely underestimated due to the Gaussian filtering applied to the east velocities, which smooths out some of the finer-scale deformation signals across the faults. Apart from these localized features, both diffuse extension across the high plateau and contraction in northeastern Tibet, not directly associated with mapped known faults, can be explained by distributed moment sources (Fang et al., 2024b). The velocity field also shows anticlockwise rotation on the major faults, while the high plateau exhibits clockwise rotation around the eastern Himalayan syntaxis (EHS) (Figure S7d), consistent with the horizontal flow revealed by GNSS observations (Figure S7a). It is important to note that the ongoing postseismic deformation from the 2008 M_w 7.9 Wenchuan earthquake has caused apparent strain concentration, contraction (Figure S7b-c), and uplifting (Figure 7c) along the Longmenshan Fault.

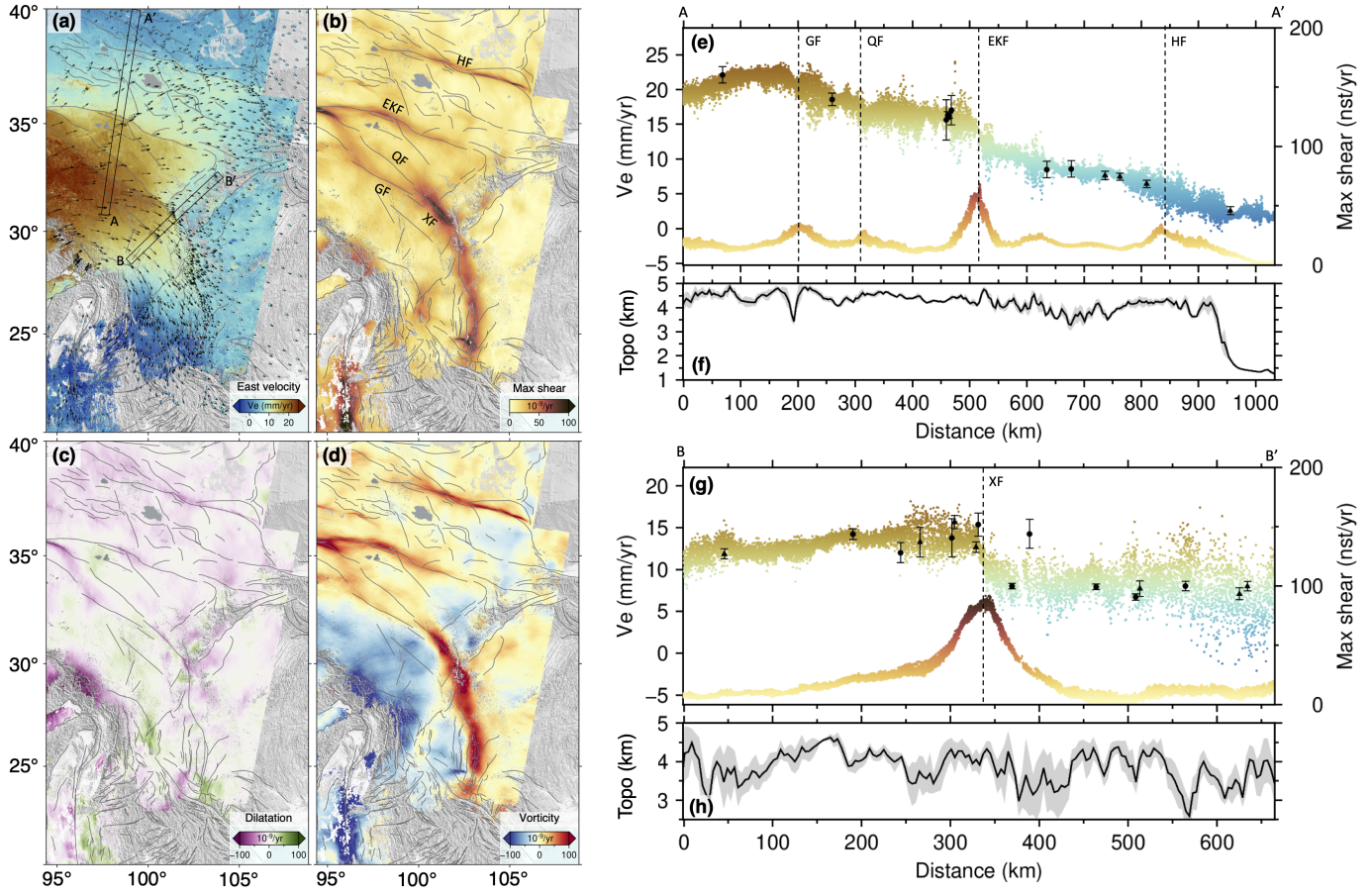


Figure S7: Velocity and strain rate maps and profiles for the region of Eastern Tibet. (a) Eastward velocity. GNSS eastward velocities are represented by coloured circles (2D sites) and triangles (3D sites). Arrows indicate horizontal GNSS velocities. The rectangle marks the location of Profiles A–A' and B-B' (20 km width), shown in (e-h). (b) Maximum shear strain rate. (c) Dilatation, with positive values indicating extension. (d) Vorticity, with positive indicating anti-clockwise rotation. (e–f) Profile A-A' through eastward velocity and maximum shear strain rate, with GNSS eastward velocities (40 km bin), faults, and topography marked on. (g-h) Profile B-B'. EKF = East Kunlun Fault, GF = Ganzi Fault, HF = Haiyuan Fault, QF = Qingshuihe Fault, XSHF = Xianshuihe Fault.

Appendix A. Supplementary Tables

Tables of GNSS studies used in point-velocity field (Tables SA1 & SA2), non-GNSS studies used in point-velocity field (Table SA3), and the list of earthquakes with coseismic effects removed in the InSAR velocity field (Table SA4).

Reference	Number of Sites	Sites Used	Region Covered	
Abbasi et al. (2023)	20	19	57.3–62.3°E	25.2–28.3°N
Ader et al. (2012)	37	6	79.9–86.9°E	6.9–32.0°N
Aktug et al. (2016)	142	128	26.7–56.2°E	26.2–39.4°N
Alothman et al. (2016)	19	18	36.1–56.1°E	16.7–33.3°N
Ashurkov et al. (2016)	12	6	103.1–127.5°E	50.3–54.0°N
Atanasova-Zlatareva (2014)	30	4	22.7–28.4°E	41.6–44.2°N
Aung et al. (2016)	8	0	–°E	–°N
Barman et al. (2017)	42	41	66.9–102.8°E	13.0–43.2°N
Bisht et al. (2021)	6	1	77.2–77.2°E	31.8–31.8°N
Bitharis et al. (2024)	212	21	20.5–27.9°E	35.2–41.3°N
Blewitt et al. (2018)	5032	438	-8.4–128.1°E	5.0–54.7°N
Bock et al. (2021)	307	72	34.6–125.4°E	6.9–54.8°N
Briole et al. (2021)	327	98	19.9–29.6°E	35.1–41.5°N
Brockmann et al. (2019)	3174	116	-4.5–27.9°E	36.0–53.3°N
Castro-Perdomo et al. (2022)	110	101	-4.0–91.1°E	9.0–52.9°N
Cheloni et al. (2014)	147	1	12.5–12.5°E	46.0–46.0°N
Choudhury et al. (2018)	1	1	72.7–72.7°E	23.2–23.2°N
Chousianitis et al. (2015)	99	98	19.8–25.4°E	36.3–41.1°N
d'Agostino et al. (2020)	343	332	1.0–31.3°E	35.1–53.9°N
Dai et al. (2023)	28	24	99.4–100.4°E	25.6–26.5°N
DeMets et al. (2020)	81	7	42.0–83.0°E	8.4–26.9°N
Devachandra et al. (2014)	19	19	66.9–114.4°E	13.0–43.8°N
Diao et al. (2019)	27	25	97.5–101.1°E	34.0–36.7°N
Dimitrov and Nakov (2022)	28	26	22.7–24.1°E	41.6–43.1°N
Duong et al. (2013)	22	22	103.0–105.3°E	20.6–22.3°N
Ergeshov et al. (2020)	6	6	60.7–71.8°E	37.5–41.5°N
Ergintav et al. (2014)	112	1	29.1–29.1°E	40.9–40.9°N
Ergintav et al. (2023)	796	720	19.5–44.0°E	33.7–43.0°N
Fang et al. (2022b)	96	91	74.1–94.4°E	13.0–34.6°N
Fazilova et al. (2018)	5	5	66.9–70.6°E	38.7–42.0°N
Fazilova et al. (2025b)	16	11	68.7–69.8°E	40.2–41.6°N
Fazilova et al. (2025a)	9	2	65.9–65.9°E	38.5–38.5°N
Floyd et al. (2023)	360	136	19.5–30.9°E	35.0–42.0°N
Frohling and Szeliga (2016)	19	4	64.4–66.6°E	26.2–29.1°N
Fu and Freymueller (2012)	25	1	85.0–85.0°E	27.2–27.2°N
Fu et al. (2020)	15	14	102.6–103.3°E	26.1–27.1°N
Gahalaut et al. (2019)	22	22	69.0–72.8°E	21.0–24.7°N
Gan et al. (2022)	501	488	95.5–107.1°E	20.6–34.0°N
Gautam et al. (2017)	6	0	–°E	–°N
Gharbia et al. (2025)	11	11	34.4–34.7°E	25.2–25.5°N
Gorshkov et al. (2023) (*LSS*)	330	201	19.9–61.0°E	41.6–55.0°N
Gorshkov et al. (2023) (*MED*)	331	191	19.9–61.0°E	41.6–55.0°N
Gupta et al. (2015)	39	0	–°E	–°N
Hamiel and Piatibratova (2021)	291	274	15.0–51.3°E	19.2–44.4°N
Hao et al. (2016)	38	2	101.5–102.2°E	25.1–28.3°N
Hao et al. (2019)	1000	969	74.3–134.3°E	18.2–53.5°N
Hao et al. (2021)	990	968	101.0–117.0°E	31.0–43.9°N
Hao et al. (2024)	177	176	99.0–112.2°E	33.6–42.3°N
Huang et al. (2023)	26	26	100.5–102.7°E	23.0–25.3°N
Jade et al. (2011)	20	0	–°E	–°N
Jade et al. (2014)	70	63	66.9–102.8°E	10.2–43.2°N
Jade et al. (2017)	80	2	78.5–93.8°E	10.7–27.6°N
Jade et al. (2020)	45	41	66.9–114.4°E	6.9–43.2°N
Jolivet et al. (2023)	39	14	32.1–33.4°E	40.7–41.0°N
Jouanne et al. (2017)	78	71	80.1–87.7°E	26.5–30.0°N
Jouanne et al. (2020)	65	64	71.6–77.5°E	31.8–36.8°N
Kadirov et al. (2014)	86	85	43.8–49.8°E	37.8–43.0°N
Kannaujiya et al. (2022)	15	9	77.6–79.6°E	29.0–30.5°N
Ghasemi Khalkhali et al. (2021)	25	18	44.2–47.7°E	37.6–39.4°N
Ghasemi Khalkhali et al. (2023a)	31	22	55.1–61.1°E	31.5–37.8°N
Ghasemi Khalkhali et al. (2023b)	10	10	55.1–62.3°E	25.3–31.3°N
Khorrami et al. (2019)	398	391	39.8–67.1°E	14.5–44.9°N
Kreemer et al. (2014)	7999	1268	-9.2–134.9°E	5.5–54.1°N
Kufner et al. (2021)	20	20	68.6–71.8°E	35.3–38.0°N
Kumar et al. (2023)	9	9	75.4–77.4°E	30.7–32.5°N
Kundu et al. (2014)	10	10	74.1–76.2°E	33.4–34.6°N
Kurt et al. (2023)	836	832	25.9–44.6°E	36.0–42.0°N
Li et al. (2017)	212	198	100.1–107.4°E	33.9–39.4°N
Li et al. (2018)	994	942	66.9–108.0°E	32.0–45.9°N
Li et al. (2021)	200	193	100.1–107.4°E	33.9–39.4°N
Li et al. (2022)	73	69	75.7–79.4°E	39.5–40.9°N
Lindsey et al. (2023)	111	74	89.5–97.7°E	16.1–25.1°N
Lukhnev et al. (2025)	95	76	89.9–114.6°E	43.1–54.9°N
Maddahi et al. (2025)	8	8	50.7–52.1°E	35.6–36.1°N
Mallick et al. (2019)	24	24	88.7–97.1°E	17.4–27.3°N
Mantovani et al. (2015)	488	20	9.8–15.1°E	37.5–45.8°N
Marechal et al. (2016)	35	15	89.4–91.5°E	26.8–28.1°N
Masson et al. (2015)	26	26	34.6–36.2°E	29.1–31.4°N
Metzger et al. (2020)	74	57	68.4–74.8°E	36.7–40.8°N
Meyer et al. (2024)	28	26	71.6–73.9°E	31.8–34.0°N
Milyukov et al. (2015)	7	2	42.5–44.7°E	43.0–43.3°N
Milyukov et al. (2022)	13	10	38.1–42.0°E	43.6–47.9°N
Mironov et al. (2021)	10	10	41.6–44.7°E	42.4–43.8°N
Mohanty et al. (2024)	32	30	76.2–80.4°E	32.5–36.0°N
Mondal et al. (2016)	14	2	78.1–80.2°E	30.1–30.3°N
Continued in the next Table...				

Table SA1: GNSS datasets used in the point-velocity field, with the number of velocities initially contributed by each study and the number retained in the final combination. The latitudinal and longitudinal ranges are the regions covered by the velocities retained here. Continued in next Table SA2.

Reference	Number of Sites	Sites Used	Region Covered	
Continued from previous Table...				
Mukul et al. (2018)	24	23	87.2–89.2°E	23.5–29.4°N
Mullick and Mukhopadhyay (2020)	51	48	86.4–92.9°E	22.1–26.5°N
Nocquet et al. (2016)	76	76	3.9–9.9°E	43.0–47.0°N
Oryan et al. (2023)	68	66	88.6–97.4°E	21.8–25.2°N
Osman Pour (*in prep.*)	57	3	51.2–51.6°E	35.9–36.1°N
Özarpacı et al. (2021)	49	26	29.4–30.4°E	40.1–40.8°N
Özbey et al. (2024)	98	91	31.1–41.4°E	29.5–40.2°N
Özdemir and Karslıoğlu (2019)	211	199	-4.0–74.7°E	30.6–52.9°N
Özkan et al. (2023)	61	21	35.5–37.0°E	35.9–37.2°N
Palano et al. (2013)	328	309	30.9–58.6°E	12.8–43.8°N
Palano et al. (2018)	835	63	35.1–62.2°E	11.5–39.8°N
Pan et al. (2019)	278	274	66.9–94.9°E	35.1–48.7°N
Pan et al. (2020)	272	265	93.0–107.0°E	34.0–40.7°N
Pan et al. (2021)	264	35	91.0–134.3°E	18.2–50.6°N
Pan et al. (2023)	52	47	66.9–89.5°E	36.4–49.8°N
Pappachen et al. (2021)	34	33	44.4–115.9°E	13.0–54.8°N
Perry et al. (2019)	79	3	70.4–71.6°E	36.7–38.7°N
Piña-Valdés et al. (2022)	3678	3524	-9.4–44.5°E	30.6–55.0°N
Pintori et al. (2022)	545	535	-0.5–20.3°E	42.4–49.8°N
Pirooznia et al. (2020)	4	3	49.6–51.3°E	36.7–37.3°N
Ponraj et al. (2019)	20	1	79.7–79.7°E	29.6–29.6°N
Porkoláb et al. (2023)	909	851	10.1–29.9°E	42.0–52.0°N
Qiao et al. (2017)	150	7	74.8–79.5°E	39.4–41.3°N
Rashwan et al. (2021)	163	151	-4.0–57.8°E	19.2–52.1°N
Ray et al. (2019)	23	23	80.5–94.5°E	23.7–30.0°N
Rudenko et al. (2013)	60	2	30.6–34.9°E	32.5–36.8°N
Rui and Stamps (2019)	1719	1098	65.8–134.3°E	10.2–53.5°N
Rui et al. (2024)	31	29	100.9–103.6°E	28.0–28.3°N
Rui et al. (2025)	276	155	101.0–104.9°E	26.1–30.0°N
Saji et al. (2020)	50	47	74.4–93.6°E	13.0–34.1°N
Saji et al. (2025)	40	39	76.9–80.6°E	28.6–31.4°N
Santamaría-Gómez et al. (2012)	69	66	-9.4–121.2°E	13.0–54.8°N
Santamaría-Gómez et al. (2024)	3686	250	-7.9–125.4°E	5.3–54.8°N
Serpelloni et al. (2013)	794	51	-6.6–35.8°E	29.5–47.2°N
Serpelloni et al. (2016)	497	464	-4.4–25.3°E	42.2–54.7°N
Serpelloni et al. (2022)	2865	264	-9.2–125.4°E	6.1–54.8°N
Sharma et al. (2020)	41	38	75.7–80.2°E	26.5–32.4°N
Sharma et al. (2021)	15	4	79.2–79.6°E	30.3–30.5°N
Shirazinejad (*in prep.*)	25	24	44.2–47.4°E	36.9–39.4°N
Shevchenko et al. (2021)	40	0	–°E	–°N
Shrungeshwara et al. (2023)	13	13	74.3–76.2°E	33.6–34.6°N
Shukurov (2020)	13	0	–°E	–°N
Singh et al. (2022)	18	18	73.9–76.2°E	32.7–34.6°N
Socquet and Janex (2019)	978	1	2.4–2.4°E	44.7–44.7°N
Sokhadze et al. (2018)	70	52	40.3–104.3°E	22.2–52.2°N
Steckler et al. (2016)	53	52	66.9–114.4°E	13.0–52.2°N
Steffen et al. (2025)	2061	1960	-9.4–44.0°E	30.6–55.0°N
Su et al. (2018)	58	47	100.1–109.3°E	33.3–38.6°N
Suribabu et al. (2022b)	8	7	69.2–70.1°E	23.1–23.2°N
Suribabu et al. (2022a)	4	4	69.0–72.0°E	21.0–22.3°N
Timofeev et al. (2024)	15	14	81.2–91.1°E	29.7–54.8°N
Vardić et al. (2022)	154	17	36.1–125.4°E	6.9–52.2°N
Verma et al. (2024)	22	13	78.9–79.8°E	29.1–29.7°N
Vila (2020)	70	24	73.8–94.8°E	13.0–28.2°N
Vilayev et al. (2017)	10	9	76.0–78.4°E	43.0–43.9°N
Viltres et al. (2020)	33	33	38.1–45.0°E	11.6–19.2°N
Viltres et al. (2022)	189	173	34.7–58.2°E	9.0–36.2°N
Wang et al. (2022b)	618	610	97.5–106.4°E	21.1–34.0°N
Wang et al. (2017a)	29	5	115.8–118.3°E	38.5–41.0°N
Wang et al. (2017b)	1846	1744	65.8–120.8°E	10.2–49.9°N
Wang and Shen (2020)	2489	2450	-4.0–134.3°E	13.0–54.8°N
Wang et al. (2020)	524	521	73.5–98.9°E	34.4–44.0°N
Wang et al. (2022a)	881	431	107.3–124.0°E	28.1–41.9°N
Wang et al. (2024b)	547	527	67.0–121.9°E	24.7–48.8°N
Wang et al. (2018)	2	2	51.3–51.3°E	35.7–35.7°N
Wang et al. (2024a)	95	77	85.5–99.1°E	35.4–41.9°N
Wani et al. (2025)	13	13	74.0–76.2°E	33.0–34.6°N
Wu et al. (2024a)	316	290	99.0–110.1°E	32.2–40.5°N
Xiong et al. (2021)	1985	1945	74.3–134.3°E	18.2–53.5°N
Yadav et al. (2019)	34	33	78.0–82.2°E	28.7–31.0°N
Yadav et al. (2021)	7	0	–°E	–°N
Yavasoglu et al. (2021)	51	2	28.2–29.3°E	41.0–41.1°N
Younes (2023)	48	21	31.1–34.3°E	23.3–31.3°N
Zhang et al. (2021)	151	139	75.4–98.7°E	20.8–34.8°N
Zhao et al. (2017)	723	663	103.1–117.0°E	32.0–43.9°N
Zhao et al. (2023)	857	331	74.3–110.3°E	18.2–48.7°N
Zheng et al. (2017)	1623	1562	66.9–134.3°E	18.2–54.8°N
Zhou et al. (2016)	152	144	56.1–121.2°E	13.0–52.2°N
Zhou et al. (2023)	25	25	102.6–103.5°E	25.5–27.1°N
Zubovich et al. (2016)	4	4	72.2–72.3°E	39.4–39.6°N

Table SA2: Continued from Table SA1. GNSS datasets used in the point-velocity field, with the number of velocities initially contributed by each study and the number retained in the final combination. The latitudinal and longitudinal ranges are the regions covered by the velocities retained here.

Reference	Number of Sites	Sites Used	Region Covered	
Altamimi et al. (2016) (DORIS)	24	0	–°E	–°N
Altamimi et al. (2016) (SLR)	34	3	-4.5–121.4°E	31.2–48.4°N
Altamimi et al. (2016) (VLBI)	83	5	20.7–82.2°E	35.4–51.3°N
Dal Zilio et al. (2020) (Levelling*)	92	90	85.0–86.0°E	27.3–28.0°N
Wu et al. (2024a) (Levelling)	316	290	99.0–110.1°E	32.2–40.5°N

Table SA3: Levelling and non-GNSS datasets used in the point-velocity field, with the number of velocities initially contributed by each study and the number retained in the final combination. DORIS - Doppler Orbitography and Radiopositioning Integrated by Satellite. SLR - Satellite Laser Ranging. VLBI - Very Long Baseline Interferometry. *Originally from Jackson and Bilham (1994).

Date	Magnitude M_W	Epicentre °E, °N	Country	Timeseries Mitigation
06/02/2023	7.8	37.014, 37.226	Kahramanmaraş, Türkiye/Syria	Ended time-series early
12/11/2017	7.3	45.959, 34.911	Ezgeleh-Sarpolzahab, Iran	Started time-series late
21/05/2021	7.3	98.251, 34.598	Maduo, China	Ended time-series early
30/10/2020	7.0	26.784, 37.897	Aegean Sea, Greece-Türkiye	Solve for coseismic offset
22/01/2024	7.0	78.654, 41.256	Kyrgyzstan-China	Ended time-series early
23/02/2023	6.9	73.229, 38.055	Tajikistan	Solve for coseismic offset
25/10/2018	6.8	20.557, 37.520	Greece	Solve for coseismic offset
24/01/2020	6.7	39.061, 38.431	Elazığ, Türkiye	Solve for coseismic offset
30/10/2016	6.6	13.096, 42.862	Norcia, Italy	Started time-series late
25/11/2016	6.6	73.978, 39.273	Pamir	Started time-series late
07/01/2022	6.6	101.29, 37.828	China	Solve for coseismic offset
05/09/2022	6.6	102.236, 29.679	China	Solve for coseismic offset
08/08/2017	6.5	103.855, 33.193	China	Solve for coseismic offset
26/06/2016	6.4	73.339, 39.479	Pamir	Started time-series late
17/11/2017	6.4	94.984, 29.8333	China	Solve for coseismic offset
29/12/2020	6.4	16.257, 45.424	Croatia	Solve for coseismic offset
26/11/2019	6.4	19.526, 41.514	Albania	Solve for coseismic offset
14/11/2021	6.4	56.072, 27.727	Iran	Solve for coseismic offset
25/11/2018	6.3	45.744, 34.361	Iran-Iraq	Solve for coseismic offset
08/08/2017	6.3	82.832, 44.302	Tian Shan	Solve for coseismic offset
22/07/2020	6.3	86.864, 33.143	Tibetan Plateau	Solve for coseismic offset
07/10/2023	6.3	61.926, 34.5982	Herat, Afghanistan	Ended time-series early
25/06/2020	6.3	82.416, 35.595	Tibetan Plateau	Solve for coseismic offset
03/03/2021	6.3	22.176, 39.755	Greece	Solve for coseismic offset
05/04/2017	6.1	60.436, 35.776	Iran	Solve for coseismic offset
01/12/2017	6.1	57.307, 30.746	Iran	Solve for coseismic offset
21/05/2021	6.1	100.008, 25.727	China	Solve for coseismic offset
23/11/2022	6.1	30.983, 40.836	Türkiye	Solve for coseismic offset
19/01/2020	6.0	77.108, 39.835	China	Solve for coseismic offset

Table SA4: List of earthquakes with potential impact on the velocity field and strain rates, and the approach used to mitigate the effect. Earthquake moment magnitudes and epicentral locations from the USGS are given. Full information on the impacted frames is given in Supplementary Material. Note that any major aftershocks of these events will also be accounted for in the mitigation process when truncating the time series. Locations of earthquakes and moment tensors are shown in Figure SB16.

Appendix B. Supplementary Appendix Figures

Supplementary figures showing the GNSS velocities in the ITRF14 reference frame and levelling points (Figure SB1, c.f. Figure 1 of the main paper) and the distribution of SAR data acquired in the ascending and descending direction (Figure SB2). The thinning of the GNSS velocities with subsequent quality control steps is shown in Figures SB3–SB6 (c.f. the final dataset used (Figure 3 of the main paper). Noise contributions to the InSAR data due to the atmosphere noise are shown for the ionospheric component (Figure SB7) and for the troposphere (Figure SB8), along with the solid earth tide. Quality control metrics of the output data from the timeseries analysis across the whole Alpine Himalayan belt are illustrated with the average coherence (Figure SB9 and for the estimated average absolute phase bias (Figure SB13).

The corrections applied to the velocity on a frame by frame basis are calculated for the tropospheric contributions to the troposphere by GACOS (Figure SB10), the ionosphere (Figure SB11), and from the Solid Earth Tide (Figure SB12). The plate motion correction applied to the average velocities is shown in Figure SB14. The set of earthquakes used to correct for offsets in the time series is in Figure SB16 and the mesh used to generate the velocity field in Figure SB18. Prior to referencing the velocities for each of the frames using VELMAP (Figure 6 of the main paper), the individual velocities are all relative to a local reference point and also contain some long-wavelength errors (Figure SB17).

The scaled uncertainties from the LiCSBAS time series and the formal uncertainties of the resulting decomposed east and vertical velocities are shown in Figure SB15 with those estimated by the VELMAP procedure in Figure SB21. Figure SB19 shows the filtered eastward component of velocity used for strain rate calculations. Uncertainty analysis is performed on the overlapping areas of the InSAR coverage (Figure SB20) where the redundant data can be used for independent estimates on uncertainty (Figure SB22).

Comparisons are made between the GNSS/levelling data and the InSAR-derived east and vertical velocities (Figure SB23), as well as with the European Ground Motion Service velocities (Figures SB30 and SB31). Comparison between the InSAR and GNSS/levelling estimates over different regional areas are given for Europe (Figure SB24), Anatolia (Figure SB25), Pamir and Tian Shan (Figure SB26) and (Figure SB27).

For visual comparison with our strain rate field (Figure 9 of the main paper) we show at the same extent and colourscale that form the Global Strain Rate Map (Figure SB28). To indicate what the InSAR adds to the result, we show how strain rate field differs with GNSS only data (Figure SB32 and Figure SB29).

Finally, we show the various contribution that InSAR and GNSS observations can make to the disaster irks management cycle (Figure SB33), and show an example of a very long period inteferogram formed from one of the earliest Sentinel-1A and 1C acquisitions made over a coherent area of South America (Figure SB34).

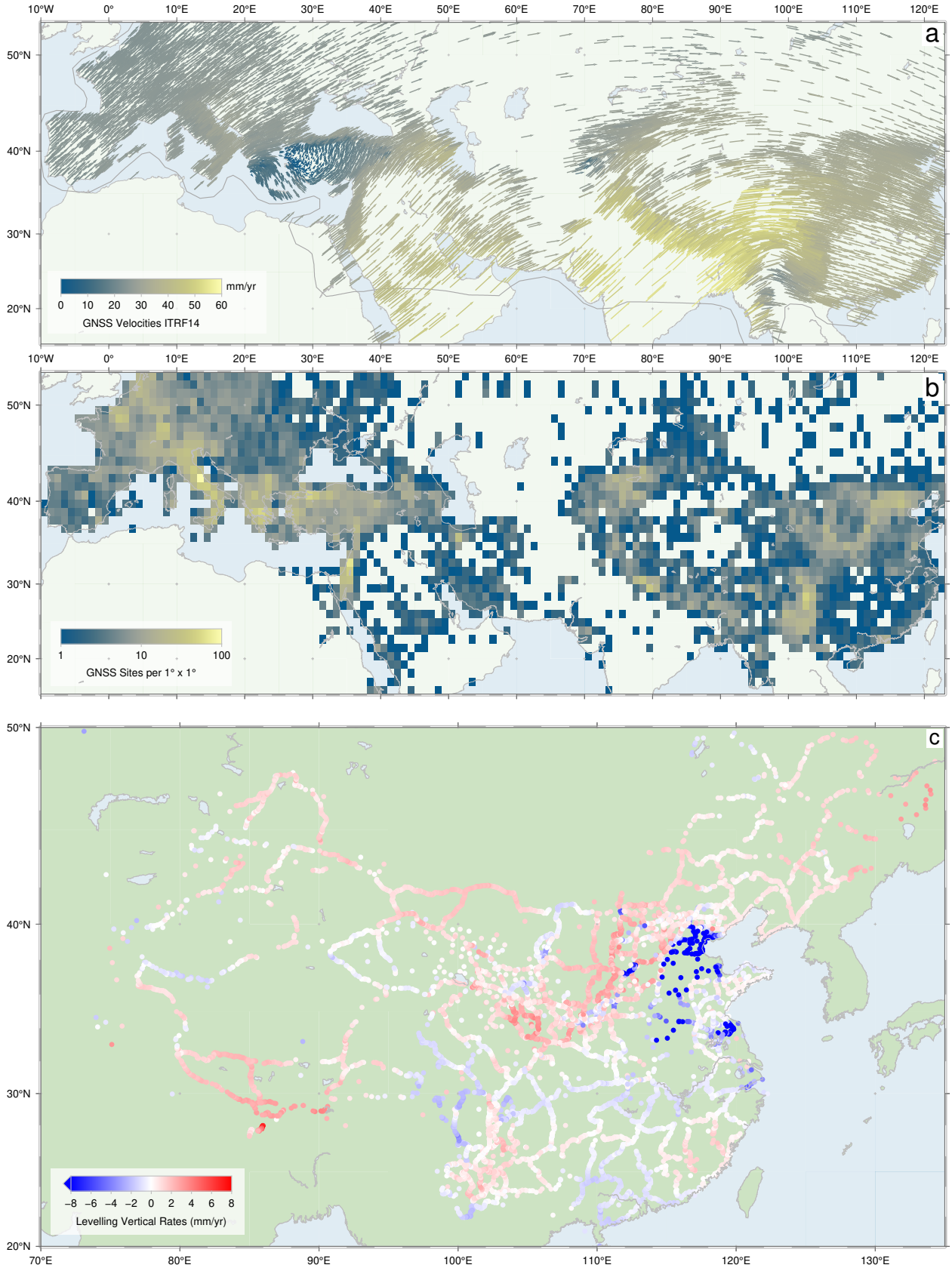


Figure SB1: (a) Compiled and aligned GNSS velocities with respect to ITRF14 (Altamimi et al., 2017). The dark grey polygon denotes the coverage area for the combined InSAR-GNSS velocity field for the mesh shown in Figure SB18. (b) Number of GNSS sites per one degree cell (note logarithmic scale). (c) Levelling vertical rates (Table SA3) from (Dal Zilio et al., 2020; Wu et al., 2024b).

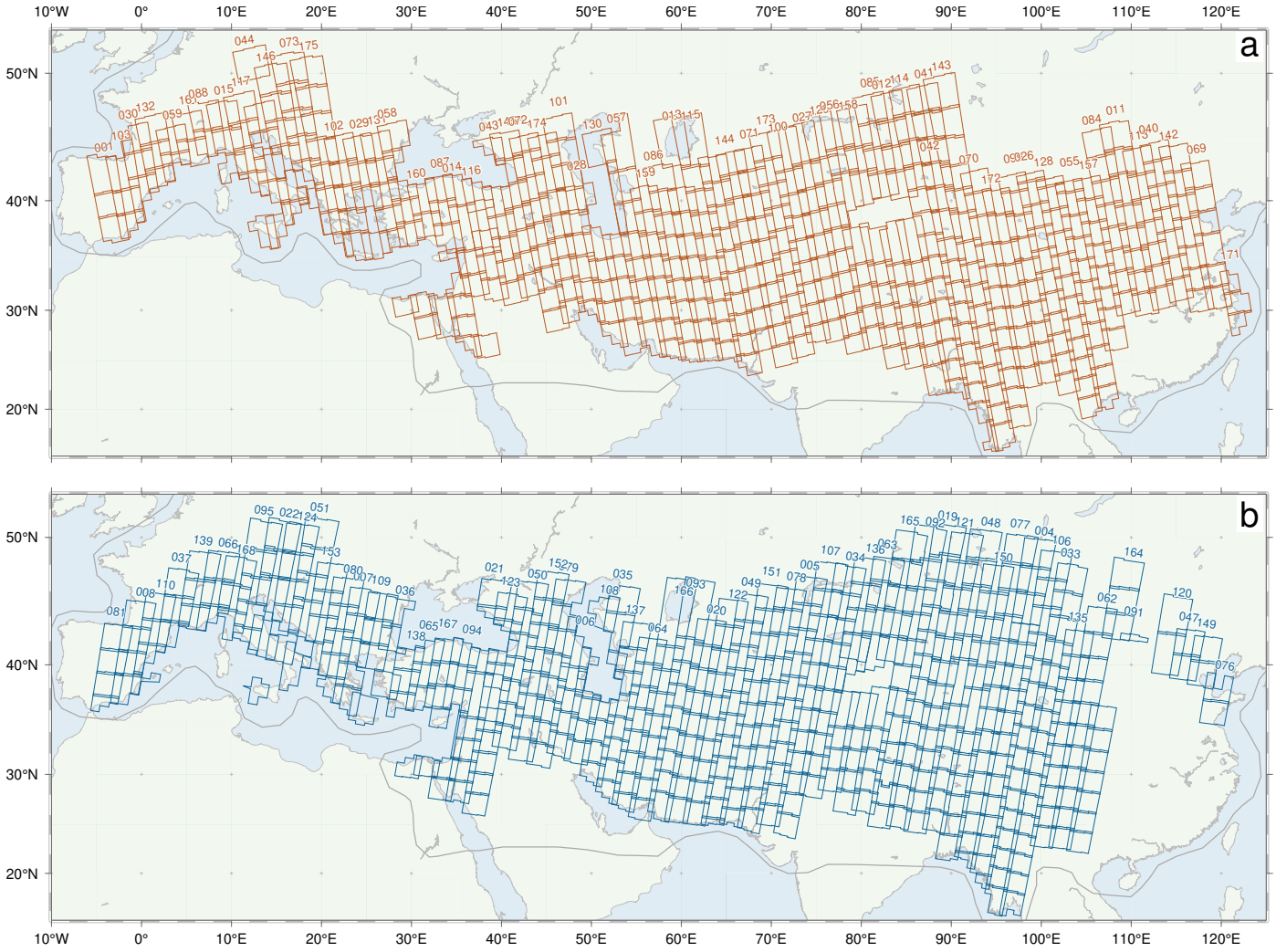


Figure SB2: Sentinel-1 data coverage from frames defined within the LiCSAR system on (a) ascending (brown) and (b) descending (blue) track directions (track/path numbers at the northern end of each track are the relative orbit numbers, 1–175). Each frame typically consists of 13 bursts on each of the 3 subswaths with one burst overlap with adjacent along track frames. Frames near coasts or at the edges of the area of interests will have differing number of bursts. The dark grey polygon denotes the coverage area for the combined InSAR-GNSS velocity field mesh.

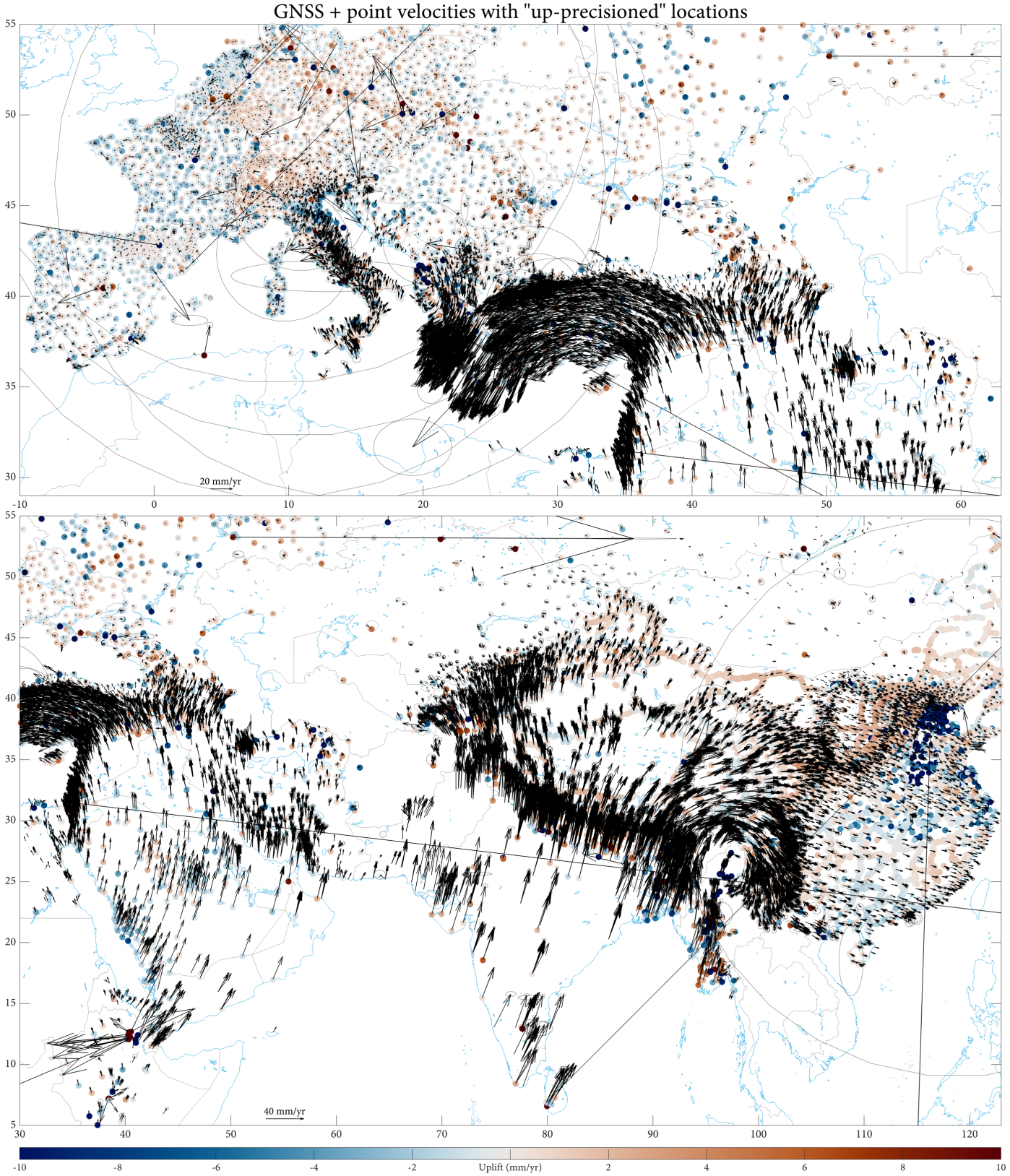


Figure SB3: The GNSS and other point velocities compiled from the published literature (Table SA1), in the western AHB (top) and eastern AHB (bottom), after “up-precisioning" of station locations. Arrows show horizontal motions with respect to the ITRF2014 Eurasia-fixed reference frame (Altamimi et al., 2017). Coloured circles denote the uplift rate for sites with a vertical component.

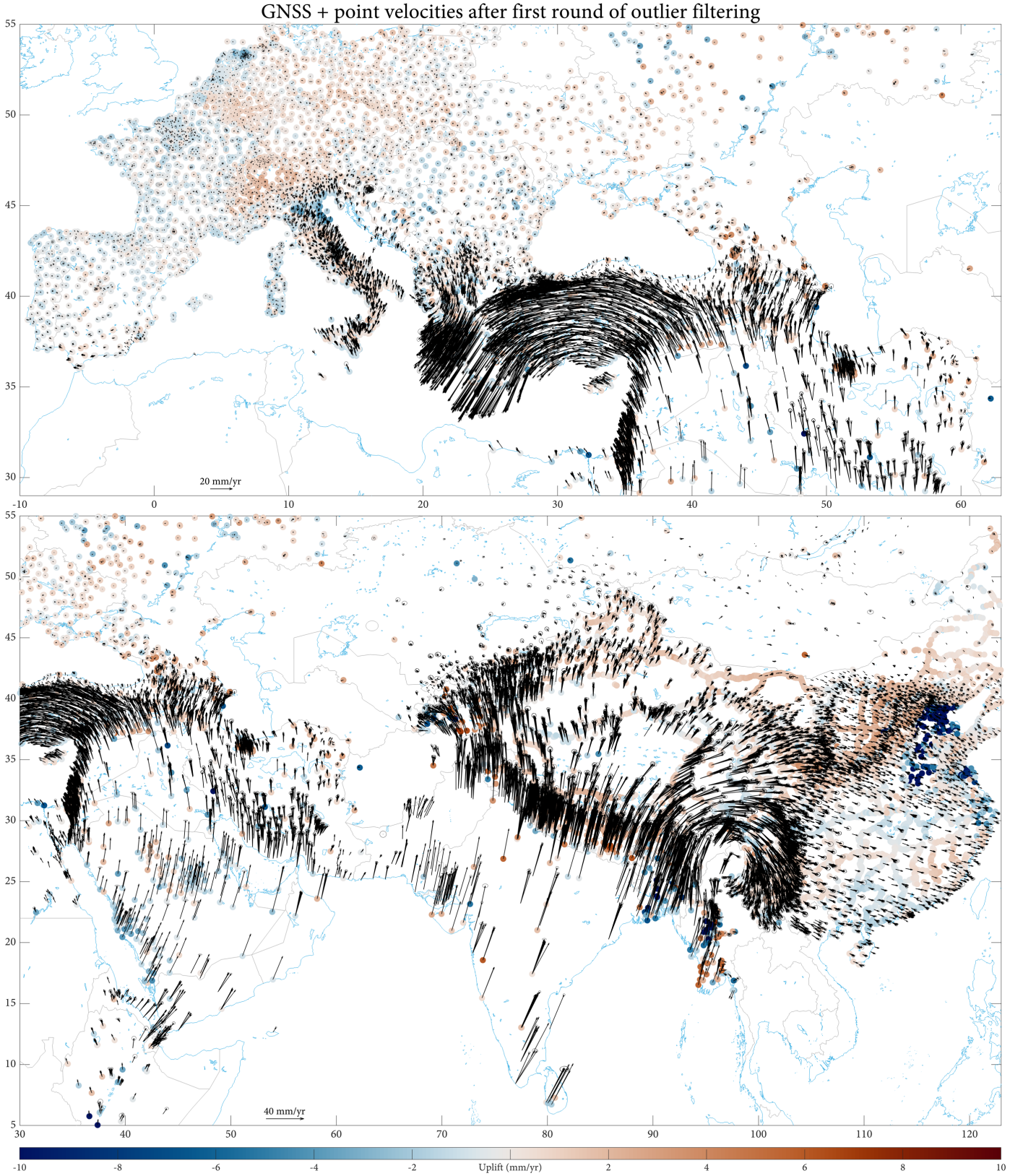


Figure SB4: The GNSS and other point velocities remaining from Figure SB3, in the western AHB (top) and eastern AHB (bottom), after the first round of removal of outliers. Arrows show horizontal motions with respect to the ITRF2014 Eurasia-fixed reference frame (Altamimi et al., 2017). Coloured circles denote the uplift rate for sites with a vertical component.

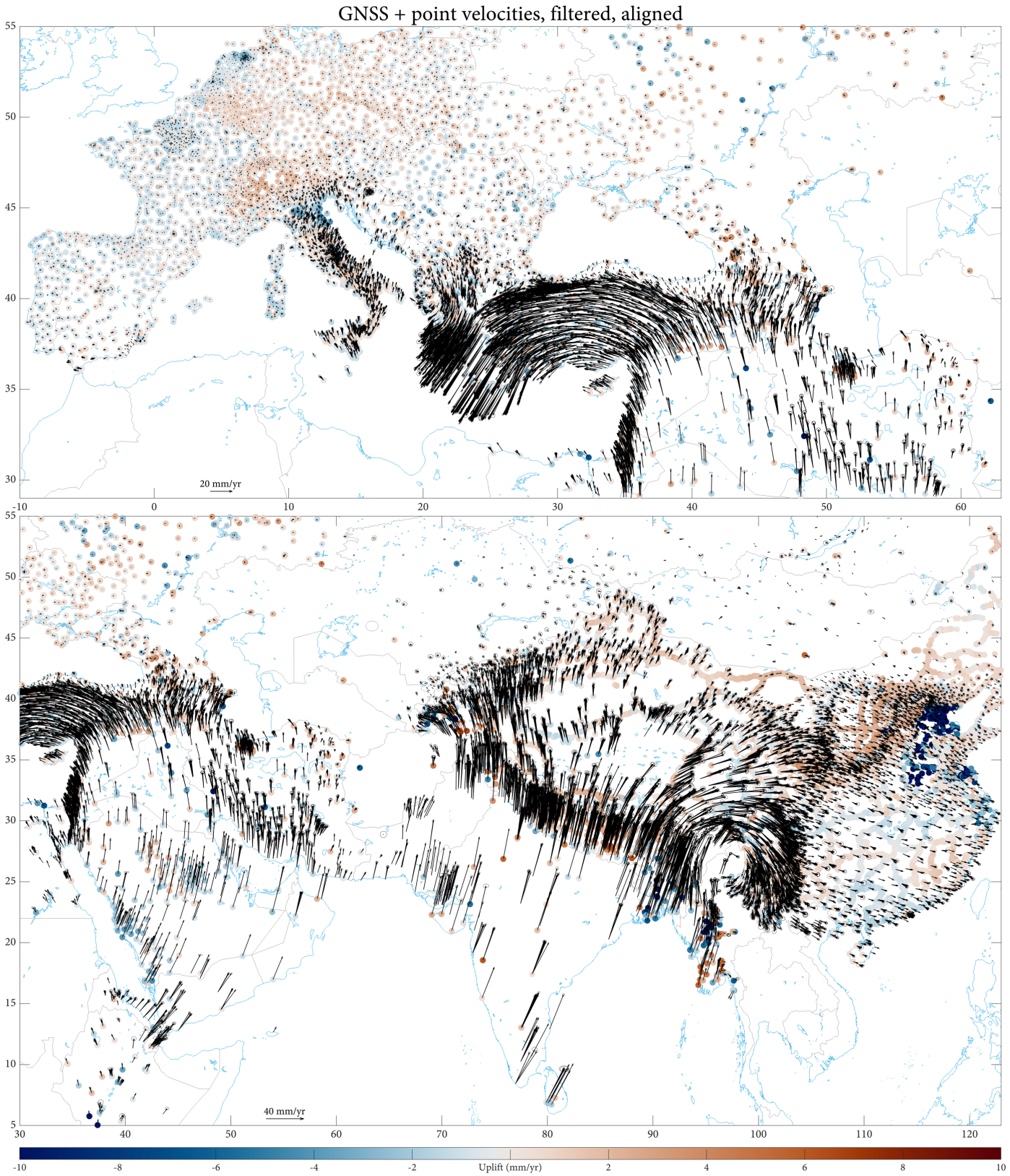


Figure SB5: The GNSS and other point velocities remaining from Figure SB4, in the western AHB (top) and eastern AHB (bottom), after the alignment step (iterative removal of systematic differences via best-fit Euler-pole rotations). Arrows show horizontal motions with respect to the ITRF2014 Eurasia-fixed reference frame (Altamimi et al., 2017). Coloured circles denote the uplift rate for sites with a vertical component.

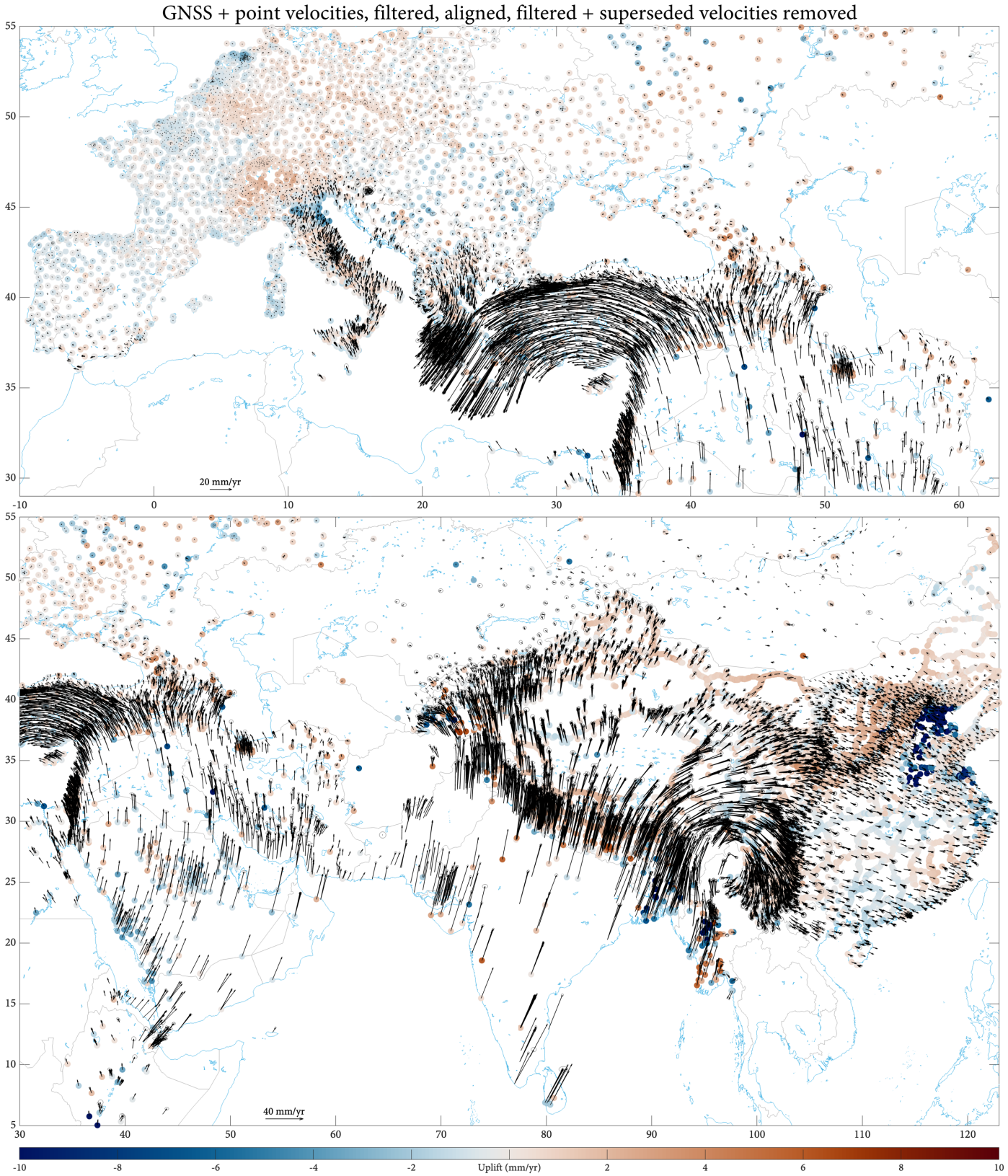


Figure SB6: The GNSS and other point velocities, remaining from Figure SB5, in the western AHB (top) and eastern AHB (bottom), after the second round of outlier removal and the removal of superseded and duplicate velocities. Arrows show horizontal motions with respect to the ITRF2014 Eurasia-fixed reference frame (Altamimi et al., 2017). Coloured circles denote the uplift rate for sites with a vertical component.

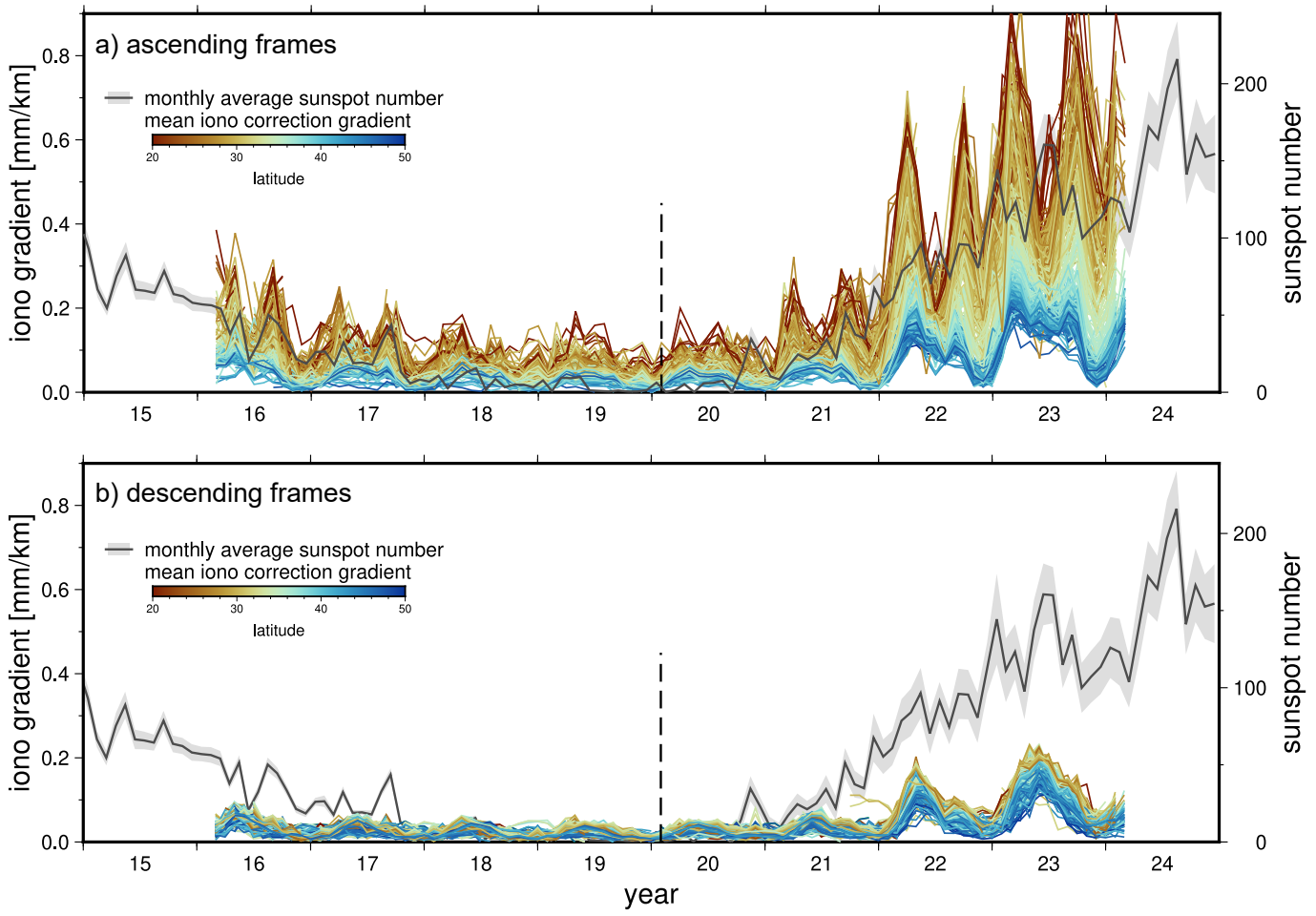


Figure SB7: Ionosphere gradient corrections for the ascending (top) and descending (bottom) frames in their monthly averages, coloured by latitude, plotted with the timeline of sunspot numbers through cycle 24 and 25 (2014–2024). Sunspot data from the World Data Center SILSO, Royal Observatory of Belgium, Brussels (Clette and Lefèvre, 2015). The correction gradients are calculated as mean absolute gradients in the direction of maximum gradient per temporal epoch w.r.t. nearest epoch to the 2020-02-01 (vertical dashed line).

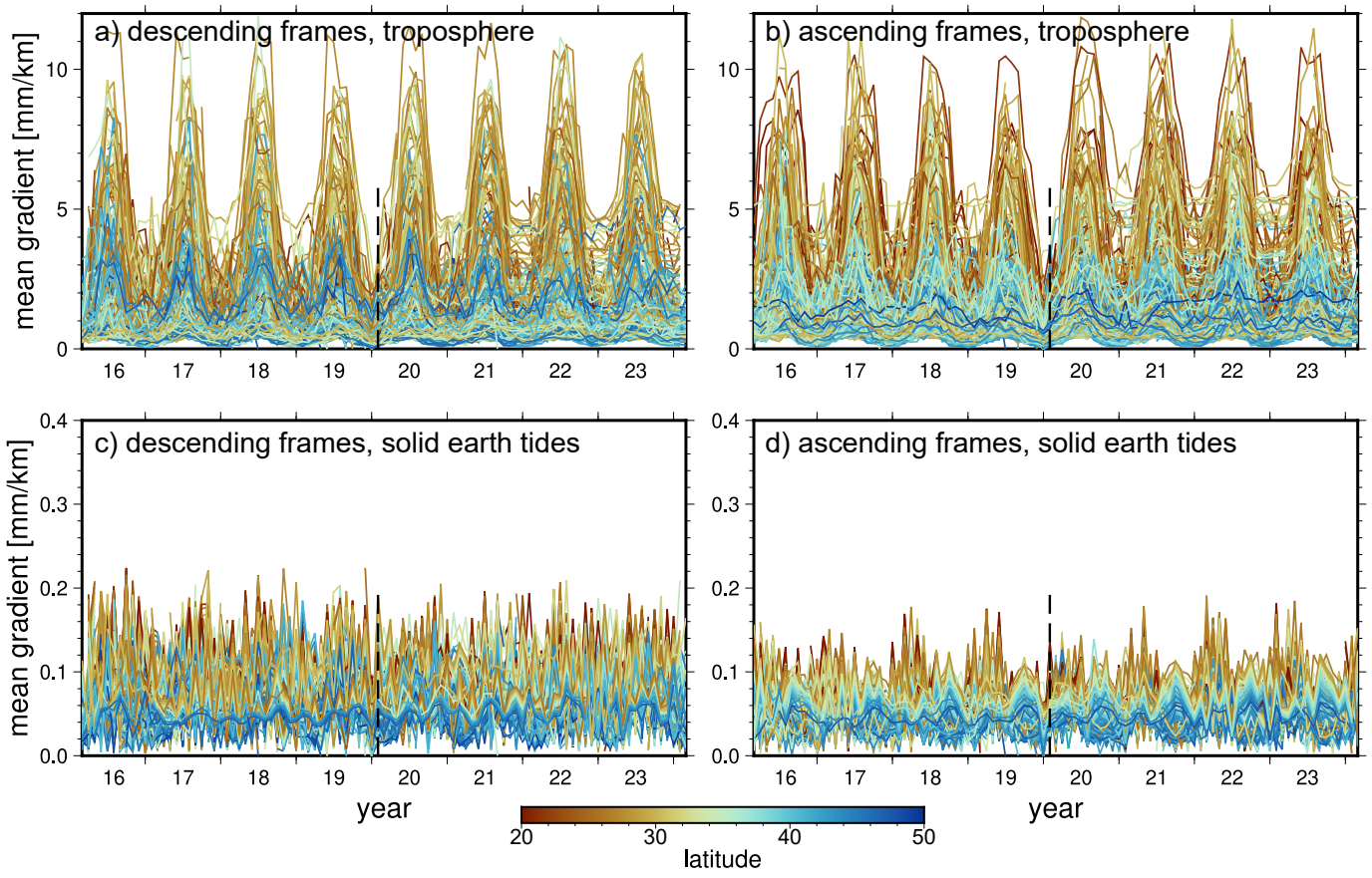


Figure SB8: Troposphere (top) and solid earth tide (bottom) gradient corrections for the descending (left) and ascending (right) frames. The correction gradients are calculated as mean absolute gradients in the direction of maximum gradient per temporal epoch w.r.t. nearest epoch to the 2020-02-01 (vertical dashed line).

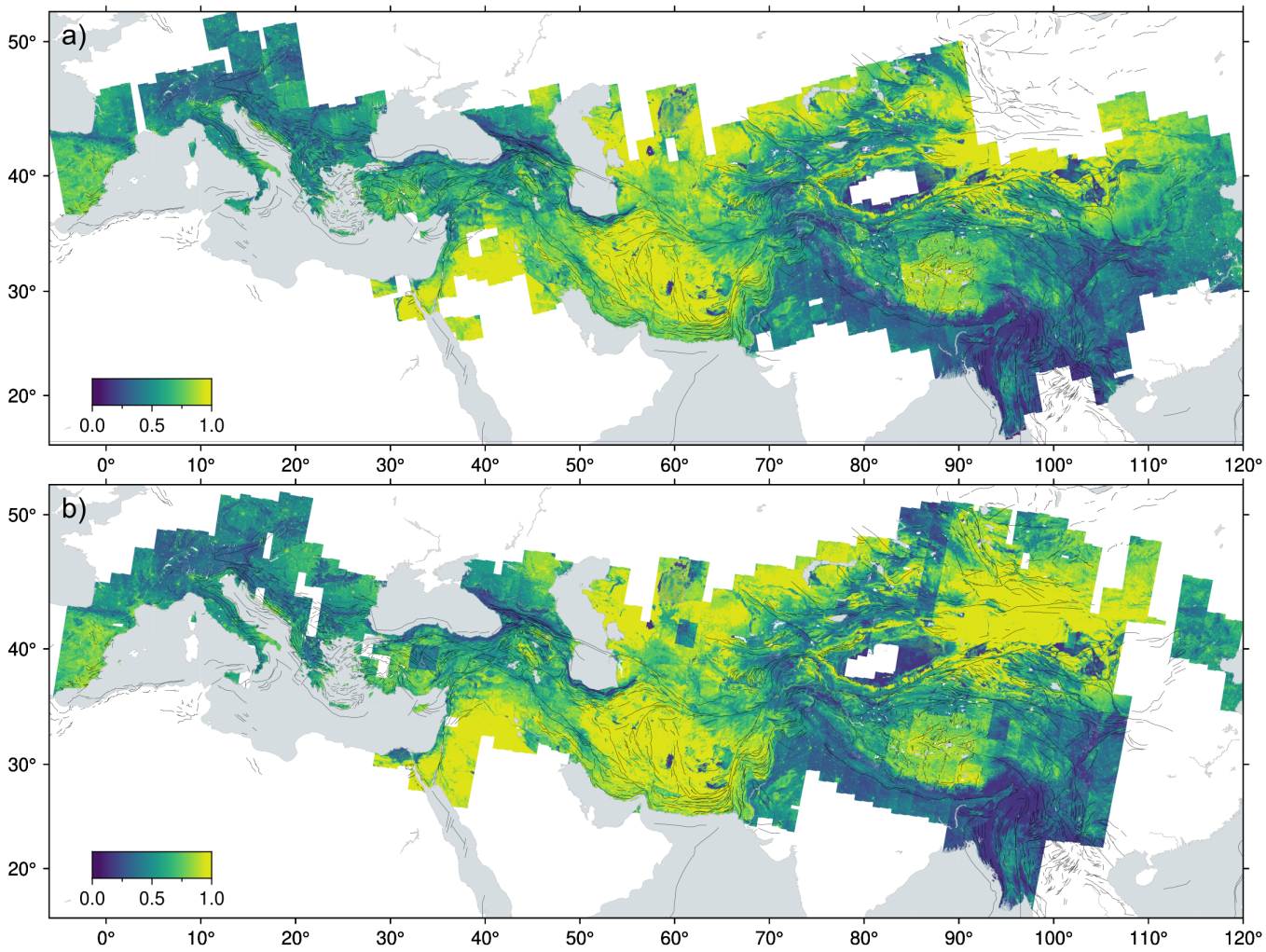


Figure SB9: Average coherence calculated for frames in a) ascending and b) descending directions.

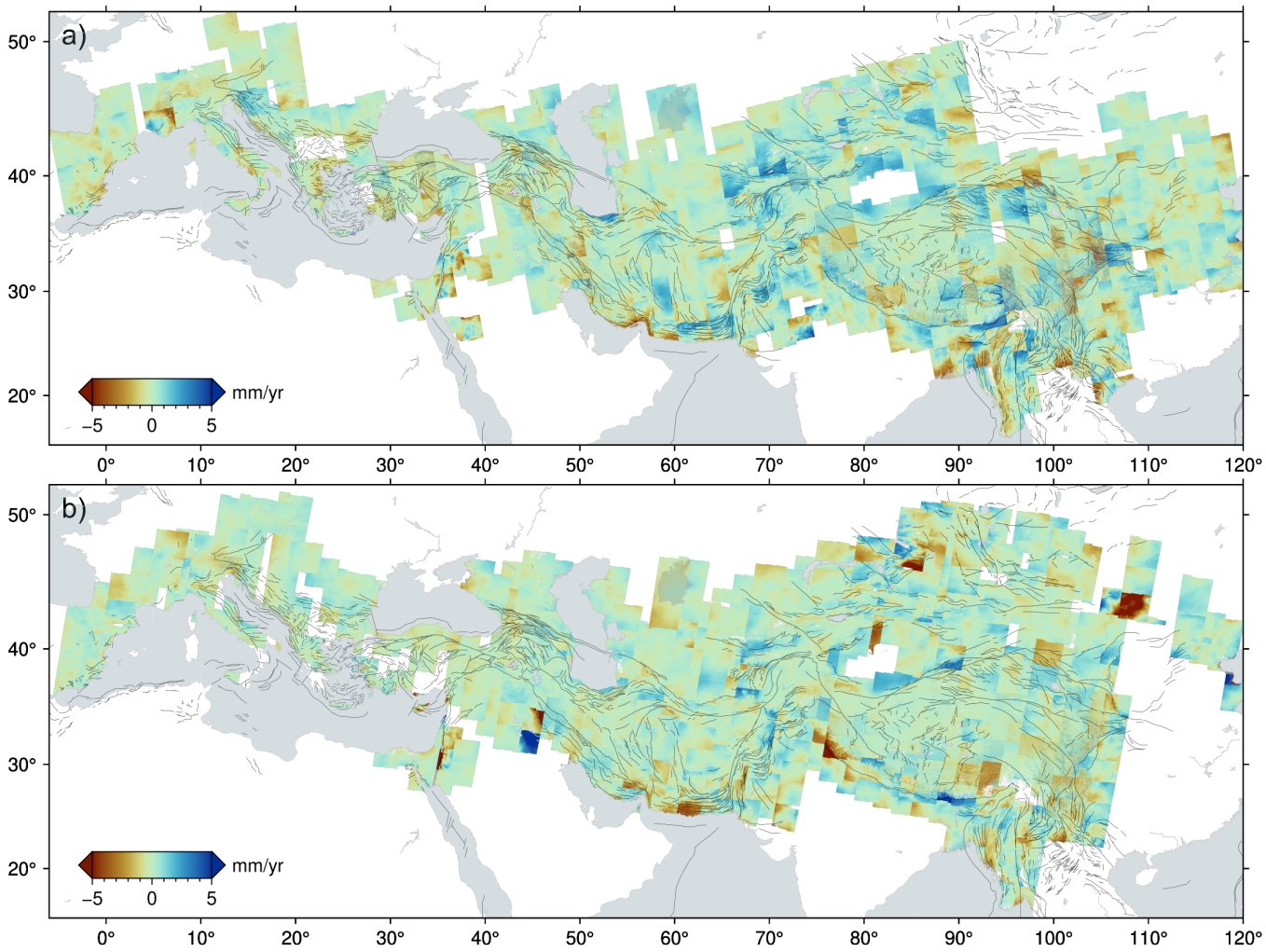


Figure SB10: GACOS troposphere correction frame by frame example in the (a) ascending and (b) descending directions.

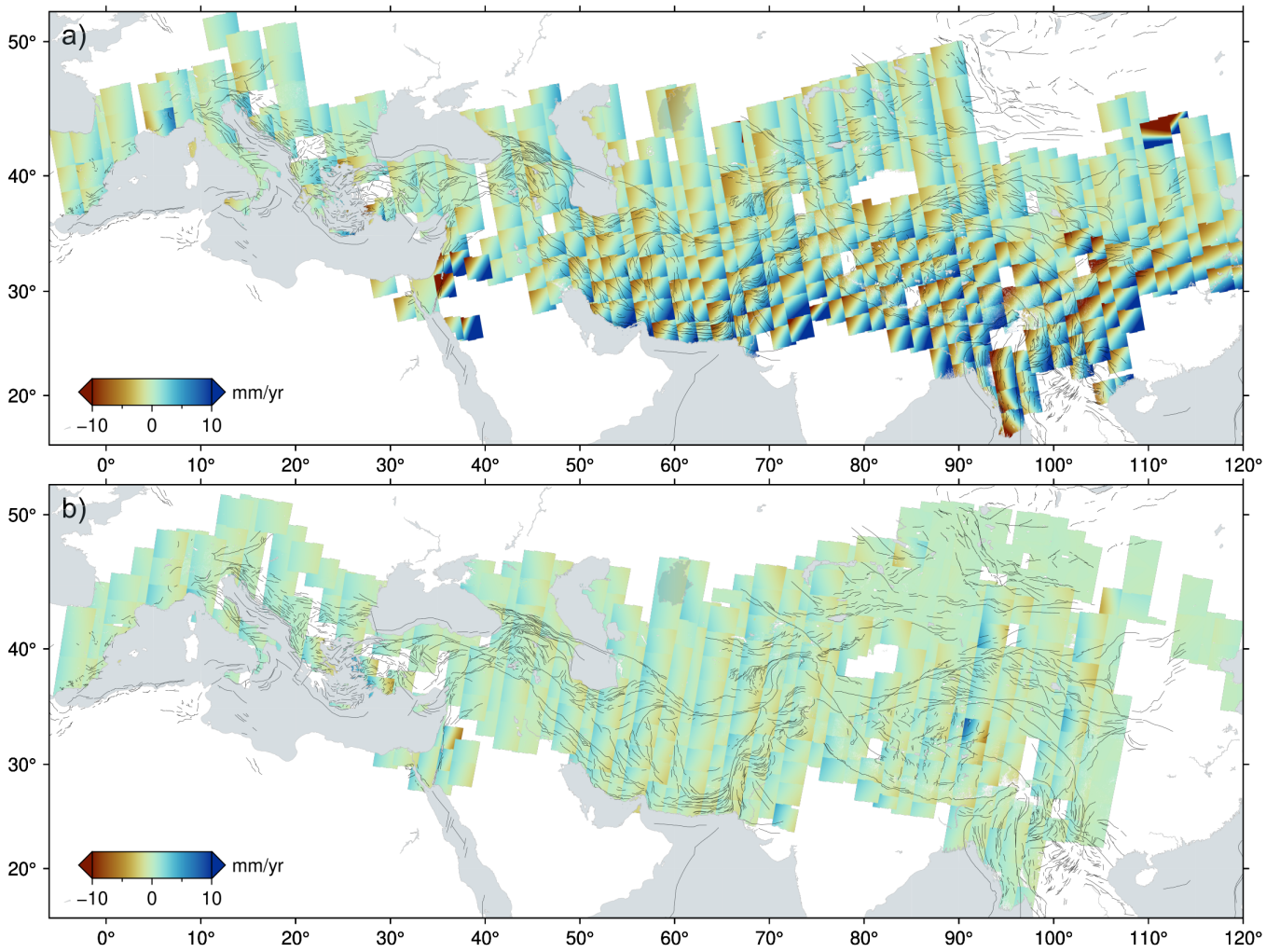


Figure SB11: Ionosphere correction frame by frame example in the (a) ascending and (b) descending directions.

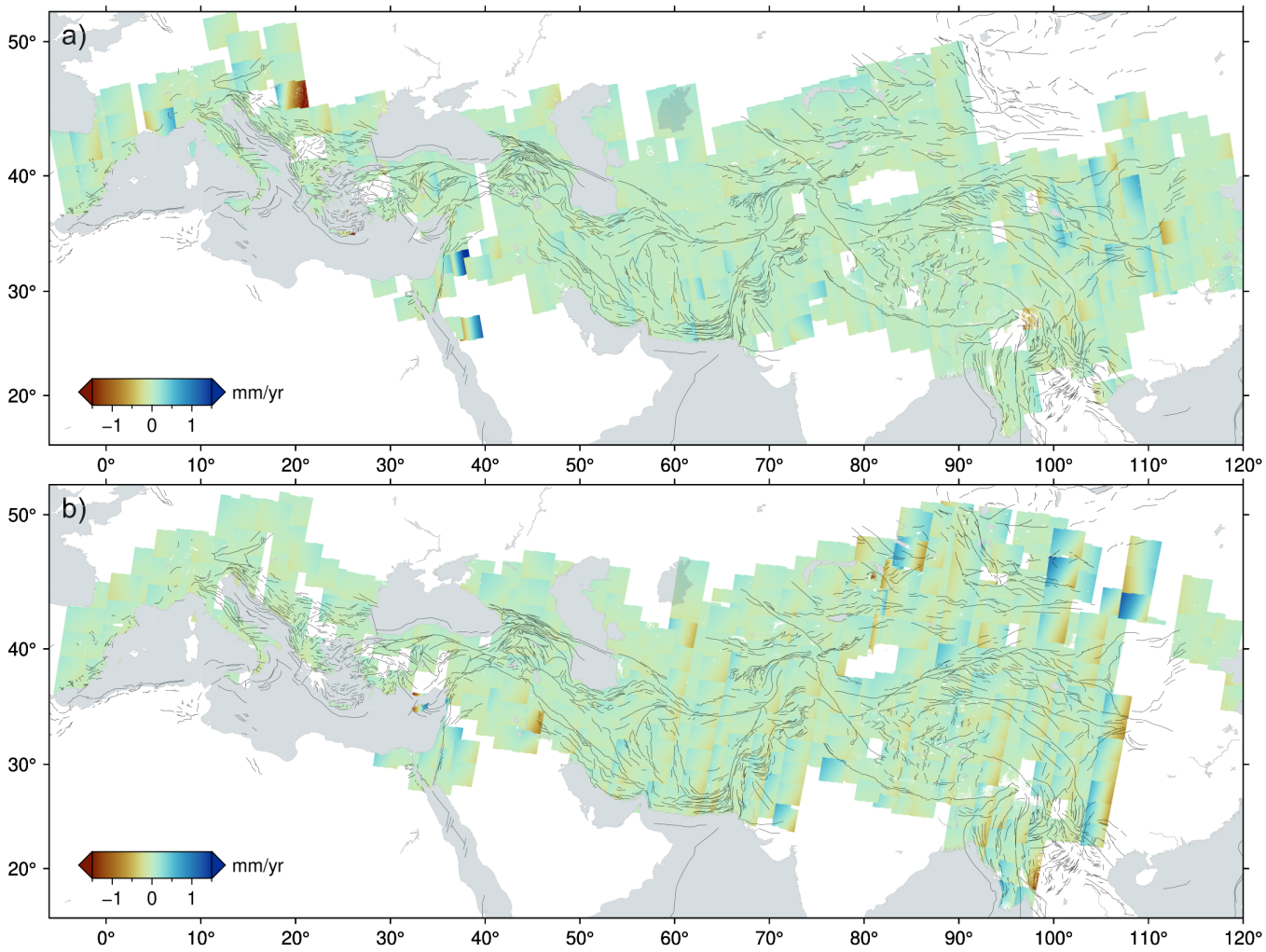


Figure SB12: Solid Earth Tide correction frame by frame example in the (a) ascending and (b) descending directions.

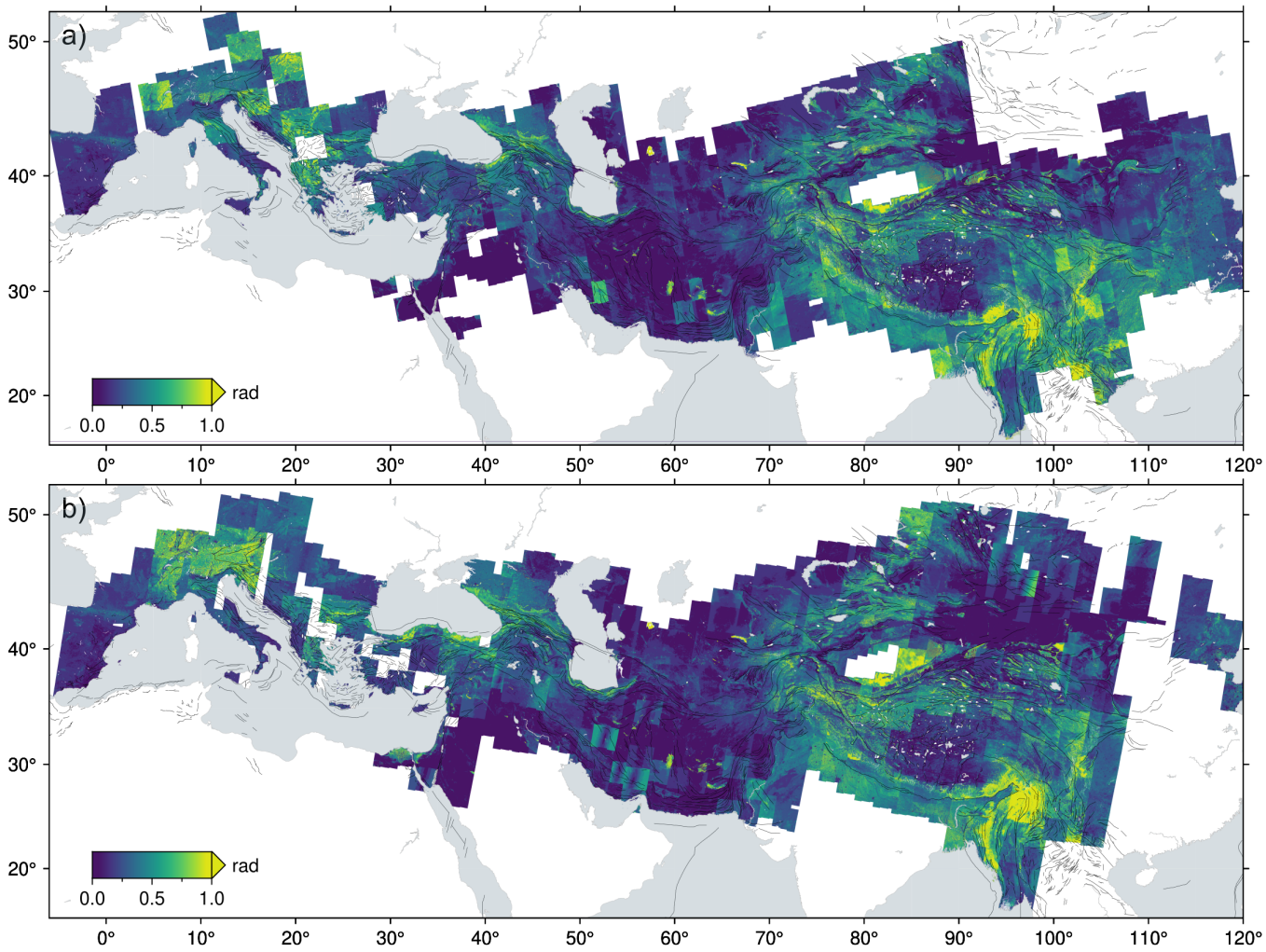


Figure SB13: Average absolute phase bias (rad) as calculated for frames in a) ascending and b) descending directions.

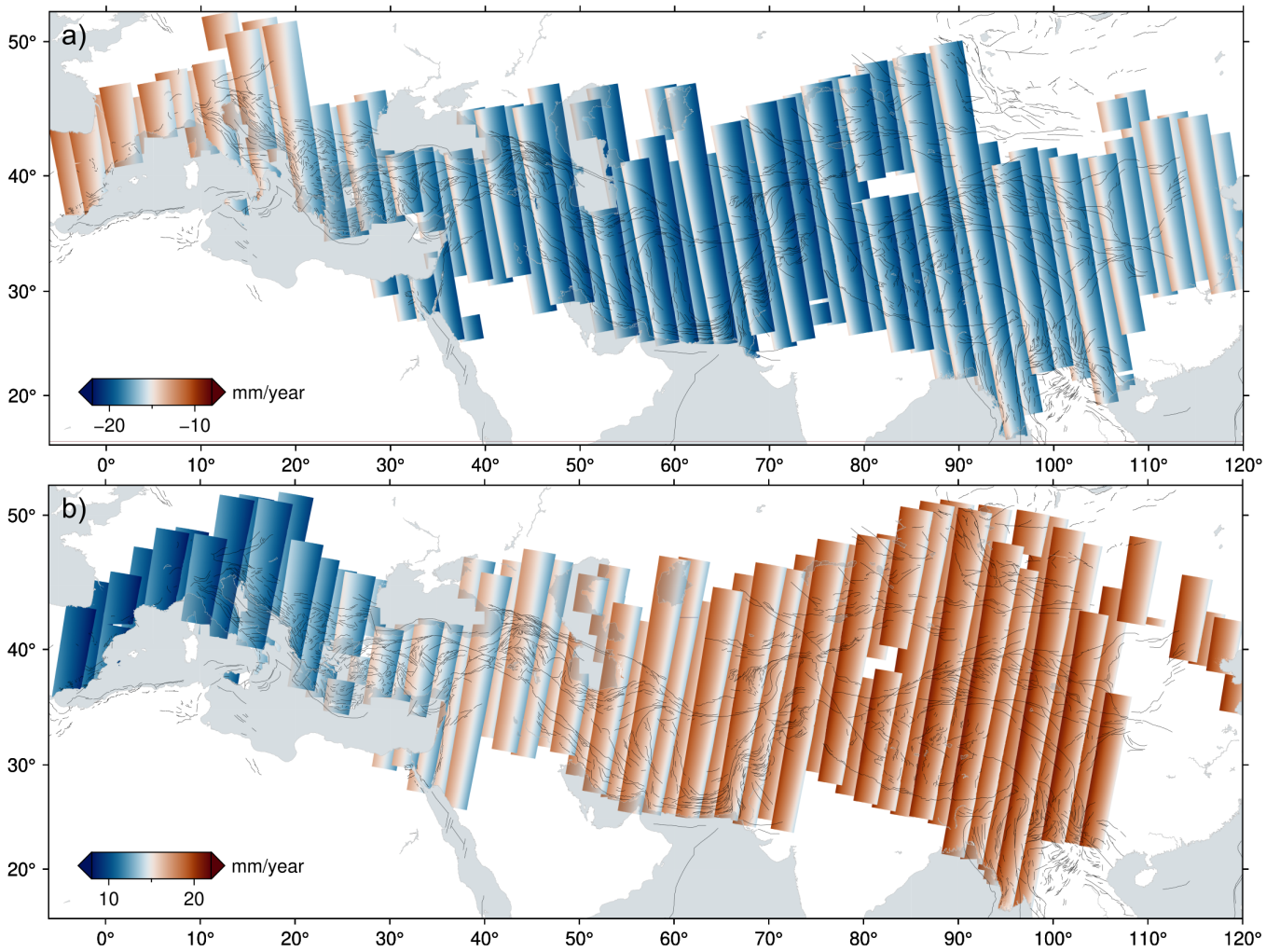


Figure SB14: Plate motion correction to the line of sight average velocities (mm/yr) for the tracks in the a) ascending and b) descending directions.

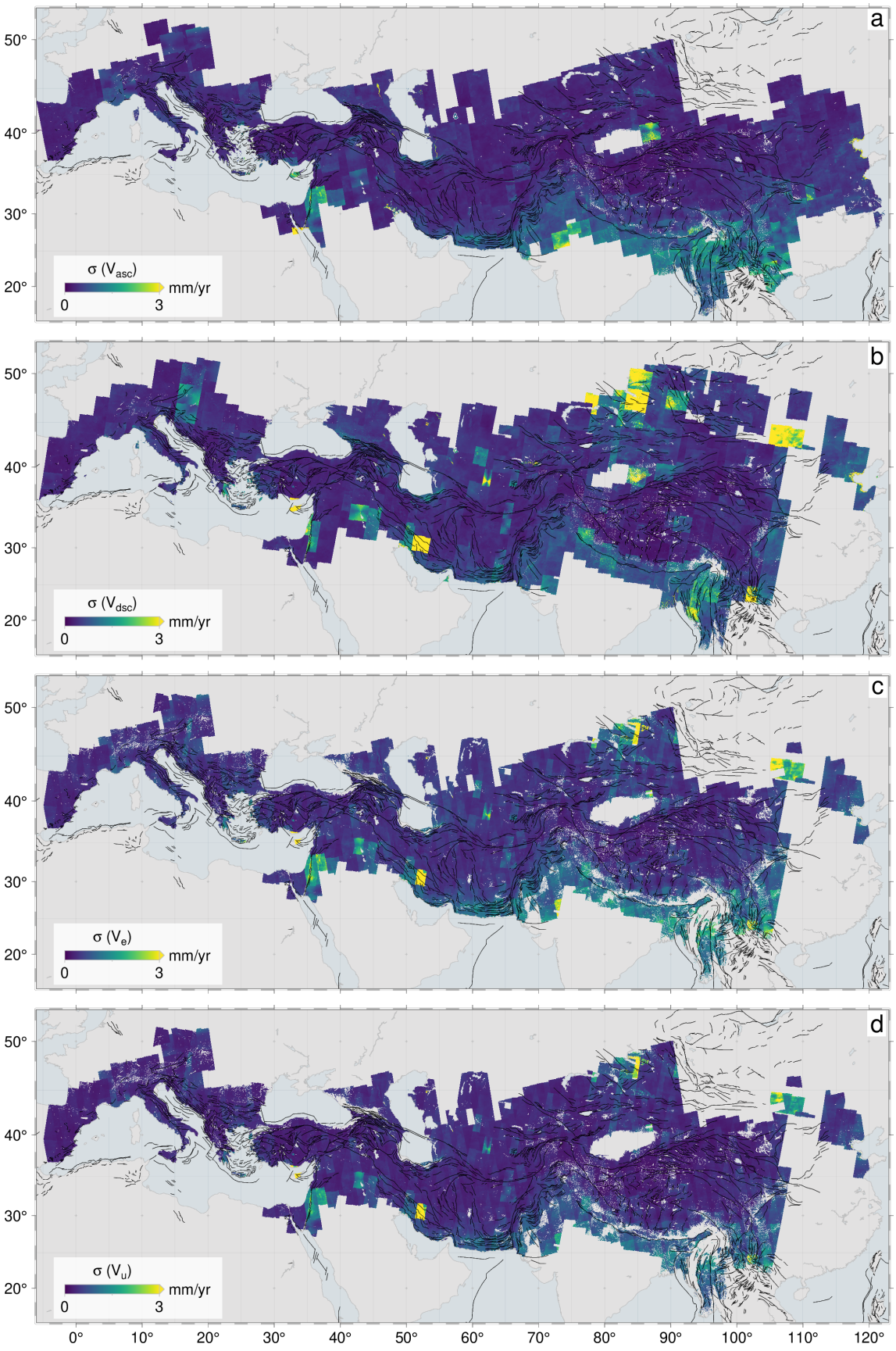


Figure SB15: Uncertainties in line of sight velocities on (a) ascending and (b) descending directions, as well as formal uncertainties of decomposed (c) east and (d) vertical velocities.

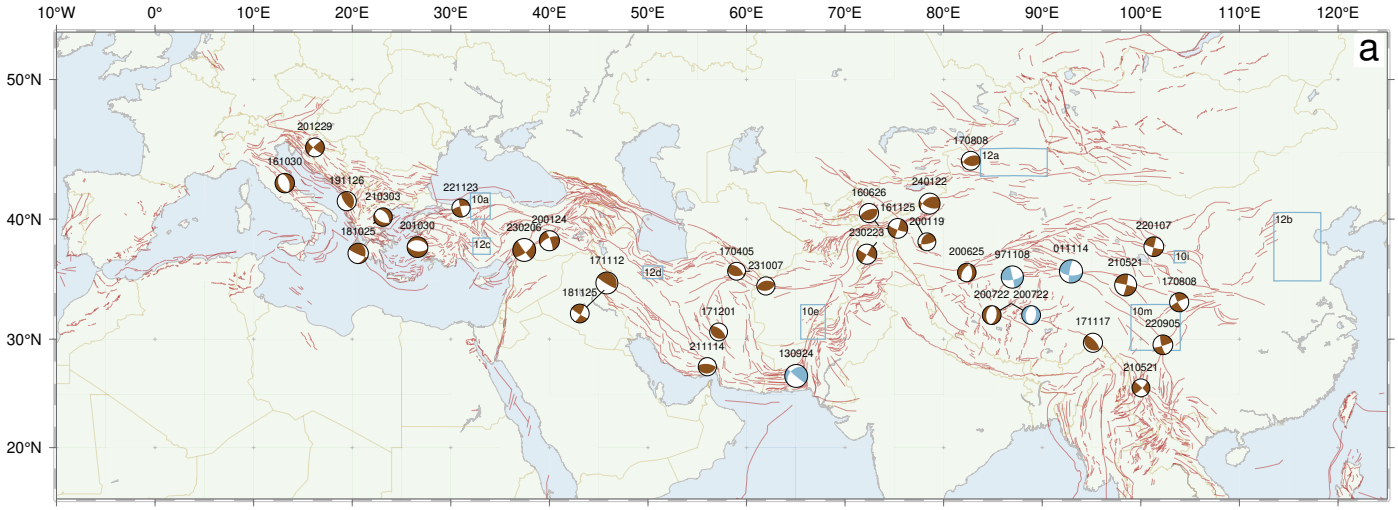


Figure SB16: Location of $M_w > 6.0$ earthquakes (denote by focal mechanism from the GCMT, (Ekström et al., 2012)) that are accounted for in the time series (Table SA4). Numbers above the focal mechanism denote the date of the earthquake (UTC, YYMMDD). Blue focal mechanism denote events with postseismic signals described in Figure 11. Blue polygon outlines show examples of regions of creeping fault segments (Figure 10) and subsidence (Figure 12).

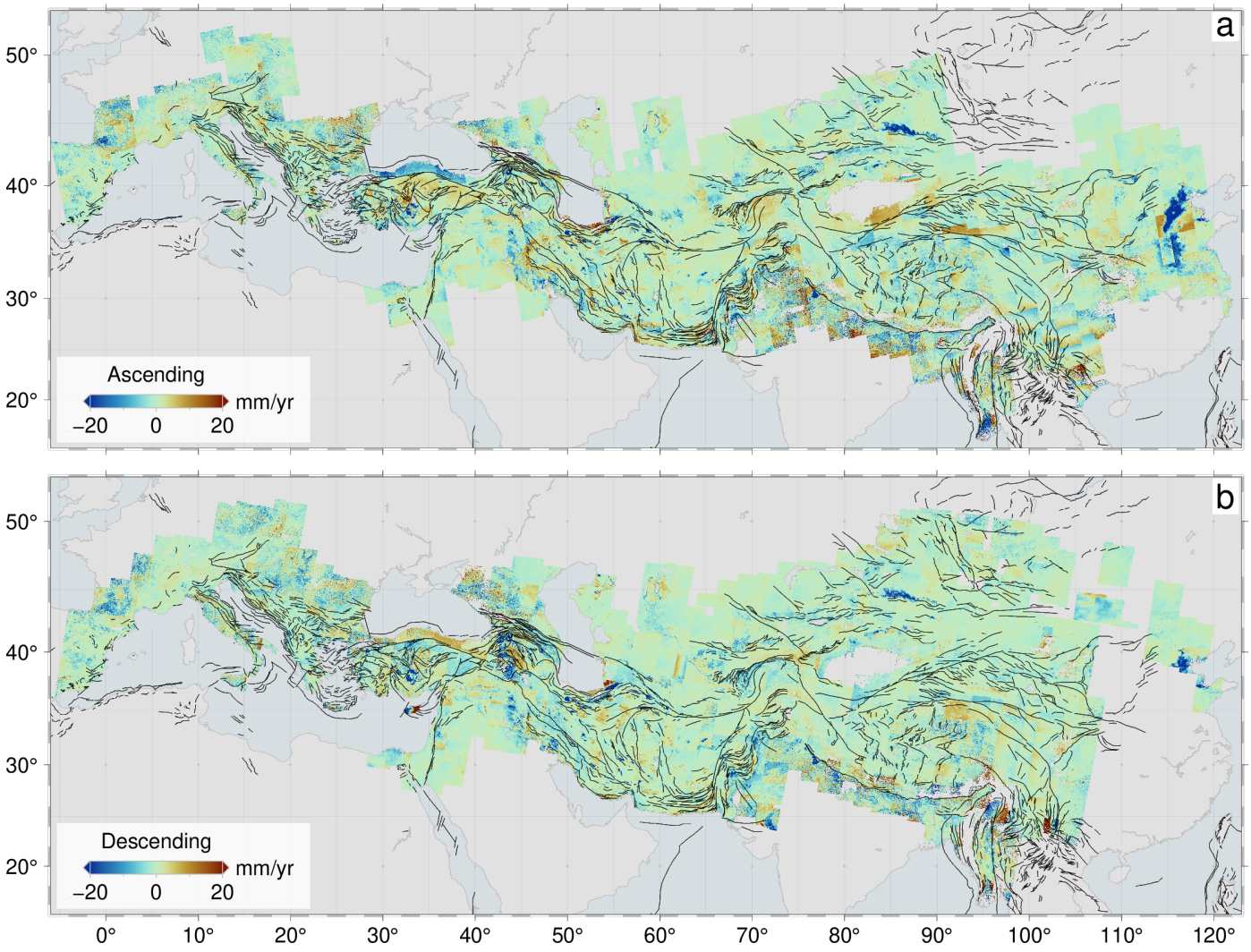


Figure SB17: Individual frame-by-frame line-of-sight velocities on (a) ascending and (b) descending directions, prior to referencing within the tying procedure implemented in VELMAP.

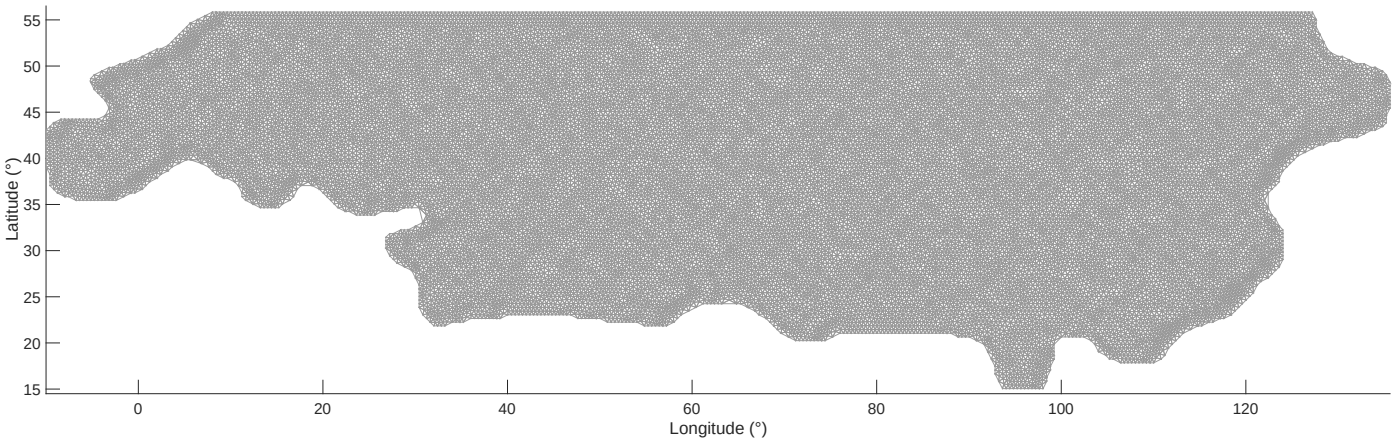


Figure SB18: (a) Triangular mesh constructed for the entire AHB, used for VELMAP processing.

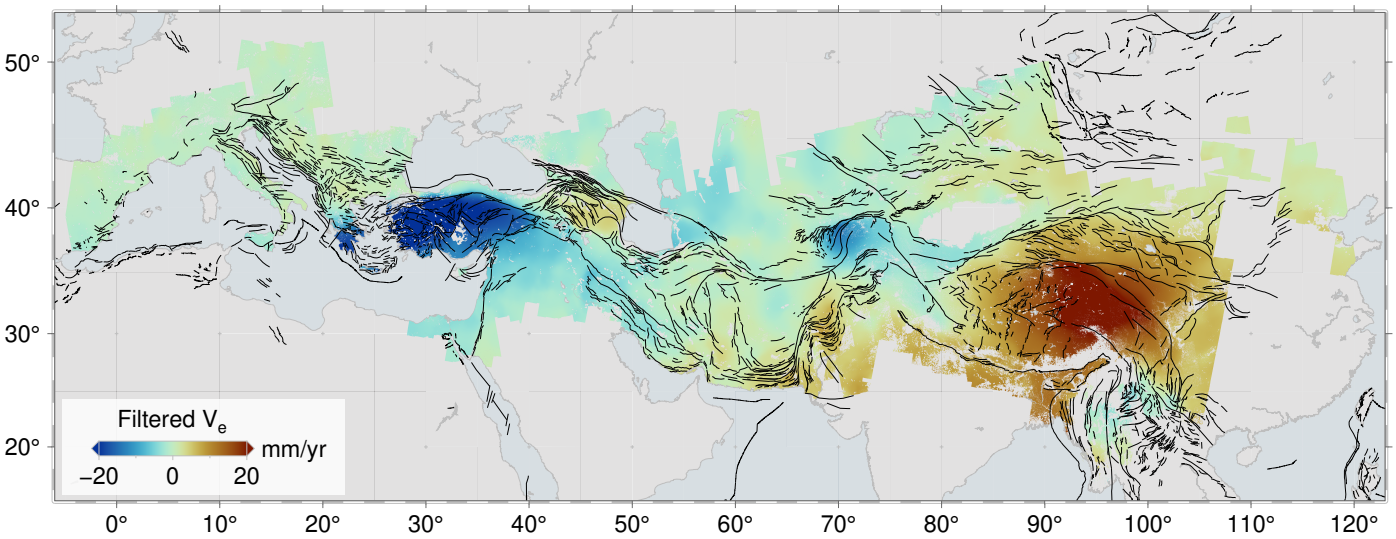


Figure SB19: Median-filtered eastward velocities with a window size of 150 km, used for strain rate calculations. Pixels with an absolute vertical velocity magnitude exceeding 20 mm/yr are masked out for strain rate analysis.

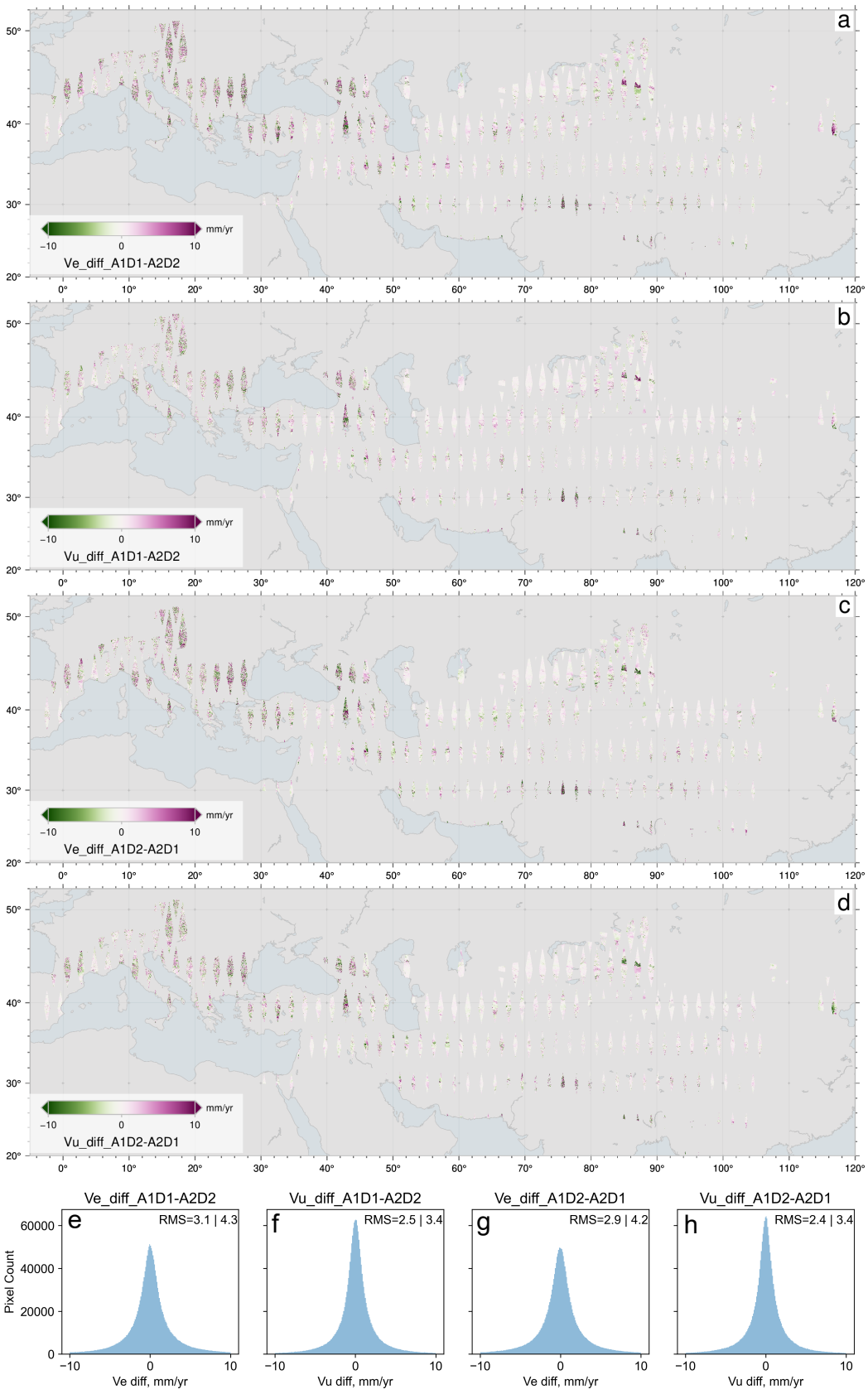


Figure SB20: (a-d) Differences in east and vertical velocities decomposed from independent ascending and descending geometries and (e-h) histograms of the differences. The RMS differences are reported in two numbers: RMS of 1-99% | RMS of all pixels. We use the RMS of 1-99% for uncertainty estimates to avoid the bias from extreme values in the lowest and highest percentile.

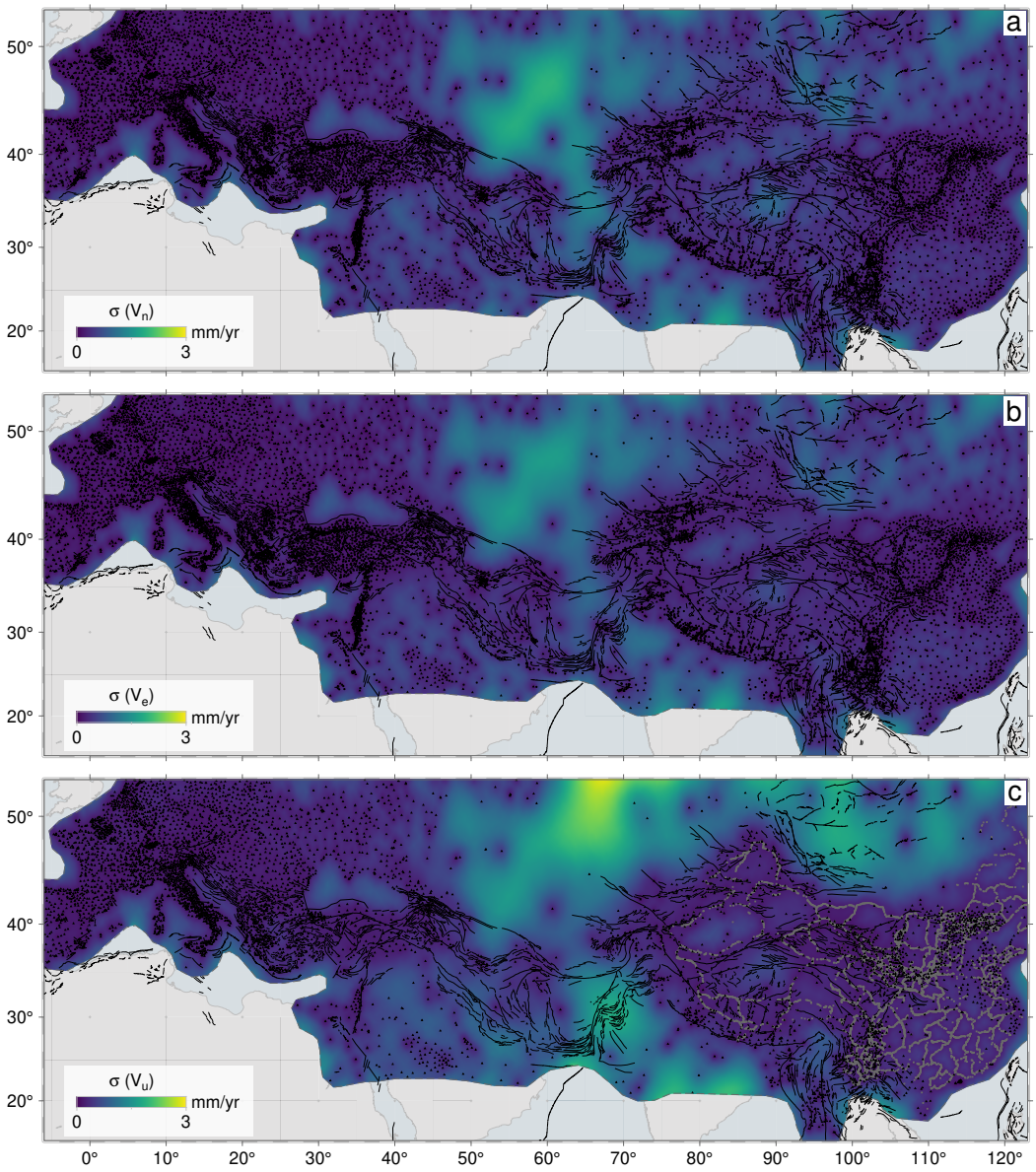


Figure SB21: Uncertainties in VELMAP-derived estimates of (a) north, (b) east, and (c) vertical velocities.

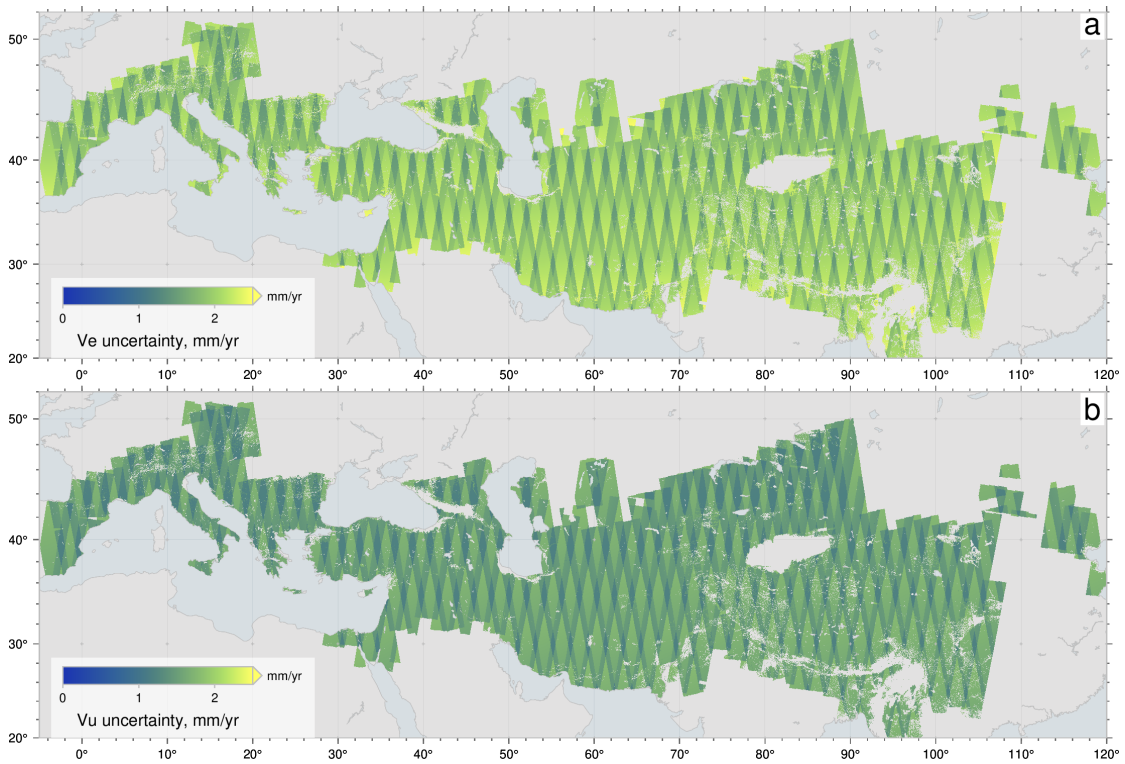


Figure SB22: Uncertainties of (a) east and (b) vertical velocities forward-calculated from estimated LOS uncertainties of 1.9 mm/yr for ascending and 1.8 mm/yr for descending. The RMS uncertainties are 1.9 mm/yr for east velocities and 1.5 mm/yr for vertical velocities.

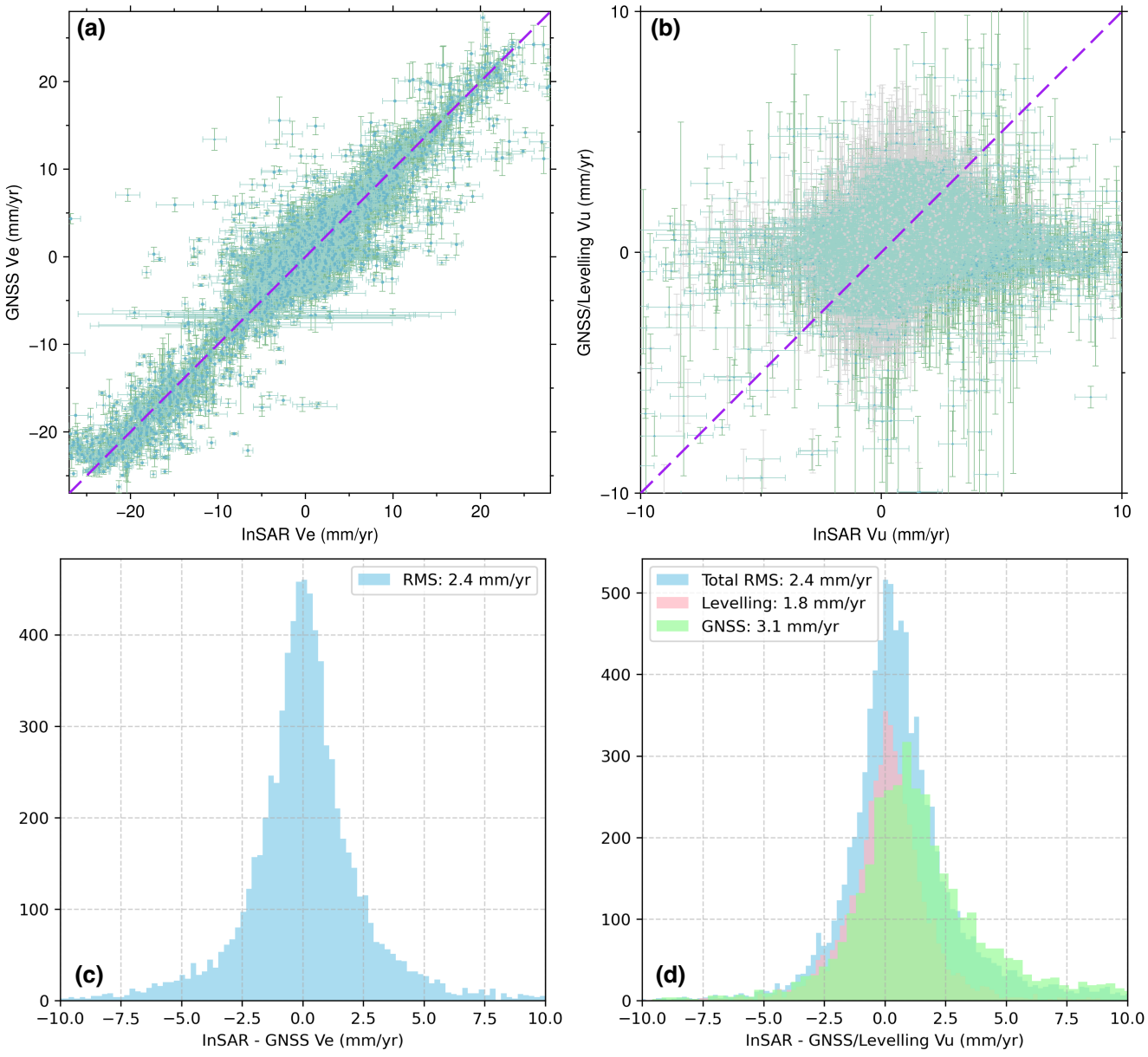


Figure SB23: Correlation plot of InSAR-derived Ve against GNSS Ve across the entire AHB. (b) Correlation plot of InSAR-derived Vu against GNSS/levelling Vu. The corresponding histograms of mismatch are shown in panels (c)–(d).

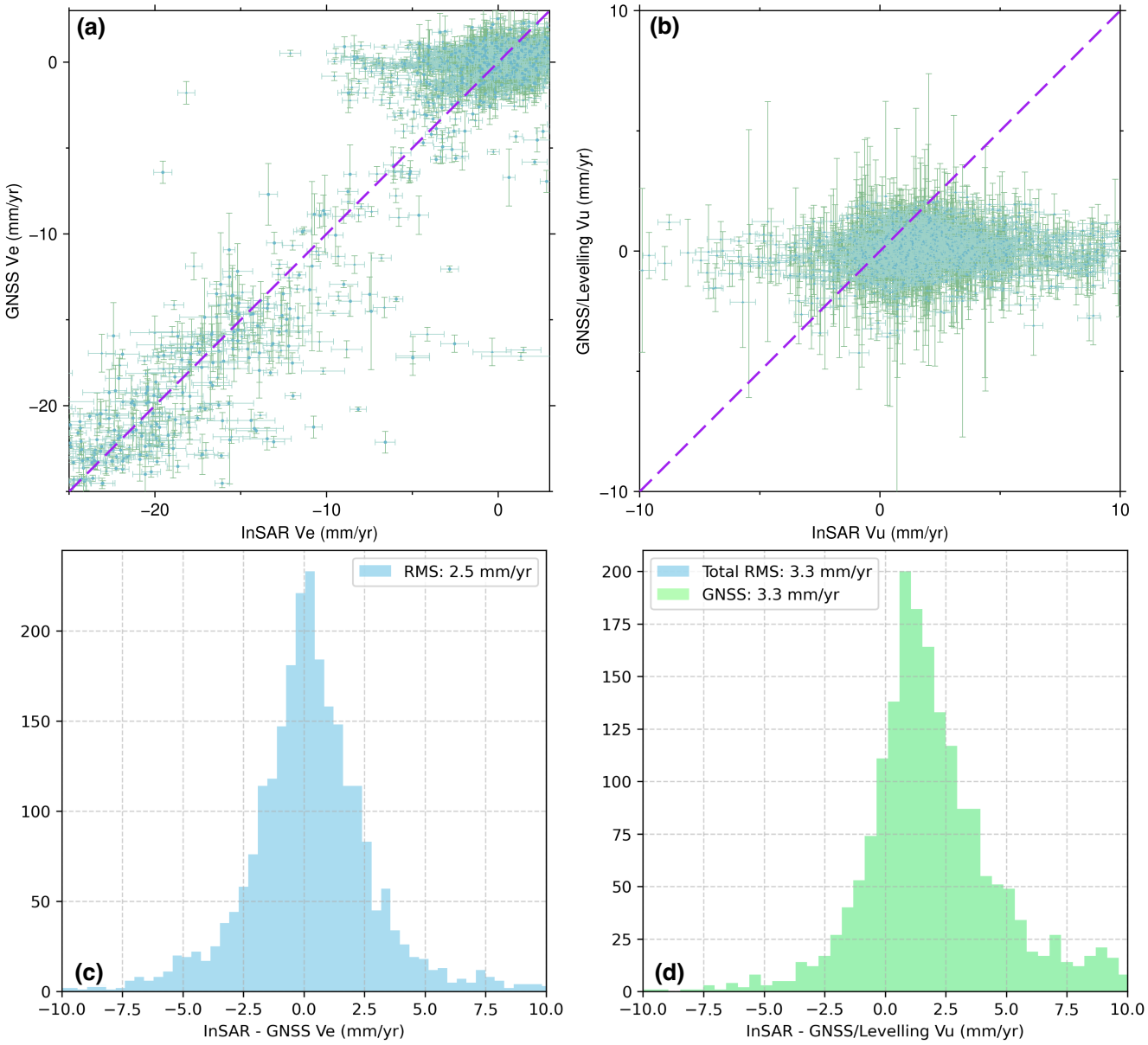


Figure SB24: Scatter and histogram plots comparing InSAR Ve (Vu) with GNSS Ve (Vu) within the same coverage area as the EGMS data.

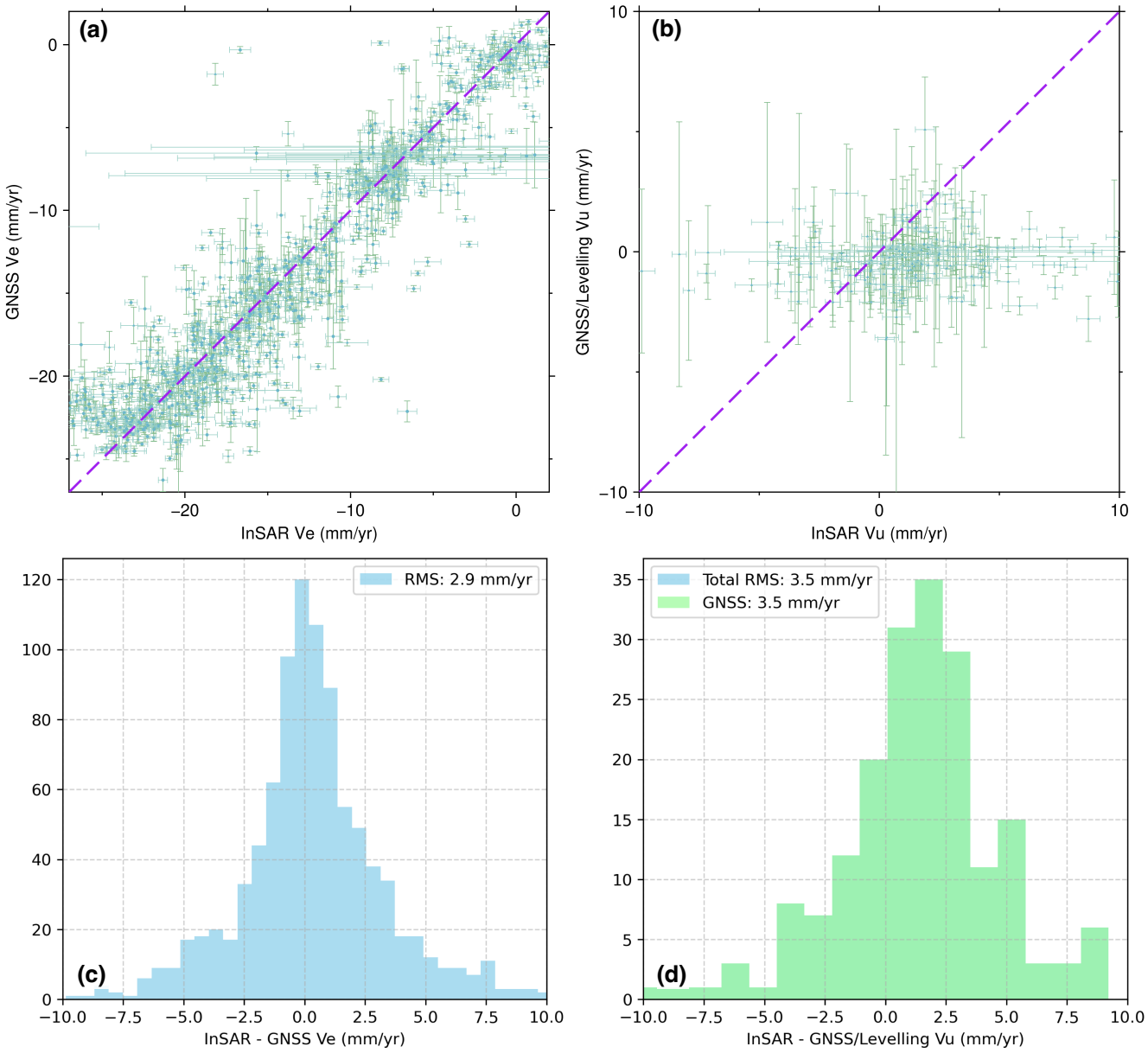


Figure SB25: Scatter and histogram plots comparing InSAR Ve (Vu) with GNSS Ve (Vu) in Anatolia.

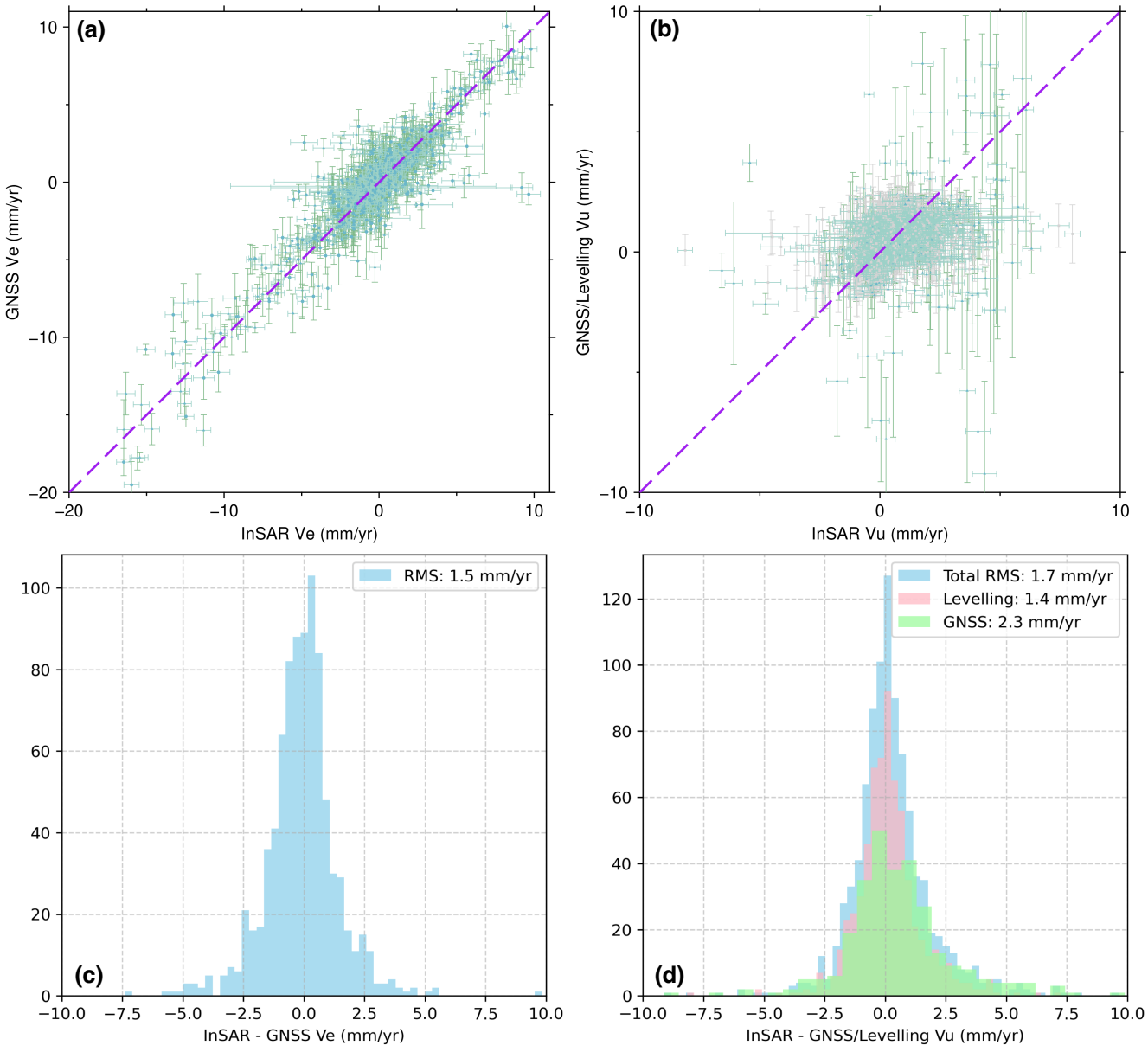


Figure SB26: Scatter and histogram plots comparing InSAR Ve (Vu) with GNSS Ve (Vu) in Pamir and Tian Shan.

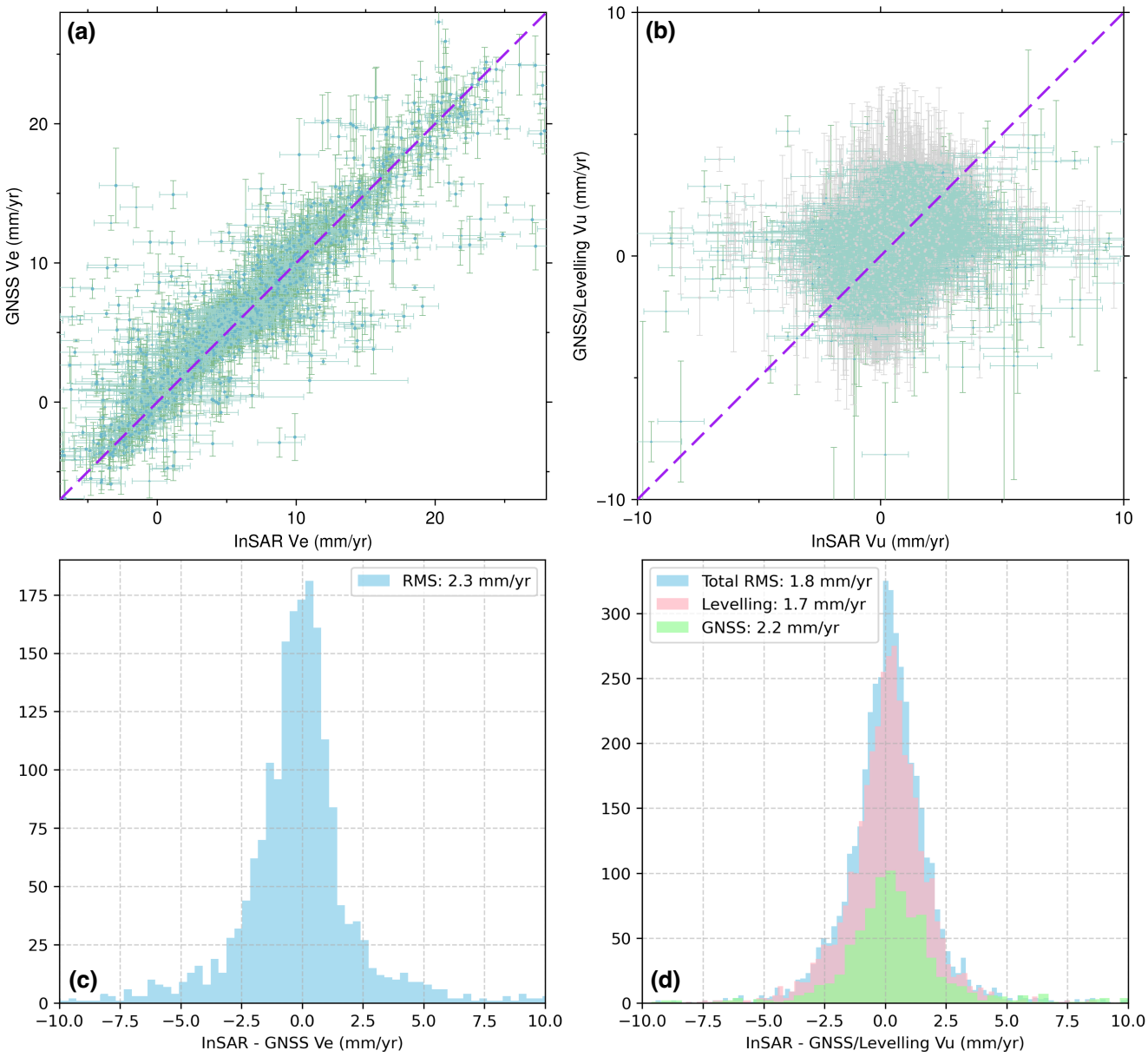


Figure SB27: Scatter and histogram plots comparing InSAR Ve (Vu) with GNSS Ve (Vu) in Tibet.

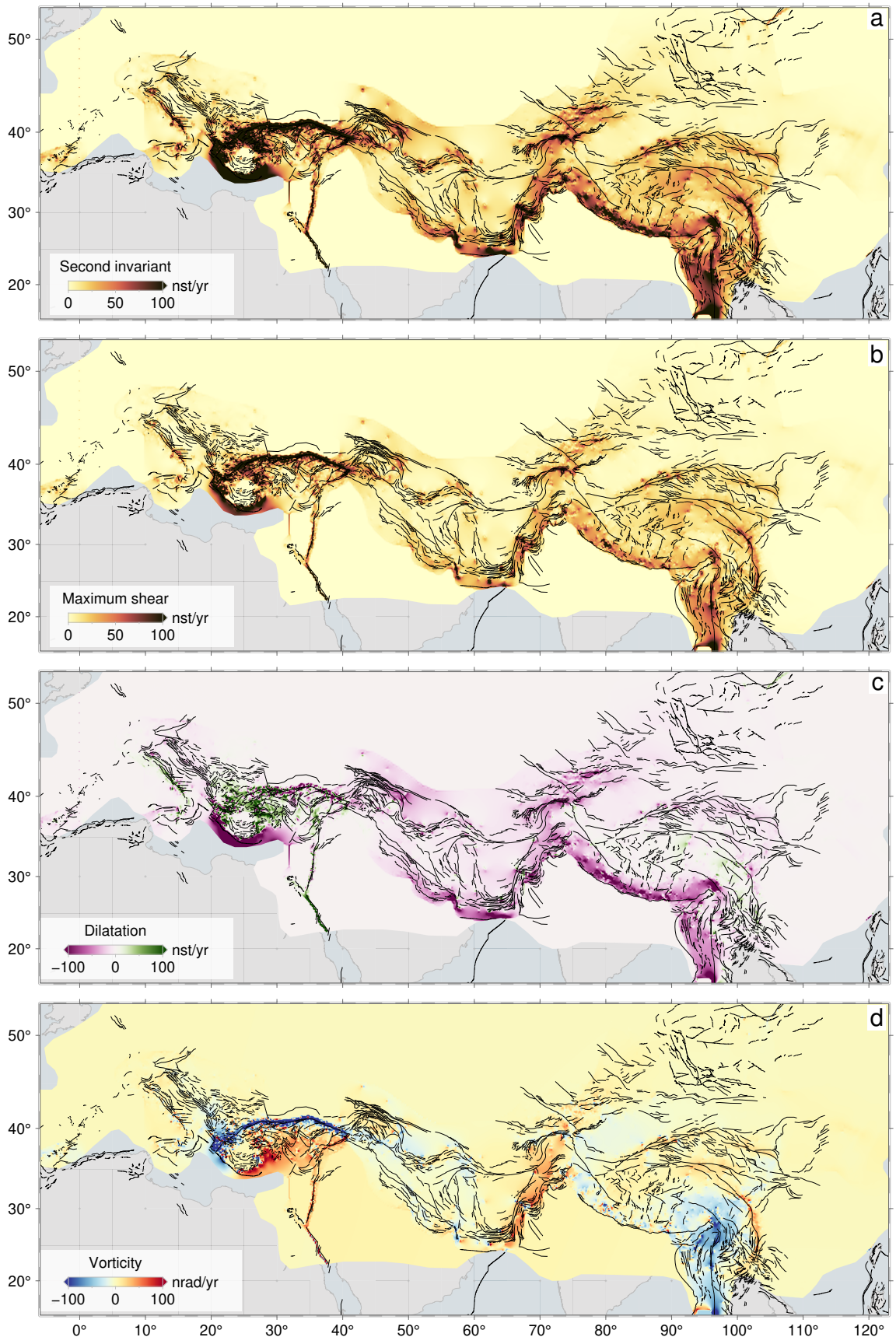


Figure SB28: Global Strain Rate Model (GSRM) v2.2 from Kreemer et al. (2014) (https://geodesy.unr.edu/GSRM/). Compare with Figure 9 for our GNSS+InSAR derived version.

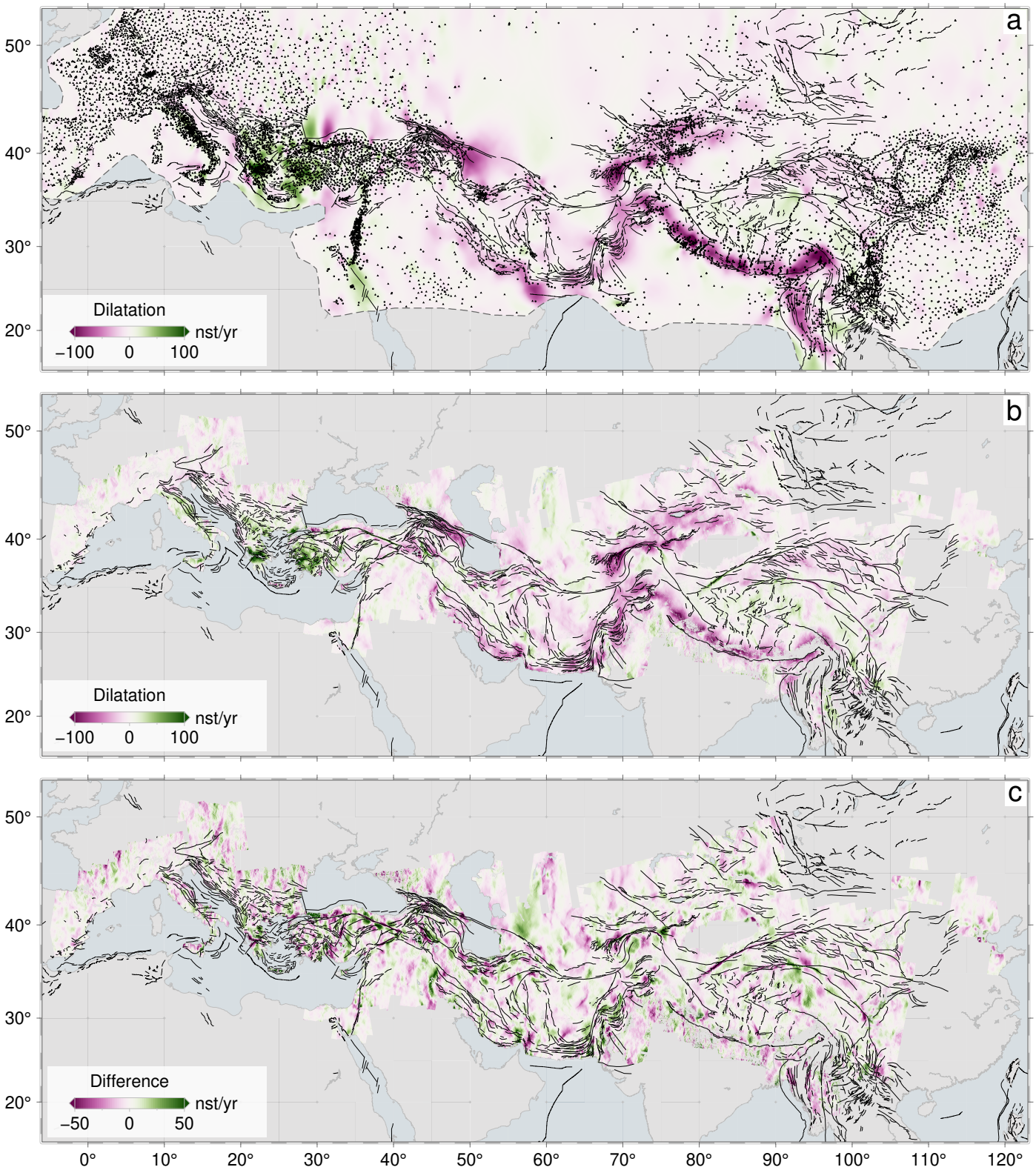


Figure SB29: Comparison of the dilatation rate field derived from (a) GNSS-only versus (b) combined GNSS+InSAR solutions. The difference is shown in panel (c).

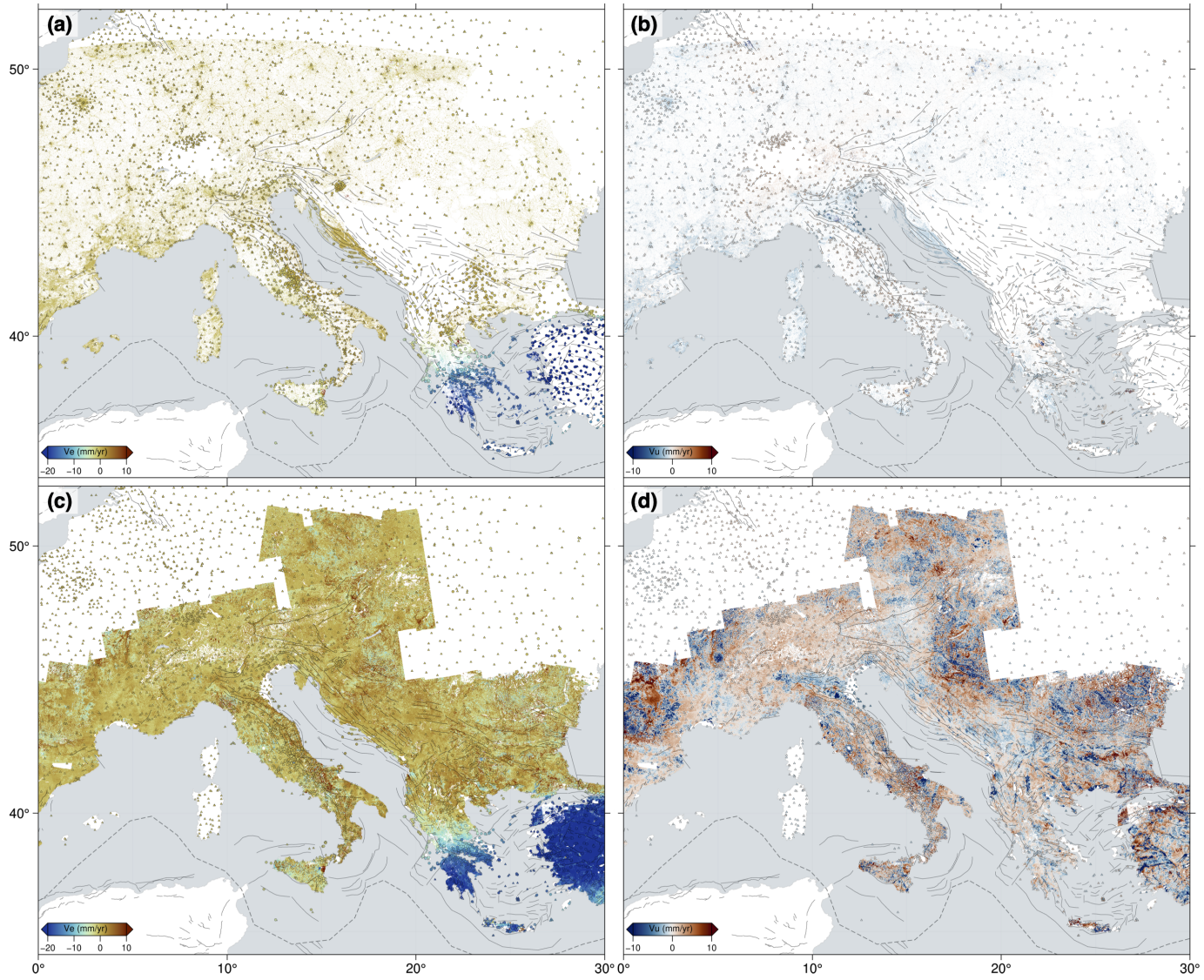


Figure SB30: Comparison with the European Ground Motion Service (EGMS) East and Vertical velocities (Costantini et al., 2021). (a)-(b) EGMS-derived Ve and Vu at a resolution of 100 m. (c)-(d) InSAR-derived Ve and Vu at 1 km resolution. Scatter and histogram plots are shown in Figures SB31 and SB24.

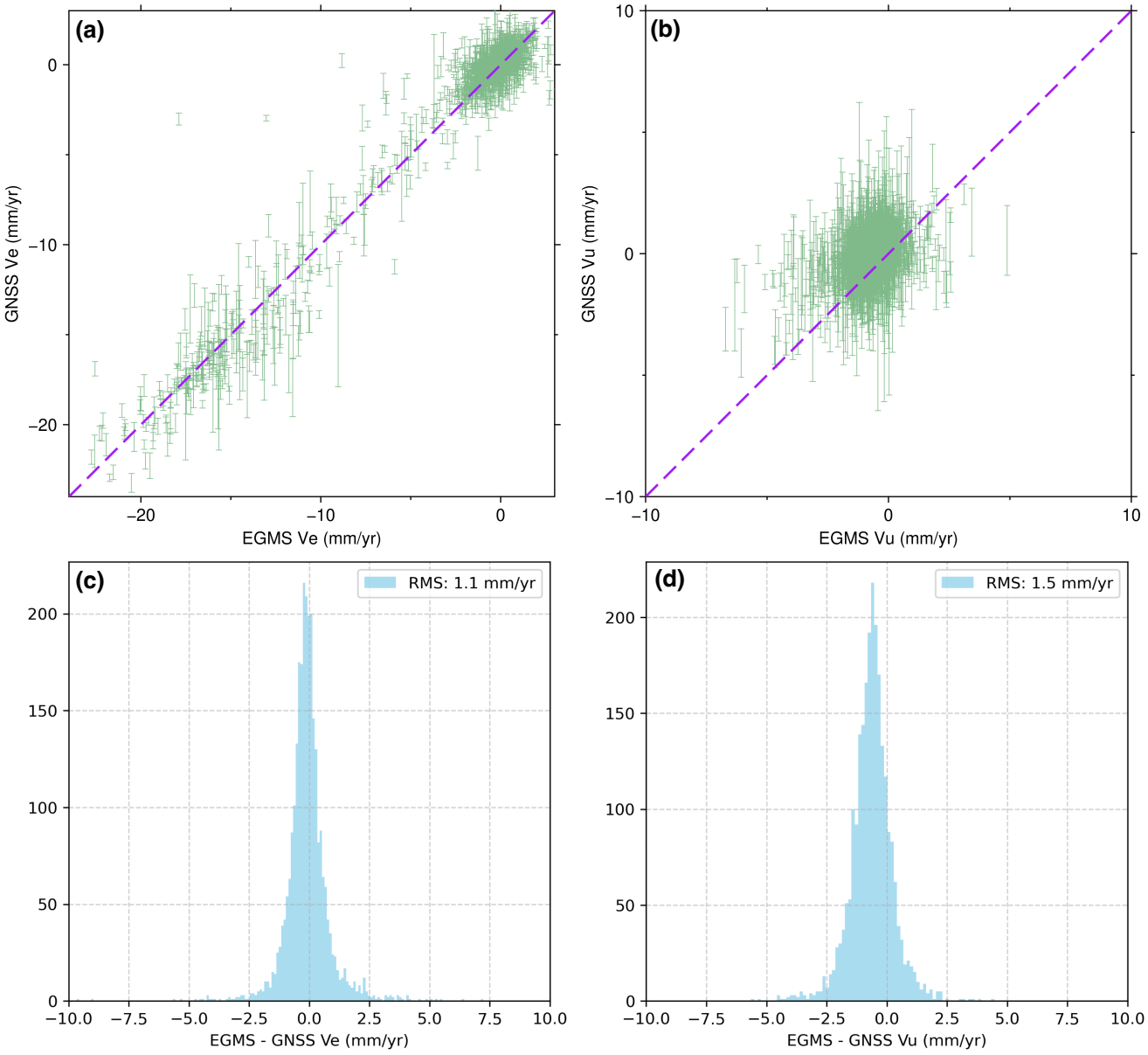


Figure SB31: Scatter and histogram plots comparing EGMS Ve (Vu) with GNSS Ve (Vu).

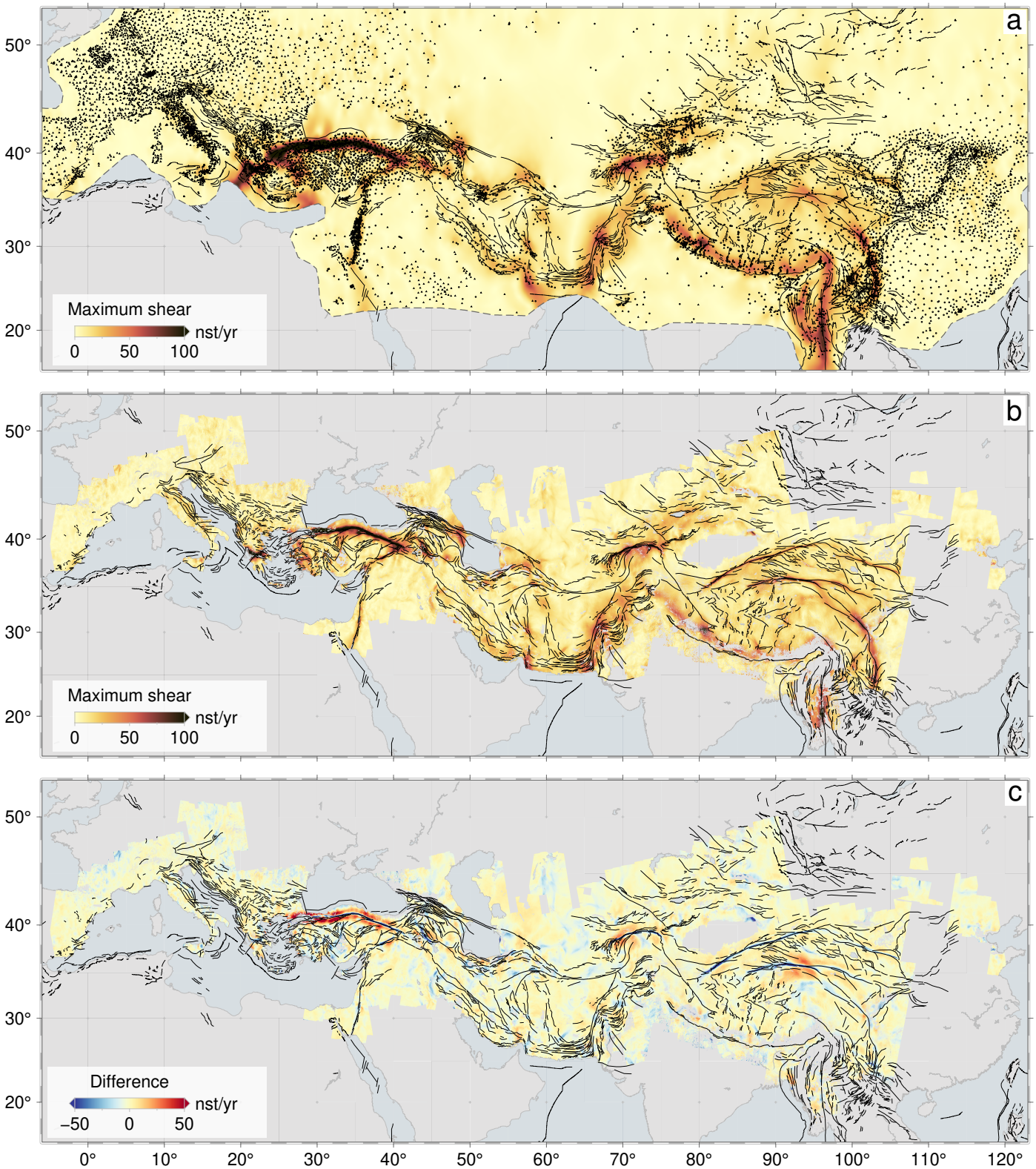


Figure SB32: Comparison of the maximum shear strain rate field derived from (a) GNSS-only versus (b) combined GNSS+InSAR solutions. The difference is shown in panel (c).

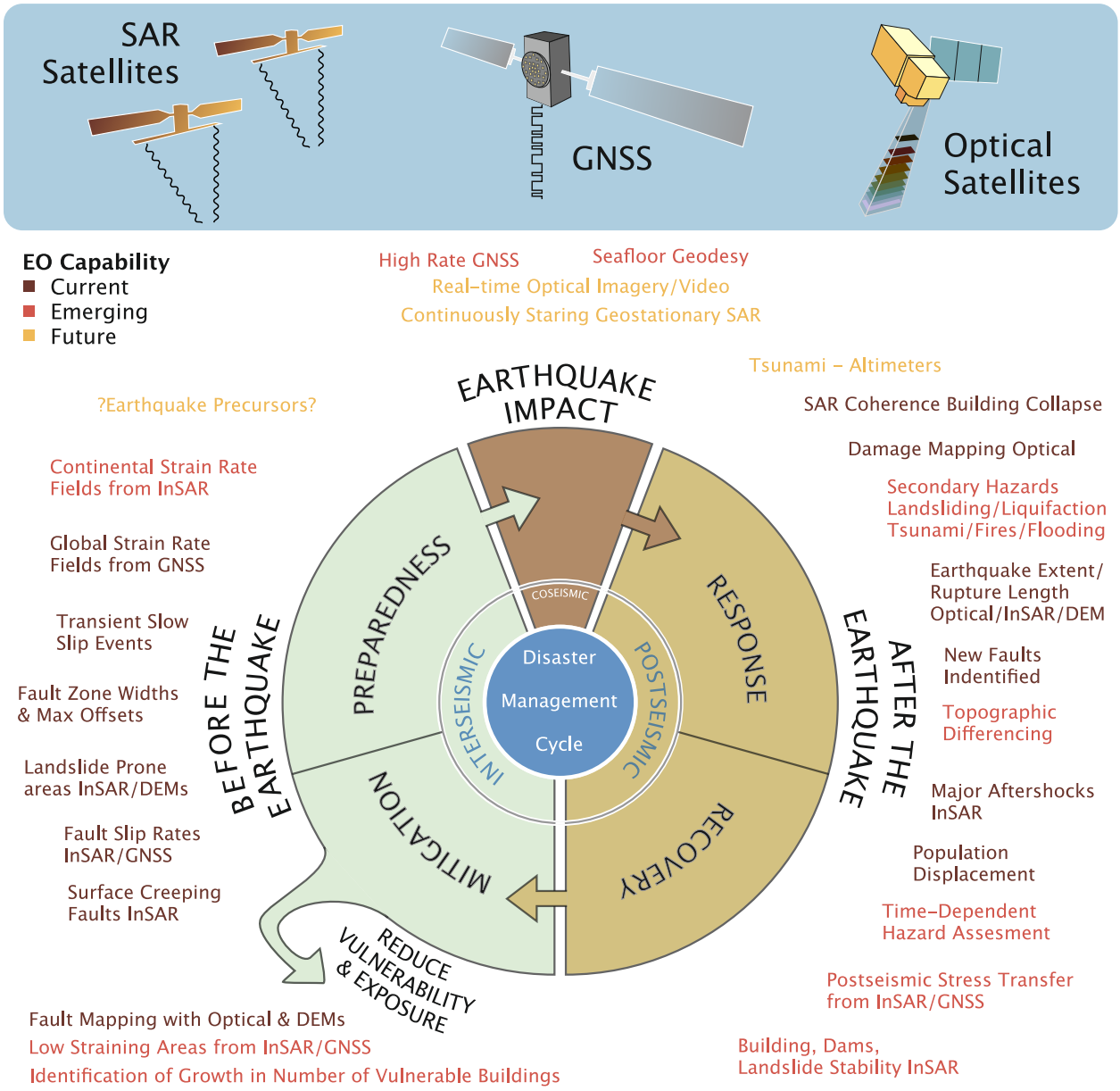


Figure SB33: SAR and GNSS contribute important Earth Observation data constraints (in addition to optical satellites) that provide information to various aspects of the disaster management cycle, such as the emerging field of generating Continental Strain Rate Fields from InSAR combined with GNSS to feed into seismic hazard calculations. Updated from Elliott (2020).

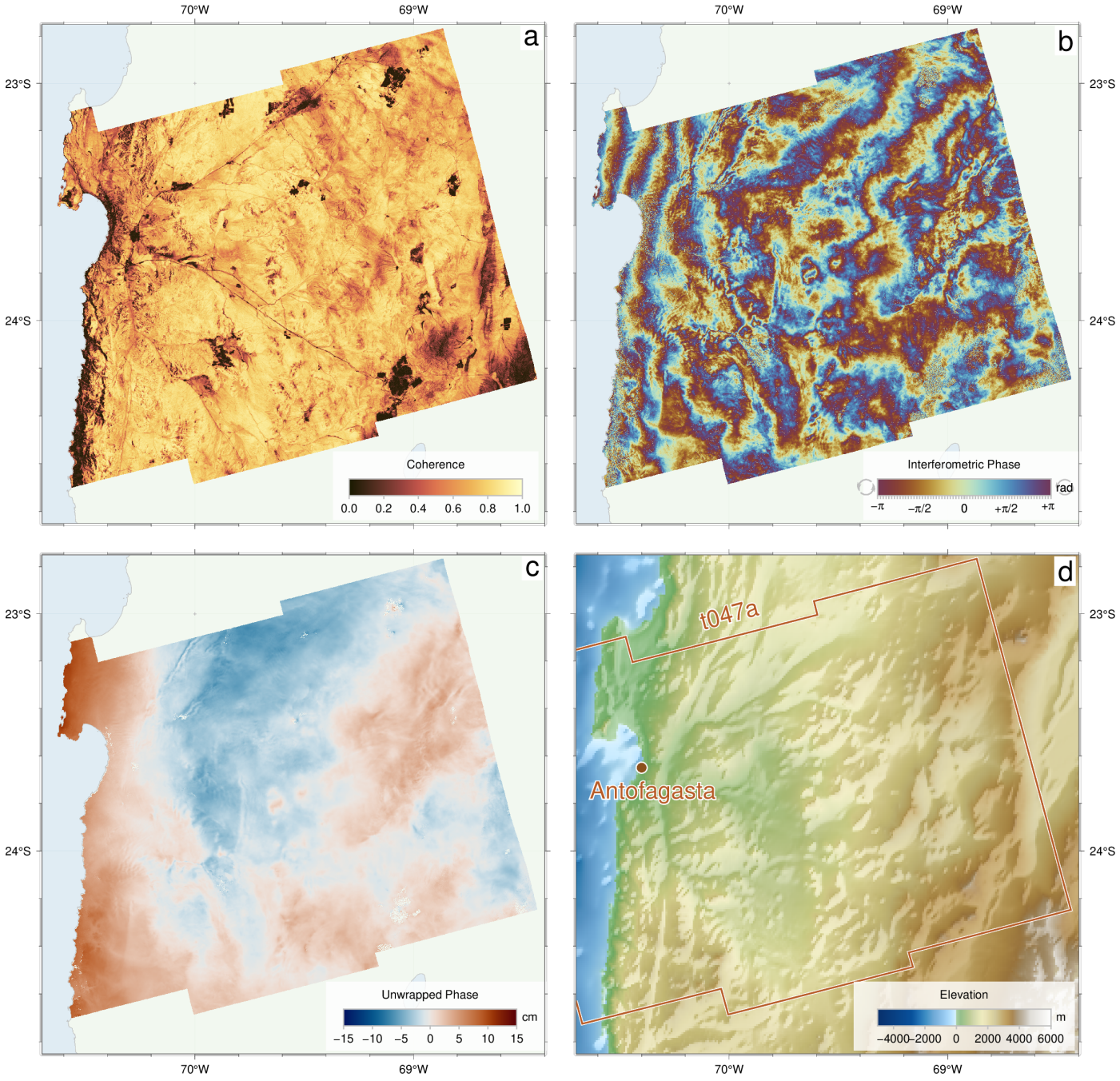


Figure SB34: Outputs from differential InSAR of one of the first Sentinel-1A ascending track 047 acquisitions in this area (20150205) with one of the first Sentinel-1C acquisitions (20250201), spanning an interval of 10 years. The region is between the Chilean Coast at Antofogasta and the Atacama Desert on the Tropic of Capricorn. As one of the driest places on earth, the coherence is maintained very well over 10 years. The unwrapped phase captures both the difference in refractivity of the atmosphere and the ocean tidal loading between the two acquisition dates, but also the cumulative displacement of 10 years of locked elastic loading along this subduction zone. (a) Coherence showing regions that have remained relatively stable (high values) and those were the land surface has changed in the 10-year period (low values, e.g., the coastal fringes in the west, settlements and agricultural patches, linear roads, salars in the east and mines such as in the south-west of the scene. (b) Interferometric phase wrapped $(-\pi, \pi)$ with increasing values indicating range increase) (c) Unwrapped Phase measuring line-of-sight displacement (positive motion, red, indicates motion towards the satellite) (d) Hillshaded Digital Elevation Model of bathymetry and topography at 30 arcseconds resolution from SRTM30_plus (Becker et al., 2009). The outline of interferogram is shown in red.

Appendix C. Supplementary Data

The supplementary material related to this article consists of two csv data tables, one for each of ascending and descending (*AHB.asc.csv & AHB.dsc.csv*) comprising the following information on the SAR frames used in the study:

Frame_ID — consisting of the track number, a unique time and the number of frames on each subswath (typically 13 on each).

TS Date Range — Time interval spanning time series.

#Epochs — Number of epochs (acquisitions) used in inversion for time series.

#Ifgms — Number of interferograms used in inversion for time series.

LICSBAS options run — the flag options and parameter values used in running the LiCSBAS inversion.

Mask Step 15 params — The Masking parameters used in step 15 of LiCSBAS to remove noise and erroneous pixels from the time series.

vstd scaling — the standard deviation uncertainties in the velocity scale by the spatial function given (exponential, linear, spherical) with the values for the nugget, sill and range given).

Earthquake Removal — the choice made whether to solve for an offset or truncate the time series based upon the impact on the frame of coseismic deformation from the list of Earthquakes in Table SA4.

References

Abbasi, M., Ghods, A., Najafi, M., Abbasy, S., Amiri, M., Shabanian, E., Kheradmandi, M., Asgari, J., 2023. Why does western Makran have a low seismicity rate? Tectonophysics 869, 230134. doi:10.1016/j.tecto.2023.230134.

Ader, T., Avouac, J.P., Liu-Zeng, J., Lyon-Caen, H., Bollinger, L., Galetzka, J., Genrich, J., Thomas, M., Chanard, K., Sapkota, S.N., Rajaure, S., Shrestha, P., Ding, L., Flouzat, M., 2012. Convergence rate across the Nepal Himalaya and interseismic coupling on the Main Himalayan Thrust: Implications for seismic hazard. Journal of Geophysical Research: Solid Earth 117. doi:10.1029/2011JB009071.

Aktug, B., Nocquet, J.M., Cingöz, A., Parsons, B., Erkan, Y., England, P., Lenk, O., Gürdal, M.A., Kilicoglu, A., Akdeniz, H., Tekgül, A., 2009. Deformation of western Turkey from a combination of permanent and campaign GPS data: Limits to block-like behavior. Journal of Geophysical Research: Solid Earth 114. doi:10.1029/2008JB006000.

Aktug, BAHADIR., Ozener, H., Dogru, AABKO., Sabuncu, A., Turgut, B., Halicioglu, K., Yilmaz, O., Havazli, E., 2016. Slip rates and seismic potential on the East Anatolian Fault System using an improved GPS velocity field. Journal of Geodynamics 94, 1–12. doi:10.1016/j.jog.2016.01.001.

Allen, M.B., 2021. Arabia-Eurasia Collision, in: Alderton, D., Elias, S.A. (Eds.), Encyclopedia of Geology (Second Edition). Academic Press, Oxford, pp. 436–450. doi:10.1016/B978-0-12-409548-9.12522-9.

Allen, M.B., Saville, C., Blanc, E.J.P., Talebian, M., Nissen, E., 2013. Orogenic plateau growth: Expansion of the Turkish-Iranian Plateau across the Zagros fold-and-thrust belt. Tectonics 32, 171–190. doi:10.1002/tect.20025.

Alothman, AO., Fernandes, RM., Bos, MS., Schillak, S., Elsaka, B., 2016. Angular velocity of Arabian plate from multi-year analysis of GNSS data. Arabian Journal of Geosciences 9, 1–10.

Altamimi, Z., Métivier, L., Rebischung, P., Rouby, H., Collilieux, X., 2017. ITRF2014 plate motion model. Geophysical Journal International 209, 1906–1912. doi:10.1093/gji/ggx136.

Altamimi, Z., Rebischung, P., Métivier, L., Collilieux, X., 2016. ITRF2014: A new release of the International Terrestrial Reference Frame modeling nonlinear station motions. Journal of geophysical research: solid earth 121, 6109–6131.

Ansari, H., De Zan, F., Parizzi, A., 2021. Study of Systematic Bias in Measuring Surface Deformation With SAR Interferometry. IEEE Transactions on Geoscience and Remote Sensing 59, 1285–1301. doi:10.1109/TGRS.2020.3003421.

Ashurkov, SV., San'Kov, VA., Serov, MA., Luk'yanov, P.Y., Grib, NN., Bordonskii, GS., Dembelov, MG., 2016. Evaluation of present-day deformations in the Amurian Plate and its surroundings, based on GPS data. Russian Geology and Geophysics 57, 1626–1634.

Atanasova-Zlatareva, M., 2014. Research of the horizontal crustal motions, based on GPS Data for the territory of Bulgaria and the Balkans (7093), in: Engaging the Challenges–Enhancing the Relevance XXV FIG Congress 2014 in Kuala Lumpur, Malaysia 16, pp. 1–11.

Aung, P.S., Satirapod, C., Andrei, C.O., 2016. Sagaing Fault slip and deformation in Myanmar observed by continuous GPS measurements. Geodesy and Geodynamics 7, 56–63.

Avouac, J.P., Ayoub, F., Wei, S., Ampuero, J.P., Meng, L., Leprince, S., Jolivet, R., Duputel, Z., Helmberger, D., 2014. The 2013, Mw 7.7 Balochistan earthquake, energetic strike-slip reactivation of a thrust fault. Earth and Planetary Science Letters 391, 128–134. doi:10.1016/j.epsl.2014.01.036.

Avouac, J.P., Burov, E.B., 1996. Erosion as a driving mechanism of intracontinental mountain growth. Journal of Geophysical Research: Solid Earth 101, 17747–17769. doi:10.1029/96JB01344.

Avouac, J.P., Tapponnier, P., 1993. Kinematic model of active deformation in central Asia. Geophysical Research Letters 20, 895–898. doi:10.1029/93GL00128.

Ballato, P., Landgraf, A., Schildgen, T.F., Stockli, D.F., Fox, M., Ghassemi, M.R., Kirby, E., Strecker, M.R., 2015. The growth of a mountain belt forced by base-level fall: Tectonics and surface processes during the evolution of the Alborz Mountains, N Iran. Earth and Planetary Science Letters 425, 204–218. doi:10.1016/j.epsl.2015.05.051.

Barbot, S., Weiss, J.R., 2021. Connecting subduction, extension and shear localization across the Aegean Sea and Anatolia. Geophysical Journal International 226, 422–445. doi:10.1093/gji/ggab078.

Barka, A., 1996. Slip distribution along the North Anatolian fault associated with the large earthquakes of the period 1939 to 1967. Bulletin of the Seismological Society of America 86, 1238–1254. doi:10.1785/BSSA0860051238.

Barka, A., Reilinger, R., 1997. Active tectonics of the Eastern Mediterranean region: Deduced from GPS, neotectonic and seismicity data. Annals of Geophysics 40. doi:10.4401/ag-3892.

Barman, P., Jade, S., Kumar, A., Jamir, W., 2017. Inter annual, spatial, seasonal, and diurnal variability of precipitable water vapour over northeast India using GPS time series. International journal of remote sensing 38, 391–411.

Becker, J.J., Sandwell, D.T., Smith, W.H.F., Braud, J., Binder, B., Depner, J., Fabre, D., Factor, J., Ingalls, S., Kim, S.H., Ladner, R., Marks, K., Nelson, S., Pharaoh, A., Trimmer, R., Rosenberg, J.V., Wallace, G., Weatherall, P., 2009. Global Bathymetry and Elevation Data at 30 Arc Seconds Resolution: SRTM30_PLUS. Marine Geodesy doi:10.1080/01490410903297766.

Bekaert, D.P.S., Handwerger, A.L., Agram, P., Kirschbaum, D.B., 2020. InSAR-based detection method for mapping and monitoring slow-moving landslides in remote regions with steep and mountainous terrain: An application to Nepal. Remote Sensing of Environment 249, 111983. doi:10.1016/j.rse.2020.111983.

Bell, M.A., Elliott, J.R., Parsons, B.E., 2011. Interseismic strain accumulation across the Manyi fault (Tibet) prior to the 1997 M $_w$ 7.6 earthquake. Geophysical Research Letters 38. doi:10.1029/2011GL049762.

Bendick, R., Bilham, R., Freymueller, J., Larson, K., Yin, G., 2000. Geodetic evidence for a low slip rate in the Altyn Tagh fault system. Nature 404, 69–72. doi:10.1038/35003555.

Bilham, R., 2019. Himalayan earthquakes: A review of historical seismicity and early 21st century slip potential. Geological Society, London, Special Publications 483, 423–482. doi:10.1144/SP483.16.

Billi, A., Cuffaro, M., Orecchio, B., Palano, M., Presti, D., Totaro, C., 2023. Retracing the Africa–Eurasia nascent convergent boundary in the western Mediterranean based on earthquake and GNSS data. Earth and Planetary Science Letters 601, 117906. doi:10.1016/j.epsl.2022.117906.

Bisht, H., Kotlia, B.S., Kumar, K., Dumka, R.K., Taloor, A.K., Upadhyay, R., 2021. GPS derived crustal velocity, tectonic deformation and strain in the Indian Himalayan arc. Quaternary International 575, 141–152.

Bitharis, S., Pikridas, C., Fotiou, A., Rossikopoulos, D., 2024. GPS data analysis and geodetic velocity field investigation in Greece, 2001–2016. GPS Solutions 28, 16.

Blewitt, G., Hammond, W., Kreemer, C., 2018. Harnessing the GPS data explosion for interdisciplinary science. eos. commentarii societatis philologae polonorum 99, e2020943118.

Bloch, W., Metzger, S., Schurr, B., Yuan, X., Ratschbacher, L., Reuter, S., Xu, Q., Zhao, J., Murodkulov, S., Oimuhammadzoda, I., 2023. The 2015–2017 Pamir earthquake sequence: Foreshocks, main shocks and aftershocks, seismotectonics, fault interaction and fluid processes. Geophysical Journal International 233, 641–662. doi:10.1093/gji/ggac473.

Bock, Y., Moore, AW., Argus, D., Fang, P., Golriz, D., Guns, K., Jiang, S., Kedar, S., Knox, SA., Liu, Z., et al., 2021. Extended solid earth science ESDR system (ES3): Algorithm theoretical basis document, NASA MEaSUREs project# NNH17ZDA001N.

Briole, P., Ganas, A., Elias, P., Dimitrov, D., 2021. The GPS velocity field of the Aegean. New observations, contribution of the earthquakes, crustal blocks model. Geophysical Journal International 226, 468–492.

Brockmann, E., Lutz, S., Zurutuza, J., Caporali, A., Lidberg, M., Völksen, C., Sánchez, L., Serpelloni, E., Bitharis, S., Pikridas, C., et al., 2019. Towards a dense velocity field in europe as a basis for maintaining the european reference frame. 27th IUGG Assembly, Montreal .

Bürgmann, R., Ayhan, M.E., Fielding, E.J., Wright, T.J., McClusky, S., Aktug, B., Demir, C., Lenk, O., Türkezer, A., 2002. Deformation during the 12 November 1999 Düzce, Turkey, Earthquake, from GPS and InSAR Data. Bulletin of the Seismological Society of America 92, 161–171. doi:10.1785/0120000834.

Bürgmann, R., Dresen, G., 2008. Rheology of the Lower Crust and Upper Mantle: Evidence from Rock Mechanics, Geodesy, and Field Observations. Annual Review of Earth and Planetary Sciences 36, 531–567. doi:10.1146/annurev.earth.36.031207.124326.

Burtman, V.S., Skobelev, S.F., Molnar, P., 1996. Late Cenozoic slip on the Talas-Ferghana fault, the Tien Shan, central Asia. GSA Bulletin 108, 1004–1021. doi:10.1130/0016-7606(1996)108<1004:LCSOTT>2.3.CO;2.

Campbell, G.E., Walker, R.T., Abdrakhmatov, K., Jackson, J., Elliott, J.R., Mackenzie, D., Middleton, T., Schwenninger, J.L., 2015. Great earthquakes in low strain rate continental interiors: An example from SE Kazakhstan. Journal of Geophysical Research: Solid Earth 120, 5507–5534. doi:10.1002/2015JB011925.

Castro-Perdomo, N., Viltres, R., Masson, F., Klinger, Y., Liu, S., Dhahry, M., Ulrich, P., Bernard, J.D., Matrau, R., Alothman, A., et al., 2022. Interseismic deformation in the Gulf of Aqaba from GPS measurements. Geophysical Journal International 228, 477–492.

Cetin, E., Cakir, Z., Meghraoui, M., Ergintav, S., Akoglu, A.M., 2014. Extent and distribution of aseismic slip on the Ismetpaşa segment of the North Anatolian Fault (Turkey) from Persistent Scatterer InSAR. Geochemistry, Geophysics, Geosystems 15, 2883–2894. doi:10.1002/2014GC005307.

Cheloni, D., D'Agostino, N., Selvaggi, G., 2014. Interseismic coupling, seismic potential, and earthquake recurrence on the southern front of the Eastern Alps (NE Italy). Journal of Geophysical Research: Solid Earth 119, 4448–4468.

Choudhury, P., Gahalaut, K., Dumka, R., Gahalaut, VK., Singh, A.K., Kumar, S., 2018. GPS measurement of land subsidence in Gandhinagar, Gujarat (Western India), due to groundwater depletion. Environmental Earth Sciences 77, 1–5.

Chousianitis, K., Ganas, A., Evangelidis, C.P., 2015. Strain and rotation rate patterns of mainland Greece from continuous GPS data and comparison between seismic and geodetic moment release. Journal of Geophysical Research: Solid Earth 120, 3909–3931.

Chousianitis, K., Sboras, S., Mouslopoulou, V., Chouliaras, G., Hristopulos, D.T., 2024. The Upper Crustal Deformation Field of Greece Inferred From GPS Data and Its Correlation With Earthquake Occurrence. Journal of Geophysical Research: Solid Earth 129, e2023JB028004. doi:10.1029/2023JB028004.

Clette, F., Lefèvre, L., 2015. SILSO Sunspot Number V2.0. doi:10.24414/QNZA-AC80.

Cohen-Waeber, J., Bürgmann, R., Chaussard, E., Giannico, C., Ferretti, A., 2018. Spatiotemporal Patterns of Precipitation-Modulated Landslide Deformation From Independent Component Analysis of InSAR Time Series. Geophysical Research Letters 45, 1878–1887. doi:10.1002/2017GL075950.

Collins, W.J., 2003. Slab pull, mantle convection, and Pangaean assembly and dispersal. Earth and Planetary Science Letters 205, 225–237. doi:10.1016/S0012-821X(02)01043-9.

Copley, A., Avouac, J.P., Royer, J.Y., 2010. India-Asia collision and the Cenozoic slowdown of the Indian plate: Implications for the forces driving plate motions. Journal of Geophysical Research: Solid Earth 115. doi:10.1029/2009JB006634.

Copley, A., Boait, F., Hollingsworth, J., Jackson, J., McKenzie, D., 2009. Subparallel thrust and normal faulting in Albania and the roles of gravitational potential energy and rheology contrasts in mountain belts. Journal of Geophysical Research: Solid Earth 114. doi:10.1029/2008JB005931.

Copley, A., Jackson, J., 2006. Active tectonics of the Turkish-Iranian Plateau. Tectonics 25. doi:10.1029/2005TC001906.

Costantini, M., Minati, F., Trillo, F., Ferretti, A., Novali, F., Passera, E., Dehls, J., Larsen, Y., Marinkovic, P., Eineder, M., Brcic, R., Siegmund, R., Kotzerke, P., Probeck, M., Kenyeres, A., Proietti, S., Solari, L., Andersen, H.S., 2021. European Ground Motion Service (EGMS), in: 2021 IEEE International Geoscience and Remote Sensing Symposium IGARSS, pp. 3293–3296. doi:10.1109/IGARSS47720.2021.9553562.

d'Agostino, N., Métois, M., Koci, R., Duni, L., Kuka, N., Ganas, A., Georgiev, I., Jouanne, F., Kaludjerovic, N., Kandić, R., 2020. Active crustal deformation and rotations in the southwestern Balkans from continuous GPS measurements. Earth and Planetary Science Letters 539, 116246.

Dai, C., Gan, W., Li, Z., Liang, S., Xiao, G., Zhang, K., Zhang, L., 2023. Characteristics of regional GPS crustal deformation before the 2021 yunnan yangbi ms 6.4 earthquake and its implications for determining potential areas of future strong earthquakes. Remote Sensing 15, 3195.

Dal Zilio, L., Jolivet, R., van Dinther, Y., 2020. Segmentation of the Main Himalayan Thrust illuminated by Bayesian inference of interseismic coupling. Geophysical Research Letters 47, e2019GL086424.

Dalaison, M., Jolivet, R., van Rijsingen, E.M., Michel, S., 2021. The Interplay Between Seismic and Aseismic Slip Along the Chaman Fault Illuminated by InSAR. Journal of Geophysical Research: Solid Earth 126, e2021JB021935. doi:10.1029/2021JB021935.

Daout, S., D'Agostino, N., Pathier, E., Socquet, A., Lavé, J., Doin, M.P., Riesner, M., Benedetti, L., 2023. Along-strike variations of strain partitioning within the Apennines determined from large-scale multi-temporal InSAR analysis. Tectonophysics 867, 230076. doi:10.1016/j.tecto.2023.230076.

Daout, S., Sudhaus, H., Kausch, T., Steinberg, A., Dini, B., 2019. Interseismic and Postseismic Shallow Creep of the North Qaidam Thrust Faults Detected with a Multitemporal InSAR Analysis. Journal of Geophysical Research: Solid Earth 124, 7259–7279. doi:10.1029/2019JB017692.

DeMets, C., Merkouriev, S., Jade, S., 2020. High-resolution reconstructions and GPS estimates of India–Eurasia and India–Somalia plate motions: 20 Ma to the present. Geophysical Journal International 220, 1149–1171. doi:10.1093/gji/ggz508.

Devachandra, M., Kundu, B., Catherine, J., Kumar, A., Gahalaut, V.K., 2014. Global positioning system (GPS) measurements of crustal deformation across the frontal eastern Himalayan syntaxis and seismic-hazard assessment. Bulletin of the Seismological Society of America 104, 1518–1524.

Diao, F., Xiong, X., Wang, R., Walter, T.R., Wang, Y., Wang, K., 2019. Slip rate variation along the Kunlun fault (Tibet): Results from new GPS observations and a viscoelastic earthquake-cycle deformation model. Geophysical Research Letters 46, 2524–2533.

Dimitrov, N., Nakov, R., 2022. GPS Results from long time monitoring of geodynamic processes in South-Western Bulgaria. Applied Sciences 12, 2682.

Ding, L., Kapp, P., Cai, F., Garzione, C.N., Xiong, Z., Wang, H., Wang, C., 2022. Timing and mechanisms of Tibetan Plateau uplift. Nature Reviews Earth & Environment 3, 652–667. doi:10.1038/s43017-022-00318-4.

Dodds, N., Daout, S., Walker, R.T., Begenjev, G., Bezmenov, Y., Mirzin, R., Parsons, B., 2022. Interseismic deformation and strain-partitioning along the Main Köpetdag Fault, Turkmenistan, with Sentinel-1 InSAR time-series. Geophysical Journal International 230, 1612–1629. doi:10.1093/gji/ggac139.

Du, J., Fu, B., Guo, Q., Shi, P., Xue, G., Xu, H., 2019. Segmentation and termination of the surface rupture zone produced by the 1932 Ms 7.6 Changma earthquake: New insights into the slip partitioning of the eastern Altyn Tagh fault system. Lithosphere 12, 19–39. doi:10.1130/L1113.1.

Duong, N.A., Sagiya, T., Kimata, F., To, T.D., Hai, V.Q., Cong, D.C., Binh, N.X., Xuyen, N.D., 2013. Contemporary horizontal crustal movement estimation for northwestern Vietnam inferred from repeated GPS measurements. Earth, Planets and Space 65, 1399–1410.

Ebmeier, S.K., Andrews, B.J., Araya, M.C., Arnold, D.W.D., Biggs, J., Cooper, C., Cottrell, E., Furtney, M., Hickey, J., Jay, J., Lloyd, R., Parker, A.L., Pritchard, M.E., Robertson, E., Venzke, E., Williamson, J.L., 2018. Synthesis of global satellite observations of magmatic and volcanic deformation: Implications for volcano monitoring & the lateral extent of magmatic domains. Journal of Applied Volcanology 7, 2. doi:10.1186/s13617-018-0071-3.

Ekström, G., Nettles, M., Dziewoński, A.M., 2012. The global CMT project 2004–2010: Centroid-moment tensors for 13,017 earthquakes. Physics of the Earth and Planetary Interiors 200–201, 1–9. doi:10.1016/j.pepi.2012.04.002.

Elliott, A., Elliott, J., Hollingsworth, J., Kulikova, G., Parsons, B., Walker, R., 2020. Satellite imaging of the 2015 M7.2 earthquake in the Central Pamir, Tajikistan, elucidates a sequence of shallow strike-slip ruptures of the Sarez-Karakul fault. Geophysical Journal International 221, 1696–1718. doi:10.1093/gji/ggaa090.

Elliott, J., Walters, R., Wright, T., 2016. The role of space-based observation in understanding and responding to active tectonics and earthquakes. Nature Communications 7, 13844. doi:10.1038/ncomms13844.

Elliott, J.R., 2020. Earth Observation for the Assessment of Earthquake Hazard, Risk and Disaster Management. Surveys in Geophysics 41, 1323–1354. doi:10.1007/s10712-020-09606-4.

Elliott, J.R., Biggs, J., Parsons, B., Wright, T.J., 2008. InSAR slip rate determination on the Altyn Tagh Fault, northern Tibet, in the presence of topographically correlated atmospheric delays. Geophysical Research Letters 35. doi:10.1029/2008GL033659.

England, P., Houseman, G., 1989. Extension during continental convergence, with application to the Tibetan Plateau. Journal of Geophysical Research: Solid Earth 94, 17561–17579. doi:10.1029/JB094iB12p17561.

England, P., Houseman, G., Nocquet, J.M., 2016. Constraints from GPS measurements on the dynamics of deformation in Anatolia and the Aegean. Journal of Geophysical Research: Solid Earth 121, 8888–8916. doi:10.1002/2016JB013382.

England, P., Molnar, P., 2005. Late Quaternary to decadal velocity fields in Asia. Journal of Geophysical Research: Solid Earth 110. doi:10.1029/2004JB003541.

England, P., Molnar, P., 2015. Rheology of the lithosphere beneath the central and western Tien Shan. Journal of Geophysical Research: Solid Earth 120, 3803–3823. doi:10.1002/2014JB011733.

England, P., Molnar, P., 2022. Changes in Plate Motions Caused by Increases in Gravitational Potential Energy of Mountain Belts. Geochemistry, Geophysics, Geosystems 23, e2022GC010389. doi:10.1029/2022GC010389.

Ergeshov, I.M., Makhmudov, M.D., Fazilova, D.S., 2020. GPS Data Pprocessing in GAMIT/GLOBK: Case Study of Permanent Stations of the Uzbekistan Network. Universum :technical sciences , 50–55.

Ergintav, S., Floyd, M., Paradissis, D., Karabulut, H., Vernant, P., Masson, F., Georgiev, I., Konca, A.Ö., Doğan, U., King, R., et al., 2023. New geodetic constraints on the role of faults and blocks vs. distribute strain in the Nubia-Arabia-Eurasia zone of active plate interactions. Turkish Journal of Earth Sciences 32, 248–261.

Ergintav, S., Vernant, P., Tan, O., Karabulut, H., Özarpacı, S., Floyd, M., Konca, A.Ö., Çakır, Z., Acarel, D., Çakmak, R., Vasyura-Bathke, H., Doğan, U., Kurt, A.İ., Özdemir, A., Ayruk, E.T., Turğut, M., Özel, Ö., Farımaz, İ., 2024. Unexpected far-field deformation of the 2023 Kahramanmaraş earthquakes revealed by space geodesy. Science 386, 328–335. doi:10.1126/science.ado4220.

Ergintav, SEMIH., Reilinger, RE., Çakmak, R., Floyd, M., Cakir, Z., Doğan, U., King, RW., McClusky, S., Özener, H., 2014. Istanbul's earthquake hot spots: Geodetic constraints on strain accumulation along faults in the Marmara seismic gap. Geophysical Research Letters 41, 5783–5788.

Eyidoğan, H., Barka, A., 1996. The 1 October 1995 Dinar earthquake, SW Turkey. Terra Nova 8, 479–485. doi:10.1111/j.1365-3121.1996.tb00773.x.

Faccenna, C., Becker, T.W., Holt, A.F., Brun, J.P., 2021. Mountain building, mantle convection, and supercontinents: Holmes (1931) revisited. Earth and Planetary Science Letters 564, 116905. doi:10.1016/j.epsl.2021.116905.

Fang, J., Houseman, G.A., Wright, T.J., Evans, L.A., Craig, T.J., Elliott, J.R., Hooper, A., 2024a. The Dynamics of the India-Eurasia Collision: Faulted Viscous Continuum Models Constrained by High-Resolution Sentinel-1 InSAR and GNSS Velocities. Journal of Geophysical Research: Solid Earth 129, e2023JB028571. doi:10.1029/2023JB028571.

Fang, J., Ou, Q., Wright, T.J., Okuwaki, R., Amey, R.M.J., Craig, T.J., Elliott, J.R., Hooper, A., Lazecký, M., Maghsoudi, Y., 2022a. Earthquake Cycle Deformation Associated With the 2021 MW 7.4 Maduo (Eastern Tibet) Earthquake: An Intrablock Rupture Event on a Slow-Slipping Fault From Sentinel-1 InSAR and Teleseismic Data. Journal of Geophysical Research: Solid Earth 127, e2022JB024268. doi:10.1029/2022JB024268.

Fang, J., Wright, T.J., Johnson, K.M., Ou, Q., Styron, R., Craig, T.J., Elliott, J.R., Hooper, A., Zheng, G., 2024b. Strain Partitioning in the Southeastern Tibetan Plateau From Kinematic Modeling of High-Resolution Sentinel-1 InSAR and GNSS. Geophysical Research Letters 51, e2024GL111199. doi:10.1029/2024GL111199.

Fang, Z., ZOU, R., LI, Z., WANG, M., TAN, K., YANG, S., WANG, Q., 2022b. Present-day vertical motions in southern Tibetan Plateau constrained by cGPS measurements. Chinese Journal of Geophysics 65, 1965–1979.

Fathian, A., Atzori, S., Nazari, H., Reicherter, K., Salvi, S., Svigkas, N., Tatar, M., Tolomei, C., Yaminifard, F., 2021. Complex co- and postseismic faulting of the 2017–2018 seismic sequence in western Iran revealed by InSAR and seismic data. Remote Sensing of Environment 253, 112224. doi:10.1016/j.rse.2020.112224.

Fazilova, D., Ehgamberdiev, S., Kuzin, S., 2018. Application of time series modeling to a national reference frame realization. Geodesy and Geodynamics 9, 281–287.

Fazilova, D., Makhmudov, M., Khalimov, B., 2025a. The analysis of crustal deformation patterns in the Tashkent region, Uzbekistan, derived from GNSS data over the period 2018–2023. Geodesy and Geodynamics 16, 137–146.

Fazilova, D., Tukhtameshov, F., Rakhimberdieva, M., Kazakov, A., Magdiev, K., 2025b. GNSS-based subsidence monitoring of Shurtan's gas reservoir in Uzbekistan. Acta IMEKO 14, 1–6.

Flesch, L.M., Haines, A.J., Holt, W.E., 2001. Dynamics of the India-Eurasia collision zone. Journal of Geophysical Research: Solid Earth 106, 16435–16460. doi:10.1029/2001JB000208.

Floyd, M., King, R., Paradissis, D., Karabulut, H., Ergintav, S., Raptakis, K., Reilinger, R., 2023. Variations in coupling and deformation along the Hellenic subduction zone. Turkish Journal of Earth Sciences 32, 262–274.

Frohling, E., Szeliga, W., 2016. GPS constraints on interplate locking within the Makran subduction zone. Geophysical Supplements to the Monthly Notices of the Royal Astronomical Society 205, 67–76.

Fu, Y., Freymueller, J.T., 2012. Seasonal and long-term vertical deformation in the Nepal Himalaya constrained by GPS and GRACE measurements. Journal of Geophysical Research: Solid Earth 117.

Fu, Z., Xu, L., Wang, Y., 2020. Seismic risk on the northern Xiaojiang fault implied by the latest and nearest GPS observations. Pure and Applied Geophysics 177, 661–679.

Funning, G.J., Parsons, B., Wright, T.J., 2007. Fault slip in the 1997 Manyi, Tibet earthquake from linear elastic modelling of InSAR displacements. Geophysical Journal International 169, 988–1008. doi:10.1111/j.1365-246X.2006.03318.x.

Gahalaut, V.K., Gahalaut, K., Dumka, R.K., Chaudhury, P., Yadav, R.K., 2019. Geodetic evidence of high compression across seismically active Kachchh paleorift, India. Tectonics 38, 3097–3107.

Galloway, D.L., Burbey, T.J., 2011. Review: Regional land subsidence accompanying groundwater extraction. Hydrogeology Journal 19, 1459–1486. doi:10.1007/s10040-011-0775-5.

Gan, W., Molnar, P., Zhang, P., Xiao, G., Liang, S., Zhang, K., Li, Z., Xu, K., Zhang, L., 2022. Initiation of clockwise rotation and eastward transport of southeastern Tibet inferred from deflected fault traces and GPS observations. GSA Bulletin 134, 1129–1142.

Gautam, P.K., Gahalaut, VK., Prajapati, S.K., Kumar, N., Yadav, R.K., Rana, N., Dabral, C.P., 2017. Continuous GPS measurements of crustal deformation in garhwal-kumaun himalaya. Quaternary International 462, 124–129.

Gharbia, A.Y.A., Gomaa, A., Saleh, M., Mousa, A.E., Abbas, I.A., Hassan, M.R., 2025. GNSS geodetic velocity prediction using ensemble tree models in Abu-Dabbab, Egypt. The Egyptian Journal of Remote Sensing and Space Sciences 28, 337–347.

Ghasemi Khalkhali, S.A., Ardalan, A.A., Karimi, R., 2021. A time series analysis of permanent GNSS stations in the northwest network of Iran. Annals of Geophysics 64, GD218–GD218.

Ghasemi Khalkhali, S.A., Azmoudeh Ardalan, A., Karimi, R., 2023a. Investigation of subsidence in the northeastern of Iran by estimating the velocity vector and uncertainty of permanent GPS stations. Journal of the Earth and Space Physics 49, 35–51.

Ghasemi Khalkhali, S.A., Azmoudeh Ardalan, A., Karimi, R., 2023b. On the anomalous crustal motions in southeastern Iran. Proceedings of the 20th Iranian Geophysical Conference .

Gorshkov, V., Gusev, I., Malkin, Z., Shestakov, N., 2023. National Report for the IAG of the IUGG 2019-2022: Positioning and applications. arXiv preprint arXiv:2307.11117 , 61–65arXiv:2307.11117.

Gruber, S., 2012. Derivation and analysis of a high-resolution estimate of global permafrost zonation. The Cryosphere 6, 221–233. doi:10.5194/tc-6-221-2012.

Guo, R., Li, L., Zhang, W., Zhang, Y., Tang, X., Dai, K., Li, Y., Zhang, L., Wang, J., 2023. Kinematic Slip Evolution During the 2022 Ms 6.8 Luding, China, Earthquake: Compatible With the Preseismic Locked Patch. Geophysical Research Letters 50, e2023GL103164. doi:10.1029/2023GL103164.

Gupta, T.D., Riguzzi, F., Dasgupta, S., Mukhopadhyay, B., Roy, S., Sharma, S., 2015. Kinematics and strain rates of the Eastern Himalayan Syntaxis from new GPS campaigns in Northeast India. Tectonophysics 655, 15–26.

Güvercin, S.E., Karabulut, H., Konca, A.Ö., Doğan, U., Ergintav, S., 2022. Active seismotectonics of the East Anatolian Fault. Geophysical Journal International 230, 50–69, doi:10.1093/gji/ggac045.

Hamiel, Y., Piatibratova, O., 2021. Spatial variations of slip and creep rates along the southern and central Dead Sea Fault and the Carmel–Gilboa Fault System. Journal of Geophysical Research: Solid Earth 126, e2020JB021585.

Hao, L., Wengui, H., Daoyang, Y., Yanxiu, S., 2015. Slip Rate of Yema River–Daxue Mountain Fault since the Late Pleistocene and Its Implications on the Deformation of the Northeastern Margin of the Tibetan Plateau. Acta Geologica Sinica - English Edition 89, 561–574. doi:10.1111/1755-6724.12447.

Hao, M., Freymueller, J.T., Wang, Q., Cui, D., Qin, S., 2016. Vertical crustal movement around the southeastern Tibetan Plateau constrained by GPS and GRACE data. Earth and Planetary Science Letters 437, 1–8.

Hao, M., Li, Y., Song, S., Zhuang, W., Wang, Q., 2024. Strain partitioning, transfer and implications for the ongoing process of intracontinental graben formation in the northwestern margin of the Ordos block, China: Insights from densified GNSS measurements. Geophysical Journal International 238, 1314–1333.

Hao, M., Li, Y., Zhuang, W., 2019. Crustal movement and strain distribution in East Asia revealed by GPS observations. Scientific Reports 9, 16797.

Hao, M., Wang, Q., Zhang, P., Li, Z., Li, Y., Zhuang, W., 2021. "Frame wobbling" causing crustal deformation around the Ordos block. Geophysical Research Letters 48, e2020GL091008.

Harkins, N., Kirby, E., Shi, X., Wang, E., Burbank, D., Chun, F., 2010. Millennial slip rates along the eastern Kunlun fault: Implications for the dynamics of intracontinental deformation in Asia. Lithosphere 2, 247–266. doi:10.1130/L85.1.

Harris, R.A., 2017. Large earthquakes and creeping faults. Reviews of Geophysics 55, 169–198. doi:10.1002/2016RG000539.

Hessami, K., Jamali, F., 2006. Explanatory Notes to the Map of Major Active Faults of Iran. Journal of Seismology and Earthquake Engineering 8, 1–11.

Hollingsworth, J., Jackson, J., Walker, R., Reza Gheitanchi, M., Javad Bolourchi, M., 2006. Strike-slip faulting, rotation, and along-strike elongation in the Kopeh Dagh mountains, NE Iran. Geophysical Journal International 166, 1161–1177. doi:10.1111/j.1365-246X.2006.02983.x.

Houseman, G., England, P., 1986. Finite strain calculations of continental deformation; 1. Method and general results for convergent zones. Journal of Geophysical Research: Solid Earth 91, 3651–3663. doi:10.1029/JB091iB03p03651.

Houseman, G.A., Molnar, P., 1997. Gravitational (Rayleigh–Taylor) instability of a layer with non-linear viscosity and convective thinning of continental lithosphere. Geophysical Journal International 128, 125–150. doi:10.1111/j.1365-246X.1997.tb04075.x.

Huang, Z., Zhou, Y., 2022. A Complete Map of Fine-Scale Slip Rate Distribution and Earthquake Potential Along the Haiyuan Fault System. Geophysical Research Letters 49, e2022GL101805. doi:10.1029/2022GL101805.

Huang, Z., Zhou, Y., Zhang, P., 2023. Newly discovered shallow creep along the Gozha Co fault in northwestern Tibet: Spatial extent, rate and temporal evolution. Earth and Planetary Science Letters 621, 118388. doi:10.1016/j.epsl.2023.118388.

Hussain, E., Kalaycıoğlu, S., Milliner, C.W.D., Çakir, Z., 2023. Preconditioning the 2023 Kahramanmaraş (Türkiye) earthquake disaster. Nature Reviews Earth & Environment 4, 287–289. doi:10.1038/s43017-023-00411-2.

Hussain, E., Wright, T.J., Walters, R.J., Bekaert, D.P.S., Lloyd, R., Hooper, A., 2018. Constant strain accumulation rate between major earthquakes on the North Anatolian Fault. Nature Communications 9, 1392. doi:10.1038/s41467-018-03739-2.

Ischuk, A., Bendick, R., Rybin, A., Molnar, P., Khan, S.F., Kuzikov, S., Mohadjer, S., Saydullaev, U., Ilyasova, Z., Schelochkov, G., Zubovich, A.V., 2013. Kinematics of the Pamir and Hindu Kush regions from GPS geodesy. Journal of Geophysical Research: Solid Earth 118, 2408–2416. doi:10.1002/jgrb.50185.

Ismail-Zadeh, A., Adamia, S., Chabukiani, A., Chelidze, T., Cloetingh, S., Floyd, M., Gorshkov, A., Gvishiani, A., Ismail-Zadeh, T., Kaban, M.K., Kadirov, F., Karapetyan, J., Kangarli, T., Kiria, J., Koulakov, I., Mosar, J., Mumladze, T., Müller, B., Sadradze, N., Safarov, R., Schilling, F., Soloviev, A., 2020. Geodynamics, seismicity, and seismic hazards of the Caucasus. Earth-Science Reviews 207, 103222. doi:10.1016/j.earscirev.2020.103222.

Jackson, M., Bilham, R., 1994. Constraints on Himalayan deformation inferred from vertical velocity fields in Nepal and Tibet. Journal of Geophysical Research: Solid Earth 99, 13897–13912. doi:10.1029/94JB00714.

Jade, S., Mir, R.R., Vivek, C.G., Shrungeshwara, TS., Parvez, IA., Chandra, R., Babu, D.S., Gupta, S.V., Ankit, Rajana, S.S.K., et al., 2020. Crustal deformation rates in Kashmir valley and adjoining regions from continuous GPS measurements from 2008 to 2019. Scientific reports 10, 17927.

Jade, S., Mukul, M., Gaur, VK., Kumar, K., Shrungeshwar, TS., Satyal, GS., Dumka, R.K., Jagannathan, S., Ananda, MB., Kumar, P.D., et al., 2014. Contemporary deformation in the Kashmir–Himachal, Garhwal and Kumaon Himalaya: Significant insights from 1995–2008 GPS time series. Journal of Geodesy 88, 539–557.

Jade, S., Raghavendra Rao, HJ., Vijayan, MSM., Gaur, VK., Bhatt, BC., Kumar, K., Jaganathan, S., Ananda, MB., Dileep Kumar, P., 2011. GPS-derived deformation rates in northwestern Himalaya and Ladakh. International Journal of Earth Sciences 100, 1293–1301.

Jade, S., Shrungeshwara, TS., Kumar, K., Choudhury, P., Dumka, R.K., Bhu, H., 2017. India plate angular velocity and contemporary deformation rates from continuous GPS measurements from 1996 to 2015. Scientific reports 7, 11439.

Jin, Z., Fialko, Y., Zubovich, A., Schöne, T., 2022. Lithospheric Deformation Due To the 2015 M7.2 Sarez (Pamir) Earthquake Constrained by 5 years of Space Geodetic Observations. Journal of Geophysical Research: Solid Earth 127, e2021JB022461. doi:10.1029/2021JB022461.

Jolivet, L., Faccenna, C., 2000. Mediterranean extension and the Africa-Eurasia collision. Tectonics 19, 1095–1106. doi:10.1029/2000TC900018.

Jolivet, M., Dominguez, S., Charreau, J., Chen, Y., Li, Y., Wang, Q., 2010. Mesozoic and Cenozoic tectonic history of the central Chinese Tian Shan: Reactivated tectonic structures and active deformation. Tectonics 29. doi:10.1029/2010TC002712.

Jolivet, R., Frank, W.B., 2020. The Transient and Intermittent Nature of Slow Slip. AGU Advances 1, e2019AV000126. doi:10.1029/2019AV000126.

Jolivet, R., Jara, J., Dalaison, M., Rouet-Leduc, B., Özdemir, A., Dogan, U., Çakir, Z., Ergintav, S., Dubernet, P., 2023. Daily to centennial behavior of aseismic slip along the central section of the North Anatolian Fault. Journal of Geophysical Research: Solid Earth 128, e2022JB026018.

Jouanne, F., Mugnier, J.L., Sapkota, S.N., Bascou, P., Pecher, A., 2017. Estimation of coupling along the Main Himalayan Thrust in the central Himalaya. Journal of Asian Earth Sciences 133, 62–71.

Jouanne, F., Munawar, N., Mugnier, J.L., Ahmed, A., Awan, A.A., Bascou, P., Vassallo, R., 2020. Seismic coupling quantified on inferred décollements beneath the western syntaxis of the Himalaya. Tectonics 39, e2020TC006122.

Kadirov, FA., Guliyev, IS., Feyzullayev, AA., Safarov, RT., Mammadov, SK., Babayev, GR., Rashidov, TM., 2014. GPS-based crustal deformations in Azerbaijan and their influence on seismicity and mud volcanism. Izvestiya, Physics of the Solid Earth 50, 814–823.

Kannaujiya, S., Yadav, R.K., Sarkar, T., Sharma, G., Chauhan, P., Pal, S.K., Roy, P.N., Gautam, P.K., Taloor, A.K., Yadav, A., et al., 2022. Unraveling seismic hazard by estimating prolonged crustal strain buildup in Kumaun-Garhwal, Northwest Himalaya using GPS measurements. Journal of Asian Earth Sciences 223, 104993.

Khorrami, F., Vernant, P., Masson, F., Nilfouroushan, F., Mousavi, Z., Nankali, H., Saadat, S.A., Walpersdorf, A., Hosseini, S., Tavakoli, P., et al., 2019. An up-to-date crustal deformation map of Iran using integrated campaign-mode and permanent GPS velocities. Geophysical Journal International 217, 832–843.

Kirby, E., Harkins, N., Wang, E., Shi, X., Fan, C., Burbank, D., 2007. Slip rate gradients along the eastern Kunlun fault. Tectonics 26. doi:10.1029/2006TC002033.

Kreemer, C., Blewitt, G., Klein, E.C., 2014. A geodetic plate motion and Global Strain Rate Model. Geochemistry, Geophysics, Geosystems 15, 3849–3889. doi:10.1002/2014GC005407.

Krüger, F., Kulikova, G., Landgraf, A., 2017. Instrumental magnitude constraints for the 11 July 1889, Chilik earthquake. Geological Society, London, Special Publications 432, 41–72. doi:10.1144/SP432.8.

Kufner, S.K., Kakar, N., Bezada, M., Bloch, W., Metzger, S., Yuan, X., Mechie, J., Ratschbacher, L., Murodkulov, S., Deng, Z., et al., 2021. The Hindu Kush slab breakoff as revealed by deep structure and crustal deformation. Nature communications 12, 1685.

Kulikova, G., 2016. Source Parameters of the Major Historical Earthquakes in the Tien-Shan Region from the Late 19th to the Early 20th Century. Ph.D. thesis. University of Potsdam. Berlin.

Kulikova, G., Krüger, F., 2015. Source process of the 1911 M8.0 Chon-Kemin earthquake: Investigation results by analogue seismic records. Geophysical Journal International 201, 1891–1911. doi:10.1093/gji/ggv091.

Kumar, P., Malik, J.N., Gahalaut, V.K., Yadav, R.K., Singh, G., 2023. Evidence of strain accumulation and coupling variation in the Himachal region of NW Himalaya from short term geodetic measurements. Tectonics 42, e2022TC007690.

Kundu, B., Yadav, R.K., Bali, B.S., Chowdhury, S., Gahalaut, VK., 2014. Oblique convergence and slip partitioning in the NW Himalaya: Implications from GPS measurements. Tectonics 33, 2013–2024.

Kurt, A.I., ÖZBAKIR, A.D., CİNGÖZ, AYHAN., Ergintav, S., DOĞAN, UĞUR., ÖZARPACI, SEDA., 2023. Contemporary velocity field for Turkey inferred from combination of a dense network of long term GNSS observations. Turkish Journal of Earth Sciences 32, 275–293.

Lasserre, C., Peltzer, G., Crampé, F., Klinger, Y., Van der Woerd, J., Tapponnier, P., 2005. Coseismic deformation of the 2001 M = 7.8 Kokoxili earthquake in Tibet, measured by synthetic aperture radar interferometry. Journal of Geophysical Research: Solid Earth 110. doi:10.1029/2004JB003500.

Li, H., Pan, J., Lin, A., Sun, Z., Liu, D., Zhang, J., Li, C., Liu, K., Chevalier, M.L., Yun, K., Gong, Z., 2016. Coseismic Surface Ruptures Associated with the 2014 Mw 6.9 Yutian Earthquake on the Altyn Tagh Fault, Tibetan Plateau. Bulletin of the Seismological Society of America 106, 595–608. doi:10.1785/0120150136.

Li, J., Yao, Y., Li, R., Yusan, S., Li, G., Freymueller, J.T., Wang, Q., 2022. Present-Day strike-slip faulting and thrusting of the Kepingtage fold-and-thrust belt in southern Tianshan: Constraints from GPS observations. Geophysical Research Letters 49, e2022GL099105.

Li, X., Jónsson, S., Cao, Y., 2021. Interseismic Deformation From Sentinel-1 Burst Overlap Interferometry: Application to the Southern Dead Sea Fault. Geophysical Research Letters 48, e2021GL093481. doi:10.1029/2021GL093481.

Li, X., Xu, W., Jónsson, S., Klinger, Y., Zhang, G., 2020. Source Model of the 2014 Mw 6.9 Yutian Earthquake at the Southwestern End of the Altyn Tagh Fault in Tibet Estimated from Satellite Images. Seismological Research Letters 91, 3161–3170. doi:10.1785/0220190361.

Li, Y., Chen, L., Liu, S., Yang, S., Yang, X., Zhang, G., 2015. Coseismic Coulomb stress changes caused by the Mw6.9 Yutian earthquake in 2014 and its correlation to the 2008 Mw7.2 Yutian earthquake. Journal of Asian Earth Sciences 105, 468–475. doi:10.1016/j.jseaes.2015.02.025.

Li, Y., Shan, X., Qu, C., Liu, Y., Han, N., 2018. Crustal deformation of the Altyn Tagh fault based on GPS. Journal of Geophysical Research: Solid Earth 123, 10309–10322.

Li, Y., Shan, X., Qu, C., Zhang, Y., Song, X., Jiang, Y., Zhang, G., Nocquet, J.M., Gong, W., Gan, W., et al., 2017. Elastic block and strain modeling of GPS data around the Haiyuan-Liupanshan fault, northeastern Tibetan Plateau. Journal of Asian Earth Sciences 150, 87–97.

Lindsey, E.O., Wang, Y., Aung, L.T., Chong, J.H., Qiu, Q., Mallick, R., Feng, L., Aung, P.S., Tin, T.Z.H., Min, S.M., et al., 2023. Active subduction and strain partitioning in western Myanmar revealed by a dense survey GNSS network. Earth and Planetary Science Letters 622, 118384.

Lukhnev, AV., Sankov, VA., Miroshnichenko, AI., Byzov, LM., Sankov, AV., Lukhneva, OF., 2025. Velocities and strain rates in the Baikal-Mongolia region from the GNSS data. Journal of Asian Earth Sciences 281, 106500.

Lv, X., Amelung, F., Shao, Y., 2022. Widespread Aseismic Slip Along the Makran Megathrust Triggered by the 2013 Mw 7.7 Balochistan Earthquake. Geophysical Research Letters 49, e2021GL097411. doi:10.1029/2021GL097411.

Mackenzie, D., Walker, R., Abdrakhmatov, K., Campbell, G., Carr, A., Gruetzner, C., Mukambayev, A., Rizza, M., 2018. A creeping intracontinental thrust fault: Past and present slip-rates on the Northern edge of the Tien Shan, Kazakhstan. Geophysical Journal International 215, 1148–1170. doi:10.1093/gji/ggy339.

Maddahi, H., Rahimi, A., Amighpey, M., 2025. Evaluating current-day vertical deformation in the North Tehran transpressional zone using global positioning system and precise leveling data. Advanced Applied Geology 15.

Maghsoudi, Y., Hooper, A.J., Wright, T.J., Lazecky, M., Ansari, H., 2022. Characterizing and correcting phase biases in short-term, multilooked interferograms. Remote Sensing of Environment 275, 113022. doi:10.1016/j.rse.2022.113022.

Mallick, R., Lindsey, E.O., Feng, L., Hubbard, J., Banerjee, P., Hill, E.M., 2019. Active convergence of the India-Burma-Sunda plates revealed by a new continuous GPS network. Journal of Geophysical Research: Solid Earth 124, 3155–3171.

Mantovani, E., Viti, M., Cenni, N., Babbucci, D., Tamburelli, C., 2015. Present velocity field in the Italian region by GPS data: Geodynamic/tectonic implications. international Journal of Geosciences 6, 1285–1316.

Marechal, A., Mazzotti, S., Cattin, R., Cazes, G., Vernant, P., Drukpa, D., Thinley, K., Tarayoun, A., Le Roux-Mallouf, R., Thapa, B.B., et al., 2016. Evidence of interseismic coupling variations along the Bhutan Himalayan arc from new GPS data. Geophysical Research Letters 43, 12–399.

Masson, F., Hamiel, Y., Agnon, A., Klinger, Y., Deprez, A., 2015. Variable behavior of the Dead Sea Fault along the southern Arava segment from GPS measurements. comptes rendus geoscience 347, 161–169.

McKenzie, D., 1972. Active Tectonics of the Mediterranean Region. Geophysical Journal International 30, 109–185. doi:10.1111/j.1365-246X.1972.tb02351.x.

McNab, F., Sloan, R.A., Walker, R.T., 2019. Simultaneous orthogonal shortening in the Afghan-Tajik Depression. Geology 47, 862–866. doi:10.1130/G46090.1.

McQuarrie, N., Stock, J.M., Verdel, C., Wernicke, B.P., 2003. Cenozoic evolution of Neotethys and implications for the causes of plate motions. Geophysical Research Letters 30. doi:10.1029/2003GL017992.

Meade, B.J., Klinger, Y., Hetland, E.A., 2013. Inference of Multiple Earthquake-Cycle Relaxation Timescales from Irregular Geodetic Sampling of Interseismic Deformation. Bulletin of the Seismological Society of America 103, 2824–2835. doi:10.1785/0120130006.

Mériaux, A.S., Ryerson, F.J., Tapponnier, P., Van der Woerd, J., Finkel, R.C., Xu, X., Xu, Z., Caffee, M.W., 2004. Rapid slip along the central Altyn Tagh Fault: Morphochronologic evidence from Cherchen He and Sulamu Tagh. Journal of Geophysical Research: Solid Earth 109. doi:10.1029/2003JB002558.

Metzger, S., Ischuk, A., Deng, Z., Ratschbacher, L., Perry, M., Kufner, S.K., Bendick, R., Moreno, M., 2020. Dense GNSS profiles across the northwestern tip of the India-Asia collision zone: Triggered slip and westward flow of the Peter the First Range, Pamir, into the Tajik Depression. Tectonics 39, e2019TC005797.

Metzger, S., Łukasz Gagała, Lothar Ratschbacher, Lazecký, M., Maghsoudi, Y., Schurr, B., 2021. Tajik Depression and Greater Pamir Neotectonics From InSAR Rate Maps. Journal of Geophysical Research: Solid Earth 126, e2021JB022775. doi:10.1029/2021JB022775.

Metzger, S., Schurr, B., Ratschbacher, L., Sudhaus, H., Kufner, S.K., Schöne, T., Zhang, Y., Perry, M., Bendick, R., 2017. The 2015 Mw7.2 Sarez Strike-Slip Earthquake in the Pamir Interior: Response to the Underthrusting of India's Western Promontory. Tectonics 36, 2407–2421. doi:10.1002/2017TC004581.

Meyer, P., Jouanne, F., Doin, M.P., Ahmed, A., Awan, A.A., Mugnier, J.L., 2024. Present-day quantification of seismic coupling along the décollement level beneath the Potwar Plateau region in Pakistan western Himalaya. Earth and Planetary Science Letters 637, 118723.

Milyukov, VK., Mironov, AP., Ovsyuchenko, AN., Gorbatikov, AV., Steblov, GM., Korzhenkov, AM., Drobyshev, VN., Khubaev, K.M., Agibalov, AO., Sentsov, AA., et al., 2022. Contemporary tectonic movements of the Western Caucasus and the Ciscaucasia based on satellite-geodetic observations. Geotectonics 56, 41–54.

Milyukov, VK., Mironov, AP., Rogozhin, EA., Steblov, GM., 2015. Velocities of contemporary movements of the Northern Caucasus estimated from GPS observations. Geotectonics 49, 210–218.

Mironov, AP., Milyukov, VK., Steblov, GM., Drobyshev, VN., Kusraev, AG., Khubaev, K.M., 2021. Crustal strains in the ossetian region of the greater caucasus based on GNSS measurements. Izvestiya, Atmospheric and Oceanic Physics 57, 1498–1513.

Mohanty, A., Gahalaut, VK., Chowdhury, S., Bansal, A.K., Gautam, P., Catherine, J., 2024. Geodetic constraints on slip rate on the Karakoram fault and its role in the Himalayan arc deformation. Earth and Planetary Science Letters 626, 118512.

Molnar, P., Dayem, K.E., 2010. Major intracontinental strike-slip faults and contrasts in lithospheric strength. Geosphere 6, 444–467. doi:10.1130/GES00519.1.

Molnar, P., England, P., 1990. Late Cenozoic uplift of mountain ranges and global climate change: Chicken or egg? Nature 346, 29–34. doi:10.1038/346029a0.

Molnar, P., Stock, J.M., 2009. Slowing of India's convergence with Eurasia since 20 Ma and its implications for Tibetan mantle dynamics. Tectonics 28. doi:10.1029/2008TC002271.

Molnar, P., Tapponnier, P., 1975. Cenozoic Tectonics of Asia: Effects of a Continental Collision. Science 189, 419–426. doi:10.1126/science.189.4201.419.

Mondal, SK., Borghi, A., Roy, PNS., Aoudia, A., 2016. GPS, scaling exponent and past seismicity for seismic hazard assessment in Garhwal–Kumaun, Himalayan region. Natural Hazards 80, 1349–1367.

Mousavi, Z., Talebian, M., Amiri, M., Walker, R.T., Marshall, N., Walpersdorf, A., 2025. Constancy of Geologic and Geodetic Fault Slip Rates Across the Arabia-Eurasia Collision Revealed Through Two Decades of Observation. Tectonics 44, e2024TC008380. doi:10.1029/2024TC008380.

Mukul, M., Jade, S., Ansari, K., Matin, A., Joshi, V., 2018. Structural insights from geodetic global positioning system measurements in the Darjiling-Sikkim Himalaya. Journal of structural geology 114, 346–356.

Mullick, M., Mukhopadhyay, D., 2020. Kinematics of faults in bengal basin: Constraints from GPS measurements. Geodesy and Geodynamics 11, 242–251.

Nissen, E., Tatar, M., Jackson, J.A., Allen, M.B., 2011. New views on earthquake faulting in the Zagros fold-and-thrust belt of Iran. Geophysical Journal International 186, 928–944. doi:10.1111/j.1365-246X.2011.05119.x.

Nocquet, J.M., 2012. Present-day kinematics of the Mediterranean: A comprehensive overview of GPS results. Tectonophysics 579, 220–242. doi:10.1016/j.tecto.2012.03.037.

Nocquet, J.M., Sue, C., Walpersdorf, A., Tran, T., Lenôtre, N., Vernant, P., Cushing, M., Jouanne, F., Masson, F., Baize, S., et al., 2016. Present-day uplift of the western Alps. Scientific reports 6, 28404.

Nucci, R., Serpelloni, E., Faenza, L., Garcia, A., Belardinelli, M.E., 2025. Geodetic Strain Rates and Seismicity Rates Along the Apennines (Italy). Journal of Geophysical Research: Solid Earth 130, e2024JB029848. doi:10.1029/2024JB029848.

Oryan, B., Betka, P.M., Steckler, M.S., Nooner, S.L., Lindsey, E.O., Mondal, D., Mathews, A.M., Akhter, S.H., Singha, S., Than, O., 2023. New GNSS and geological data from the Indo-Burman subduction zone indicate active convergence on both a locked megathrust and the Kabaw Fault. Journal of Geophysical Research: Solid Earth 128, e2022JB025550.

Ou, Q., Daout, S., Weiss, J.R., Shen, L., Lazecký, M., Wright, T.J., Parsons, B.E., 2022. Large-Scale Interseismic Strain Mapping of the NE Tibetan Plateau From Sentinel-1 Interferometry. Journal of Geophysical Research: Solid Earth 127, e2022JB024176. doi:10.1029/2022JB024176.

Özalaybey, S., Ergin, M., Aktar, M., Tapirdamaz, C., Biçmen, F., Yörük, A., 2002. The 1999 İzmit Earthquake Sequence in Turkey: Seismological and Tectonic Aspects. Bulletin of the Seismological Society of America 92, 376–386. doi:10.1785/0120000838.

Özarpacı, S., Doğan, U., Ergintav, S., Çakır, Z., Özdemir, A., Floyd, M., Reilinger, R., 2021. Present GPS velocity field along 1999 Izmit rupture zone: Evidence for continuing afterslip 20 yr after the earthquake. Geophysical Journal International 224, 2016–2027.

Özbey, V., Sengör, A.M.C., Henry, P., Özeren, M.S., Haines, A.J., Klein, E.C., Tarı, E., Zabcı, C., Chousianitis, K., Güvercin, S.E., et al., 2024. Kinematics of the Kahramanmaraş triple junction and of Cyprus: Evidence of shear partitioning. BSGF-Earth Sciences Bulletin 195, 15.

Özdemir, S., Karslıoğlu, M.O., 2019. Soft clustering of GPS velocities from a homogeneous permanent network in Turkey. Journal of Geodesy 93, 1171–1195.

Özkan, A., Yavaşoğlu, H.H., Masson, F., 2023. Present-day strain accumulations and fault kinematics at the Hatay Triple Junction using new geodetic constraints. Tectonophysics 854, 229819.

Palano, M., Imprescia, P., Agnon, A., Gresta, S., 2018. An improved evaluation of the seismic/geodetic deformation-rate ratio for the Zagros Fold-and-Thrust collisional belt. Geophysical Journal International 213, 194–209.

Palano, M., Imprescia, P., Gresta, S., 2013. Current stress and strain-rate fields across the dead sea fault system: Constraints from seismological data and GPS observations. Earth and Planetary Science Letters 369, 305–316.

Pan, Y., Chen, R., Yi, S., Wang, W., Ding, H., Shen, W., Chen, L., 2019. Contemporary mountain-building of the Tianshan and its relevance to geodynamics constrained by integrating GPS and GRACE measurements. Journal of Geophysical Research: Solid Earth 124, 12171–12188.

Pan, Y., Hammond, W.C., Ding, H., Mallick, R., Jiang, W., Xu, X., Shum, CK., Shen, W., 2021. GPS imaging of vertical bedrock displacements: Quantification of two-dimensional vertical crustal deformation in China. Journal of Geophysical Research: Solid Earth 126, e2020JB020951.

Pan, Y., Jiang, W., Ding, H., Shum, CK., Jiao, J., Li, J., 2023. Intradecadal fluctuations and three-dimensional crustal kinematic deformation of the tianshan and pamir derived from multi-geodetic imaging. Journal of Geophysical Research: Solid Earth 128, e2022JB025325.

Pan, Z., Yun, Z., Shao, Z., 2020. Contemporary crustal deformation of Northeast Tibet from geodetic investigations and a comparison between the seismic and geodetic moment release rates. Physics of the Earth and Planetary Interiors 304, 106489.

Pappachen, J.P., Sathiyaseelan, R., Gautam, P.K., Pal, S.K., 2021. Crustal velocity and interseismic strain-rate on possible zones for large earthquakes in the Garhwal–Kumaun Himalaya. Scientific Reports 11, 21283.

Parsons, A.J., Hosseini, K., Palin, R.M., Sigloch, K., 2020. Geological, geophysical and plate kinematic constraints for models of the India-Asia collision and the post-Triassic central Tethys oceans. Earth-Science Reviews 208, 103084. doi:10.1016/j.earscirev.2020.103084.

Peltzer, G., Brown, N.D., Mériaux, A.S., van der Woerd, J., Rhodes, E.J., Finkel, R.C., Ryerson, F.J., Hollingsworth, J., 2020. Stable Rate of Slip Along the Karakax Section of the Altyn Tagh Fault from Observation of Interglacial and Postglacial Offset Morphology and Surface Dating. Journal of Geophysical Research: Solid Earth 125, e2019JB018893. doi:10.1029/2019JB018893.

Penney, C., Tavakoli, F., Saadat, A., Nankali, H.R., Sedighi, M., Khorrami, F., Sobouti, F., Rafi, Z., Copley, A., Jackson, J., Priestley, K., 2017. Megathrust and accretionary wedge properties and behaviour in the Makran subduction zone. Geophysical Journal International 209, 1800–1830. doi:10.1093/gji/ggx126.

Perry, M., Kakar, N., Ischuk, A., Metzger, S., Bendick, R., Molnar, P., Mohadjer, S., 2019. Little geodetic evidence for localized Indian subduction in the Pamir-Hindu Kush of Central Asia. Geophysical Research Letters 46, 109–118.

Piña-Valdés, J., Socquet, A., Beauval, C., Doin, M.P., D'Agostino, N., Shen, Z.K., 2022. 3D GNSS Velocity Field Sheds Light on the Deformation Mechanisms in Europe: Effects of the Vertical Crustal Motion on the Distribution of Seismicity. Journal of Geophysical Research: Solid Earth 127, e2021JB023451. doi:10.1029/2021JB023451.

Pintori, F., Serpelloni, E., Gualandi, A., 2022. Common-mode signals and vertical velocities in the greater Alpine area from GNSS data. Solid Earth Sciences Library 13, 1541–1567.

Pirooznia, M., Naeeni, M.R., Yousefzadeh, T., 2020. Point wise determination of vertical deformation at southern coastal areas of caspian sea by combination of satellite altimetry and tide gauge observations. Annals of Geophysics 63, GD656–GD656.

Poland, M.P., Zebker, H.A., 2022. Volcano geodesy using InSAR in 2020: The past and next decades. Bulletin of Volcanology 84, 27. doi:10.1007/s00445-022-01531-1.

Ponraj, M., Amirtharaj, S., Sunil, PS., Saji, A.P., Kumar, K.V., Arora, SK., Reddy, CD., Begum, SK., 2019. An assessment of present-day crustal deformation in the Kumaun Himalaya from GPS observations. Journal of Asian Earth Sciences 176, 274–280.

Porkoláb, K., Broerse, T., Kenyeres, A., Békési, E., Tóth, S., Magyar, B., Wesztergom, V., 2023. Active tectonics of the Circum-Pannonian region in the light of updated GNSS network data. Acta Geodaetica et Geophysica 58, 149–173.

Qi, W., Xuejun, Q., Qigui, L., Freymueller, J., Shaomin, Y., Caijun, X., Yonglin, Y., Xinzhao, Y., Kai, T., Gang, C., 2011. Rupture of deep faults in the 2008 Wenchuan earthquake and uplift of the Longmen Shan. Nature Geoscience 4, 634–640. doi:10.1038/ngeo1210.

Qiao, X., Yu, P., Nie, Z., Li, J., Wang, X., Kuzikov, S.I., Wang, Q., Yang, S., 2017. The crustal deformation revealed by GPS and InSAR in the northwest corner of the Tarim Basin, northwestern China. Pure and Applied Geophysics 174, 1405–1423.

Qiao, X., Zhou, Y., 2021. Geodetic imaging of shallow creep along the Xianshuihe fault and its frictional properties. Earth and Planetary Science Letters 567, 117001. doi:10.1016/j.epsl.2021.117001.

Rashwan, M., Sawires, R., Radwan, A.M., Sparacino, F., Peláez, J.A., Palano, M., 2021. Crustal strain and stress fields in Egypt from geodetic and seismological data. Remote Sensing 13, 1398.

Ray, J.D., Vijayan, M.S.M., Kumar, A., 2019. Noise characteristics of GPS time series and their influence on velocity uncertainties. Journal of Earth System Science 128, 146.

Reilinger, R., McClusky, S., 2011. Nubia–Arabia–Eurasia plate motions and the dynamics of Mediterranean and Middle East tectonics. Geophysical Journal International 186, 971–979. doi:10.1111/j.1365-246X.2011.05133.x.

Rey, P., Vanderhaeghe, O., Teyssier, C., 2001. Gravitational collapse of the continental crust: Definition, regimes and modes. Tectonophysics 342, 435–449. doi:10.1016/S0040-1951(01)00174-3.

Reynolds, K., Copley, A., Hussain, E., 2015. Evolution and dynamics of a fold-thrust belt: The Sulaiman Range of Pakistan. Geophysical Journal International 201, 683–710. doi:10.1093/gji/ggv005.

Rizza, M., Abdrakhmatov, K., Walker, R., Braucher, R., Guillou, V., Carr, A.S., Campbell, G., McKenzie, D., Jackson, J., Aumaître, G., Bourlès, D.L., Keddadouche, K., 2019. Rate of Slip From Multiple Quaternary Dating Methods and Paleoseismic Investigations Along the Talas-Fergana Fault: Tectonic Implications for the Tien Shan Range. Tectonics 38, 2477–2505. doi:10.1029/2018TC005188.

Royden, L.H., Burchfiel, B.C., van der Hilst, R.D., 2008. The Geological Evolution of the Tibetan Plateau. Science 321, 1054–1058. doi:10.1126/science.1155371.

Rudenko, S., Schön, N., Uhlemann, M., Gendt, G., 2013. Reprocessed height time series for GPS stations. Solid Earth Sciences Library 4, 23–41.

Rui, X., Lindsey, EO., Wu, JP., 2024. Geodetic slip rate partitioning in the central Anninghe and Daliangshan faults: Effects of fault geometry, elastic heterogeneity, and viscoelastic rheology. Tectonophysics 872, 230174.

Rui, X., Stamps, D.S., 2019. A geodetic strain rate and tectonic velocity model for China. Geochemistry, Geophysics, Geosystems 20, 1280–1297.

Rui, X., Williams, CA., Stamps, DS., Fang, LH., 2025. Crustal heterogeneity and fault parametrization effects on seismic hazards assessment: Southeastern margin of the Tibetan Plateau case study. Geophysical Journal International 240, 886–903.

Rust, D., Korzhenkov, A., Tibaldi, A., 2018. Geologic Slip-Rate Determinations on the Talas-Fergana Fault: Mismatch With Geodetic Slip Rate. Geophysical Research Letters 45, 3880–3888. doi:10.1002/2017GL076990.

Ryder, I., Bürgmann, R., Pollitz, F., 2011. Lower crustal relaxation beneath the Tibetan Plateau and Qaidam Basin following the 2001 Kokoxili earthquake. Geophysical Journal International 187, 613–630. doi:10.1111/j.1365-246X.2011.05179.x.

Ryder, I., Parsons, B., Wright, T.J., Funning, G.J., 2007. Post-seismic motion following the 1997 Manyi (Tibet) earthquake: InSAR observations and modelling. Geophysical Journal International 169, 1009–1027. doi:10.1111/j.1365-246X.2006.03312.x.

Saji, A.P., Sunil, PS., Sreejith, KM., Gautam, P.K., Kumar, K.V., Ponraj, M., Amirtharaj, S., Shaju, R.M., Begum, SK., Reddy, CD., et al., 2020. Surface deformation and influence of hydrological mass over Himalaya and North India revealed from a decade of continuous GPS and GRACE observations. Journal of Geophysical Research: Earth Surface 125, e2018JF004943.

Saji, A.P., Sunil, PS., Sreejith, KM., Kumar, K.V., Ponraj, M., Amirtharaj, S., 2025. Interseismic strain rate and fault coupling along the central Himalayan seismic gap from new GPS data. Geophysical Journal International 242, ggaf186.

Sánchez, L., Völksen, C., Sokolov, A., Arenz, H., Seitz, F., 2018. Present-day surface deformation of the Alpine region inferred from geodetic techniques. Earth System Science Data 10, 1503–1526. doi:10.5194/essd-10-1503-2018.

Santamaría-Gómez, A., Gravelle, M., Collilieux, X., Guichard, M., Míguez, B.M., Tiphaneau, P., Wöppelmann, G., 2012. Mitigating the effects of vertical land motion in tide gauge records using a state-of-the-art GPS velocity field. Global and Planetary Change 98, 6–17.

Santamaría-Gómez, A., Rietbroek, R., Rebischung, P., Frederikse, T., Legrand, J., 2024. Combined global GNSS velocity field. International Association of Geodesy Symposia 157.

Schurr, B., Ratschbacher, L., Sippl, C., Gloaguen, R., Yuan, X., Mechie, J., 2014. Seismotectonics of the Pamir. Tectonics 33, 1501–1518. doi:10.1002/2014TC003576.

Şengör, A.M.C., Tüysüz, O., İmren, C., Sakınç, M., Eyidoğan, H., Görür, N., Pichon, X.L., Rangin, C., 2005. The North Aanatolian Fault: A New Look. Annual Review of Earth and Planetary Sciences 33, 37–112. doi:10.1146/annurev.earth.32.101802.120415.

Serpelloni, E., Cavaliere, A., Martelli, L., Pintori, F., Anderlini, L., Borghi, A., Randazzo, D., Bruni, S., Devoti, R., Perfetti, P., et al., 2022. Surface velocities and strain-rates in the Euro-Mediterranean region from massive GPS data processing. Frontiers in Earth Science 10, 907897.

Serpelloni, E., Faccenna, C., Spada, G., Dong, D., Williams, S.D., 2013. Vertical GPS ground motion rates in the Euro-Mediterranean region: New evidence of velocity gradients at different spatial scales along the Nubia-Eurasia plate boundary. Journal of Geophysical Research: Solid Earth 118, 6003–6024.

Serpelloni, E., Vannucci, G., Anderlini, L., Bennett, RA., 2016. Kinematics, seismotectonics and seismic potential of the eastern sector of the European Alps from GPS and seismic deformation data. Tectonophysics 688, 157–181.

Sharma, G., Kannaujiya, S., Gautam, PKR., Taloor, A.K., Champatiray, PK., Mohanty, S., 2021. Crustal deformation analysis across garhwal himalaya: Part of western himalaya using GPS observations. Quaternary International 575, 153–159.

Sharma, Y., Pasari, S., Ching, K.E., Dikshit, O., Kato, T., Malik, J.N., Chang, C.P., Yen, J.Y., 2020. Spatial distribution of earthquake potential along the Himalayan arc. Tectonophysics 791, 228556.

Shen, L., Hooper, A., Elliott, J., 2019. A Spatially Varying Scaling Method for InSAR Tropospheric Corrections Using a High-Resolution Weather Model. Journal of Geophysical Research: Solid Earth 124, 4051–4068. doi:10.1029/2018JB016189.

Shen, L., Hooper, A., Elliott, J.R., Wright, T.J., 2024. Variability in interseismic strain accumulation rate and style along the Altyn Tagh Fault. Nature Communications 15, 6876. doi:10.1038/s41467-024-51116-z.

Shen, Z.K., Lü, J., Wang, M., Bürgmann, R., 2005. Contemporary crustal deformation around the southeast borderland of the Tibetan Plateau. Journal of Geophysical Research: Solid Earth 110. doi:10.1029/2004JB003421.

Shevchenko, V., Krupennikova, I., Lukk, A., 2021. Gps kinematics of the northern part of the eurasian continent and its possible geodynamic interpretation. Izvestiya, Physics of the Solid Earth 57, 825–833.

Shrungeshwara, TS., Narukula, B., Jade, S., Ghavri, S., Vivek, C.G., Parvez, IA., 2023. Implications of seismic and GNSS strain rates in Himachal, Kashmir and Ladakh. Scientific Reports 13, 21652.

Shukurov, Z.F., 2020. Processing and Analysis of GNSS Measurement Data in the GAMIT-GLOBK Software. Uzbekistan Academy of Sciences , 24.

Singh, A., Bhat, GM., Singh, Y., 2022. Assessment of velocity pattern of lithotectonic segments of the kashmir himalaya: Constraints from GPS measurements. Journal of The Indian Association of Sedimentologists (peer reviewed) 39, 96–101.

Smith, G., McNeill, L., Henstock, T.J., Bull, J., 2012. The structure and fault activity of the Makran accretionary prism. Journal of Geophysical Research: Solid Earth 117. doi:10.1029/2012JB009312.

Smith, G.L., McNeill, L.C., Wang, K., He, J., Henstock, T.J., 2013. Thermal structure and megathrust seismogenic potential of the Makran subduction zone. Geophysical Research Letters 40, 1528–1533. doi:10.1002/grl.50374.

Socquet, A., Janex, G., 2019. GNSS position and velocity solutions calculated in the frame work of the EPOS initiative with GAMIT-GLOBK. doi:10.17178/GNSS.products.EPOS.2019.

Sokhadze, G., Floyd, M., Godoladze, T., King, R., Cowgill, E.S., Javakhishvili, Z., Hahubia, G., Reilinger, R., 2018. Active convergence between the Lesser and Greater Caucasus in Georgia: Constraints on the tectonic evolution of the Lesser–Greater Caucasus continental collision. Earth and Planetary Science Letters 481, 154–161. doi:10.1016/j.epsl.2017.10.007.

Steckler, M.S., Mondal, D.R., Akhter, S.H., Seeber, L., Feng, L., Gale, J., Hill, E.M., Howe, M., 2016. Locked and loading megathrust linked to active subduction beneath the Indo-Burman Ranges. Nature Geoscience 9, 615–618.

Steffen, R., Steffen, H., Kenyeres, A., Nilsson, T., Lidberg, M., 2025. EuVeM2022—a European three-dimensional GNSS velocity model based on least-squares collocation. Geophysical Journal International 241, 437–453. doi:10.1093/gji/ggaf052.

Storetvedt, K.M., 1990. The Tethys Sea and the Alpine-Himalayan orogenic belt; mega-elements in a new global tectonic system. Physics of the Earth and Planetary Interiors 62, 141–184. doi:10.1016/0031-9201(90)90198-7.

Styron, R., Pagani, M., 2020. The GEM Global Active Faults Database. Earthquake Spectra 36, 160–180. doi:10.1177/8755293020944182.

Su, X., Yao, L., Wu, W., Meng, G., Su, L., Xiong, R., Hong, S., 2018. Crustal deformation on the northeastern margin of the Tibetan plateau from continuous GPS observations. Remote Sensing 11, 34.

Sun, J., Yue, H., Shen, Z., Fang, L., Zhan, Y., Sun, X., 2018. The 2017 Jiuzhaigou Earthquake: A Complicated Event Occurred in a Young Fault System. Geophysical Research Letters 45, 2230–2240. doi:10.1002/2017GL076421.

Suribabu, D., Dumka, R.K., Kothyari, GC., Swamy, KV., Prajapati, S., 2022a. Identification of crustal deformation in the Saurashtra region, western India: Insights from PSI and GNSS derived investigation. Acta Geodaetica et Geophysica 57, 639–659.

Suribabu, D., Dumka, R.K., Paikray, J., Kothyari, G.C., Thakkar, M., Swamy, K.V., Taloor, A.K., Prajapati, S., 2022b. Geodetic characterization of active katrol hill fault (KHF) of central mainland kachchh, western india. Geodesy and Geodynamics 13, 247–253.

Szeliga, W., Bilham, R., Kakar, D.M., Lodi, S.H., 2012. Interseismic strain accumulation along the western boundary of the Indian subcontinent. Journal of Geophysical Research: Solid Earth 117. doi:10.1029/2011JB008822.

Tapponnier, P., Mercier, J.L., Armijo, R., Tonglin, H., Ji, Z., 1981. Field evidence for active normal faulting in Tibet. Nature 294, 410–414. doi:10.1038/294410a0.

Tapponnier, P., Molnar, P., 1977. Active faulting and tectonics in China. Journal of Geophysical Research (1896-1977) 82, 2905–2930. doi:10.1029/JB082i020p02905.

Tapponnier, P., Zhiqin, X., Roger, F., Meyer, B., Arnaud, N., Wittlinger, G., Jingsui, Y., 2001. Oblique Stepwise Rise and Growth of the Tibet Plateau. Science 294, 1671–1677. doi:10.1126/science.105978.

Tatar, O., Sözbilir, H., Koçbulut, F., Bozkurt, E., Aksoy, E., Eski, S., Özmen, B., Alan, H., Metin, Y., 2020. Surface deformations of 24 January 2020 Sivrice (Elazığ)–Doğanyol (Malatya) earthquake (Mw = 6.8) along the Pütürge segment of the East Anatolian Fault Zone and its comparison with Turkey's 100-year-surface ruptures. Mediterranean Geoscience Reviews 2, 385–410. doi:10.1007/s42990-020-00037-2.

Taymaz, T., Jackson, J., McKenzie, D., 1991. Active tectonics of the north and central Aegean Sea. Geophysical Journal International 106, 433–490. doi:10.1111/j.1365-246X.1991.tb03906.x.

Taymaz, T., Yilmaz, Y., Dilek, Y., 2007. The geodynamics of the Aegean and Anatolia: Introduction, in: Taymaz, T., Yilmaz, Y., Dilek, Y. (Eds.), The Geodynamics of the Aegean and Anatolia. Geological Society of London. volume 291, p. 0. doi:10.1144/SP291.1.

Thatcher, W., 2009. How the Continents Deform: The Evidence From Tectonic Geodesy*. Annual Review of Earth and Planetary Sciences 37, 237–262. doi:10.1146/annurev.earth.031208.100035.

Thompson, S.C., Weldon, R.J., Rubin, C.M., Abdrakhmatov, K., Molnar, P., Berger, G.W., 2002. Late Quaternary slip rates across the central Tien Shan, Kyrgyzstan, central Asia. Journal of Geophysical Research: Solid Earth 107, ETG 7–1–ETG 7–32. doi:10.1029/2001JB000596.

Timofeev, V.Y., Ardyukov, DG., Timofeev, AV., 2024. Variations of displacement fields and seismicity in the mountainous altai. Journal of Volcanology and Seismology 18, 351–365.

Vardić, K., Clarke, P.J., Whitehouse, P.L., 2022. A GNSS velocity field for crustal deformation studies: The influence of glacial isostatic adjustment on plate motion models. Geophysical Journal International 231, 426–458.

Verma, H., Pasari, S., Sharma, Y., Ching, K.E., 2024. High-resolution velocity and strain rate fields in the Kumaun Himalaya: An implication for seismic moment budget. Journal of Geodynamics 160, 102023.

Vila, A., 2020. University of Houston. Ph.D. thesis. Ground Movements along the Himalayan Arc Derived from GPS Observations (1995-2019).

Vilayev, AV., Zhantayev, Z.S., Bibosinov, A.Z., 2017. Monitoring crustal movements in northern Tianshan Mountain based on GPS technology. Geodesy and geodynamics 8, 155–159.

Viltres, R., Jónsson, S., Alothman, A.O., Liu, S., Leroy, S., Masson, F., Doubre, C., Reilinger, R., 2022. Present-Day Motion of the Arabian Plate. Tectonics 41, e2021TC007013. doi:10.1029/2021TC007013.

Viltres, R., Jónsson, S., Ruch, J., Doubre, C., Reilinger, R., Floyd, M., Ogubazghi, G., 2020. Kinematics and deformation of the southern red sea region from gps observations. Geophysical Journal International 221, 2143–2154.

Walker, R., Jackson, J., 2004. Active tectonics and late Cenozoic strain distribution in central and eastern Iran. Tectonics 23. doi:10.1029/2003TC001529.

Walker, R.T., Bezmenov, Y., Begenjev, G., Carolin, S., Dodds, N., Gruetzner, C., Jackson, J.A., Mirzin, R., Mousavi, Z., Rhodes, E.J., 2021. Slip-Rate on the Main Köpetdag (Kopeh Dagh) Strike-Slip Fault, Turkmenistan, and the Active Tectonics of the South Caspian. Tectonics 40, e2021TC006846. doi:10.1029/2021TC006846.

Wallace, K., Yin, G., Bilham, R., 2004. Inescapable slow slip on the Altyn Tagh fault. Geophysical Research Letters 31. doi:10.1029/2004GL019724.

Walters, R.J., England, P.C., Houseman, G.A., 2017. Constraints from GPS measurements on the dynamics of the zone of convergence between Arabia and Eurasia. Journal of Geophysical Research: Solid Earth 122, 1470–1495. doi:10.1002/2016JB013370.

Wang, D., Elliott, J.R., Zheng, G., Wright, T.J., Watson, A.R., McGrath, J.D., 2024a. Deciphering interseismic strain accumulation and its termination on the central-eastern Altyn Tagh fault from high-resolution velocity fields. Earth and Planetary Science Letters 644, 118919. doi:10.1016/j.epsl.2024.118919.

Wang, D., Zhao, B., Li, J., Metzger, S., Gu, C., Wang, W., Zheng, G., Yu, J., Qiao, X., 2024b. Recent block kinematics and fault slip rates in the pamir, central asia, from an integrated GNSS velocity field. Tectonics 43, e2024TC008475.

Wang, D., Zhao, B., Li, Y., Yu, J., Chen, Y., Zhou, X., 2022a. Determination of tectonic and nontectonic vertical motion rates of the North China Craton using dense GPS and GRACE data. Journal of Asian Earth Sciences 236, 105314.

Wang, D., Zhao, B., Yu, J., Tan, K., 2020. Active tectonic deformation around the Tarim Basin inferred from dense GPS measurements. Geodesy and Geodynamics 11, 418–425.

Wang, H., Avouac, J.P., Shao, Z., Liu, X., Wei, W., Zhan, S., Dai, X., Lou, Y., 2022b. CSES community deformation models in Southwest China, in: China Seismic Experimental Site: Theoretical Framework and Ongoing Practice. Springer, pp. 111–133.

Wang, H., Wright, T.J., 2012. Satellite geodetic imaging reveals internal deformation of western Tibet. Geophysical Research Letters 39. doi:10.1029/2012GL051222.

Wang, H., Xu, C., Ge, L., 2007. Coseismic deformation and slip distribution of the 1997 Mw 7.5 Manyi, Tibet, earthquake from InSAR measurements. Journal of Geodynamics 44, 200–212. doi:10.1016/j.jog.2007.03.003.

Wang, L., Chen, C., Du, J., Wang, T., 2017a. Detecting seasonal and long-term vertical displacement in the North China Plain using GRACE and GPS. Hydrology and Earth System Sciences 21, 2905–2922.

Wang, M., Shen, Z.K., 2020. Present-day crustal deformation of continental China derived from GPS and its tectonic implications. Journal of Geophysical Research: Solid Earth 125, e2019JB018774.

Wang, Q., Wyman, D.A., Li, Z.X., Sun, W., Chung, S.L., Vasconcelos, P.M., Zhang, Q., Dong, H., Yu, Y., Pearson, N., Qiu, H., Zhu, T., Feng, X., 2010. Eocene north–south trending dikes in central Tibet: New constraints on the timing of east–west extension with implications for early plateau uplift? Earth and Planetary Science Letters 298, 205–216. doi:10.1016/j.epsl.2010.07.046.

Wang, S.Y., Chen, JL., Wilson, C.R., Li, J., Hu, X.G., 2018. Vertical motion at TEHN (Iran) from Caspian Sea and other environmental loads. Journal of Geodynamics 122, 17–24.

Wang, W., Qiao, X., Ding, K., 2021. Present-Day Kinematics in Southeastern Tibet Inferred From GPS Measurements. Journal of Geophysical Research: Solid Earth 126, e2020JB021305. doi:10.1029/2020JB021305.

Wang, W., Qiao, X., Yang, S., Wang, D., 2017b. Present-day velocity field and block kinematics of Tibetan Plateau from GPS measurements. Geophysical Journal International 208, 1088–1102.

Wani, A.A., Bali, B.S., Mir, S.A., Wani, M.I., 2025. Kinematics of the kashmir himalaya: Inferences from geological and geodetic data. Geodesy and Geodynamics .

Warners-Ruckstuhl, K.N., Govers, R., Wortel, R., 2013. Tethyan collision forces and the stress field of the Eurasian Plate. Geophysical Journal International 195, 1–15. doi:10.1093/gji/ggt219.

Watson, A.R., Elliott, J.R., Lazecký, M., Maghsoudi, Y., McGrath, J.D., Walters, R.J., 2024. An InSAR-GNSS Velocity Field for Iran. Geophysical Research Letters 51, e2024GL108440. doi:10.1029/2024GL108440.

Weiss, J.R., Walters, R.J., Morishita, Y., Wright, T.J., Lazecky, M., Wang, H., Hussain, E., Hooper, A.J., Elliott, J.R., Rollins, C., Yu, C., González, P.J., Spaans, K., Li, Z., Parsons, B., 2020. High-Resolution Surface Velocities and Strain for Anatolia From Sentinel-1 InSAR and GNSS Data. Geophysical Research Letters 47, e2020GL087376. doi:10.1029/2020GL087376.

Wen, Y., Li, Z., Xu, C., Ryder, I., Bürgmann, R., 2012. Postseismic motion after the 2001 MW 7.8 Kokoxili earthquake in Tibet observed by InSAR time series. Journal of Geophysical Research: Solid Earth 117. doi:10.1029/2011JB009043.

Whitehouse, P.L., 2018. Glacial isostatic adjustment modelling: Historical perspectives, recent advances, and future directions. Earth Surface Dynamics 6, 401–429. doi:10.5194/esurf-6-401-2018.

Wolf, S.G., Huismans, R.S., Braun, J., Yuan, X., 2022. Topography of mountain belts controlled by rheology and surface processes. Nature 606, 516–521. doi:10.1038/s41586-022-04700-6.

Wright, T.J., 2016. The earthquake deformation cycle. Astronomy & Geophysics 57, 4.20–4.26. doi:10.1093/astrogeo/atw148.

Wright, T.J., Parsons, B., England, P.C., Fielding, E.J., 2004. InSAR Observations of Low Slip Rates on the Major Faults of Western Tibet. Science 305, 236–239. doi:10.1126/science.1096388.

Wright, T.J., Parsons, B.E., Jackson, J.A., Haynes, M., Fielding, E.J., England, P.C., Clarke, P.J., 1999. Source parameters of the 1 October 1995 Dinar (Turkey) earthquake from SAR interferometry and seismic bodywave modelling. Earth and Planetary Science Letters 172, 23–37. doi:10.1016/S0012-821X(99)00186-7.

Wu, C., Zhang, P., Zhang, Z., Zheng, W., Xu, B., Wang, W., Yu, Z., Dai, X., Zhang, B., Zang, K., 2023. Slip partitioning and crustal deformation patterns in the Tianshan orogenic belt derived from GPS measurements and their tectonic implications. Earth Science Reviews 238, 104362. doi:10.1016/j.earscirev.2023.104362.

Wu, D.L., Ge, W.P., Liu, S.Z., Yuan, D.Y., Zhang, B., Wei, C.M., 2024a. Present-day 3D crustal deformation of the northeastern tibetan plateau from space geodesy. Geophysical Research Letters 51, e2023GL106143.

Wu, P.C., Wei, M.M., D'Hondt, S., 2022. Subsidence in Coastal Cities Throughout the World Observed by InSAR. Geophysical Research Letters 49, e2022GL098477. doi:10.1029/2022GL098477.

Wu, S., Yang, Z., Ding, X., Zhang, B., Zhang, L., Lu, Z., 2020. Two decades of settlement of Hong Kong International Airport measured with multi-temporal InSAR. Remote Sensing of Environment 248, 111976. doi:10.1016/j.rse.2020.111976.

Wu, Y., Su, G., Nie, J., Chen, C., Chen, Z., Yu, H., Yin, H., Chang, L., Tang, Z., Pang, Y., et al., 2024b. High-precision vertical deformation of the Chinese mainland constrained by levelling and GNSS data. Geophysical Journal International 239, 971–981.

Xiong, Z., Zhuang, J., Zhou, S., Matsu'ura, M., Hao, M., Wang, Q., 2021. Crustal strain-rate fields estimated from GNSS data with a Bayesian approach and its correlation to seismic activity in Mainland China. Tectonophysics 815, 229003.

Xu, Q., Hetzel, R., Hampel, A., Wolff, R., 2021. Slip Rate of the Danghe Nan Shan Thrust Fault from 10Be Exposure Dating of Folded River Terraces: Implications for the Strain Distribution in Northern Tibet. Tectonics 40, e2020TC006584. doi:10.1029/2020TC006584.

Xu, X., Wen, X., Han, Z., Chen, G., Li, C., Zheng, W., Zhnag, S., Ren, Z., Xu, C., Tan, X., Wei, Z., Wang, M., Ren, J., He, Z., Liang, M., 2013. Lushan MS7.0 earthquake: A blind reserve-fault event. Chinese Science Bulletin 58, 3437–3443. doi:10.1007/s11434-013-5999-4.

Yadav, A., Kannaujiya, S., RAY, P.K.C., Yadav, R.K., Gautam, P.K., 2021. Estimation of crustal deformation parameters and strain build-up in Northwest Himalaya using GNSS data measurements. Contributions to Geophysics and Geodesy 51, 225–243.

Yadav, R.K., Gahalaut, V.K., Bansal, A.K., Sati, SP., Catherine, J., Gautam, P., Kumar, K., Rana, N., 2019. Strong seismic coupling underneath Garhwal–Kumaun region, NW himalaya, india. Earth and Planetary Science Letters 506, 8–14.

Yamasaki, T., Houseman, G.A., 2012. The crustal viscosity gradient measured from post-seismic deformation: A case study of the 1997 Manyi (Tibet) earthquake. Earth and Planetary Science Letters 351–352, 105–114. doi:10.1016/j.epsl.2012.07.030.

Yang, J., Xu, C., Wen, Y., 2023. Coseismic and early postseismic deformation associated with the January 2022 Mw 6.6 Menyuan earthquake, NE Tibet, revealed by InSAR Observations. Tectonophysics 868, 230090. doi:10.1016/j.tecto.2023.230090.

Yang, Z., Li, Z., Zhu, J., Wang, Y., Wu, L., 2020. Use of SAR/InSAR in Mining Deformation Monitoring, Parameter Inversion, and Forward Predictions: A Review. IEEE Geoscience and Remote Sensing Magazine 8, 71–90. doi:10.1109/MGRS.2019.2954824.

Yavasoglu, HH., Tiryakioglu, I., Karabulut, MF., Eyubagil, EE., Ozkan, A., Masson, F., Klein, E., Gulal, VE., Alkan, RM., Alkan, MN., et al., 2021. New geodetic constraints to reveal seismic potential of central Marmara region, Turkey. Bollettino di Geofisica Teorica ed Applicata 62, 513–526.

Yilmaz, Y., Gürer, Ö.F., 2024. Tectonic development of western Anatolian extensional province. International Geology Review 66, 755–785. doi:10.1080/00206814.2023.2209865.

Yin, A., 2010. Cenozoic tectonic evolution of Asia: A preliminary synthesis. Tectonophysics 488, 293–325. doi:10.1016/j.tecto.2009.06.002.

Yin, A., Dang, Y.Q., Zhang, M., Chen, X.H., McRivette, M.W., 2008. Cenozoic tectonic evolution of the Qaidam basin and its surrounding regions (Part 3): Structural geology, sedimentation, and regional tectonic reconstruction. GSA Bulletin 120, 847–876. doi:10.1130/B26232.1.

Yin, A., Harrison, T.M., 2000. Geologic Evolution of the Himalayan-Tibetan Orogen. Annual Review of Earth and Planetary Sciences 28, 211–280. doi:10.1146/annurev.earth.28.1.211.

Younes, SA., 2023. Study of crustal deformation in Egypt based on GNSS measurements. Survey Review 55, 338–349.

Yuan, Z., Liu-Zeng, J., Zhou, Y., Li, Z., Wang, H., Yao, W., Han, L., 2020. Paleoseismologic record of earthquakes along the Wuzunxiaoer section of the Altyn Tagh fault and its implication for cascade rupture behavior. Science China Earth Sciences 63, 93–107. doi:10.1007/s11430-019-9376-8.

Zhang, L., Liang, S., Yang, X., Dai, C., 2021. The migration of the crustal deformation peak area in the eastern Himalayan Syntaxis inferred from present-day crustal deformation and morpho-tectonic markers. Geodesy and Geodynamics 12, 165–174.

Zhang, P.Z., Molnar, P., Xu, X., 2007. Late Quaternary and present-day rates of slip along the Altyn Tagh Fault, northern margin of the Tibetan Plateau. Tectonics 26. doi:10.1029/2006TC002014.

Zhao, B., Zhang, C., Wang, D., Huang, Y., Tan, K., Du, R., Liu, J., 2017. Contemporary kinematics of the Ordos block, North China and its adjacent rift systems constrained by dense GPS observations. Journal of Asian Earth Sciences 135, 257–267.

Zhao, D., Qu, C., Shan, X., Gong, W., Weng, H., Chen, H., Wu, D., 2024. An Updated Fault Coupling Model Along Major Block-Bounding Faults on the Eastern and Northeastern Tibetan Plateau From a Stress-Constrained Inversion of GPS and InSAR Data. Journal of Geophysical Research: Solid Earth 129, e2023JB028483. doi:10.1029/2023JB028483.

Zhao, Q., Chen, Q., van Dam, T., She, Y., Wu, W., 2023. The vertical velocity field of the Tibetan Plateau and its surrounding areas derived from GPS and surface mass loading models. Earth and Planetary Science Letters 609, 118107.

Zheng, G., Wang, H., Wright, T.J., Lou, Y., Zhang, R., Zhang, W., Shi, C., Huang, J., Wei, N., 2017. Crustal deformation in the India-Eurasia collision zone from 25 years of GPS measurements. Journal of Geophysical Research: Solid Earth 122, 9290–9312.

Zheng, R., Zou, R., Dong, R., Fang, Z., Wang, Q., 2024. The 2024 Mw 7.0 Wushi Earthquake in Southern Tianshan Convergent Zone: Finite-Fault Model for the Coseismic Rupture and Aftershock. Seismological Research Letters 96, 816–827. doi:10.1785/0220240126.

Zhou, Y., He, J., Oimahmadov, I., Gadoev, M., Pan, Z., Wang, W., Abdulov, S., Rajabov, N., 2016. Present-day crustal motion around the Pamir Plateau from GPS measurements. Gondwana Research 35, 144–154.

Zhou, Y., Ren, C., Ghosh, A., Meng, H., Fang, L., Yue, H., Zhou, S., Su, Y., 2022. Seismological Characterization of the 2021 Yangbi Foreshock-Mainshock Sequence, Yunnan, China: More than a Triggered Cascade. Journal of Geophysical Research: Solid Earth 127, e2022JB024534. doi:10.1029/2022JB024534.

Zhou, Y., Xu, L., Pan, Z., Hao, M., Li, C., 2023. A potential earthquake with magnitude Mw 7.2 on the northern Xiaojiang fault revealed by GNSS measurement. Remote Sensing 15, 944.

Zubovich, A., Metzger, S., Schöne, T., Kley, J., Mosienko, O., Zech, C., Moldobekov, B., Shsarshebaev, A., 2022. Cyclic Fault Slip Under the Magnifier: Co- and Postseismic Response of the Pamir Front to the 2015 Mw7.2 Sarez, Central Pamir, Earthquake. Tectonics 41, e2022TC007213. doi:10.1029/2022TC007213.

Zubovich, A., Schöne, T., Metzger, S., Mosienko, O., Mukhamediev, S., Sharshebaev, A., Zech, C., 2016. Tectonic interaction between the Pamir and Tien Shan observed by GPS. Tectonics 35, 283–292.

Zubovich, A.V., Wang, X.q., Scherba, Y.G., Schelochkov, G.G., Reilinger, R., Reigber, C., Mosienko, O.I., Molnar, P., Michajljow, W., Makarov, V.I., Li, J., Kuzikov, S.I., Herring, T.A., Hamburger, M.W., Hager, B.H., Dang, Y.m., Bragin, V.D., Beisenbaev, R.T., 2010. GPS velocity field for the Tien Shan and surrounding regions. Tectonics 29. doi:10.1029/2010TC002772.

Zwieback, S., Liu, L., Rouyet, L., Short, N., Strozzi, T., 2024. Advances in InSAR Analysis of Permafrost Terrain. Permafrost and Periglacial Processes 35, 544–556. doi:10.1002/ppp.2248.